THE UNIVERSE IN MANY NUTSHELLS:
HIGH RESOLUTION SIMULATIONS OF CMB WEAK GRAVITATIONAL LENSING

by

MATTEO CALABRESE

Supervisor: Carlo Baccigalupi

Co-Supervisor: Carmelita Carbone

Co-Supervisor: Giulio Fabbian

A thesis
submitted to SISSA
in fulfilment of the
requirements for the degree of
Doctor of Philosophy
in Astrophysics.

Scuola Internazionale Superiore di Studi Avanzati
2015

Abstract

This Thesis presents a new method to simulate and study weak gravitational lensing of the Cosmic Microwave Background (CMB) and its correlation with the Large Scale Structure (LSS). We exploit ray-tracing techniques to follow the photons' path from the last scattering surface, as they travel throughout a Universe which is expanding and evolving. The main analysis revolves around the concept of a light-cone, by compressing the information of N-Body numerical simulations into a set of lensing planes, which deflect the light as predicted by (weak) gravitational lensing. We perform several different numerical tests in order to establish the accuracy of our reconstruction and the precision of our simulations up to the arc-minute scale, as we explore these effects by the means of the two-points statistics. The main goal is to model non-linear effects of weak lensing by going beyond the first-order result of the Born approximation. We compare our simulations with analytical and semi-analytical predictions, as we study the signal behaviour at different scales and regimes. We confirm the validity of first order approach up to very small scales ($\ell \approx 4000$ with the current simulation's set-up, corresponding to few arc-minutes on the sky), when we find some tension especially with the signal predicted by high-order perturbation theory in the power spectrum. Finally, we implement a methodology for creating mock catalogues of galaxies populating N-Body simulations, in order to apply our pipeline to model the cross-correlation between large scale structure traces such as CMB lensing and galaxy catalogues. We show how the simulated signal can be recovered and compared with theoretical expectations and observations, enabling a thorough investigation of structure formation over cosmic time and allowing for a better understanding of cosmology and astrophysics. The resulting, end-to-end pipeline going from simulated CMB and LSS, through lensing and cross correlation of the distorted anisotropies and the lenses themselves as traced by galaxies, is part of the suites of codes and validation infrastructure while approaching high resolution and sensitivity for CMB and LSS observations, such as the Euclid satellite, or the POLARBEAR ground experiment.

Contents

Introduction

A new dawn has broken, marking the beginning of a new era: the era of precision cosmology where we can begin to talk with relative certainty about the origin of structure and the content of matter and energy in the Universe.

Recent measurements of the Planck satellite [1] has unveiled a Universe well described by a cosmological model known as ΛCDM. In this model, the Universe is expanding from the Big Bang, accelerated by a Dark Energy (DE) component well described by a cosmological constant Λ. Cold Dark Matter (CDM or simply DM) is responsible for the matter halos around galaxies and galaxy clusters, while a smaller part is left to play to leptons and baryons. The robustness of the this model comes primarily from advanced and enduring studies on the Cosmic Microwave Background (CMB), a radiation emerging from a dark, distant past, where photons were tightly coupled with matter in the same primordial bath. At the age of recombination of hydrogen nuclei, suddenly these photons are let free by a Universe which is expanding and cooling down: matter perturbations are imprinted and stored via Thomson scattering in this primordial light, producing anisotropies in the CMB signal both in total intensity (T) and in polarization, described by the Stokes parameters Q and U. According to ΛCDM, an early era of accelerated expansion, the inflation, would generate the approximately scale invariant, Gaussian, density perturbations we observe in CMB anisotropies and Large Scale Structure (LSS), and perhaps, excitations of tensor perturbations in the metric as well, known as cosmological Gravitational Waves (GWs).

The Planck satellite was able to show these CMB anisotropies over the whole sky down to a resolution of 5 arc-minutes, confirming theoretical predictions and expectations of ΛCDM model. A further step in terms of constraining power on cosmological parameters will be achieved with the high accuracy measurements of the CMB by current and future high sensitivity ground-based and balloon-borne experiment like, e.g, EBEX [2], and POLARBEAR [3], SPTpol [4], ACTpol [5], Spider [6] and Keck array [7]. These are designed to measure in particular the so-called B-modes of polarization which could provide a direct evidence for primordial GWs generated in many inflationary scenarios if indeed such signal is detected on the degree scale.

If the CMB is a picture frozen in time, a snapshot of a distant past, the Universe itself has changed and evolved up to present day. In addi-

tion to the primary anisotropies previously described, so-called secondary anisotropies are imprinted in the CMB radiation by the interaction of its photons with the LSS of the Universe along their paths from the last scattering surface to the observer. One of the most important sources of these secondary anisotropies is the gravitational lensing effect: growing and evolving matter inhomogeneities bend the geodesic path of the light, modifying the primordial CMB signal's statistical properties. Lensing distorts the primordial polarization patterns converting gradient-like E-modes into curl-like components of the polarization tensor (B-modes), generating power on the sub-degree scale where we expect the primordial signal to be negligible. This effect, even if theoretically predicted a long time ago, has been measured only recently by many different probes; the latest Planck release of 2015 has confirmed the signal with a very high significance.

The interest and scientific case for CMB lensing as a cosmological probe lies in the possibility of extracting information about the projected large scale structure potential, and thus to constrain the late-time evolution of the Universe, e.g. the effect of the DE and massive neutrinos properties. Nowadays experiments and measurements require a high-resolution, high-sensitivity reconstruction of the lensing signal. The most valued price is obviously to model correctly the B-mode of CMB polarization, from the smaller scales, where the effect of gravitational lensing is at most visible, to larger scales, where - if a signal is present - is mainly activated by primordial physics at the birth of CMB, i.e. GWs. The most accurate way to obtain those predictions is to perform ray-tracing of CMB photons through large, high resolution N-Body numerical simulations to study the full non-linear and hierarchical growth of cosmic structures. Although this approaches are computationally very demanding, they allow to check and balance the approximations and assumptions made in widely-used semi-analytic models, adjusting and extending these models if necessary.

A further step to probe DE would be to cross correlate the CMB lensing with the observations of the actual lenses in LSS surveys as seen by independent tracers of the matter distribution. This option has already been exploited to obtained astrophysical and cosmological information by, e.g., SPT, ACT and, more recently, by POLARBEAR collaborations [8, 9, 10, 11, 12], but a major improvement is expected in about a decade with the observations of the ESA-Euclid satellite. This mission will combine arc-second imaging of billions of galaxies with photometric redshift accuracy corresponding to the percent level, between redshifts $0 \lesssim z \lesssim 2$ [13, 14]. This Thesis aims at filling a gap in modern cosmology in terms of support to these ambitious goals, by constructing a methodology, implementation and validation infrastructure for high resolution and sensitivity

CMB lensing measurements, per sé and in cross-correlation with LSS.

Outline of the Thesis This Thesis is organised as follows: in the first Chapter, Chap. 1, we will review some of the main features of our current cosmological model, carefully focusing on the theory and applications of weak gravitational lensing, as background for our ray-tracing algorithm. The next Chapter, Chap. 2, will discuss the other big theoretical pillar of this work, the CMB. After introducing the formalism of the CMB statistics, we will describe its main cosmological application, and recall some of the most recent observations. The third and central Chapter, Chap. 3, will be finally dedicated to our ray-tracing algorithm, to show how it models lensed CMB fields, both temperature and polarization. This work has been presented for the first time to the astrophysical community in [15]. In Chapter 4 we will show a further improvement of our algorithm as we move towards even higher resolutions to study different lensing observables; this study will be included in a forthcoming paper [16]. Chapter 5 contains the outline of our algorithm for creation of mock catalogues, out of N-Body simulations. This procedure completes our pipeline for simulation of CMB-LSS cross-correlation via gravitational lensing, enabling us to be accurate in forecasting, including systematics and uncertainties of forthcoming LSS and CMB observations. On this subject, we intend to publish two different papers: one which will expand and improve the current XC analysis based on the Planck and Herschel datasets [17] and a further article concerning the actual simulation pipeline itself [18]. Finally, in Chapter 6 we discuss our work and present forthcoming applications. Most of the subjects touched in this Thesis has been developed within the Euclid collaboration and has been presented at several Euclid Consortium Meetings thoughout the four years of my Ph.D.

CHAPTER 1

General Cosmology and Gravitational Lensing

> In every systematic inquiry (methods) where there are first principles, or causes, or elements, knowledge and science result from acquiring knowledge of these; [...] It is clear, then, that in the science of nature as elsewhere, we should try first to determine questions about the first principles.[...] Hence it is necessary for us to progress, following this procedure, *from the things that are less clear by nature, but clearer to us, towards things that are clearer and better known by nature.*
>
> *Aristotle*, Phys. 184a10-21

As suggested by Aristotle, we start this Thesis from the first principle, which in cosmology takes the unimaginative name of *Cosmological Principle*. It states that "Viewed on a sufficiently large scale, the properties of the Universe are the same for all observers" (William Keel). Its deep philosophical meaning lies in the fact that the Universe which we can see is a fair sample of the whole, and that the same physical laws apply throughout. In essence, this is a relief to all of us observers of nature: the Universe is knowable and is playing fair with scientists. [19] The cosmological principle depends on a definition of "observer", meaning any observer at any location in the Universe; in the words of Andrew Liddle, another way to put it is "the cosmological principle [means that] the Universe looks the same whoever and wherever you are".

The hypothesis of a perfectly isotropic and homogeneous Universe, is corroborated - as the scientific method would require - by observational evidence if cosmological observations are carried out on sufficiently large enough volumes. The clearest modern evidence for the cosmological principle is measurements of the CMB. Isotropy and homogeneity is reflected in its random appearance. "Sufficiently" is the key word here: if we restrain progressively more and more the observational scale, the Universe shows an increasing in-homogeneous structure, corresponding to galaxies and clusters of galaxies. We think that these structures grew gravitationally from very small "primordial perturbations". In the inflationary paradigm, these primordial perturbations were at one stage quantum fluctuations, which were inflated to macroscopic scales. When gravity acted

on these small perturbations, it made denser regions even more dense, and under-dense regions even more under dense, resulting in the structures we see today. Because the fluctuations were thought to be small once, it makes sense to treat the growth of perturbations in an expanding Universe in linear theory. There are several excellent reviews of this, for example see Efstathiouś review in "Physics of the Early Universe" (Davies, Peacock & Heavens [20]) or "Structure formation in the Universe" (T. Padmanabhan, [21]).

However complex it may be, this overall picture needs to be verified by several observations and experiments. In the other half of this chapter, we will recall the principle of gravitational lensing and its mechanisms, a superb tool to test and verify the first principles described above. Since Newton, it had been speculated that masses should deflect light, but only thanks to Einstein's General Relativity (GR) we are able to fully describe this phenomenon. Matter intervening along the light paths of photons causes a displacement and a distortion of ray bundles. The properties and the interpretation of this effect depend on the projected mass density integrated along the line of sight and on the distances to the observer, the lens and the source. The sensitivity to mass density implies that gravitational lensing effects can probe the mass of deflectors, without regard to their dynamical stage and the nature of the deflecting matter. This is therefore a unique tool to probe the matter distribution in gravitational systems as well as to study the dynamical evolution of structures in the Universe.

This Chapter deals with the basic tools and equipment in cosmology. The first half, Sec. 1.1 introduces the background metric and content of the Universe 1.1.1, and describes how, starting from Its initial conditions 1.1.2, It has evolved throughout Its history 1.1.3. The second half of this Chapter is dedicated to the weak lensing formalism, Sec. 1.2, focusing on how the light propagates throughout the matter structure 1.2.1, the main approximations used in this work 1.2.2 and describing the most important lensing observables 1.2.3.

1.1. FRW COSMOLOGY

The simplest model for the Universe can be based on the assumption that the matter distribution is homogeneous and isotropic. This apparent simplistic framework has been proved to be right over the years by many observations of galaxy surveys and of the CMB itself [22]: 3D space has geometrical proprieties which are independent of the location (*homogeneous*) and are the same in all directions (*isotropic*). In any Universe that obey to

these rules, it is possible to choose a comoving coordinate system in which the metric has the form:

$$\mathrm{d}s^2 = -c^2\mathrm{d}t^2 + a^2(t)\left[\frac{\mathrm{d}\chi^2}{1-K\chi^2} + \chi^2\left(\mathrm{d}\theta^2 + \sin^2\theta\mathrm{d}\phi^2\right)\right], \tag{1.1}$$

called the *Robertson-Walker* metric (RW) [23, 24]. With a suitable definition of the units of χ, the curvature constant K may be assumed to have only three possible values: $K = 0$ for a spatially flat Universe; $K = 1$ for a closed Universe (positive curvature) and $K = -1$ for an open Universe (negative curvature). The factor a determines the overall scale of the spatial metric and is a function of time. It represents the cosmic expansion factor and gives the rate at which two points at fixed comoving coordinates $(\chi_1, \theta_1, \phi_1)$ and $(\chi_2, \theta_2, \phi_2)$ increase their mutual physical distance as $a(t)$ increases.

The spatial coordinates (χ, θ, ϕ) are time independent as such dependence is locked into the scale factor but the coordinate $a \cdot \chi$ has dimension of distance. If $a(t)$ grows with time, every observer sees all the other points in the Universe receding from him, as observed in the Hubble law. The instantaneous distance between us and a galaxy can be written as

$$r = \int_0^\chi \mathrm{d}r = a(t)\int_0^\chi \frac{\mathrm{d}\chi}{\sqrt{1-K\chi^2}}, \tag{1.2}$$

from which we can define the Hubble constant $H(a)$ as is related to the scale

$$H \equiv \frac{\dot{a}}{a}. \tag{1.3}$$

It is customary to describe Hubble constant with the parameter h, as

$$H_0 = 100h\ \mathrm{km/s/Mpc}. \tag{1.4}$$

Light rays travel along null geodesics, i.e. $\mathrm{d}s^2 = 0$. For a radial light ray we have in addition the angular part $\mathrm{d}\Omega^2 = \mathrm{d}\theta^2 + \sin^2\theta\mathrm{d}\phi^2 = 0$, so that Eq. (1.1) can give the relation between comoving radial distance and the cosmic time t when the photon arriving at the observer at t_0 was emitted, or:

$$c\mathrm{d}t = a(t)\mathrm{d}\chi, \tag{1.5}$$

$$\chi = \int_t^{t_0} \frac{c\mathrm{d}t}{a(t)}. \tag{1.6}$$

Now if we let a source at distance χ emit two photons at t and $t + \mathrm{d}t_{em}$, which the observer detects at t_0 and $t_0 + \mathrm{d}t_{obs}$. Employing Eq. (1.6) for both photons, it follows that $dt_{em} = a(t)\mathrm{d}t_{obs}$, or expressed in frequencies:

$$\frac{\nu_{em}}{\nu_{obs}} = \frac{1}{a(t)} \equiv (1+z), \tag{1.7}$$

where the redshift z was defined. Note that the redshift z is explicitly linked to the expansion parameter a as:

$$(1+z) = \frac{a(t_0)}{a(t)}.$$

Solving the integral on the r.h.s of Eq (1.2) for a different geometry of the Universe, we can define the comoving angular diameter $f_K(\chi)$ as:

$$f_K(\chi) \equiv \begin{cases} 1/\sqrt{K}\sin\left(\sqrt{K}\chi\right), & \text{if } K > 0 \\ \chi, & \text{if } K = 0 \\ 1/\sqrt{-K}\sinh\left(\sqrt{-K}\chi\right), & \text{if } K < 0 \end{cases} \tag{1.8}$$

where K is the external curvature of space.

Two important ways of distance determination in cosmology are measuring the apparent length of a standard ruler or the apparent brightness of a standard candle. While in a Euclidean space both would yield the same result, they become ambiguous in a RW space-time. For the first method consider two light rays emitted simultaneously from the edges of a source with diameter $\mathrm{d}l$, which arrive at the observer enclosing an angle $\mathrm{d}\theta$. The angular diameter distance then is defined as

$$D_A \equiv \frac{\mathrm{d}l}{\mathrm{d}\theta} = a(t) f_K(\chi), \tag{1.9}$$

as can be read off from the metric (1.1). The second method requires knowledge of the luminosity L of a given source. Assuming that the source radiates isotropically, its photons have spread out over an area $4\pi f_K^2(\chi)$ when arriving at the observer, are redshifted by a factor $(1+z)^{-1}$ and furthermore have their arrival frequency reduced by the same factor. The flux measured by the observer is then

$$F = \frac{L}{4\pi(1+z)^2 f_K^2(\chi)}. \tag{1.10}$$

The luminosity distance is defined analogously to Euclidean space as

$$D_L \equiv \sqrt{\frac{L}{4\pi F}} = (1+z) f_K(\chi) = (1+z)^2 D_A. \tag{1.11}$$

The RW models defines a distance scale which sets the causality structure in the Universe called (particle) horizon. This represents the largest comoving distance from which light could have reached us by now. It is defined as a function of the so-called conformal time τ

$$\tau = \int_0^t \frac{\mathrm{d}t}{a(t)}. \tag{1.12}$$

Since the Big Bang, photons can have travelled only a finite distance, which is called the horizon d_h. Its physical size at given cosmic time t or scale factor a can be computed from (1.6):

$$d_h = a(t) \int_0^t \frac{cdt'}{a(t')} = a \int_0^a \frac{cda'}{a'^2 H(a')}. \tag{1.13}$$

Obviously, regions which are separated by a distance larger than the horizon size cannot be in causal contact. However, this may change at later times, since the horizon size increases with time.

1.1.1. Friedmann equations

We have not made any *a priori* hypothesis on the scale factor function, the metric presented in the previous section is defined for any behaviour of $a(t)$. We are working in a General Relativity framework, we expect that the evolution of the Universe space-time can be determined by applying Einstein field equations of Gravitation to link the scale factor to the energy-momentum tensor of the Universe. Since a comoving observer sees a perfect isotropic Universe, if we decide to model matter and energy as a fluid, its energy-momentum tensor $T_{\mu\nu}$ necessarily takes the form of a perfect fluid at rest in comoving coordinates:

$$T_{\mu\nu} = (\rho + p) u_\mu u_\nu + p g_{\mu\nu}, \tag{1.14}$$

where ρ and p are functions of time and represent the energy density and pressure of the fluid, $g_{\mu\nu}$ is the metric tensor and u^μ is the four-velocity which in this frame takes the simple form $u^\mu = (-1, 0, 0, 0)$. ρ and p can be related by the energy conservation equation,$T^\mu_{\nu;\mu} = 0$, as

$$\dot{\rho} + 3\frac{\dot{a}}{a}(\rho + p) = 0, \tag{1.15}$$

and their relationship can be inferred when a suitable equation of state $p = p(\rho)$ couples the two quantities for any matter component present in the Universe.

The time dependence can be worked out by solving Einstein equations for the gravitational field:

$$G_{\mu\nu} = R_{\mu\nu} - \frac{1}{2}g_{\mu\nu}R - \Lambda g_{\mu\nu} = 8\pi G T_{\mu\nu}; \tag{1.16}$$

if the matter of the Universe is that of a perfect fluid described in (1.14), and the Einstein tensor $G_{\mu\nu}$ is computed for the RW metric, these equations reduce to the system of two equations:

$$\left(\frac{\dot{a}}{a}\right)^2 \equiv H^2 = \frac{8\pi G}{3}\rho + \frac{\Lambda}{3} - \frac{K}{a^2} \tag{1.17}$$

$$\frac{\ddot{a}}{a} = -\frac{4\pi G}{3}(\rho + 3p) + \frac{\Lambda}{3} \tag{1.18}$$

which are usually called *Friedmann equations*, or *Friedmann-Lemaître-Robertson-Walker* (FLRW) models after the name of the four scientists who first proposed and investigated these kind of solutions to the Einstein equations [25, 26, 27]. The equations connect three variables, $a(t)$, $\rho(t)$ and $p(t)$; an equation of state $p = p(\rho)$ and proper conditions at a given time are needed for the integration. It is conventional to specify the boundary conditions in terms of two other parameters directly connected with observations. The first one is the Hubble constant $H_0 = (\dot{a}/a)$(at present), which is historically observed to have the value $100h$, km s^{-1} Mpc^{-1}.Secondly, it is conventional to define the density of different constituents of the Universe in terms of the critical density ρ_c,

$$\rho_c = \frac{3H_0^2}{8\pi G}. \tag{1.19}$$

The critical density is the value that makes the geometry of the Universe flat ($K = 0$ in the FLRW equations). The ratio ρ/ρ_c is usually denoted by the symbol Ω. The total density due to all constituents will be taken to be $\Omega_0\rho_c$. From a heuristic point of view the Friedmann equations can be seen as the equivalent of the energy conservation principle and the second law of dynamics for classical mechanics (non relativistic). Adopting the expression of the FLRW metric two points at distance $r = a(t)\chi$ (where χ is the fixed comoving distance) will move with velocity $v = \dot{a}\chi = Hd$ as predicted by the Hubble's law.

Content of the Universe

A combination of experimental measures, including studies of the CMB, LSS, the Type-Ia supernovae magnitude-redshift relation and galaxy clusters, have now placed strong constrains on the parameters of our cosmological model. Historically, most of the tighter constrains comes from the

CMB analysis performed over the recent years by different groups and collaborations. The picture that emerges from the latest data, [28] is one in which the density of the Universe is shared between dark energy (Ω_Λ), dark matter (Ω_{dm}) and baryonic matter (Ω_b) with a Hubble parameter of 67.74 ± 0.46 km/s/Mpc. Densities are usually expressed in terms of the cosmological density parameter, $\Omega = \rho/\rho_{crit}$. The main constituents of the Universe and their contribution to Ω are listed in Table 1.1.

Table 1.1 The content of the Universe, adapted from [28]

Component	**Contribution to** Ω
CMB radiation	$\Omega_{\rm rad} \approx 4.7\ 10^{-5}$
massless neutrinos	$\Omega_\nu \simeq 3\ 10^{-5}$
massive neutrinos	$\Omega_\nu \simeq 6\ 10^{-2}\ \left(\frac{<m_\nu>}{1ev}\right)$
baryons	$\Omega_b = 0.0486 \pm 0.0005$
(of which stars)	$\Omega_s \simeq (0.0023 - 0.0041)$
dark matter	$\Omega_{dm} = 0.3089 \pm 0.0062$
dark energy	$\Omega_\Lambda = 0.6911 \pm 0.0062$

Dark matter makes up most of the matter content of the Universe today. Various dynamical tests, as well as measurements of gravitational lensing around clusters are converging on a value of $\Omega_{dm} \sim 0.3$. The abundance of baryons, instead, is now known with reasonable precision from comparing the abundance of chemical elements predicted by Big Bang theory [29] with observations. Since Ω_{dm} is much larger than Ω_b, it follows that the dark matter cannot be made of baryons, but it is necessarily a *non-baryonic* component. The most popular candidate for the dark matter is a hypothetical elementary particle like those predicted by super-symmetric theories of particle physics. These particles are generically referred as Cold Dark Matter or CDM. At the moment of recombination, these particles are not relativistic, so that their velocities' dispersion is irrelevant to the growth of density perturbations. The formation pattern is bottom-up: smaller substructures collapse earlier and form more extend ones. In a hot dark matter Universe, instead, particles are *hot*, with a high velocity dispersion which prevents the aggregation at lower scales. Hot-dark matter particles, like massive neutrinos ($m_\nu \sim 5\,eV$) foretell a top-down model, where bigger objects fragment into smaller ones. The latter case is however not supported by cosmological observations.

A recent addition to the cosmic budget is the dark energy, direct evidence first provided by studies of Type-Ia [30] supernovae of an accelerating Universe expansion. Fig. 1.1 shows an up-to-date recap of distance measurements using these type of standard candles. The data are plot-

ted with the ΛCDM best-fit, confirming a wonderful agreement between theoretical expectations and experimental results. Within the Friedmann cosmology, the most simple agent that can produce these acceleration is an Einstein constant being different from 0, in particular consistent with the value $\Omega_\Lambda \simeq 0.7$. When all components are added together, the picture is a flat Universe

$$\Omega = \Omega_b + \Omega_{dm} + \Omega_\Lambda \simeq 1. \tag{1.20}$$

Given such a cosmological model, the Universe is 13.798 ± 0.037 Gyr old. Galaxies probably began forming at $z \sim 20 - 50$ when the first sufficient deep dark matter potential wells formed to allow gas to cool and condense to form galaxies [32, 33]. Generally speaking, the overall model is called ΛCDM and it has been confirmed by several independent observations.

The cosmological constant was first introduced by Einstein while looking for a solution of Friedmann equations describing a static Universe ($\dot{a} = 0$). The role of the cosmological constant on its own will therefore cause the Universe to accelerate. The modern point of view on the cosmological constant problem goes further than the ad-hoc geometrical hypothesis of Einstein and looks at the cosmological constant as the result of the minimum energy state being non-zero in Quantum Field Theory (QFT). Moving the cosmological constant term on the right hand side of Eq. (1.16) it is clear that the vacuum energy behaves like a perfect fluid with an equation of state $w = -1$. Such fluid has a constant energy density because

$$\rho_\Lambda \propto a^0 = \frac{\Lambda}{8\pi G}. \tag{1.21}$$

The energy-density connected to the cosmological constant tends therefore to dominate over matter and radiation energy density, which decrease as the Universe expands. Solutions of the Friedmann equations in presence of a dominating positive (negative) cosmological constant are called *de Sitter* (anti-*de Sitter*) solutions and require the scale factor to evolve (recollapse) exponentially with time

$$a(t) \propto e^{Ht}, \tag{1.22}$$

because the Hubble parameter H is constant.

Once the equation of state is specified the Friedmann equations can be solved for $a(t)$ and $\rho(t)$. Commonly, it takes the form of

$$p = \omega\rho, \ \text{ with } \ 0 \leq \omega \leq 1, \tag{1.23}$$

where $\omega = 0$ for collision-less non-relativistic matter, $\omega = 1/3$ for radiation and $\omega = -1$ for the vacuum; when assuming an adiabatic expansion of the

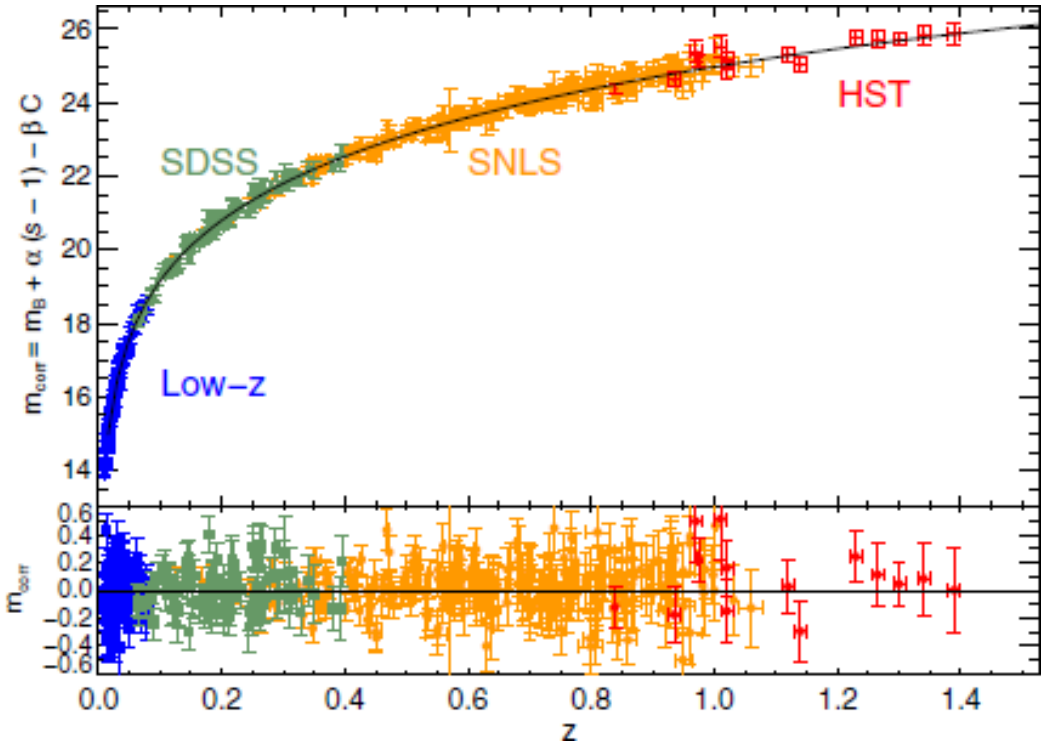

Figure 1.1 From [31]: measurements of luminosity distance using type-Ia supernovae in terms of apparent magnitude m_{corr} (top) and residual from the best fit cosmological model (bottom) using data from different surveys. The apparent magnitude is computed as $m_{\text{corr}} = m_B + \alpha(s-1) - \beta\mathcal{C}$, where m_B is the rest-frame peak B band magnitude of an SN, s is the stretch (a measure of the shape of the SN light-curve), and $\mathcal{C}$ is colour measure for the SN. α and β are nuisance parameters which characterize the stretch-luminosity and colour-luminosity relationships, reflecting the well-known broader-brighter and bluer-brighter relationships, respectively. The uncertainties on the cosmological parameter estimations from supernovae measurements are now basically only dominated by systematic errors.

Universe, we get the expression from Eq. (1.15)

$$\rho a^{3(1+\omega)} = \text{const.} \tag{1.24}$$

which links the expansion factor with the type of matter (ω) and Universe considered. Here some limiting cases:

1. *radiation-dominated* Universe with an equation of state $p = (1/3)\rho$; the evolution of density - thanks to the previous equation with $\omega = 1/3$ - is $\rho_r = \rho_{r0}(1+z)^4$;

2. *matter-dominated* Universe with an equation of state $p = 0$; in this case density goes as $\rho_m = \rho_{m0}(1+z)^3$;

3. *non-baryonic dust* Universe, possibly made of weakly interacting particles with an equation of state $p \approx 0$.

4. *non-standard components*, concerning the presence of dark energy; if a cosmological constant is assumed this is equivalent to consider a fluid with the equation of state $p \approx -\rho$.

Once the ratio between density and radiation increases with redshift we can conclude that at high z the Universe was radiation dominated. The transition between the radiation-dominated epoch and the matter-dominated one is called *equity* ($z \approx 5900$). Finally for a more complete view, we will report here the solution of Friedmann equations for some particular cosmological models. This is a useful but dated classification, based on a geometrical description of the Universe's evolution. Nowdays, especially with the *pletora* of dark energy models, geometry cannot determine alone how the Universe evolves, as the expansion history of a flat Universe with a small cosmological constant Λ can be mimic by a more complex scenario where the geometry and the DE content of the Universe vary and change.

- Einstein-de Sitter Universe (EdS); $\Omega_m = 1,\ \omega = 0, 1/3$

$$(\text{matter dominated}) \ \Rightarrow a(t) \propto t^{\frac{2}{3}}$$
$$(\text{radiation dominated}) \ \Rightarrow a(t) \propto t^{\frac{1}{2}}$$

  The expansion factor a grows indefinitely with time; moreover an Einstein-de Sitter Universe approximates the expansion of flat Universe in the first epochs when the curvature term in Friedmann equation is negligible.

- Open Universe: $\Omega_m < 1$.

  As in the previous case the expansion factor grows indefinitely with time. If $\Omega \sim 0$, then $a(t) \propto t$: the expansion is linear with time. This kind of Universe approximates the expansion of an open Universe when $a(t)$ is large, so that the density term is small and the deceleration term ($\ddot{a} \simeq 0$) is negligible.

- Closed Universe : $\Omega_m > 1$

  In this case it is possible to show that, at a certain time, the expansion factor becomes negative. The solution is therefore symmetric with respect time and consequently there are two singularities, the Big Bang and the so-called the Big Crunch.

- de Sitter Universe: $p = -\rho$.

  This situation correspond to the vacuum domination. The expansion in this case is exponential: $a(t) \propto e^{Ht}$.

1.1.2. Initial conditions

Galaxies and other cosmic structures are the result of the growth and slow amplification of small primordial density perturbations by gravity. This simple idea, even if quite simple and natural, could explain what has produced those perturbations in the first place. Only in the early 1980s a new mechanism capable of creating such density perturbations was found: *inflation*. The Big-Bang model with standard energetic content (matter or radiation) yields a decelerated expansion. On the contrary, inflation proposed a period of accelerated expansion in the very early Universe, typically ending at an energy of the order 10^{16} GeV (Grand Unification scale). During this period the geometry is close to de Sitter meaning that the expansion is exponential. Initially, it was meant to solve several conceptual problems that arose with the standard Big-Bang model [34, 35]:

- flatness problem: the spatial curvature is observationally constrained to be negligible ($\Omega_K \ll 1$) today [28]. However, using Eq. (1.15) we can prove that Ω_K grows with time, thus backward extrapolation yields that spatial curvature becomes vanishingly small as time rolls back. This necessitates unnatural initial conditions (fine-tuning problem). Inflation solves this issue by washing out spatial curvature through accelerated expansion, so that Ω_K becomes arbitrarily small at the end of inflation if that period lasted long enough.

- causal horizon: for a standard energetic content, the particle horizon at recombination (the time when the CMB were last scattered, see Chap. 2) is small compared to the typical distance between two points of the last scattering surface. This means that these points did not have time to communicate. Nevertheless, these points have a thermal equilibrium emission with extremely close temperature (to 10^{-5} precision, see e.g. [36, 37]). This again necessitates fine-tuned initial conditions which are unnatural. Inflation solves this problem, as the accelerated expansion means that these points were in fact much closer in a distant past, close enough to be in causal connection.

- monopole problem: most extensions of the standard model of particle physics predict the creation in the early Universe of magnetic monopoles (an elementary particle with the equivalent of an electric charge but sourcing the magnetic field B instead of E). However no magnetic monopole has been observed to date in the Universe. Inflation solves this apparent paradox by completely diluting the monopole density, so that there may be an arbitrarily small number of monopoles in the observable Universe.

Inflation can account for the amplification of quantum fluctuations in the density field to macroscopic scales and become established as genuine adiabatic ripples in the energy density [38, 39, 40, 41]. The basic idea is that quantum fluctuations of the inflaton are stretched out by the fast expansion and are frozen when their wavelength becomes larger than the Hubble length c/H. The details are complex and would necessitate a long description (see e.g. [42]). Nevertheless, one can show that the resulting density perturbations $\delta\rho/\rho$ (related to the gravitational potential Φ through the Poisson equation) have a nearly scale-invariant power spectrum :

$$P_\delta(k) \propto k^{n_S} \tag{1.25}$$

with $n_S \sim 1$. More precisely it would be exactly scale invariant ($n_S = 1$) if the background evolution was de Sitter, i.e. $a(t) \propto e^{Ht}$. The deviation to scale invariance can be linked to this deviation and is a general prediction of inflation models [38, 35, 40], which yield a spectral index close to, but smaller than, unity; and indeed Planck has revealed a near scale invariant spectrum, detecting significantly the deviation to scale invariance (at 68% C.L Planck CMB alone gives $n_S = 0.9667 \pm 0.0040$ [28]. As for the background, the slow roll parameters govern the magnitude of non-linearity in the perturbation evolution equations; as the vacuum initial condition

is Gaussian, it is not surprising that the resulting density perturbation are Gaussian to leading order. In a general way, for inflation to generate non-Gaussian primordial perturbations, we need either the initial conditions to be non-Gaussian or the evolution to be non-linear. The latter possibility is model dependent [43, 44, 45], and thus motivates the search for primordial non-Gaussianity as it may discriminate inflation models. Indeed these models are degenerate at the power spectrum level, as they are all built to reproduce near scale invariance.

1.1.3. Evolution of density perturbations

Primordial fluctuations grow by gravitational instability: the dark matter components, being no pressured, undergo gravitational collapse and, as such, these perturbations will grow. The linear theory of cosmological perturbations is well understood and provides an accurate description of their early ages. Once the perturbations become non-linear, their evolution is significantly more complicated, but simple arguments (e.g. spherical top-hat collapse) provide insight into the basic behaviour. The result is a network of halos string along walls and filaments forms, creating a cosmic web. This web is consistent with measurements of galaxy and quasar clustering on a wide range of scales.

The type of DM defines how structures evolve. In a CDM scenario, the relative velocities of particles are not-relativistic, and non-essential to the perturbation growth. Small density fluctuations - having lower dynamical times - are the first to collapse. The picture is a bottom-up model: bigger structures form by subsequent mergers of smaller ones. At late times, LSS forms a complex web: at large scales filaments of DM are separated by large void areas, halos form in these filaments and host clusters of galaxies. Figure 1.2 illustrates the spatial distribution of dark matter at the present day, in a series of simulations covering a large range of scales. The top-left panel illustrates the "Hubble volume simulation": on these large scales, the distribution is very smooth. Interesting structures begin to appear when we look at the DM distribution in a slice from a volume approximately 2000 times smaller. At this resolution, the characteristic filamentary appearance of the DM distribution is clearly visible. In the bottom-right panel we can recognize individual galactic-size halos, as we zoom again in the box by a factor of 5.7 in volume. These halos preferentially occur along filaments, at whose intersection large halos form that will host galaxy clusters. Finally, the bottom-left panel zooms into an individual galactic-size halo. As we will extensively discuss along this Thesis, LSS formation and evolution is studied by means of large numerical simu-

lations, called N-Body, reproducing the action of Gravity in an expanding environment (see, e.g. for Reviews [46, 47, 48]). As a good comparison, Fig. 1.3 shows the galaxy distribution as observed by the Sloan Digital Sky Survey, SDSS[1] [49]. Structure growth can roughly be divided into three regimes. Shortly after the end of inflation, virtually all density fluctuations are larger than the horizon size at that time, and therefore require a treatment within the framework of General Relativity. However, at these times, the perturbations are very small, so that linear perturbation theory is sufficient. As time goes by, more and larger fluctuations enter the horizon, then allowing for a simpler linear Newtonian description. Eventually small-scale perturbations will enter the non-linear regime, which is difficult to describe analytically, and therefore usually is studied using N-body simulations.

Sub-horizon perturbations
A Newtonian approach is valid on sub-Hubble scales ($\lambda < c/H$) where general relativity effects are negligible (see e.g. Weinberg (1972) for a much more complete discussion [54]). If a single pressure-less fluid dominates the inhomogeneities, e.g., in matter- or Λ-dominated era, the Poisson equation, mass conservation and Euler equation take the form:

$$\nabla^2_{\rm ph}\Phi = 4\pi G\rho; \tag{1.26}$$

$$\left.\frac{\partial\rho}{\partial t}\right|_{\rm ph} + \nabla_{\rm ph}\left(\rho\mathbf{v}\right) = 0; \tag{1.27}$$

$$\rho\left.\frac{\partial\mathbf{v}}{\partial t}\right|_{\rm ph} + \rho\left(\mathbf{v}\cdot\nabla_{\rm ph}\right)\mathbf{v} = -\rho\nabla_{\rm ph}\Phi; \tag{1.28}$$

where $\mathbf{v}$ is the velocity field, Φ is the Newtonian Gravitational potential, and the subscript *ph* denotes that derivatives are taken with respect to physical positions $r = a(t)\chi$, where χ is the comoving position. The physical and comoving time-derivative are also different, as the time-derivative is meant to be taken at constant spatial coordinates. The conversion between physical and comoving derivatives, the latter being noted with a subscript *co*, are:

$$\nabla_{\rm ph} = \frac{1}{a}\nabla_{\rm co}, \tag{1.29}$$

$$\left.\frac{\partial}{\partial t}\right|_{\rm ph} = \left.\frac{\partial}{\partial t}\right|_{\rm co} - H\boldsymbol{\chi}\cdot\nabla_{\rm co}. \tag{1.30}$$

[1] http://www.sdss.org/

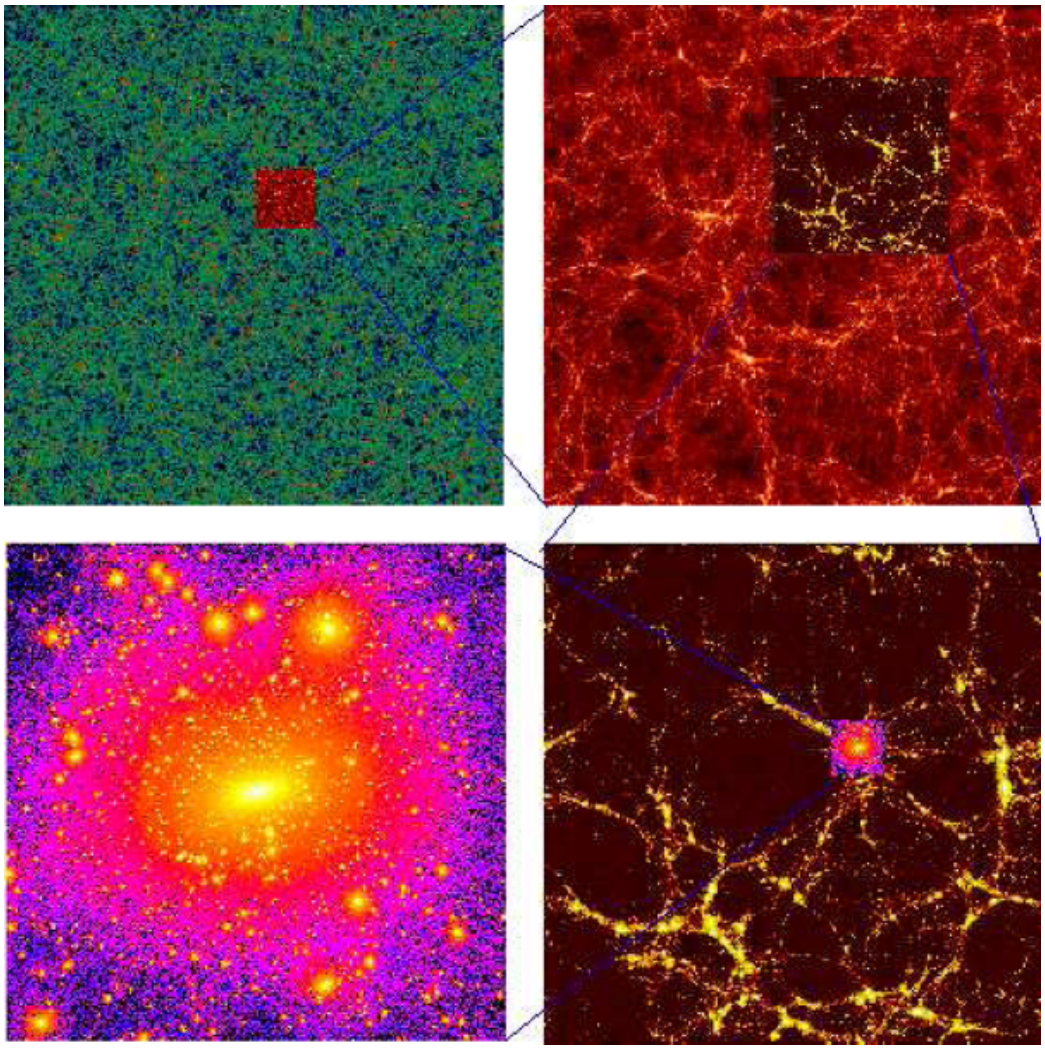

Figure 1.2 Example of a LSS N-Body Universe. The picture is taken from [50], denoting 4 different numerical simulations of the DM in the ΛCDM cosmology. Each panel is a thin slice of the cubical simulation volume and shows the slightly smoothed density field defined by the number of DM particles. In particular, denoting the number of particles in each simulation by N_p, the length of the simulation cube (*box size*) by L, and the particle mass by m_p the characteristics of each panel are as follows. Top-left (the "Hubble volume simulation", [51]): $N_p = 10^9$, $L = 3000$ h^{-1}Mpc, $m_p = 2.2 \times 10^{12}$ h$^{-1}M_\odot$. Top-right [52]: $N_p = 16.8 \times 10^6$, $L = 250$ h^{-1}Mpc, $m_p = 6.9 \times 10^{10}$ h$^{-1}M_\odot$. Bottom-right [52]: $N_p = 16.8 \times 10^6$, $L = 140$ h^{-1}Mpc, $m_p = 1.4 \times 10^{10}$ h$^{-1}M_\odot$. Bottom-left [53]: $N_p = 7 \times 10^6$, $L = 0.5$ h^{-1}Mpc, $m_p = 6.5 \times 10^5$ h$^{-1}M_\odot$.

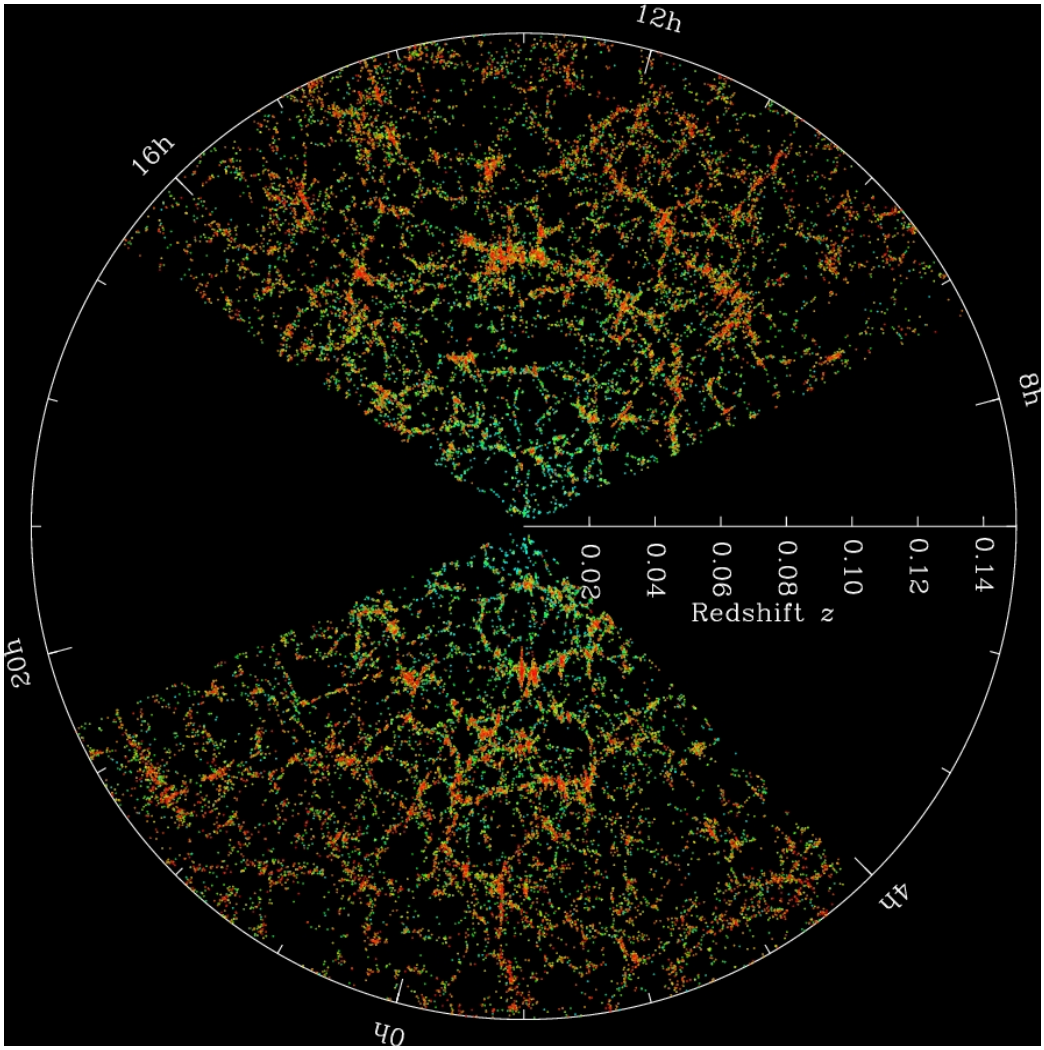

Figure 1.3 Example of a LSS observations of the Universe. The picture shows the galaxy distribution observed by the Sloan Digital Sky Survey [49]. Galaxies had been first identified on 2D images, then their distances is measured from their spectrum to create a 3D map where each galaxy is shown as a single point; the colour bar shows the local density. The galaxy sample covers an observed volume of about $0.2h^{-3}$ Gpc^3.

We will note $\delta_{\rm m} = \frac{\rho - \bar{\rho}}{\bar{\rho}}$ the relative perturbation of matter density, comprising baryonic matter and DM, and δv the velocity perturbation. Notice that the quoted perturbation variables represent a sub-set of the ones obtained by means of a GR classification cosmological perturbations [55, 56]. In particular, we consider here only scalar perturbations, and no anisotropic stress, making the two scalar Gravitational potentials indistinguishable. In this framework, density fluctuations, their peculiar velocity and the associated Gravitational potential are sufficient to describe the all processes we are interested in. We will comment specifically where this might not be the case in the rest of the Thesis. If we linearise Eqs. (1.28) around the background solution ($\rho = \bar{\rho}(t)$, $v = Hr$,$\Phi = 0$), we get in comoving coordinates:

$$\nabla^2_{\rm co}\Phi = 4\pi G a^2 \bar{\rho}\delta_{\rm m}; \tag{1.31}$$

$$\left.\frac{\partial \delta_{\rm m}}{\partial t}\right|_{\rm co} + \frac{1}{a}\nabla_{\rm co}\cdot\delta\mathbf{v} = 0; \tag{1.32}$$

$$\left.\frac{\partial \delta\mathbf{v}}{\partial t}\right|_{\rm co} + H\delta\mathbf{v} = -\frac{1}{a}\nabla_{\rm co}\Phi. \tag{1.33}$$

These equations can be combined to obtain a second-order differential equation on $\delta_{\rm m}$ only:

$$\ddot{\delta}_{\rm m} + 2H\dot{\delta}_{\rm m} = 4\pi G\bar{\rho}\delta_{\rm m} \tag{1.34}$$

where, for simplicity, the comoving time-derivative is noted with an overdot. As there are only time derivatives involved, this equation has separable solutions, i.e. of the form $\delta_{\rm m}(\mathbf{x}, t) = D(t)f(\mathbf{x})$. Moreover, the differential equation is of second-order, so there are two independent solutions, with amplitude fixed by the initial conditions:

$$\delta_{\rm m}(\mathbf{x}, t) = D^+(t)\delta^+_{\rm m}(\mathbf{x}, t_i) + D^-(t)\delta^-_{\rm m}(\mathbf{x}, t_i). \tag{1.35}$$

Let us note that the right-hand side of Eq (1.34) can also be written $\frac{3}{2}H^2\delta_{\rm m}$. Using the Friedmann equations (1.18), we see that the Hubble parameter H is solution of Eq. (1.34), hence $D^-(t) = H(t)/H(t_i)$. The other mode can be searched for in the form $D^+(t) = H(t)g(t)$, which leads to a first order differential equation on g. Hence we find:

$$D^+(t) \propto H(t)\int_{t_i}^{t} \frac{{\rm d}t}{\left[a(t)H(t)\right]^2} = H\int_{a_i}^{a}\frac{{\rm d}a}{\left(aH\right)^3}. \tag{1.36}$$

During matter domination $D^+ \propto a \propto t^{2/3}$ and $D^- \propto t^{-1}$, so that the corresponding solutions are respectively called the growing mode and the decaying mode.

Matter perturbations are small, they grow linearly without mixing their Fourier modes. No extra non-Gaussianity is generated and this stands as well for the velocity and gravitational potential fields. However, perturbations eventually grow out of the linear regime, and non-linear dynamics is not solvable analytically. As the non-linear terms in Eq. (1.28) involve spatial derivatives, the non-linearity affects predominantly small scales. In the Fourier range, large scales are hence still in the linear regime while small scales are non-linear. As time goes by, the non-linear range extends to larger and larger scales. The non-linearity can be tackled perturbatively, e.g. with Eulerian or Lagrangian perturbation theory (see [57] for a review). The linear approach described previously then gives the first order solution, and the system is solved iteratively order by order. Higher orders of computation, re-summation of loops contributions etc, enable the domain of validity to extend to smaller scales. But perturbation theory eventually fails in the fully non-linear regime [58]. In regimes where non-linearity effects become important, other approximation or hypothesis (spherical collapse, Zeldovich approximation, ...) can be considered. However, for linear perturbations, it is often sufficient to consider DM as an ideal fluid with a unique velocity at each point in space. This is a good approximation if the density fluctuations are small, so that the DM particles mainly follow the mean flow determined by the large-scale gravitational potential. This approximation breaks down when high density regions form, where particle trajectories cross frequently. Actually, because of its non-linear character, lack of symmetry and general complexity, the formation of cosmic structure is best approached theoretically using numerical simulations.

Super-horizon perturbations
If a perturbation is of a size comparable to or larger than the horizon size, the Newtonian description breaks down and general relativistic effects have to be taken into account. The basic picture can be obtained by considering a homogeneous, spherical overdensity. This will obey the same expansion equation as the background Universe, just with a slightly different mean density. From the Friedmann Eq. (1.18) it follows for the background Universe that:

$$t = \int_a^{a_0} \frac{\mathrm{d}a'}{\sqrt{\frac{8\pi G}{3}\rho a'^2 - Kc^2}} \tag{1.37}$$

The same can be written down for the perturbation, with $\rho \to \rho + \delta\rho$ and a slightly different scale factor a. Comparing these two cases at the

same cosmic time and specialising either to matter or radiation dominance yields a relation between the two scale factors, from which the density contrast of the perturbation can be computed. The result is that $\delta \propto a^2$ while radiation is the dominant species, and $\delta \propto a$ during matter dominance.

These considerations show that there is a characteristic scale in structure growth, namely the horizon size at matter-radiation equality, corresponding to a length scale of $d_{\mathrm{H}}(a_{\mathrm{eq}}) \approx 12(\Omega_{\mathrm{m}}h)^{-2}$ Mpc [58, 57].

Fourier analysis of density perturbations

The Fourier transform of the density contrast, $\tilde{\delta}(\mathbf{k}, t)$ is defined as

$$\delta(\mathbf{x}, t) = \int \frac{\mathrm{d}^3 k}{(2\pi)^3} e^{i\mathbf{k}\cdot\mathbf{x}} \tilde{\delta}(\mathbf{k}, t). \tag{1.38}$$

With this, the linear evolution equations (1.33) in Fourier space are

$$\frac{\partial \tilde{\delta}}{\partial t} + \frac{i}{a}\tilde{\mathbf{v}} \cdot \mathbf{k} = 0, \tag{1.39}$$

$$\frac{\partial \tilde{v}}{\partial t} + \frac{\dot{a}}{a}\tilde{\mathbf{v}} = \frac{-i\mathbf{k}}{a}\tilde{\Phi}, \tag{1.40}$$

$$-k^2\tilde{\Phi} = \frac{3H_0^2\Omega_{\mathrm{m}}}{2a}\tilde{\delta}. \tag{1.41}$$

where the tilde represents Fourier-transformed quantities. This shows that in the linear regime, all Fourier modes evolve independently of each other. This is no longer true when δ approaches unity and higher-order terms in the series expansion of δ have to be taken into account, causing strong mode coupling.

For the simple case of purely linear structure growth of sub-horizon perturbations during the matter dominated area, the growth factor can be computed easily. The Fourier modes of the density contrast then evolve according to

$$\delta_k(z = 0) = \frac{\delta_k(z)}{D^+(z)}. \tag{1.42}$$

This is of course an oversimplified description, because the Universe was not always matter-dominated; moreover the transition from radiation to matter dominance - thus changing the expansion law of the Universe - leads to a suppression of small-scale perturbations. Furthermore, the latter ones can be erased as soon as they enter the horizon due to relativistic particles streaming out of the shallower potential wells. Depending on the nature of the DM particles, this effect is more or less pronounced. If it consisted of light particles that are relativistic for quite a long time (Hot Dark Matter, HDM), only the largest perturbations will survive this so-called

free streaming. To account for these complications, the transfer function $T(k)$ is introduced to evolve the density contrast from a redshift z at which no scale of interest has entered the horizon to present time:

$$\delta_k(z=0) = \frac{\delta_k(z)}{D^+(z)} T(k). \tag{1.43}$$

The transfer function encodes all effects of linear evolution of fluctuations, in a GR treatment of cosmological perturbations. It is evaluated above at present, but of course it can be also expressed at a generic time. This is actually exploited for computing initial conditions in N-body simulations, as we shall see in the following sections. Usually, the transfer function is parametrised using the shape parameter $\Gamma \equiv \Omega_{\rm m} h$, which reflects the characteristic scale introduced by the horizon size at matter-radiation-equality; this parametrization, however, neglects the effect of baryons on small scales (high-k), as it depends on the dark matter contribution only.

In this final part of this Chapter we will define the basics of gravitational lensing, which are necessary for the discussion in this thesis. For a complete and exhaustive review, see [59, 60].

One of the earliest experimental tests of general relativity was the measurement of the deflection of light in the gravitational field of the sun. It was found to be consistent with Einstein's prediction of the deflection angle due to a point mass:

$$\alpha = \frac{4GM}{c^2}\frac{1}{r}, \tag{1.44}$$

where r is the impact parameter of the light ray. This result can be derived in the limit of weak gravitational fields ($\Phi/c^2 \ll 1$) and small deflections of the light ray. In this case, the metric can be written as

$$\mathrm{d}s^2 = -\left(1+\frac{2\Phi}{c^2}\right)c^2\mathrm{d}t^2 + \left(1-\frac{2\Phi}{c^2}\right)\left(\mathrm{d}x^2+\mathrm{d}y^2+\mathrm{d}z^2\right). \tag{1.45}$$

Since $\mathrm{d}s^2 = 0$ for a photon, this leads to

$$\mathrm{d}t = \sqrt{\frac{1-2\Phi/c^2}{c^2+2\Phi}}\mathrm{d}l \approx \frac{1}{c}\left(1-2\Phi/c^2\right)\mathrm{d}l, \tag{1.46}$$

where the coordinate distance between two points on the light ray $\mathrm{d}l \equiv \mathrm{d}x^2+\mathrm{d}y^2+\mathrm{d}z^2$ was defined. This is a relation between coordinate time interval $\mathrm{d}t$ and the line element along the ray. This suggests, in analogy to standard optics, to define the refractive index

$$n \equiv 1 - 2\Phi/c^2, \tag{1.47}$$

so that $v/c = 1/n$, v being the velocity of light in a specific medium. By Fermat's principle, the actual light path is the one that minimises the functional

$$t = \frac{1}{c}\int n(\mathbf{x})\mathrm{d}l. \tag{1.48}$$

Since deflections along the ray are expected to be relatively weak, we can choose the z-coordinate to parametrize the light path, so that

$$t = \frac{1}{c}\int \mathrm{d}z\, n(\mathbf{x})\sqrt{\left(\frac{\mathrm{d}x}{\mathrm{d}z}\right)^2+\left(\frac{\mathrm{d}y}{\mathrm{d}z}\right)^2+1}. \tag{1.49}$$

Varying $x(z)$ with fixed endpoints and requiring the resulting δt to vanish, one obtains

$$\frac{\mathrm{d}}{\mathrm{d}z}\left[n(\mathbf{x})\left(\left(\frac{\mathrm{d}x}{\mathrm{d}z}\right)^2+\left(\frac{\mathrm{d}y}{\mathrm{d}z}\right)^2+1\right)^{-1/2}\frac{\mathrm{d}x}{\mathrm{d}z}\right] = \frac{\partial n}{\partial x}\left[\left(\frac{\mathrm{d}x}{\mathrm{d}z}\right)^2+\left(\frac{\mathrm{d}y}{\mathrm{d}z}\right)^2+1\right]^{1/2}. \tag{1.50}$$

Multiplying by $\mathrm{d}z$ and integrating from source to observer, the result is

$$\left[n(\mathbf{x})\frac{\mathrm{d}x}{\mathrm{d}l}\right]_{\text{source}}^{\text{obs.}} = \int_{\text{source}}^{\text{obs.}} \frac{\partial n}{\partial x}\mathrm{d}l. \tag{1.51}$$

If the distance of source and observer to the deflecting mass is large, $n = 1$ at their positions and

$$\left.\frac{\mathrm{d}x}{\mathrm{d}s}\right|_{\text{obs.}} - \left.\frac{\mathrm{d}x}{\mathrm{d}s}\right|_{\text{source}} = \int_{\text{source}}^{\text{obs.}} \frac{\partial n}{\partial x}\mathrm{d}l. \tag{1.52}$$

The left hand side of this equation is nothing but the 1-component of the deflection angle $\boldsymbol{\alpha}$. The same calculation can be performed varying $y(z)$, yielding a similar expression for the 2-component, such that, finally

$$\boldsymbol{\alpha} = \int_{\text{source}}^{\text{obs.}} \nabla_{\perp} n(\mathbf{x})\mathrm{d}l = \frac{2}{c^2}\int_{\text{source}}^{\text{obs.}} \nabla_{\perp}\Phi\mathrm{d}l. \tag{1.53}$$

The result for a point mass may be obtained by inserting $\Phi = \frac{GM}{\sqrt{x^2+y^2+z^2}}$ then integrating along the unperturbed ray.

In most lensing applications, the size of the lens is much smaller than the dimensions of the whole lens system. For example, compare the size of a typical galaxy ($d < 1$ Mpc) to the typical distances between source, lens and observer, which can be of the order of 1 Gpc. Compared to the use of the full three-dimensional mass density $\rho(\mathbf{x})$ of the lens, it is thus an excellent approximation to use just a two-dimensional projection $\Sigma(\boldsymbol{\xi})$ of the lensing mass onto a plane perpendicular to the line of sight through the lens centre. The deflection is then assumed to occur only when the ray intersects the lens plane. One effect of gravitational lensing is an apparently different position of the lensed object on the sky than would be observed in absence of lensing. The overall set-up of a lens system and the relation between source and image coordinates with respect to the optical axis, defined as the line connecting observer and lens centre, is shown in Fig. 1.4. From this, by simple geometry one finds the lens equation

$$\boldsymbol{\eta} = \frac{D_{\mathrm{s}}}{\mathrm{D_d}}\boldsymbol{\xi} - D_{\mathrm{ds}}\hat{\boldsymbol{\alpha}}(\boldsymbol{\xi}). \tag{1.54}$$

Introducing angular coordinates, so that $\boldsymbol{\eta} = D_{\mathrm{s}}\boldsymbol{\beta}$ and $\boldsymbol{\xi} = D_{\mathrm{d}}\boldsymbol{\theta}$, and the scaled deflection $\boldsymbol{\alpha} \equiv \frac{D_{\mathrm{ds}}}{D_{\mathrm{s}}}\hat{\boldsymbol{\alpha}}$ the lens equation takes the simple form

$$\boldsymbol{\beta} = \boldsymbol{\theta} - \frac{D_{\mathrm{ds}}}{D_{\mathrm{s}}}\hat{\boldsymbol{\alpha}} = \boldsymbol{\theta} - \boldsymbol{\alpha}. \tag{1.55}$$

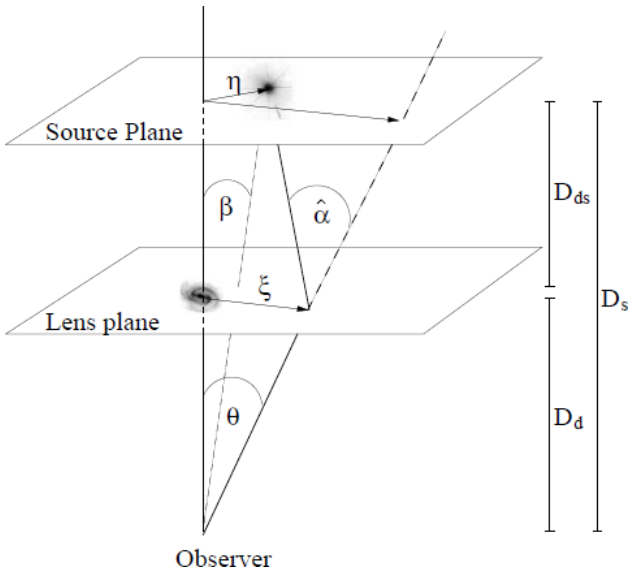

Figure 1.4 Geometry of a typical lens system.

Given a fixed source position $\boldsymbol{\beta}$, this is a non-linear equation for the image position $\boldsymbol{\theta}$, which under certain circumstances allows more than one solution, meaning that the source is multiply imaged. Eq. (1.55) defines a mapping $\boldsymbol{\theta} \to \boldsymbol{\beta}(\boldsymbol{\theta})$ from image to source plane, which in the case of multiple images is not globally invertible. If the images of the lensed object are small compared to the scales on which the deflection angle changes, and so the lens properties do not change much across one image, local information may be obtained by linearising the lens mapping.

1.2.1. Light propagation in an in-homogeneous Universe

The general treatment is given by directly solving Einstein's equations; we choose a coordinate system $(t, \beta_1, \beta_2, \chi)$ based on physical time t, two angular coordinates $\boldsymbol{\beta} = (\beta_1, \beta_2)$, and line-of-sight comoving distance χ. The space-time metric of the model is then given by a FLRW metric:

$$\mathrm{d}s^2 = -c^2\mathrm{d}t^2 + a^2(t)\left\{\mathrm{d}\chi^2 + f_K^2(\chi)\left[\mathrm{d}\beta_1^2 + \cos^2(\beta_1)\mathrm{d}\beta_2^2\right]\right\} \tag{1.56}$$

Note that the choice for the angular coordinates $\boldsymbol{\beta} = (\beta_1, \beta_2)$ differs from the usual one for spherical coordinates, see Fig. 1.5. The choice will be more convenient for the small-angle approximation. We can furthermore assume that the space-time metric of the model is given by a weakly per-

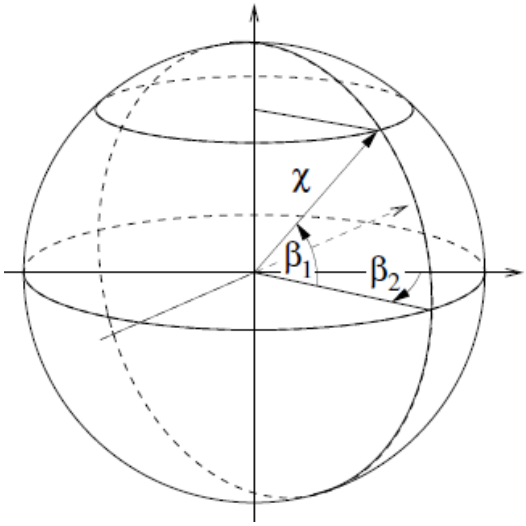

Figure 1.5 Illustration of the spatial part of the used space-time coordinate system: a spherical coordinate system (β_1, β_2, χ) based on two angular coordinates $\boldsymbol{\beta} = (\beta_1, \beta_2)$ and line-of-sight χ.

turbed FLRW metric:

$$\mathrm{d}s^2 = -\left(1 + \frac{2\Phi}{c^2}\right) c^2 \mathrm{d}t^2 + \left(1 - \frac{2\Phi}{c^2}\right) a^2(t) \left\{\mathrm{d}\chi^2 + f_K^2(\chi) \left[\mathrm{d}\beta_1^2 + \cos^2(\beta_1)\mathrm{d}\beta_2^2\right]\right\}. \tag{1.57}$$

Here, $\Phi = \Phi(t, \boldsymbol{\beta}, \chi)$ denotes the peculiar gravitational potential. Whereas the cosmological constant Λ, the curvature K, and the mean matter density $\bar{\rho}_\mathrm{m}$ determine the evolution of the scale factor a [via Eq.(1.18)], local deviations from the mean density determine the peculiar gravitational potential Φ. The potential and the density contrast δ_m then satisfy the Poisson equation

$$\nabla^2_\mathrm{co}(\boldsymbol{\beta}, \chi)\Phi(t, \boldsymbol{\beta}, \chi) = \frac{4\pi G \bar{\rho_\mathrm{m}}(t)}{a(t)} \delta_\mathrm{m}(t, \boldsymbol{\beta}, \chi), \tag{1.58}$$

where $\nabla^2_\mathrm{co}(\boldsymbol{\beta}, \chi)$ denotes the 3D Laplace operator with respect to comoving coordinates. This operator can also be expressed as

$$\nabla^2_\mathrm{co}(\boldsymbol{\beta}, \chi) = \frac{1}{f_K^2(\chi)} \left[\nabla^2_{\mathrm{co},\mathbb{S}^2}(\boldsymbol{\beta}, \chi) + \frac{\partial}{\partial\chi} f_K^2(\chi) \frac{\partial}{\partial\chi}\right], \tag{1.59}$$

where $\nabla^2_{\mathrm{co},\mathbb{S}^2}(\boldsymbol{\beta}, \chi)$ denotes the Laplace-Beltrami operator on the two-sphere $\mathbb{S}^2$. Note that this equation can be made more complicated adding other terms on the r.h.s to include curvature or other gauge terms. If one restricts

the discussion to matter in form of a pressure-less fluid of non-relativistic particles with conserved particle number, then

$$\bar{\rho}_{\rm m}(t) = \bar{\rho}_{\rm m} = \frac{3H_0^2\Omega_{\rm m}}{8\pi G} \tag{1.60}$$

and hence,

$$\nabla^2_{\rm co}(\boldsymbol{\beta},\chi)\Phi(t,\boldsymbol{\beta},\chi) = \frac{3H_0^2\Omega_{\rm m}}{2a(t)}\delta_{\rm m}(t,\boldsymbol{\beta},\chi). \tag{1.61}$$

If the previous Equation holds, the potential Φ depends only on the matter distribution and the scale factor, but not on the cosmological constant Λ. As a consequence, there is no effect of the cosmological constant Λ on the light deflection. Only the involved distances along the l.o.s. may be affected by Λ.

In Einstein's General Relativity, photon paths are null geodesics of the space-time metric. Using an affine parameter λ to parametrise the light path $\{q^\mu\}$,

$$q^\mu(\lambda) = (t(\lambda), \beta_1(\lambda), \beta_2(\lambda), \chi(\lambda))\,, \tag{1.62}$$

the null equation reads [54]:

$$0 = \sum_{\alpha\beta} g_{\alpha\beta}\frac{{\rm d}q^\alpha}{{\rm d}\lambda}\frac{{\rm d}q^\beta}{{\rm d}\lambda}, \tag{1.63}$$

while the geodesic equation for the light path reads:

$$\frac{{\rm d}^2q^\mu}{{\rm d}\lambda^2} = \sum_{\alpha\beta}\Gamma^\mu_{\alpha\beta}\frac{{\rm d}q^\alpha}{{\rm d}\lambda}\frac{{\rm d}q^\beta}{{\rm d}\lambda}. \tag{1.64}$$

Now let us return to discuss the light propagation in an in-homogeneous Universe. If a light ray reaching the observer at $(t_0, 0, 0, 0)$ in the global coordinate system $q^\mu = (t, \beta_1, \beta_2, \chi)$ is never strongly deflected, its direction $({\rm d}q^\mu/{\rm d}\lambda)$ is always almost "radial". This means that the comoving radial coordinate χ can be used to parametrise the light-ray. This is equivalent to the "small deflection angle" approximation (see, e.g., [61]) for light paths reaching the observer. To be precise, we neglect in the calculation of the angular coordinates of the light path:

- all terms of second and higher order in the peculiar potential Φ, accounting or the fact that the metric (1.56) is valid only in the weak-field limit $\Phi/c^2 \ll 1$;

- all terms of second and higher order in the angular velocities ($\mathrm{d}\boldsymbol{\beta}/\mathrm{d}\chi$), ignoring complications in the equations of motion for photons due to non-radial directions, e.g. in presence of a varying gravitational potential Φ, global curvature K, or time-dependent scale factor a;
- all terms of first and higher order in both the peculiar potential Φ and angular velocities ($\mathrm{d}\boldsymbol{\beta}/\mathrm{d}\chi$), in this case ignoring photons that travel not exactly in the radial direction, as there can be a non-zero χ-component contributing to the deflection of the photon in the angular direction.

The first approximation is justified if the peculiar gravitational field strength is small. The second and third approximations are justified if the photon direction has only very small angular components. See [62], for a discussion of the importance of additional contributions neglected by these approximations.

The lens equation

Solving the geodesic equation for the assumed metric, one obtains the following: an observer at space-time point $(t_0, 0, 0)$ in a Universe with a weakly perturbed FLRW metric (1.57) is receiving a photon with incident direction $\boldsymbol{\beta}$ from a source at redshift z. The position $(t, \boldsymbol{\beta}, \chi)$ of the source is then found by tracing back the photon along the light path $(t(\chi), \boldsymbol{\beta}(\boldsymbol{\beta}, \chi), \chi)$, where

$$\beta_i(\boldsymbol{\theta}, \chi) = \theta_i - \frac{2}{c^2}\int_0^\chi \frac{f_K(\chi - \chi')}{f_K(\chi) f_K(\chi')} \Phi_{,\beta_i}\left(t(\chi'), \boldsymbol{\beta}(\boldsymbol{\theta}, \chi'), \chi'\right) \mathrm{d}\chi'. \tag{1.65}$$

For a given mass distribution $\rho(t, \boldsymbol{\beta}, \chi)$ generating a gravitational potential $\Phi(t, \boldsymbol{\beta}, \chi)$, this equation can be integrated numerically. The relative position of nearby light rays is quantified by:

$$\begin{aligned} A_{ij}(\boldsymbol{\theta}, \chi) &= \frac{\partial \beta_i(\boldsymbol{\theta}, \chi)}{\partial \theta_j} \\ &= \delta^K_{ij} - \frac{2}{c^2}\int_0^\chi \frac{f_K(\chi - \chi')}{f_K(\chi) f_K(\chi')} \Phi_{,\beta_i\beta_k}\left(t(\chi'), \boldsymbol{\beta}(\boldsymbol{\theta}, \chi'), \chi'\right) A_{kj}(\boldsymbol{\theta}, \chi') \mathrm{d}\chi'. \end{aligned} \tag{1.66}$$

where δ^K_{ij} is the Kronecker delta. The image distortions of small light sources can be described by the distortion matrix $\mathbf{A}(\boldsymbol{\theta}, \chi) \equiv \{A_{ij}(\boldsymbol{\theta}, \chi)\}$. The lens-map can also be written as $\boldsymbol{\beta} = \boldsymbol{\theta} + \boldsymbol{\alpha}(\boldsymbol{\theta}, \chi)$, such that the (scaled) deflection angle becomes:

$$\alpha_i(\boldsymbol{\theta}, \chi) = -\frac{2}{c^2}\int_0^\chi \frac{f_K(\chi - \chi')}{f_K(\chi) f_K(\chi')} \Phi_{,\beta_i}\left(t(\chi'), \boldsymbol{\beta}(\boldsymbol{\theta}, \chi'), \chi'\right) \mathrm{d}\chi'; \tag{1.67}$$

encoding the deviation of the angular photon positions caused by a given gravitational field Φ. Known source image and position can give a complete information on the lens map and hence the underlying matter distribution. However, often we can infer only positions and shapes of objects from the data, not the intrinsic source positions, shapes, or sizes. Thus, for every lens map satisfying the observational constraints on image positions and shapes, there is a whole family of lens maps that all yield the same observed images, but for different source positions and shapes. This is known as *mass sheet degeneracy*.

1.2.2. Approximations to the lens equation

After having defined the basics of Gravitational Lensing, we will conclude this Chapter by giving some of the main approximations which are used for computing the effect in a variety of cases, which we will exploit in the following.

The first-order approximation
The approximate solution

$$\beta_i^{\rm 1st}(\boldsymbol{\theta},\chi) = \theta_i - \frac{2}{c^2}\int_0^\chi \frac{f_K(\chi-\chi')}{f_K(\chi)f_K(\chi')}\Phi_{,\theta_i}\left(t(\chi'),\boldsymbol{\theta},\chi'),\chi'\right)\mathrm{d}\chi', \tag{1.68}$$

can obtained by taking the "unperturbed" path $(t(\chi),\boldsymbol{\theta},\chi)$ as input is called the *first-order approximation* to the lens equation. This is also know as *the Born approximation*. Using the first-order lens potential

$$\psi^{\rm 1st}(\boldsymbol{\theta},\chi) = \frac{2}{c^2}\int_0^\chi \frac{f_K(\chi-\chi')}{f_K(\chi)f_K(\chi')}\Phi\left(t(\chi'),\boldsymbol{\theta},\chi'),\chi'\right)\mathrm{d}\chi', \tag{1.69}$$

and the (scaled) deflection angle

$$\alpha_i^{\rm 1st}(\boldsymbol{\theta},\chi) = -\psi^{\rm 1st}{}_{,\theta_i}\left(\boldsymbol{\theta},\chi\right); \tag{1.70}$$

this can be written as:

$$\beta_i^{\rm 1st}(\boldsymbol{\theta},\chi) = \theta_i + \alpha_i^{\rm 1st}(\boldsymbol{\theta},\chi). \tag{1.71}$$

The resulting approximation to the distortion reads:

$$\begin{aligned} A_{ij}^{\rm 1st}(\boldsymbol{\theta},\chi) &= \delta_{ij}^K - \frac{2}{c^2}\int_0^\chi \frac{f_K(\chi-\chi')}{f_K(\chi)f_K(\chi')}\Phi_{,\theta_i\theta_j}\left(t(\chi'),\boldsymbol{\theta},\chi'\right)\mathrm{d}\chi' \\ &= \delta_{ij}^K + U_{ij}(\boldsymbol{\theta},\chi), \end{aligned} \tag{1.72}$$

where the shear matrix is defined as:

$$U_{ij}^{1\mathrm{st}}(\boldsymbol{\theta},\chi) = -\psi^{1\mathrm{st}}{}_{,\theta_i\theta_j}(\boldsymbol{\theta},\chi). \tag{1.73}$$

The shear matrix $\mathbf{U}^{1\mathrm{st}}$, and hence the distortion matrix $\mathbf{A}^{1\mathrm{st}}$ are manifestly symmetric, and thus free of non-diagonal terms. Applying the Laplace operator on the 2-sphere $\nabla^2_{\mathrm{co},\mathbb{S}^2}(\boldsymbol{\beta},\chi)$ to the first-order lens potential $\psi^{1\mathrm{st}}(\boldsymbol{\theta},\chi)$, while neglecting the second integral (see, e.g., [63], for a discussion) and using Eq. (1.61), one obtains for the first-order lens potential:

$$\nabla^2_{\mathrm{co},\mathbb{S}^2}\psi^{1\mathrm{st}}(\boldsymbol{\theta},\chi) = 2\kappa^{1\mathrm{st}}(\boldsymbol{\theta},\chi), \tag{1.74}$$

where $\kappa^{1\mathrm{st}}(\boldsymbol{\theta},\chi)$ denotes the first-order lensing convergence:

$$\kappa^{1\mathrm{st}}(\boldsymbol{\theta},\chi) = \frac{3H_0^2\Omega_{\mathrm{m}}}{2c^2}\int_0^{\chi}\frac{f_K(\chi-\chi')f_K(\chi')}{f_K(\chi)a(t(\chi'))}\delta_{\mathrm{m}}\left(t(\chi'),\boldsymbol{\theta},\chi'\right)\mathrm{d}\chi'. \tag{1.75}$$

The lens potential thus satisfies the Poisson equation.

The multiple-lens-plane approximation

A feasible computational scheme to calculate the photon path is based on a discretization of the lens equation (1.65). We considered an ordered partition of the interval $[0,\chi_{\max}]$ into $N_{\max}$ sub-intervals ($\chi_{\max}$ being the largest source distance of any interest). Then the lens equation becomes:

$$\begin{aligned}\beta_i(\boldsymbol{\theta},\chi_{\max}) &= \theta_i - \frac{2}{c^2}\sum_{k=1}^{N_{\max}}\frac{f_K(\chi_{\max}-\chi^{(k)})}{f_K(\chi^{(k)})f_K(\chi_{\max})}\psi^{(k)}{}_{,\beta_i}\left(\boldsymbol{\beta}^{(k)}(\boldsymbol{\theta})\right)\\ &= \theta_i - \frac{2}{c^2}\sum_{k=1}^{N_{\max}}\frac{f_K(\chi_{\max}+\chi^{(k)})}{f_K(\chi^{(k)})f_K(\chi_{\max})}\alpha_i^{(k)}\left(\boldsymbol{\beta}^{(k)}(\boldsymbol{\theta})\right),\end{aligned} \tag{1.76}$$

where

$$\boldsymbol{\alpha}^{(k)}(\boldsymbol{\beta}) = -\nabla_{\boldsymbol{\beta}}\psi^{(k)}(\boldsymbol{\beta}), \tag{1.77}$$

$$\psi^{(k)} = \int_{\chi_{\mathrm{L}}^{(k)}}^{\chi_{\mathrm{U}}^{(k)}}\mathrm{d}\chi\psi(\boldsymbol{\beta},\chi), \tag{1.78}$$

$$\boldsymbol{\beta}^{(k)}(\boldsymbol{\theta}) = \boldsymbol{\beta}(\boldsymbol{\theta},\chi^{(k)}) = \boldsymbol{\theta} + \sum_{i=1}^{k-1}\frac{f_K^{(k,i)}}{f_K^{(k)}}\boldsymbol{\alpha}^{(i)}(\boldsymbol{\beta}^{(i)}(\boldsymbol{\theta})), \tag{1.79}$$

with $f_K^{(k)} = f_K(\chi^{(k)})$ and $f_K^{(k,i)} = f_K(\chi^{(k)}-\chi^{(i)})$. The result of the derivation (1.76) is called *multiple-lens-plane approximation*. The derivation exploits the fact that $f_K(\chi)$ and $\boldsymbol{\beta}(\boldsymbol{\theta},\chi)$ are continuous, slowly varying functions of χ. In contrast, the lens potential $\psi(t,\boldsymbol{\beta},\chi)$ (unlike the gravitational potential Φ) can vary with χ as rapidly as the matter distribution

$\delta_{\rm m}(t,\boldsymbol{\beta},\chi)$. The lensing potential still obeys the Poisson Equation, with the (discretised)-convergence

$$\kappa^{(k)}(\boldsymbol{\beta}) = \frac{4\pi G\bar{\rho}_{\rm m}}{c^2}\frac{f_K^{(k)}}{a^{(k)}}\Sigma^{(k)}(f_K^{(k)}\boldsymbol{\beta}), \tag{1.80}$$

proportional to the comoving surface mass density

$$\Sigma^{(k)}(\mathbf{x}) = \int_{\chi_{\rm L}^{(k)}}^{\chi_{\rm U}^{(k)}} {\rm d}\chi\delta_{\rm m}(t(\chi),\mathbf{x},\chi), \tag{1.81}$$

with the abbreviations $t^{(k)} = t(\chi^{(k)})$ and $a^{(k)} = a\left(t(\chi^{(k)}\right)$, while the subscript L and U relate to the lower and upper limit of the discretised interval k, where $\chi^{(k)} = (\chi_{\rm L} + \chi_{\rm U})/2$. Usually - and also in the following Chapters - we refer as $\chi_{\rm L}$ being $\chi^{(k)} - \Delta^{(k)}\chi/2$ or $\chi_{\rm U} \equiv \chi^{(k)} + \Delta\chi^{(k)}/2$, if $\Delta\chi^{(k)}$ is the thickness of the whole k-interval. The multiple-lens-plane approximation appears as if the continuous matter distribution has been approximated by a number of thin lens planes located at distances $\chi^{(k)}$ from the observer, and the light deflection by these lens planes is approximated using the sudden-deflection approximation.

Equation (1.76) is not practical for tracing rays through many lens planes. An alternative expression is obtained as follows (see, e.g., [64], for a different derivation): The angular position $\boldsymbol{\beta}^{(k)}$ of a light ray on the lens plane k is related to its positions $\boldsymbol{\beta}^{(k-2)}$ and $\boldsymbol{\beta}^{(k-1)}$ on the two previous lens planes by (see Fig.1.6):

$$f_K^{(k)}\boldsymbol{\beta}^{(k)} = f_K^{(k)}\boldsymbol{\beta}^{(k-2)} + f_K^{(k,k-2)}\boldsymbol{\epsilon}^{(k-2)} + f_K^{(k,k-1)}\boldsymbol{\alpha}^{(k-1)}(\boldsymbol{\beta}^{(k-1)}), \tag{1.82}$$

where

$$\boldsymbol{\epsilon}^{(k-2)} = \frac{f_K^{(k-1)}}{f_K^{(k-1,k-2)}}\left(\boldsymbol{\beta}^{(k-1)} - \boldsymbol{\beta}^{(k-2)}\right). \tag{1.83}$$

Hence,

$$\begin{aligned}\boldsymbol{\beta}^{(k)}(\boldsymbol{\theta}) = &\left(1 - \frac{f_K^{(k-1)}}{f_K^{(k)}}\frac{f_K^{(k,k-2)}}{f_K^{(k-1,k-2)}}\right)\boldsymbol{\beta}^{(k-2)}(\boldsymbol{\theta})\\ &+ \frac{f_K^{(k-1)}}{f_K^{(k)}}\frac{f_K^{(k,k-2)}}{f_K^{(k-1,k-2)}}\boldsymbol{\beta}^{(k-1)}(\boldsymbol{\theta})\\ &+ \frac{f_K^{(k,k-1)}}{f_K^{(k)}}\boldsymbol{\alpha}^{(k-1)}(\boldsymbol{\beta}^{(k-1)}(\boldsymbol{\theta})).\end{aligned} \tag{1.84}$$

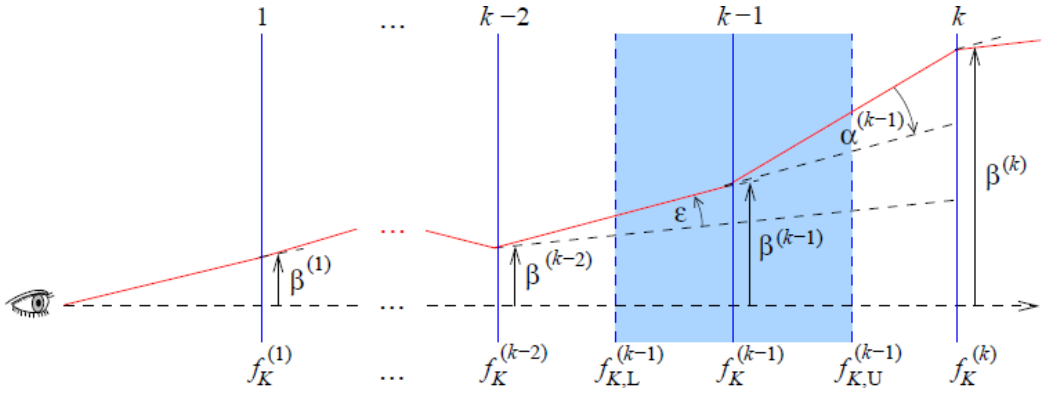

Figure 1.6 From [65]: schematic view of the observer's backward light cone in the multiple-lens-plane approximation. A light ray (red line) experiences a deflection when passing through a lens plane (solid blue lines). The deflection angle $\boldsymbol{\alpha}^{(k-1)}$ of a ray passing through the lens plane at distance $f_K^{(k-1)}$ from the observer is obtained from the matter distribution between $f_{K,\mathrm{L}}^{(k-1)}$ and $f_{K,\mathrm{U}}^{(k-1)}$ projected onto the plane. Using this deflection angle and the ray's angular positions $\boldsymbol{\beta}^{(k-1)}$ and $\boldsymbol{\beta}^{(k-2)}$ on the two previous planes, the angular position $\boldsymbol{\beta}^{(k)}$ on the current plane can be computed.

For a light ray reaching the observer from angular position $\boldsymbol{\beta}$ on the first lens plane, one can compute its angular position on the other lens planes by iterating (1.84) with initial values $\boldsymbol{\beta}^{(0)} = \boldsymbol{\beta}^{(1)} = \boldsymbol{\theta}$. Differentiating (1.84) with respect to $\boldsymbol{\theta}$, one obtains a recurrence relation for the distortion matrix

$$\begin{aligned} A_{ij}^{(k)}(\boldsymbol{\theta}) = &\left(1 - \frac{f_K^{(k-1)}}{f_K^{(k)}} \frac{f_K^{(k,k-2)}}{f_K^{(k-1,k-2)}}\right) A_{ij}^{(k-2)}(\boldsymbol{\theta}) \\ &+ \frac{f_K^{(k-1)}}{f_K^{(k)}} \frac{f_K^{(k,k-2)}}{f_K^{(k-1,k-2)}} A_{ij}^{(k-1)}(\boldsymbol{\theta}) \\ &+ \frac{f_K^{(k,k-1)}}{f_K^{(k)}} U_{im}^{(k-1)}(\boldsymbol{\beta}^{(k-1)}(\boldsymbol{\theta})) A_{mj}^{(k-1)}(\boldsymbol{\theta}), \end{aligned} \tag{1.85}$$

with

$$U_{ij}^{(k)}(\boldsymbol{\beta}) = \frac{\partial^2 \psi^{(k)}(\boldsymbol{\beta})}{\partial \beta_i \partial \beta_j}. \tag{1.86}$$

Unlike in the first-order lensing approximation, the distortion matrix (1.85) is not symmetric in general. For the reduced distortion matrix $\mathbf{U}^{(k)} =$

$\mathbf{A}^{(k)} - \mathbf{1}$, the recurrence relation reads:

$$\begin{aligned} U_{ij}^{(k)}(\boldsymbol{\theta}) = &\left(1 - \frac{f_K^{(k-1)}}{f_K^{(k)}} \frac{f_K^{(k,k-2)}}{f_K^{(k-1,k-2)}}\right) U_{ij}^{(k-2)}(\boldsymbol{\theta}) \\ &+ \frac{f_K^{(k-1)}}{f_K^{(k)}} \frac{f_K^{(k,k-2)}}{f_K^{(k-1,k-2)}} U_{ij}^{(k-1)}(\boldsymbol{\theta}) \\ &+ \frac{f_K^{(k,k-1)}}{f_K^{(k)}} U_{im}^{(k-1)}(\boldsymbol{\beta}^{(k-1)}(\boldsymbol{\theta})) \left[U_{mj}^{(k-1)}(\boldsymbol{\theta}) + \delta_{mj}^K\right]. \end{aligned} \tag{1.87}$$

1.2.3. Standard decomposition of the distortion field

The position of the light ray with respect to the global coordinate system is given by the lens equation (1.65), the relative position of nearby light rays is quantified by the distortion matrix (1.66). The distortion matrix is usually decomposed into a rotation matrix and a symmetric matrix:

$$\mathbf{A}(\boldsymbol{\theta}, \chi) = \begin{pmatrix} \cos\omega & -\sin\omega \\ \sin\omega & \cos\omega \end{pmatrix} \begin{pmatrix} 1-\kappa-\gamma_1 & -\gamma_2 \\ -\gamma_2 & 1-\kappa+\gamma_1 \end{pmatrix} \tag{1.88}$$

The decomposition defines the rotation angle $\omega = \omega(\boldsymbol{\theta}, \chi)$, the convergence $\kappa = \kappa(\boldsymbol{\theta}, \chi)$, and the two components $\gamma_1 = \gamma_1(\boldsymbol{\theta}, \chi)$ and $\gamma_2 = \gamma_2(\boldsymbol{\theta}, \chi)$ of the shear, which may be combined into the complex shear $\gamma = \gamma_1 + i\gamma_2$. The (signed) magnification $\mu(\boldsymbol{\theta}, \chi)$ of an image is given by the inverse determinant of the distortion matrix:

$$\mu = (\det\mathbf{A})^{-1}. \tag{1.89}$$

The reduced shear $g = \gamma/(1-\kappa)$ determines the major-to-minor axis ratio

$$r = \left|\frac{1+|g|}{1-|g|}\right| \tag{1.90}$$

of the elliptical images of sufficiently small circular sources. The determinant and trace of the distortion matrix,

$$\det\mathbf{A} = A_{11}A_{22} - A_{12}A_{21}, \tag{1.91}$$

$$\mathrm{tr}\mathbf{A} = A_{11} + A_{22}, \text{ resp.} \tag{1.92}$$

may be used to categorise images [66].

The convergence defines at first order the magnification of the intensity of a source. It causes an isotropic focusing of light rays, leading to

an isotropic magnification of a source, i.e., the source is mapped onto an image with the same shape but larger size. The γ shear parameter defines how the background signal is distorted by lensing and the parameter ω how this image is rotated. The distortion $\boldsymbol{\alpha}$ (referred to as field rotation) is purely a gradient term this is zero at lowest order and represents the eventual curl component of the displacement vector [67]. The curl component however appears naturally if the light is deflected by several sources at the same time even if $\omega = 0$ for each of the lenses separately. The power spectrum of this kind field rotation is expected to be a sub-percent correction in the convergence power spectrum on all scales and is smaller than the uncertainties on the contribution of the non linear effect on the lensing potential. A curl component can also be generated by first order effect of lensing due to gravitational waves, cosmic strings collisions or residual vector perturbation in the universe [68, 69, 70] although they are expected to be sub-dominant with respect to the standard gradient term arising from density perturbations.

Magnification, convergence, shear, etc. can be calculated by:

$$\mu = (\det \mathbf{A})^{-1} = (A_{11}A_{22} - A_{12}A_{21})^{-1}, \tag{1.93}$$

$$\omega = -\arctan \frac{A_{12} - A_{21}}{A_{11} + A_{22}}, \tag{1.94}$$

$$\kappa = 1 - \frac{A_{11} + A_{22}}{2\cos\omega} = 1 - \frac{1}{2}(A_{11} + A_{22})\sec\omega, \tag{1.95}$$

$$\gamma_1 = -\frac{1}{2}\left[(A_{11} - A_{22})\cos\omega + (A_{12} + A_{21})\sin\omega\right], \tag{1.96}$$

$$\gamma_2 = -\frac{1}{2}\left[(A_{12} + A_{21})\cos\omega + (A_{22} - A_{11})\sin\omega\right]. \tag{1.97}$$

$$\tag{1.98}$$

Using some algebra, one can express the modulus square of the reduced shear by:

$$|g|^2 = 1 - 4\frac{A_{11}A_{22} - A_{12}A_{21}}{(A_{11} + A_{22})^2 + (A_{12} - A_{21})^2} = \frac{(A_{11} - A_{22})^2 + (A_{12} + A_{21})^2}{(A_{11} + A_{22})^2 + (A_{12} - A_{21})^2}. \tag{1.99}$$

If one considers only weak lensing, one can expect κ, γ_1, γ_2, and ω to be small compared to unity. Then, one can expand the distortion matrix (1.88) up to linear order in these quantities:

$$\mathbf{A}(\boldsymbol{\theta}, \chi) = \begin{pmatrix} 1 - \kappa - \gamma_1 & -\gamma_2 - \omega \\ -\gamma_2 + \omega & 1 - \kappa + \gamma_1 \end{pmatrix} \tag{1.100}$$

One can use this decomposition even in the case when κ, γ_1, γ_2, and ω are not small, but then the relations between the quantities defined by

the decomposition (1.100) and the lensing observables become quite complicated. However, the decomposition (1.100) is easier to use in certain calculations than the decomposition (1.88). In the case of weak rotation, magnification, convergence, etc. can be calculated by:

$$\mu = (\det\mathbf{A})^{-1} = (A_{11}A_{22} - A_{12}A_{21})^{-1}, \tag{1.101}$$

$$\omega = -\frac{1}{2}\left(A_{12} - A_{21}\right), \tag{1.102}$$

$$\kappa = 1 - \frac{1}{2}(A_{11} + A_{22}), \tag{1.103}$$

$$\gamma_1 = -\frac{1}{2}(A_{11} - A_{22}), \tag{1.104}$$

$$\gamma_2 = -\frac{1}{2}(A_{12} + A_{21}), \tag{1.105}$$

$$|g|^2 = \frac{(A_{11} - A_{22})^2 + (A_{12} + A_{21})^2}{(A_{11} + A_{22})^2}. \tag{1.106}$$

Using the reduced distortion matrix

$$\mathbf{U} = \mathbf{A} - \mathbf{1} = \left(\frac{\partial\boldsymbol{\alpha}}{\partial\boldsymbol{\beta}}\right) = \begin{pmatrix} -\kappa - \gamma_1 & -\gamma_2 - \omega \\ -\gamma_2 + \omega & -\kappa + \gamma_1 \end{pmatrix}, \tag{1.107}$$

one obtains:

$$\mu = (\det\mathbf{1} + \mathbf{U})^{-1} = (U_{11}U_{22} - U_{12}U_{21} + U_{11} + U_{22} + 1)^{-1}, \tag{1.108}$$

$$\omega = -\frac{1}{2}\left(U_{12} - U_{21}\right), \tag{1.109}$$

$$\kappa = -\frac{1}{2}(U_{11} + U_{22}), \tag{1.110}$$

$$\gamma_1 = -\frac{1}{2}(U_{11} - U_{22}), \tag{1.111}$$

$$\gamma_2 = -\frac{1}{2}(U_{12} + U_{21}), \tag{1.112}$$

$$|g|^2 = \frac{(U_{11} - U_{22})^2 + (U_{12} + U_{21})^2}{(U_{11} + U_{22} + 2)^2}. \tag{1.113}$$

CHAPTER 2

Primary anisotropies and gravitational lensing of the Cosmic Microwave Background

> Cosmology is a science which has only a few observable facts to work with.
>
> *Robert W. Wilson, Nobel Lectures*

The CMB is the remaining light from the first instants of the Universe, emerging from a time where photon and electron are melt together in a hot, opaque, ionised and dense plasma. As the Universe expands and cools down, the temperature drops below $T \approx 3000K$, even the photons at high energy are not anymore sufficient to keep the hydrogen ionized and thus electrons and protons starts recombining. This period in the history of the Universe is called *recombination*. As a consequence, the major source of opacity in the primordial plasma disappears, the mean free path of photons increases and the Universe becomes transparent to radiation. The light could then propagate freely, photons coming from this epoch represent therefore the most distant signal we can observe.

The first CMB detection was made by Penzias and Wilson in 1965, who found an excess of antenna temperature of $3K$ uniformly distributed on the sky. However, only in the early nineties the FIRAS instrument on COBE satellite [36] was able to measure its spectrum with great accuracy. As the photons were tightly coupled to the matter before being release, they have a black body spectrum distribution with a today temperature of $T_{\rm CMB} = 2.7260 \pm 0.0013K$, measured with incredible precision by [71], as shown in Fig. 2.1. The frequency peak is at $\nu = 160$ GHz that is to say photons belong to the microwave domain. Moreover, this light appears to be isotropic in the sky once we have removed the so-called dipole due to the motion of the Sun in the CMB photon bath. COBE confirmed for the first time that the Universe at the time of recombination was indeed constituted of a photon baryon plasma in thermodynamic equilibrium, as theoretical predicted in the hot Big Bang cosmological model.

In this Chapter we will investigate in details the nature of the CMB radiation, in particular the anisotropies found in the signal, signpost of

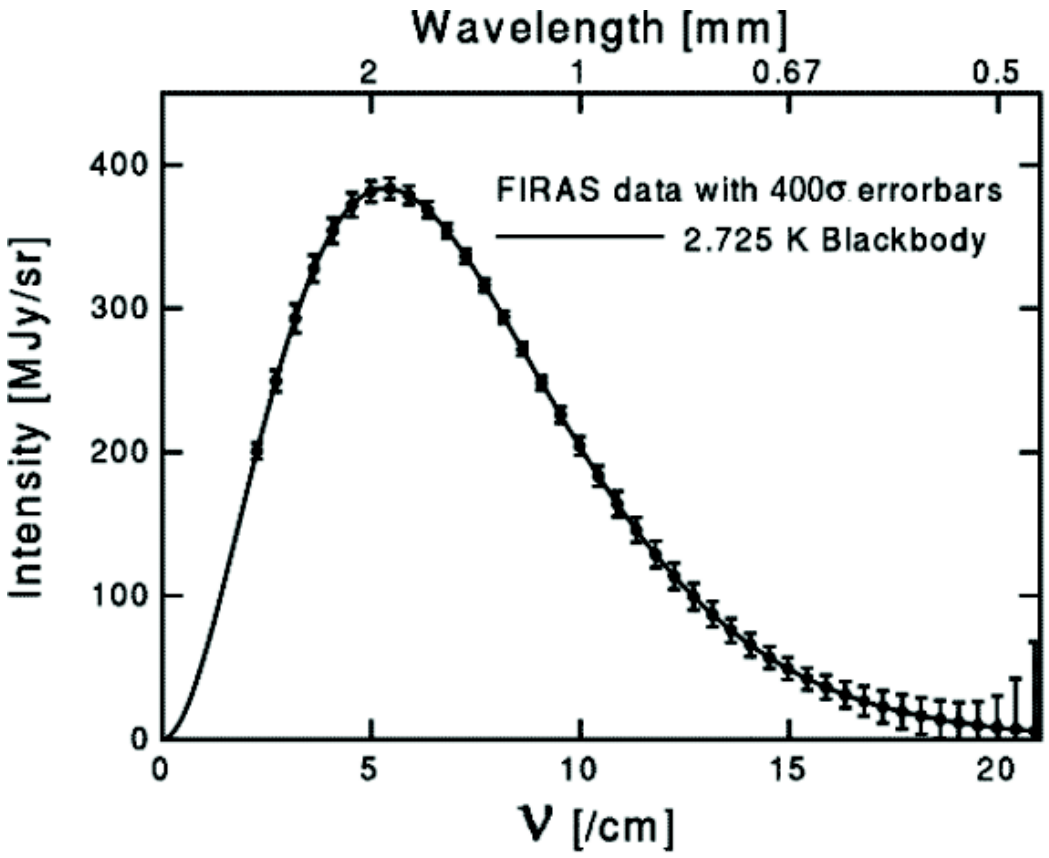

Figure 2.1 The black body spectrum of the CMB measured by the FIRAS instrument of COBE satellite [72].

the matter perturbation described in the previous Chapter. The first Section 2.1 is dedicated to a mathematical and physical description of CMB primary anisotropies, and their relation to the matter perturbation (Sec. 2.1.1). We will review as well the polarization signal coming out the CMB (Sec. 2.1.2). The second part of the Chapter treats secondary anisotropies in the CMB signal, in particular the effect of gravitational lensing as already described in the previous Chapter, Sec. 2.2. Weak lensing effects on the temperature (Sec. 2.2.1) as well as on polarization fields (Sec. 2.2.2) carry huge cosmological implications, as discussed in Sec. 2.2.3. The final part recalls the opening quote of this Chapter, as we discussed the main observational successes in the CMB physics (Sec. 2.3), their application to cosmology (Sec. 2.3.1) and their interaction with other astronomical observations, as cross-correlation (XC) studies (Sec. 2.3.2).

2.1. CMB PRIMARY ANISOTROPIES

At first, the CMB appears to be roughly homogeneous over the whole sky. The COBE satellite however revealed the presence of tiny fluctuations of the CMB temperature. These fluctuations are known to have an amplitude of:

$$\frac{\Delta T}{T_{\rm CMB}} = 10^{-5}. \tag{2.1}$$

Their spatial correlations give a prodigious amount of information on the Universe history either on its primordial or in its late time state. Figure 2.2 displays a full-sky projection of the latest CMB temperature fluctuations map as released in 2015 by the Planck Collaboration [73]. These fluctuations are due entirely to the physics of the early Universe. Before the recombination era, baryons, electrons and photons were tightly coupled together through Thomson and Coulomb scattering, i.e., the scattering rate between them was much larger than the expansion rate set by the Hubble time scale. For this reason, the primordial plasma can be considered as a single photon-baryon fluid. Dark matter inhomogeneities do not interact directly with photons, but they affect the gravitational structure of the system, thus changing the evolution of the photon-baryon fluid. Those perturbations grow though the effect of gravity and influence the distribution of baryons. After the recombination, photons decouple from matter, and basically travel "freely" towards us.

The basic observable of CMB is its intensity as a function of frequency and direction $\hat{\mathbf{n}} = (\theta, \phi)$ in the sky. Since the CMB spectrum is a blackbody with a nearly constant temperature across the sky, we can describe

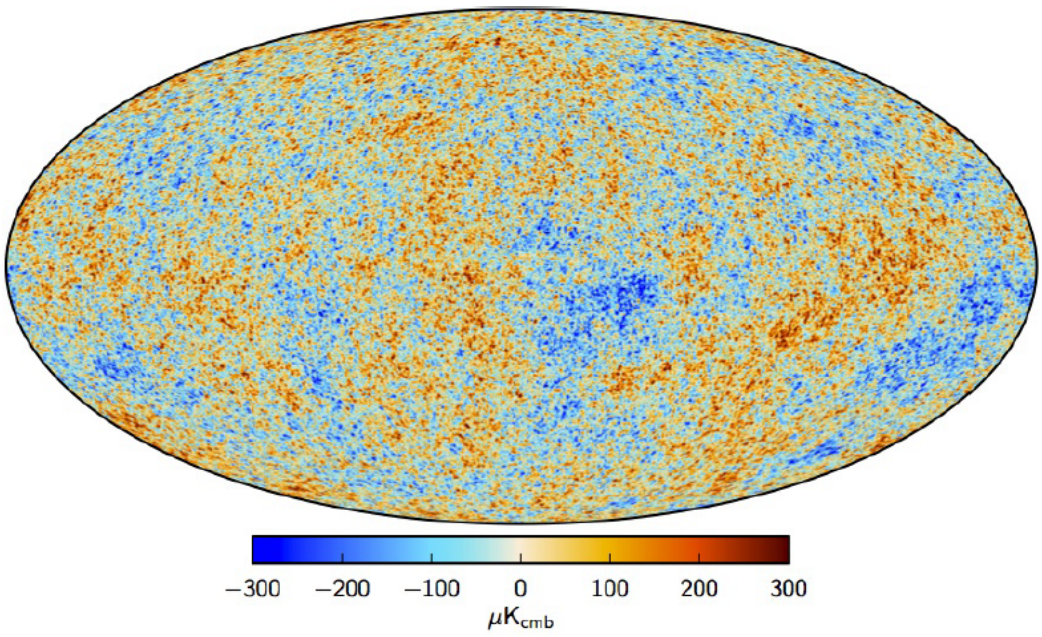

Figure 2.2 Mollweide projection of the CMB temperature fluctuations, Planck Collaboration 2015 [73].

its intensity simply in terms of temperature fluctuations,

$$\Theta(\hat{\mathbf{n}}) = \frac{\Delta T}{T}(\hat{\mathbf{n}}). \tag{2.2}$$

Instead of handling the large temperature fluctuations map, we can take advantage of the fact that the CMB signal is distributed and well-defined over the whole sky. Therefore, we can safely use a set of orthonormal functions to describe its projection over the sphere: the spherical harmonics. The CMB temperature anisotropies are usually decomposed on the spherical harmonics as:

$$\Theta_{\ell m} = \int \mathrm{d}\hat{\mathbf{n}} Y^*_{\ell m}(\hat{\mathbf{n}})\Theta(\hat{\mathbf{n}}). \tag{2.3}$$

The temperature can indeed be expanded in modes on the sphere with the multipoles ℓ - analogue to the Fourier wavenumber $|k|$ - the inverse of the scale between two points on the sky and m the orientation on the sphere. Small values therefore correspond to large angular scales on the celestial sphere.

The coefficients of this decomposition contain all the information on the amplitude of the fluctuations for a given scale, and therefore on the

state of the scalar and tensor perturbations at the time of the last scattering surface. To extract as much information as possible, we can deal with their statistics. If we assume that fluctuations in CMB are Gaussian, as the density fluctuations produced during inflation, the multipole moments of the temperature field are characterised completely by their power spectrum (or the Fourier transform of the 2-point correlation function in real space),

$$\langle \Theta_{\ell m} \Theta^*_{\ell' m'} \rangle = \delta^K_{\ell \ell'} \delta^K_{m m'} C_\ell. \tag{2.4}$$

Since for an angular scale on the sky $\theta = 2\pi/\ell$, large multipoles correspond to small angular scales and $\ell \sim 200$ represents a degree scale separation. A peculiar feature arises from this definition: as we only have access to one observable Universe, we only do have a finite amount of information to sample the $a_{\ell m}$ distribution. In fact, the power spectrum represents the average power at a given multipole ℓ an observer would see in an ensemble of several universes; however, a real observer is limited to the observation of one Universe and one sky with only one set of $\Theta_{\ell m}$, thus $2\ell + 1$ harmonics for each ℓ. The fact that there are only $2\ell + 1$ m-samples of the power in each multipole moment leads to a sample variance on the power spectra equals to

$$\Delta C_\ell = \sqrt{\frac{2}{(2\ell + 1) f_{\rm sky}}} C_\ell. \tag{2.5}$$

This inherent uncertainty on the observed angular power spectrum is called the *cosmic variance*. For a given ℓ, there are indeed $2\ell + 1$ independent modes, so that the cosmic variance is larger at low ℓ. In the above formula we also inserted the fraction of the observed sky $f_{\rm sky}$ to show that if only a part of the sky is limited, then the number of accessible modes (or number of degrees of freedom) decreases, as angular scales larger than the size of the observed sky patch are not accessible. In general, leaving aside contamination of external sources and instrumental issues, the determination of low multipoles of the spectra is intrinsically affected by a great uncertainty while, even at relatively intermediate multipoles, measurements of the power spectra are statistically more accurate.

2.1.1. The Boltzmann equation and the photon distribution

The evolution of an in-homogeneous black-body photons-distribution in time is described by a a Boltzmann equation in an expanding background; in particular, the Boltzmann equation describes the evolution of a phase space distribution $f = f(\mathbf{x}, \mathbf{p})$ of a system due to the effects of specifics

forcing effects which can be incorporated in a functional C of the phase space distribution itself:

$$\frac{\mathrm{d}f}{\mathrm{d}t} = C[f]. \tag{2.6}$$

Since the distribution of the CMB photons has been shown to be extremely isotropic, we can adopt a perturbative approach an express the phase space distribution in terms of the temperature anisotropies Θ,

$$f(\mathbf{x}, \mathbf{p}, t) = \left[exp\left(\frac{p}{kT(t)\left[1 + \Theta(\mathbf{x}, \hat{p}, t)\right]} \right) - 1 \right], \tag{2.7}$$

where Θ does not depend directly on the absolute value of the momenta p, as in Compton scatter the energy photon momentum variation is small at this energy condition. Collisions of electrons with photons affect the electrons distribution, since the scattering rate depends on the inverse of the mass of the particles. Therefore, the collision term can be computed from first principles using Feynman rules and is given by [74, 55]

$$C[f(\mathbf{p})] = -p\frac{\partial f^0}{\partial p} n_e \sigma_{\mathrm{T}} \left[\Theta_0 - \Theta(\hat{p}) + \hat{p} \cdot \mathbf{v}_b\right], \tag{2.8}$$

where σ_{T} is the Thompson cross section. Θ_0 is the monopole part of the perturbation which represents the deviation of the monopole (or CMB temperature) at a given point of space from its average on all the Universe,

$$\Theta_0 = \Theta_0(\mathbf{x}, t) \equiv \frac{1}{4\pi} \int \mathrm{d}\Omega \Theta(\hat{p}, \mathbf{x}, t), \tag{2.9}$$

and f^0 means the photon distribution (2.7) at the zero-th order in Θ. The general multipole of the perturbation distribution is defined in terms of a multipole expansion of the distribution on Legendre polynomials $\mathcal{P}_\ell$,

$$\Theta_\ell = \frac{i^\ell}{4\pi} \int_{-1}^{1} \mathrm{d}\Omega \mathcal{P}_\ell(\mathbf{x}) \Theta(\mathbf{x}). \tag{2.10}$$

The f^0 distribution can be derived as a series expansion of Eq. (2.7) and represent the equilibrium distribution of the solution of the Boltzmann equation when the thermodynamic equilibrium is reached , i.e. in presence of no collision ($C = 0$). The collision term shows how the effect of Compton scattering on the photon distribution is to drive the perturbation Θ towards its monopole value, washing out all the other multipole moments of the distribution. However the presence of the bulk velocity of the electrons and protons, $\mathbf{v}_b$, adds a dipolar term to the photon distribution by the effect of gravitational interactions. In the case for a perfect

fluid, the photons distribution is therefore characterised by a dipole and a monopole terms thanks to a very efficient Compton scattering.

Acoustic oscillations
Coulomb scattering forces electron and protons to maintain charge neutrality, leading their overdensities to a common value and the velocities of the two species to be the same:

$$\delta_e = \delta_p \equiv \delta_b, \tag{2.11}$$

$$\mathbf{v}_e = \mathbf{v}_p \equiv \mathbf{v}_b. \tag{2.12}$$

In the Newtonian gauge, the Boltzmann equation reduces to a set of linear differential equation coupling the photons distribution to the gravitational field and curvature perturbation, together with the bulk velocity of the photon baryon fluid. In this context it is convenient to solve the Boltzmann equation in the harmonic domain, as the different Fourier modes couple when non linear effects become important, which is not the case at that epoch. For the baryons the Boltzmann equation reads:

$$\dot{\tilde{\delta}}_b + ik\tilde{\mathbf{v}}_b + 3\dot{\tilde{\Phi}} = 0, \tag{2.13}$$

$$\dot{\tilde{\mathbf{v}}}_b + \frac{\dot{a}}{a}\tilde{\mathbf{v}}_b + ik\tilde{\Psi} = \frac{\dot{\tau}}{R}\left[3i\tilde{\Theta}_1 + \tilde{\mathbf{v}}_b\right], \tag{2.14}$$

where time derivatives from now on are taken with respect to the conformal time. Note that in this case we report the full derivation, as we include as well the scalar potential Ψ to be distinguished from the standard gravitational potential Φ in general conditions in which viscosity exists (like the non-negligible one caused by neutrinos at last scattering) giving rise to an anisotropic stress. In the previous equation we can define the optical depth given by the electron density in the plasma at a given conformal time as

$$\tau(\chi) \equiv \int_{\chi}^{\chi_0} \mathrm{d}\chi' n_e \sigma_{\mathrm{T}} a, \tag{2.15}$$

and the ratio between photon and baryon density as

$$\frac{1}{R} \equiv \frac{4\rho_\gamma}{3\rho_b}. \tag{2.16}$$

Defining μ as the angle between the photon direction and the wave vector, the Boltzmann equation for photons in the Fourier domain reads

$$\dot{\tilde{\Theta}} + ik\mu\tilde{\Theta} + ik\tilde{\Psi} = -\dot{\tau}\left[\tilde{\Theta}_0 - \tilde{\Theta} + \mu\tilde{v}_b\right]. \tag{2.17}$$

For a tightly coupled photon-baryon fluid, the Boltzmann equation for photons can be solved in terms of a multipole expansion, turning then the differential equation (2.17) into a virtually infinite set of coupled equations for multipole moments $\tilde{\Theta}_\ell$. This is particularly convenient since multipole moments higher than the dipole are suppressed by a factor τ and start being somehow important only close to recombination. Expanding the monopole and dipole and neglecting all the second order terms damped by the optical depth, the monopole of the photon distribution evolves in the following way:

$$c_s^2 \frac{\mathrm{d}}{\mathrm{d}\chi}\left(c_s^{-2}\dot{\tilde{\Theta}}\right) + c_s^2 k^2 \tilde{\Theta} = -\frac{k^2}{3}\tilde{\Psi} - c_s^2 c_s^2 \frac{\mathrm{d}}{\mathrm{d}\chi}\left(c_s^{-2}\dot{\tilde{\Phi}}\right), \tag{2.18}$$

where the sound speed $c_s = 1/\sqrt{3(1+R)}$ is reduced by the presence of the baryons mass with respect to a standard perfect relativistic fluid of photons, where $c_s = 1/\sqrt{3}$. Dropping the tilde for the Fourier mode for sake of simplicity, we can recast the previous Equation as

$$\frac{\mathrm{d}^2}{\mathrm{d}\chi^2}\left[\Theta_0 + \Phi\right] + \frac{\dot{R}}{1+R}\frac{\mathrm{d}}{\mathrm{d}\chi}\left[\Theta_0 + \Phi\right] + k^2 c_s^2 \left[\Theta_0 + \Phi\right] = \frac{k^2}{3}\left[\frac{1}{1+R}\Phi - \Psi\right], \tag{2.19}$$

which is the equation of a damped harmonic oscillator with a forcing term. A further simplification can be obtained if we set to zero Ψ and Φ, thus neglecting the damping term and curvature and gravitational perturbation; each different mode, as soon as its wavelength is smaller than the causal horizon, propagates as an acoustic oscillation. Pressure gradients due to photons behave like a restoring force to any initial perturbation in the system, which oscillates at the speed of sound c_s, and the photon baryon fluid heats and cools as it is compressed and rarefied by the sound waves. The main effect of gravity is to make oscillation as a competition between a pressure gradient $k\Theta_0$ and potential gradients $k\Psi$ with an equilibrium position when the quantity $\Theta_0 + \Psi$, which can be seen as an effective temperature, is equal to zero. Acoustic oscillations arise therefore from the infall and compression of the fluid into gravitational potential wells generated by dark matter, which keep growing since dark matter does not interact with photons, and by the restoring opposition due to photon pressure. The system keeps oscillating with peaks and throats until recombination comes; then photons start to free streaming towards us, oscillations in the photons distribution are frozen as they were at the last scattering surface. Modes which have their maxima or minima of oscillation at the moment of recombination correspond to peaks in the power spectrum. The first peak represents a mode caught in its first compression by recombination

and the second one represents a mode who went through a full cycle of compression and rarefaction at recombination (i.e., was at his minimum at that time). On the contrary, wavemodes with a wavenumber greater than the wavenumber corresponding to the sound horizon size at recombination ($k_* = \pi/s_*$, with s_* is the distance sound has travelled inside the horizon at recombination) never underwent to the acoustic cycle therefore are kept equal to their initial condition.

Oscillations damping
The photon baryon fluid in reality is not a perfect fluid and viscosity and heat conduction give rise to a process of diffusion inside the plasma resulting in an overall decrease of the amplitude of the peaks of acoustic waves as a function of time. The heat conduction is generated once electrons start recombining with protons and the photons mean-free path for Compton process gradually increases. Photons can therefore stream away from the over-dense hot regions towards the under-dense (cool) ones erasing fluctuations smaller (or comparable) with the mean free path of the electrons in the plasma, which is, at most, equal to the depth of Last Scattering Surface. Viscosity effects, conversely, are coupled to the production of a quadrupole moment in the photon temperature distribution which becomes important towards recombination. The final oscillator equation [75, 76, 77] is then

$$c_s^2 \frac{\mathrm{d}}{\mathrm{d}\chi}\left(c_s^{-2}\dot{\Theta}\right) + \frac{k^2 c_s^2}{\dot{\tau}}\left[A_h + A_\nu\right]\dot{\Theta}_0 + c_s^2 k^2 \Theta_0 = -\frac{k^2}{3}\Psi - c_s^2 \frac{\mathrm{d}}{\mathrm{d}\chi}\left(c_s^{-2}\dot{\Phi}\right), \quad (2.20)$$

where A_h, A_ν are the heat conduction and viscosity coefficient,

$$A_h = \frac{R^2}{1+R} \qquad A_\nu = \frac{8}{9}. \quad (2.21)$$

We expect then that inhomogeneities are damped by and exponential factor of order $e^{-(k/k_D)^2}$ where the damping scale is approximately of the order $\sqrt{\dot{\tau}/\chi}$, corresponding to the geometric mean of the mean free path and the horizon. A detailed numerical resolution of the solution of Eq. (2.20) shows that the peaks beyond the third one are substantially suppressed by diffusive effects. Intuitively, as diffusion length ultimately depends on the comoving mean free path, which is in turn controlled by the free electron density ($\lambda_C \propto \sqrt{\chi_e n_b}$), the damping scale can be used to prove the baryon content of the Universe. The effect approximately scales as $(\Omega_b h^2)^{-1/4}$.

Projecting anisotropies on the present sky
Once we have determined the evolution of a Fourier mode till the last

scattering surface, we then have to propagate the signal until the present epoch. This involves a projection from an Euclidean flat space where Fourier modes are defined onto the sky where observation are carried out (i.e., a 2D-sphere). This requires the evaluation of the source functions, i.e., the evaluation of all the multipole moments of the photon distribution today as a function of monopole, dipole and eventually quadrupole at the time of recombination. This is nowadays at the basis of current implementation of numerical solvers of cosmological Boltzmann equations [78]:

$$\begin{aligned}\Theta_\ell(k,\chi_0) \simeq & \left[\Theta_0(k,\chi_*) + \Psi(k,\chi_*)\right] j_\ell(k\chi_*) + 3\Theta_1(k,\chi_*) j'_\ell(kf_*) \\ & + \int_{\chi_*}^{\chi_0} \mathrm{d}\chi e^{-\tau} \left[\dot{\Psi} - \dot{\Phi}\right] j_\ell(k f_K(\chi)),\end{aligned} \tag{2.22}$$

where j_ℓ are the spherical Bessel functions, $f_* = f_K(\chi_*)$ is the angular diameter distance to the last scattering surface χ_* and $f_K(\chi)$ the angular diameter distance between us and an observer situated at χ. Eq. (2.22) shows that the fluctuations of the CMB temperature, while travelling towards us, can be affected by the evolution of the gravitational potential in time (represented by the third terms of the equation, which is referred to as Sachs-Wolfe effect [79], and Doppler effects due to the baryon peculiar velocity along the line of sight (see Eq. (2.14)). Today's anisotropies can be interpreted as the result of intrinsic temperature fluctuation Θ_0, modified by the gravitational redshifting effect of the potential Ψ and the Doppler shift from scattering off moving matter. The final integrated Sachs-Wolfe term involves the integral of the time derivatives of Ψ and Φ meaning that for a deeper potential well in time, photons receive a net blueshift in crossing it and the CMB appears hotter.

Once the multipoles of the distribution are known, we can finally compute the expected angular power spectrum of the CMB temperature anisotropies as a simple projection:

$$C_\ell^{\Theta\Theta} = \frac{2}{\pi} \int \mathrm{d}k k^2 \Theta_\ell^2(k,\chi_0). \tag{2.23}$$

2.1.2. CMB Polarization

Like the reflection off a surface, the Thomson scattering can generate a linear polarization in the scattered radiation: we should expect the CMB to be polarized. Nevertheless, in the primordial Universe made of the plasma, the light is coming from every direction before reaching the scattering electron: Thomson scattering of an isotropic light beam on an electron would

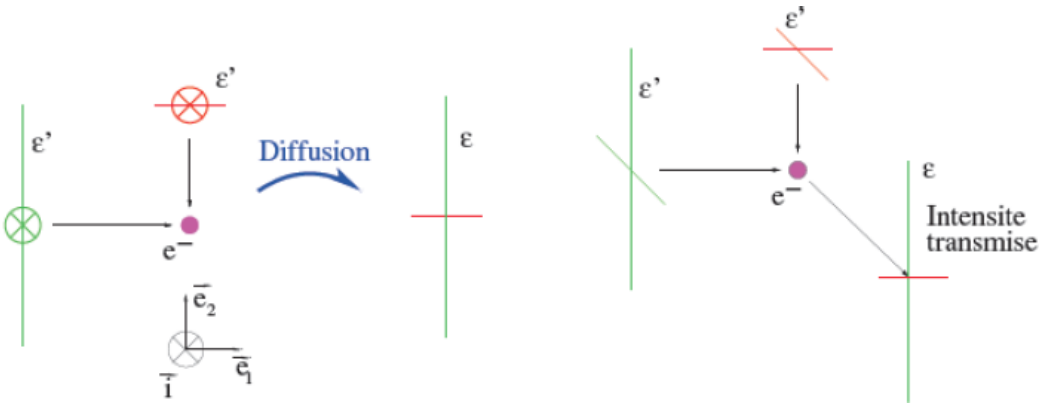

Figure 2.3 Transmitted intensity after scattering of photons presenting a quadrupolar anisotropy on a free electron. On the left panel, two incident perpendicular light beams with different intensity and the resulting intensity are depicted as projected on the plane orthogonal to the line of sight. The right panel displays the same scheme in pseudo-perspective. Picture taken from [80].

not select a specific polarization direction, leaving the net outgoing radiation unplaced. In order to observe a net polarization of the CMB light, it is necessary for the incoming light to be anisotropic for the scattering electron. As we can see from Figure 2.3 in order to produce a net polarized radiation, the incoming radiation must have a nonzero quadrupole. Since Thomson scattering produces polarization only when the incident field has a quadrupole moment, we expect the eventual polarization from the decoupling epoch to be smaller than the intensity anisotropies, as before recombination the coupling regime substantially suppressed multipoles higher than the dipole. The quadrupolar origin of the polarization can be explicitly derived [74] by computing the Stokes parameters (see later) for Thomson scattering using a harmonic decomposition of the intensity. A quadrupole corresponds to the $\ell = 2$ components in the spherical harmonics expansion. Thus the contribution from $Y_{\ell=2,m}$ (with $m \in [-2; 2]$) of the intensity decomposition alone therefore causes the CMB polarization.

Source of polarization

Let's consider now which kind of primordial perturbation can generate polarization perturbations. In the early Universe we saw that the radiation field at a given point has a dominant monopole corresponding to the temperature and a dipole corresponding to a Doppler shift velocity of the fluid, while the higher multipole were damped by the high opacity. At re-

combination a quadrupole is produced as photons free streaming begins: the photons mean free path increases progressively and every electron sees more and more anisotropic incoming radiation, due to both density and dipolar (velocity) perturbations present at that time. In the electron reference frame, only the quadrupolar component $Y_{\ell=2,m}$ of the intensity decomposition on the spherical harmonics contributes to the CMB polarization. There exists several configurations that coincide with a quadrupolar pattern corresponding to the different values of the azimuthal number m ($m \in [-2; 2]$). Consequently, the perturbations of the background sourcing quadrupolar anisotropies come in three flavours: scalar ($m = 0$), vector ($m = \pm 1$) and tensor ($m = \pm 2$). Each of them cause distinct polarization pattern.

- $m = 0$: scalar perturbations

  The scalar perturbations are fluctuations of energy density which are translated into potential fluctuations. At scales where the gravitation exceeds the pressure, over(under)-densities do attract (respectively repel) the surrounding matter. As the gravity has a radial symmetry, this system has an azimuthal symmetry. As a consequence, this radial case corresponds to the Y_{20} component of the decomposition on spherical harmonics. In the case of an over-density, an electron falling into the gravitational potential is accelerating towards the centre. The forward plasma is thus falling faster than the electron while the backward plasma is falling slower than the electron. Therefore, the electron sees the forward and backward plasma receding from him. The photons being tightly coupled to the plasma, the intensity distribution of the incoming light gets the same pattern: the electron sees light showing a quadrupolar anisotropy as sketched in the left panel of Fig. 2.3. Moreover, in this case, the polarization pattern will necessarily be radial. Indeed, the scattered light is polarized in the direction orthogonal to the incoming light. As the electron sees a more intense light in the direction tangent to its trajectory, the outgoing light is polarized along the radius of the perturbation as shown in the right panel of Fig. 2.3. In the same way, the polarization pattern is tangential for an under-density. The symmetry of the perturbation is then memorised at the level of the polarization pattern.

- $m = \pm 1$: vector perturbations

  Vector perturbations represent a vortical motions in the primordial plasma such that the velocity field in the primordial plasma acquires

also a curl-like component. They correspond to the $Y_{2,\pm1}$ component. Such perturbations are negligible as they do not outlast the inflationary phase due to their amplitude being proportional to the inverse of the scale factor, $\propto a^{-1}(t)$. Therefore, they will not be taken into account in the present manuscript.

- $m = \pm2$: tensor perturbations

  Tensor perturbations conversely play a significant role in the generation of polarization in CMB as first noted in [81]. The tensor perturbations of the perturbed metric stands for gravitational waves. When a gravitational wave go through a circle of motionless test particles, the circle is deformed, distorted into an ellipse whose semi-major axis becomes semi-minor axis as the spatial phase changes from crest to trough. The photons, coupled to the plasma, are therefore redshifted in one direction while they are blueshifted in the orthogonal direction. An electron being localised at the centre of the test particles therefore sees quadrupolar anisotropy of the light intensity. The associated stretching of the photons wavelengths produces a characteristic quadrupole proportional to the $Y_{2,\pm2}$ harmonics which can be converted into polarization through Thomson scattering [82]. The induced polarization pattern has a radial and a curl component.

In general, for a given mode, a polarization pattern on the sky cannot be separated into modes with different m because, since we can observe only one Universe, we expect to observe the ensemble averaged power for each multipole. Nevertheless there are some peculiarities of polarization patterns which survives the average and are still distinguishable, such as its parity and its correlation with temperature fluctuations.

Statistics of CMB Polarization

Before proceeding further in the analysis of CMB polarization, it is useful to recall the definition and peculiarities of the quantities required to describe a polarized radiation. A radiation field is conventionally described in terms of 4 parameters called *Stokes parameters*. Taking a (nearly) monochromatic wave with frequency ω_0 (i.e. with amplitude and phase slowly varying with time respect to the inverse of its frequency), the components of the wave electric field can be written, in a given point of the space as

$$E_x = a_x \cos\left(\omega_0 t - \theta_x(t)\right) \qquad E_y = a_y \cos\left(\omega_0 t - \theta_y(t)\right), \tag{2.24}$$

and its Stokes parameters are defines as follows [83]

$$I \equiv \langle a_x^2 \rangle + \langle a_y^2 \rangle; \tag{2.25}$$
$$Q \equiv \langle a_x^2 \rangle - \langle a_y^2 \rangle; \tag{2.26}$$
$$U \equiv \langle 2a_x a_y \cos \theta_x - \theta_y \rangle; \tag{2.27}$$
$$V \equiv \langle 2a_x a_y \sin \theta_x - \theta_y \rangle; \tag{2.28}$$
$$\tag{2.29}$$

where brackets stand for time-average. The parameter I gives the intensity of the radiation and together with the parameter V, which describes circular polarization, is a frame orientation-independent quantity, while Q and U, describe linear polarization in direction North-South or East-West (Q) and NW-SE or NE-SW (U) according to their sign, are not. The physical observable connected to polarization is defined as a "vector without head" $P = P[Q, U]$ orthogonal to waves direction of propagation, having magnitude $\sqrt{Q^2 + U^2}$ and polar angle $\alpha = \frac{1}{2} \arctan\left(\frac{U}{Q}\right)$. This quantity is not a real vector because it has no orientation, since it describes only the plane where the electric field oscillates. Being linearly polarized, the CMB polarization can be described only by the two Stokes parameters (Q, U). Being a fundamental observable for cosmology, as we will further comment in the following, the CMB polarization is the target of Planck and many suborbital CMB experiments. An example of detection of cosmological Q and U pattern is reported in Figure 2.4 where the measurements concerns a sky area relatively free of foreground emission, at an angular resolution of a few arc-minutes, and sensitivity at μK level. The Figure shows maps of the observed CMB Q and U Stokes parameter derived from the POLARBEAR CMB observations in [84].

The CMB polarization is a unique property of the primordial Universe because it traces the density perturbations and the primordial gravitational waves amplitude. In the same manner as temperature, the polarization angular power spectra would be a useful tool directly extract the cosmological information. Nonetheless, the (Q, U) Stokes parameters define a spin-(± 2) field and therefore depend on a change of coordinate system: constructing their power spectra is consequently intricate but doable as in [85]. Constructing temperature-like quantity from (Q, U) parameters could avoid this complexity. I will expose how to build such temperature-like quantities, which are the so-called E and B modes, in the harmonic domain. Following [86], we can define encompass all the information about polarization thanks to the (Q, U) Stokes parameters, the polarization fields

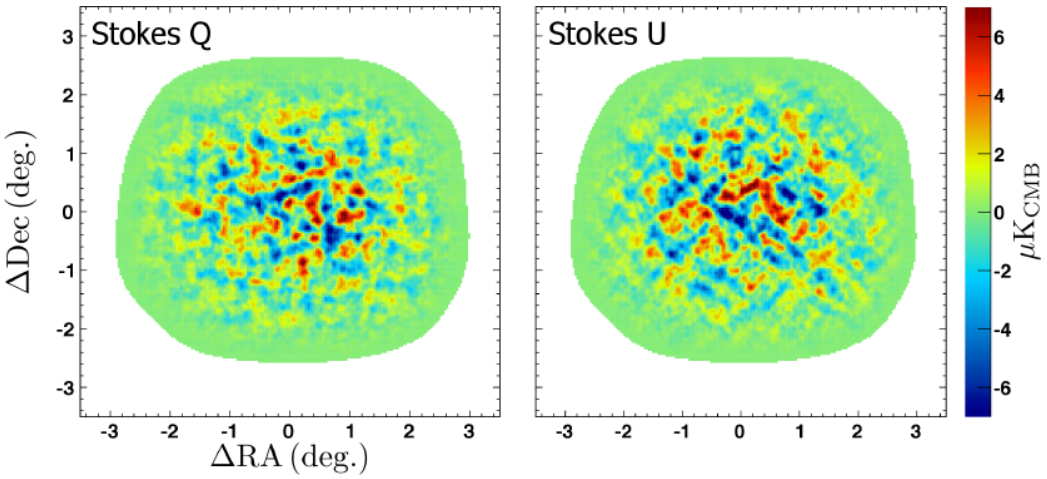

Figure 2.4 Q and U maps from [84].

$P_{\pm 2}$ along the line of sight $\hat{\mathbf{n}}$ as:

$$P_{\pm 2}(\hat{\mathbf{n}}) = Q(\hat{\mathbf{n}}) \pm iU(\hat{\mathbf{n}}). \tag{2.30}$$

Under a rotation of an angle γ, such a field $P_{\pm 2}$ is transformed into $P'_{\pm 2}$ following:

$$P'_{\pm 2}(\hat{\mathbf{n}}) = e^{\pm 2i\gamma} P_{\pm 2}(\hat{\mathbf{n}}). \tag{2.31}$$

This is why the polarization field is by definition a spin-(± 2) field. It thus can be decomposed over the basis of the spin spherical harmonics:

$$P_{\pm 2}(\hat{\mathbf{n}}) = \sum_{\ell m} {}_{\pm 2}a_{\ell m}\, {}_{\pm 2}Y_{\ell m}(\hat{\mathbf{n}}), \tag{2.32}$$

or equivalently:

$${}_{\pm 2}a_{\ell m} = \int \mathrm{d}\Omega\, {}_{\pm 2}Y_{\ell m}(\hat{\mathbf{n}}) P_{\pm 2}(\hat{\mathbf{n}}) \tag{2.33}$$

The spin-raising ∂ and spin-lowering $\bar{\partial}$ operators, built from the derivatives on the sphere, respectively increase or decrease the spin of a unity as shown in [86]. The spin-(± 2) spherical harmonics, ${}_{\pm 2}Y_{\ell m}$, are linked to the standard spherical harmonics following:

$${}_{2}Y_{\ell m} = \frac{1}{\sqrt{\alpha_\ell}} \partial\partial Y_{\ell m}, \tag{2.34}$$

$${}_{-2}Y_{\ell m} = \frac{1}{\sqrt{\alpha_\ell}} \bar{\partial}\bar{\partial}, Y_{\ell m}, \tag{2.35}$$

with $\alpha_\ell = \sqrt{\frac{(\ell+2)!}{(\ell-2)!}}$. A spin-0 quantity can thus be deduced from the spin-(± 2) polarization field multipoles in Eq. (2.33) using twice the spin-raising ∂ and spin-lowering $\bar{\partial}$ operators and by integrating by part:

$$ {}_2a_{\ell m} = \frac{1}{\alpha_\ell} \int \mathrm{d}\Omega Y^*_{\ell m}(\hat{\mathbf{n}}) \bar{\partial}\bar{\partial} P_{+2}(\hat{\mathbf{n}}), \tag{2.36} $$

$$ {}_{-2}a_{\ell m} = \frac{1}{\alpha_\ell} \int \mathrm{d}\Omega Y^*_{\ell m}(\hat{\mathbf{n}}) \partial\partial P_{-2}(\hat{\mathbf{n}}). \tag{2.37} $$

From the spin multipole coefficients ${}_{\pm 2}a_{\ell m}$, two new relevant multipoles are introduced:

$$ a^E_{\ell m} = -\frac{1}{2} \left[{}_2a_{\ell m} + {}_{-2}\, a_{\ell m} \right], \tag{2.38} $$

$$ a^B_{\ell m} = \frac{i}{2} \left[{}_2a_{\ell m} - {}_{-2}\, a_{\ell m} \right]. \tag{2.39} $$

The E and B multipoles are characterised by their behaviour under parity change. If the coordinate system $(\hat{e}_x, \hat{e}_y)$ undergoes a parity transformation in $(\hat{e}'_x, \hat{e}'_y) = (\hat{e}_x, -\hat{e}_y)$, then the Stokes parameters are straightforwardly expressed as $Q' = Q$ and $U' = -U$. Consequently, the E multipoles $a^E_{\ell m}$ are not changed under this transformation while the B modes multipoles $a^B_{\ell m}$ become $-a^B_{\ell m}$. The behaviour of E and B multipoles under parity change is the reason for their denomination recalling the electric and magnetic field properties. The built E and B multipoles, $a^E_{\ell m}$ and $a^B_{\ell m}$ respectively, are the coefficients of the scalar E and B modes fields:

$$ E(\hat{\mathbf{n}}) = \sum_{\ell m} a^E_{\ell m} Y_{\ell m}(\hat{\mathbf{n}}), \tag{2.40} $$

$$ B(\hat{\mathbf{n}}) = \sum_{\ell m} a^B_{\ell m} Y_{\ell m}(\hat{\mathbf{n}}). \tag{2.41} $$

Alternatively, the E and B modes have a unequivocal correspondence with respectively divergent- and curl-like quantity as shown in [87]. As a result, the decomposition in the harmonic domain of the spin-(± 2) polarization field allows the construction of the scalar quantities E and B. In Figures 2.5,2.6 shows E-modes and B-modes polarization patterns generated by scalar ($\ell = 2$, $m = 0$) and tensor ($\ell = 2$, $m = 2$) matter density perturbations. The main issue for interpreting the E and B modes is that they are not locally related to the (Q, U) Stokes parameters. We cannot deduce the value for E or B modes on a given pixel from the observed (Q, U) parameters on the same pixel. Nonetheless, the E and B modes have characteristic polarization patterns. As shown above, the E-modes are an even quantity

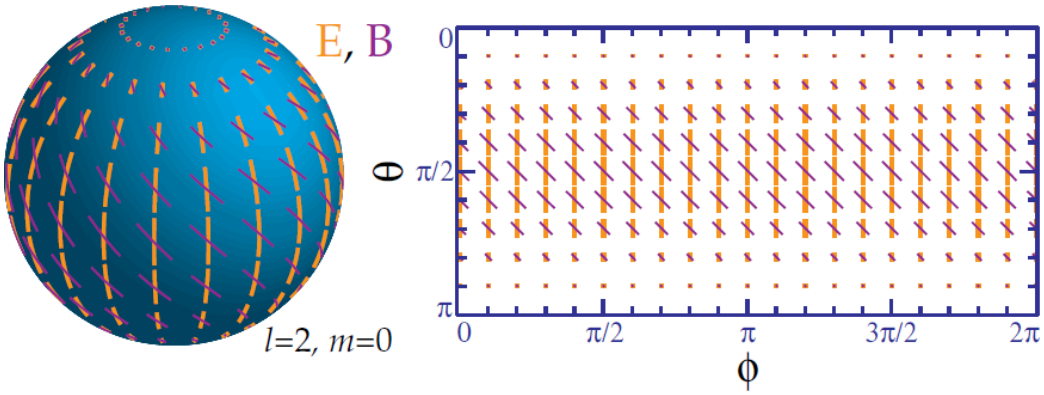

Figure 2.5 Polarization pattern for $\ell = 2$, $m = 0$, note the azimuthal symmetry. From [82].

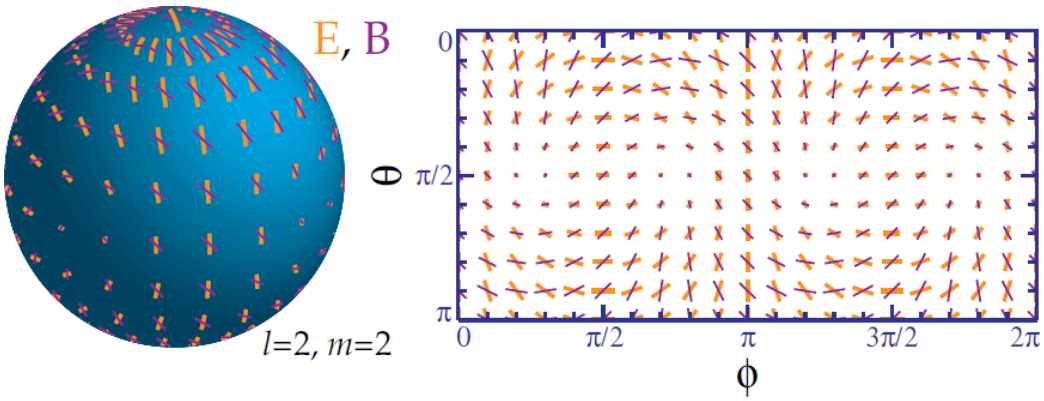

Figure 2.6 Polarization pattern for $\ell = 2$, $m = 2$, note the azimuthal symmetry. From [82].

therefore the corresponding polarization pattern should be also parity invariant. On the contrary, the B-modes are an odd quantity as their sign change under a parity transformation (see Figures 2.5,2.6). From previous considerations, we have acknowledged that the scalar perturbations always produce a symmetric polarization pattern, so they only account for the even E modes. Gravitational waves are partly invariant and partly variant under a parity transformation. The even gravitational waves can thus induce both temperature (T-modes) and E-modes. The odd gravitational waves can however only generate B modes pattern in the CMB, unlike scalar perturbations. In other words, primordial B-modes are only a signature of the tensor perturbations.

However, as we will extensively discuss in the following, CMB photons have crossed gravitational potentials implying that they are deflected, which results in E-modes deformation. The distorted E-modes behave like B-modes and are thus called the lensed B-modes. Fortunately, this only affects the small angular scales of the B-modes pattern while the primordial signal in B-modes is expected to be predominant on the largest scales. Thus, the large scales B-modes are a powerful probe of the primordial Universe as they are a signature of the primordial gravitational waves. The latter also affect the temperature and E modes anisotropies power spectra. Nonetheless, the contribution from the scalar perturbations overwhelms the tensor perturbations presumed to below. Thus, the B-modes power spectra is a key quantity to target the primordial Universe.

Polarization power spectra

The CMB temperature and polarization power spectra are built thanks to the scalar description of the polarization field. Similarly to the temperature, the polarized power spectra are defined by:

$$\langle a^{T}_{\ell m} a^{T*}_{\ell' m'} \rangle = C^{TT}_{\ell} \delta^{K}_{\ell\ell'} \delta^{K}_{mm'}, \tag{2.42}$$
$$\langle a^{E}_{\ell m} a^{E*}_{\ell' m'} \rangle = C^{EE}_{\ell} \delta^{K}_{\ell\ell'} \delta^{K}_{mm'}, \tag{2.43}$$
$$\langle a^{B}_{\ell m} a^{B*}_{\ell' m'} \rangle = C^{BB}_{\ell} \delta^{K}_{\ell\ell'} \delta^{K}_{mm'}, \tag{2.44}$$
$$\langle a^{T}_{\ell m} a^{E*}_{\ell' m'} \rangle = C^{TE}_{\ell} \delta^{K}_{\ell\ell'} \delta^{K}_{mm'}, \tag{2.45}$$
$$\langle a^{T}_{\ell m} a^{B*}_{\ell' m'} \rangle = C^{TB}_{\ell} \delta^{K}_{\ell\ell'} \delta^{K}_{mm'}, \tag{2.46}$$
$$\langle a^{E}_{\ell m} a^{B*}_{\ell' m'} \rangle = C^{EB}_{\ell} \delta^{K}_{\ell\ell'} \delta^{K}_{mm'}, \tag{2.47}$$

with $a^{T/E/B}_{\ell m}$ the coefficients of the decomposition of the T ,E and B modes on the spherical harmonics $Y_{\ell m}$ and ${}_{\pm 2}Y_{\ell m}$. Furthermore, as the E modes are even and the B modes are odd, the TB and EB cross-correlations are expected to vanish in the standard model of cosmology as the Universe

is parity invariant. It is worth reminding that although the B modes are odd, their power spectrum is even because it involves squared quantities. The Figure 2.7 shows the scalar (left panel) and tensor (right panel) part of the temperature as well as the polarized power spectra, from [88]. The temperature is, as expected, at least an order of magnitude higher than the polarization. Furthermore, the temperature and the E-modes are anti-correlated because of the E-modes amount for the velocity gradient in the primordial plasma, whereas the T-modes are only sensitive to the velocity itself. Moreover, the bump at $\ell \lesssim 10$ in the polarized power spectra is the signature of a second scattering process during the reionisation, the formation of the first stars. Besides, the B-modes power spectra is decomposed on its expected primordial tensor part, peaking at low ℓ, and its lensing scalar part, dominating at $\ell \sim 1000$. In the end, the detected power spectra are the sum of the two, scalar and tensor, contributions. Nevertheless, the temperature, E-modes power spectra and TE correlations are dominated by the scalar contribution which is at least one order of magnitude higher than the tensor contribution, as clearly shown on Fig. 2.7. It establishes the B-modes as a unique signature of the tensor perturbations at low ℓ.

2.2. Secondary anisotropies

On their way towards us, CMB photons interact with cosmic structures and their frequency, density and velocity fields of the Universe, as energy or direction of propagation are affected. These effects are known as secondary anisotropies; they can be split into two major categories: gravitational effects (gravitational lensing, the Rees-Sciama effect, ...) and scattering effects due to the interaction between CMB photons and free electrons. In this Section, we will briefly describe the main processes, although we will almost uniquely focus on the interaction between CMB light and matter, i.e. the weak lensing of CMB. A complete review of those secondary anisotropies can be found in [89].

As the photons travel from the last scattering surface to the observer, they are sensitive to the evolution of the large-scale structure gravitational potentials which modify anisotropies. Density perturbations cease to grow as the DE component starts to dominate the energy balance in the Universe: the gravitational potentials must then decay. When a photon falls into a gravitational potential well, it gets blue-shifted causing an effective heating, while, on the contrary if it tries to climb out of it, its frequency gets red-shifted. On the other hand, the opposite effect occurs in under-dense regions and the overall contributions tend to cancel each others for small scales where the photons traverse many crests and troughs of the potential

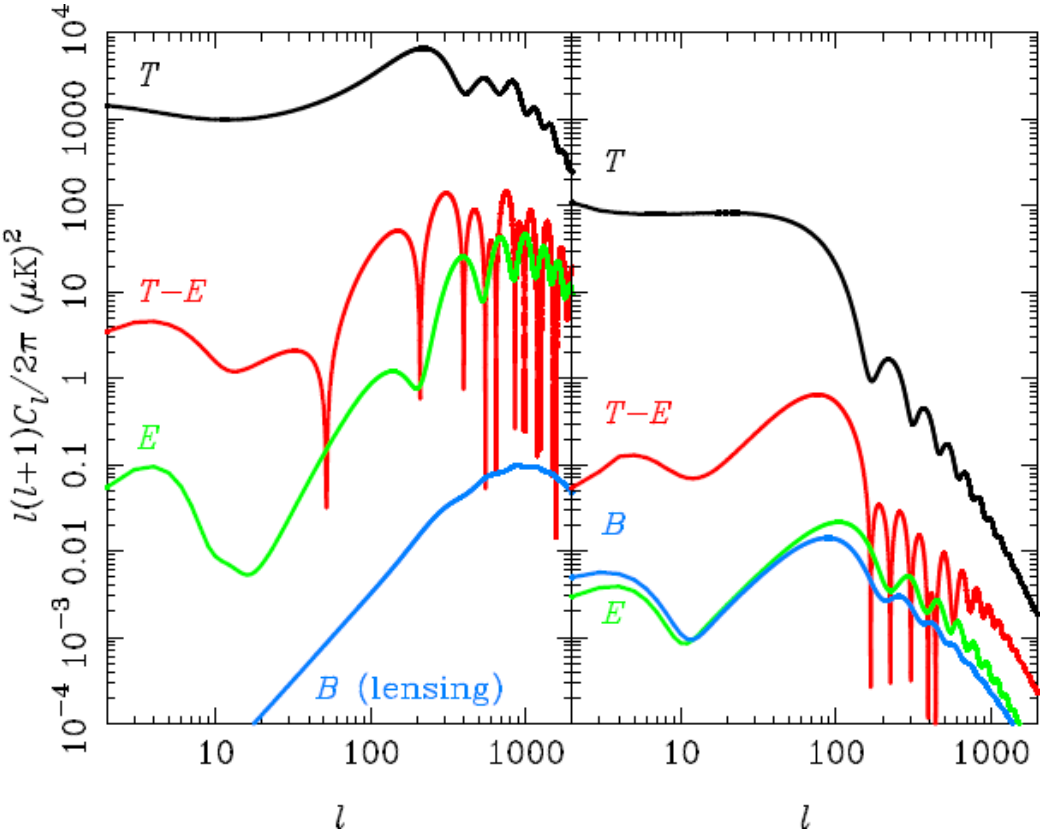

Figure 2.7 Scalar (tensor) contributions to the power spectra T, E- and B-modes and to the TE correlations on the left (right) panel, from [88].

perturbations during the matter-dark energy transition. For this reason the (late-time) integrated Sachs-Wolfe (ISW) effect (see e.g. [90, 91]), is mainly visible at large scales or low multipoles which are scale who have just recently entered the horizon. The ISW effect is therefore one of the most direct signature of the dark energy available in the CMB and is in principle sensitive to its equation of state and clustering properties, although the uncertainty due to cosmic variance prevents a precise measurement of these effects from the power spectrum. The cancellation of the ISW effect on small scales that we just discussed, is only true at linear order and if the non linear effects of the evolution of the gravitational potentials are non negligible, a second order non linear ISW effect may generate anisotropies on large scales. This is usually referred to as Reese-Sciama effect.

In addition to CMB anisotropies generated by evolution of LSS, the CMB photons are affected by all the astrophysical source and effects able to put back in contact electrons and photons by Doppler effects. CMB photons can cross clusters of galaxies, where the temperature of gas can reach 10 keV and the free electrons thermal velocity is a consistent fraction of the speed of light; the net result is a transfer of energy between hot electron gas and cooler CMB photons through inverse Compton scattering. This energy transfer, called thermal Sunyaev-Zeldovich effect (tSZ) leaves a spectral distortion in CMB photons because some of them are shifted from the Rayleigh-Jeans side of the spectrum to the Wien tail due to the energy scattering energy transfer [92]. This effect is one the greatest contribution to temperature anisotropies beyond the damping region until the arc-minute scale, where clusters become unresolved and their contribution is diffused on the whole sky and analogous to a white noise. However, the contribution to power spectrum does not affect significantly the acoustic peaks below the damping scale. Since the frequency spectrum of tSZ is known precisely and differs significantly from the one of CMB, the tSZ effect can be removed with multi-frequency observations or by observing close to 217GHz where the effect is null. Despite being a contaminant to the primordial anisotropies signal itself, the tSZ effect is a powerful cosmological probe as it can be used to detect galaxy cluster and produce cluster catalogues with very precise mass properties [93, 94, 95, 96]. In addition to the thermal SZ effect, anisotropies can be induced by the motion of cluster through Doppler effects of baryons (kinetic SZ effects) although the produced level of anisotropy is confined to a significantly narrow range of angular scales.

Weak lensing of CMB A CMB photon, on its way from the LSS to our observation point, will encounter several density perturbations when trav-

elling in matter dominated era. Since the depth of the potentials is of the order of 10^{-5}, the average size of potential wells is given by the scale of the peak of the matter power spectrum around 300 Mpc and the distance from the last scattering surface is about 14000 Mpc, the number of deviation that a CMB photon experiences during its journey is more or less 50. We might expect the lensing effect to become significant on the CMB power spectrum at $\ell \simeq 3000$, where the primordial (or unlensed) CMB has very little power due to the Silk damping and therefore lensing can become the leading effect. However, the deviations of the photons are coherent on the size comparable to the comoving size of the lens and therefore affects the spectra on wide range of angular scales down to few degrees.

The main theoretical framework of weak lensing has been extensively treated in the previous Chapter. Here we recall some useful definitions, as we discuss weak lensing quantities and properties in light of CMB physics. In a standard Universe with a weakly perturbed Friedmann-Lemaitre-Robertson-Walker (FLRW) metric (see Sec. 1.2), a light ray approaching a matter density distribution is deviated by an angle

$$\delta\boldsymbol{\beta} = -2\nabla_{\perp}\Phi\delta\chi, \tag{2.48}$$

where $\delta\boldsymbol{\beta}$ is the deflection, Φ is the Newtonian potential and $\nabla_{\perp}$ denotes the spatial gradient on a plane perpendicular to the light propagation direction. Notice that the previous relation, as well as the treatment in the present chapter, is valid for FLRW cosmologies, free in particular of anisotropic stress, so that only one of the two scalar potentials of the metric, matters. For a complete casting of the theory of weak gravitational lensing in generalized cosmologies, see [97].

The gradient in Eq. (2.48) is defined in the small-angle limit as $\nabla_{\perp} = (\partial/\partial\beta_1, \partial/\partial\beta_2)$ where (β_1, β_2) describe a coordinate system orthogonal to the light ray trajectory. This deflection can be related to the observed angle $\delta\boldsymbol{\theta}$ subtended by a photon coming from the CMB at a distance $\chi_{\rm CMB}$, and deviated from a lens at the angular diameter distance $f_K(\chi)$. Integrating over the whole distance between us and the LSS to take into account all the possible deflections from all the potential gradients present in this region, we obtain a total deflection in terms of the potential gradients along the line of sight:

$$\boldsymbol{\alpha} = -2\int_0^{\chi_{\rm CMB}} \mathrm{d}\chi \frac{f_K(\chi_{\rm CMB}-\chi)}{f_K(\chi_{\rm CMB})}\nabla_{\perp}\Phi(\chi\hat{\mathbf{n}}, \chi_0-\chi), \tag{2.49}$$

where $\chi_{\rm CMB}-\chi$ is the conformal time at which the photon was at position $\hat{\mathbf{n}}$ and χ_0 the present epoch. Lensing by transverse gradients does not change

the frequency of the photons and hence does not affect the frequency distribution in a given direction except by changing the angular position of the source. If our source plane is CMB, the lensed CMB will have therefore the same black-body spectrum as the unlensed CMB and multi-frequency surveys cannot be used to isolate the lensing effect on CMB. As frequency is not altered and photons are simply moved around, the observable distribution of photons would thus be exact to the one present at the moment of their emission.

Starting from Eq. 2.49, which represents the total displacement vector of photons coming in one direction due to gravitational lensing, we can define an integral potential called lensing potential from which we can compute the displacement vector applying a transverse differential operator $\nabla_\perp$. The latter can be expressed as a function of the canonical covariant derivative on the sphere: $\nabla_\perp = \nabla\hat{\mathbf{n}}/f_K(\chi)$ and has the following explicit form:

$$\psi = -2\int_0^{\chi_{\rm CMB}} \mathrm{d}\chi \frac{f_K(\chi_{\rm CMB}-\chi)}{f_K(\chi_{\rm CMB})f_K(\chi)}\Phi(\chi\hat{\mathbf{n}}, \chi_0-\chi). \tag{2.50}$$

Despite, in a flat Universe, the potential is singular in $\chi = 0$ because of the $1/\chi$ term coming from f_K, the potential is well defined because, the divergence only affects the monopole term of the multipole expansion of Φ which does not contribute to the deflection angle. If we approximate the recombination as instantaneous the CMB is described by a single source plane at $\chi = \chi_{\rm CMB}$. If we consider the potential Φ as Gaussian, the lensing potential is Gaussian too and therefore can be completely described by its power spectrum. In order to evaluate it we can expand the lensing potential in standard scalar spherical harmonics. Since the lensing potential is a statistically isotropic field, we then define its angular power spectrum in the usual way

$$\psi(\hat{\mathbf{n}}) = \sum_{\ell m} \psi_{\ell m} Y_{\ell m}(\hat{\mathbf{n}}), \tag{2.51}$$

$$\langle \psi_{\ell m}\psi^*_{\ell' m'}\rangle = \delta^K_{\ell\ell'}\delta^K_{mm'}C^\psi_\ell. \tag{2.52}$$

We can evaluate numerically the power spectrum of the lensing potential in terms of the gravitational potential power spectrum $\Phi(\mathbf{x};\chi)$ with a simple expansion of in Fourier modes and a projection on the 2D sphere using the Bessel function as it is done for the CMB power spectrum [98]:

$$C^\psi_\ell = 16\pi \int \frac{\mathrm{d}k}{k}\mathcal{P}_R(k)\left[\int_0^{\chi_{\rm CMB}} \mathrm{d}\chi T_\psi(k;\chi_0-\chi) j_\ell(k\chi)\frac{\chi_{\rm CMB}-\chi}{\chi_{\rm CMB}\chi}\right]^2, \tag{2.53}$$

where $\mathcal{P}_R(k)$ is the power spectrum of the comoving curvature perturbation set at the inflationary time and $T_\psi(k;\chi_0-\chi)$ is the transfer func-

tion such that the gravitational potential at later epoch χ is $\Phi(k;\chi) = T_\psi(k;\chi)\mathcal{R}(k)$. Since the deflection angle is the gradient of the lensing potential, its power spectrum can be defined in terms of the power spectrum of the lensing potential

$$C_\ell^{\alpha\alpha} = (\ell+1)\ell\, C_\ell^{\psi\psi}. \tag{2.54}$$

The lensing potential receives contributions from matter perturbations located out to quite high redshift and nearby low redshift potentials only contribute to large scales due to ISW effect so the lensing potential power spectrum is weakly sensitive to recent non-linear evolution. As we can see from the top panel of Fig. 2.8, the deflection power spectrum peaks at $\ell \simeq 60$ where anisotropies on these scales receive contributions from theoretically all redshifts, but in particular $1 \lesssim z \lesssim 6$ where the CMB lensing signal receives the bulk of its power. The bottom panel of the same Figure split the lensing potential signal in its various contribution from a whole range of wavenumbers k. Lensing is predominantly affected by linear and quasi non-linear scales; non-linear corrections becomes more important only at small angular scales while the region close to the peak is weakly affected. They can be estimated using numerical simulations [99, 100] or semi-analytic models like `Halofit` [101, 102] which are expected to be accurate at few percent level for standard ΛCDM. Including non-linear corrections will not introduce a significant level of non-Gaussianity on the lensing potential. These are reduced by the fact that the photon is deflected several times during its journey from the LSS and the lensing potential is effectively more Gaussian than the gravitational potential itself.

2.2.1. The lensed CMB Temperature power spectrum

In order to calculate the effect of lensing on CMB temperature anisotropies, we can restrain ourselves for sake of simplicity to a perturbative expansion of the CMB observable field. Lensing remaps the CMB temperature fluctuations:

$$\tilde{\Theta}(\hat{\mathbf{n}}') = \Theta(\hat{\mathbf{n}} + \boldsymbol{\alpha}) = \Theta(\hat{\mathbf{n}} + \nabla\psi), \tag{2.55}$$

where we denoted with a tilde a lensed quantity. This relation can be expanded as

$$\begin{aligned}\tilde{\Theta}(\hat{\mathbf{n}}) &= \Theta(\hat{\mathbf{n}}') = \Theta(\hat{\mathbf{n}} + \boldsymbol{\alpha}) \\ &\approx \Theta(\hat{\mathbf{n}}) + \nabla^a\psi(\hat{\mathbf{n}})\nabla_a\Theta(\hat{\mathbf{n}}) + \frac{1}{2}\nabla^a\psi(\hat{\mathbf{n}})\nabla^b\psi(\hat{\mathbf{n}})\nabla_a\nabla_b\Theta(\hat{\mathbf{n}}) + ...\end{aligned} \tag{2.56}$$

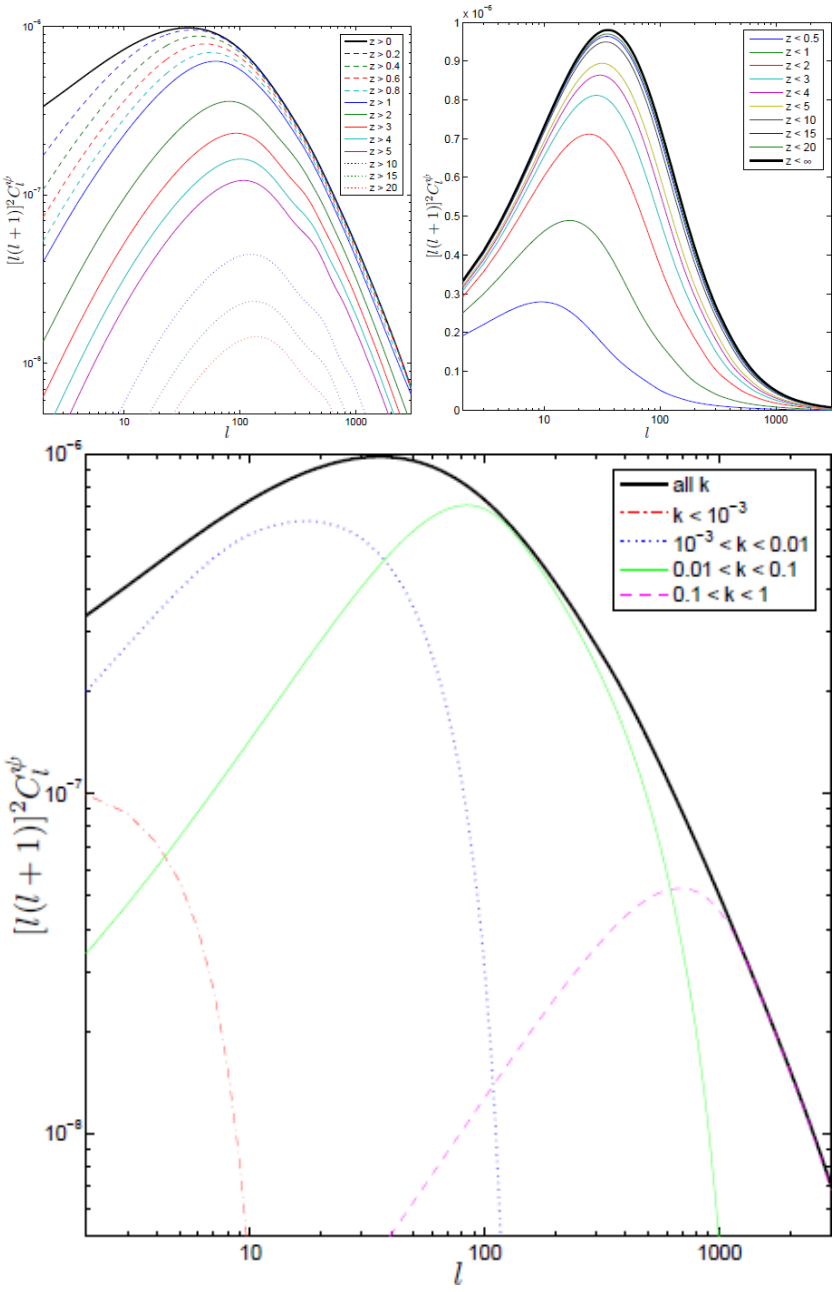

Figure 2.8 From [98]. **Top panel**: cumulative contribution of different redshifts to the power spectrum of the lensing potential $C_\ell^{\psi\psi}$ for a concordance ΛCDM model, in both linear (right-hand plot) and log-linear (left-hand plot) scale. **Bottom panel**: Contributions of different wavenumbers k (in Mpc^{-1}) to the power spectrum of the lensing potential for a concordance ΛCDM model.

If we expand this relation in Fourier domain - assuming a flat sky approximation for sake of clarity and simplicity - the last equation reads

$$\tilde{\Theta}(\boldsymbol{\ell}) \approx \Theta(\boldsymbol{\ell}) + \int \frac{\mathrm{d}^2\boldsymbol{\ell}'}{2\pi} \boldsymbol{\ell}' \cdot (\boldsymbol{\ell} - \boldsymbol{\ell}') \psi(\boldsymbol{\ell} - \boldsymbol{\ell}') \Theta(\boldsymbol{\ell}') \\ - \frac{1}{2} \int \frac{\mathrm{d}^2\boldsymbol{\ell}_1}{2\pi} \int \frac{\mathrm{d}^2\boldsymbol{\ell}_2}{2\pi} \boldsymbol{\ell}_1 \cdot [\boldsymbol{\ell}_1 + \boldsymbol{\ell}_2 - \boldsymbol{\ell}] \, \boldsymbol{\ell}_1 \cdot \boldsymbol{\ell}_2 \Theta(\boldsymbol{\ell}_1) \psi(\boldsymbol{\ell}_2) \psi^*(\boldsymbol{\ell}_1 + \boldsymbol{\ell}_2 - \boldsymbol{\ell}). \tag{2.57}$$

The series expansion is not a good approximation on all scales. On intermediate scales the lensing deflection is of the same order of the angular scales of the anisotropies which are being deflected, and a perturbative expansion in the deflection angle is not suitable for a precise estimate of the effect. Nevertheless, this simple approach is useful to understand the most important effects and correct on a good range of angular scales and, for some purposes detailed in the following, sufficiently accurate.

We can deduce the lensed CMB power spectrum in the usual way as lensing from a statistical isotropic field like lensing potential does not brake the statistical isotropic properties of the CMB:

$$\begin{aligned} \langle \Theta(\boldsymbol{\ell}) \Theta^*(\boldsymbol{\ell}') \rangle &= C_\ell^\Theta \delta^D(\boldsymbol{\ell} - \boldsymbol{\ell}'); \\ C_\ell^\Theta &\approx \left(1 - \ell^2 R^\psi\right) + \int \frac{\mathrm{d}\boldsymbol{\ell}'}{4\pi^2} \left[\boldsymbol{\ell}' \cdot (\boldsymbol{\ell} - \boldsymbol{\ell}')\right]^2 C^\psi_{|\boldsymbol{\ell} - \boldsymbol{\ell}'|} C^\Theta_{\ell'}; \end{aligned} \tag{2.58}$$

$$R^\psi = \frac{1}{2} \langle |\nabla \psi|^2 \rangle = \frac{1}{4\pi} \int \frac{\mathrm{d}\ell}{\ell} \ell^4 C_\ell^\psi. \tag{2.59}$$

In the last equation we neglected the temperature-lensing potential correlation, since the $\Theta\psi$ correlation is small on most of the angular scales and its effect on the lensed power spectrum is small. The lensed power spectrum, at the first order in C_ℓ^ψ, differs from the unlensed coefficients by a term proportional to the deflection power angle R^ψ and by an integral term which has the form of a convolution of the unlensed temperature spectrum with the lensing potential power spectrum. This convolution effectively smooths out the main peaks and troughs of the unlensed spectrum and cause a fractional change in the power spectrum equal to several percent at $\ell \simeq 1000$. On small scales, where there is little power in the unlensed CMB because of Silk damping, the convolution transfers power from large scales to small scales increasing the small scales power (cf. Fig. 2.9). Even if, as we note previously, the series expansion is not accurate on intermediate scales, on very small scales ($\ell \gg 3000$) it becomes again accurate because the anisotropies in the unlensed CMB are

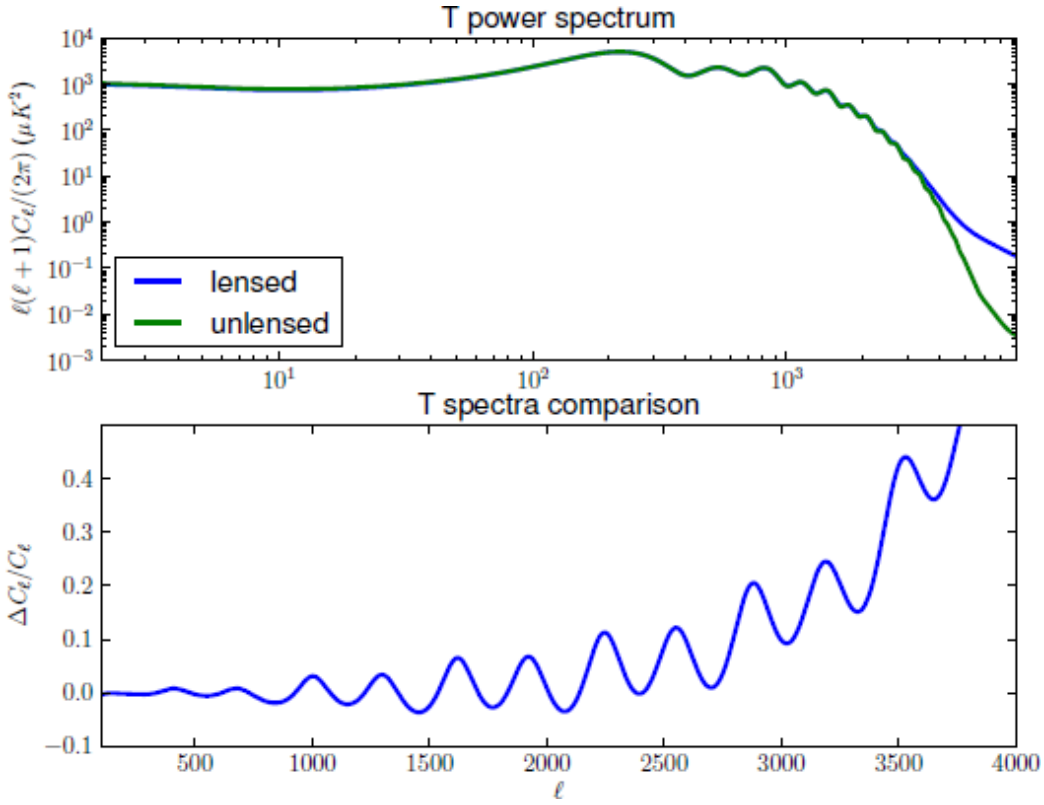

Figure 2.9 Adapted from [98]. **Top panel**: lensed and unlensed temperature power spectrum. In the small scale limit the power of the lensed spectrum is proportional to lensing potential power spectrum. **Bottom panel**: fractional difference between lensed and unlensed temperature power spectrum. As a result of lensing, acoustic peaks are smoothed and through are filled in.

wiped out by diffusion damping and the unlensed spectrum is very close to isotropic. The total variance of the temperature field at a point is conserved by lensing and this reflects the fact that weak lensing only modifies photons directions and hence spatial correlation structure but does not change variance in any given direction:

$$\sum_{\ell} C_{\ell}^{\Theta}(2\ell+1) = \sum_{\tilde{\ell}} \tilde{C}_{\tilde{\ell}}^{\Theta}(2\tilde{\ell}+1). \tag{2.60}$$

A more exact calculation can be obtained using the curved sky approach implemented in [103, 104] although for an exact calculation as implemented in modern Boltzmann codes, the lensed CMB power spectrum is derived using method involving the real space correlation function methods. We refer the reader to [105, 106, 107] for more details.

2.2.2. Lensing of CMB polarization

The presence of a quadrupole moment at last scattering generates a polarization signal which will also be lensed by potential gradients along the line of sight. This effect can be modelled in a way similar to temperature lensing with the further complication that polarization is not a scalar field but a spin-(± 2) (tensor) field.

The CMB radiation field is characterised by a 2x2 intensity tensor whose components are the Stokes parameters. As we have previously discussed the Q and U parameters are not invariant under rotation of an angle Γ around the direction of observation $\hat{\mathbf{n}}$, thus we can construct two quantities from the Q and U parameters which have a definite spin value

$$P = (Q \pm iU)'(\hat{\mathbf{n}}) = e^{\mp 2i\Gamma}(Q \pm iU)(\hat{\mathbf{n}}). \tag{2.61}$$

Evaluation of polarization power spectra is similar to the temperature case. We can first remap the polarization spin field with the usual lensing equation and then use a perturbative expansion to evaluate the leading term contributing to the power spectra,

$$\begin{aligned}\tilde{P}_{ab}(\hat{\mathbf{n}}) &= P_{ab}(\hat{\mathbf{n}}') = P_{ab}(\hat{\mathbf{n}} + \boldsymbol{\alpha}) \\ &\approx P_{ab}(\hat{\mathbf{n}}) + \nabla^c\psi(\hat{\mathbf{n}})\nabla_c P_{ab}(\hat{\mathbf{n}}) + \frac{1}{2}\nabla^c\psi(\hat{\mathbf{n}})\nabla^d\psi(\hat{\mathbf{n}})\nabla_c\nabla_d P_{ab}(\hat{\mathbf{n}}) + ...\end{aligned} \tag{2.62}$$

Fourier transforming this quantity with the proper flat sky version of the spin spherical harmonic and then computing the power spectrum would

lead to a lensed E and B-modes polarization power spectra [103, 108, 109]:

$$\tilde{C}_\ell^E = \left(1 - \ell^2 R^\psi\right) C_\ell^E + \int \frac{\mathrm{d}^2\boldsymbol{\ell}'}{(2\pi)^2} \left[\boldsymbol{\ell}' \cdot (\boldsymbol{\ell} - \boldsymbol{\ell})\right]^2 C^\psi_{|\boldsymbol{\ell}-\boldsymbol{\ell}'|} C^E_{\ell'} \cos^2 2(\phi_{\ell'} - \phi_\ell), \tag{2.63}$$

$$\tilde{C}_\ell^B = \int \frac{\mathrm{d}^2\boldsymbol{\ell}'}{(2\pi)^2} \left[\boldsymbol{\ell}' \cdot (\boldsymbol{\ell} - \boldsymbol{\ell})\right]^2 C^\psi_{|\boldsymbol{\ell}-\boldsymbol{\ell}'|} C^E_{\ell'} \sin^2 2(\phi_{\ell'} - \phi_\ell), \tag{2.64}$$

$$\tilde{C}_\ell^{\Theta E} = \left(1 - \ell^2 R^\psi\right) C_\ell^{\Theta E} + \int \frac{\mathrm{d}^2\boldsymbol{\ell}'}{(2\pi)^2} \left[\boldsymbol{\ell}' \cdot (\boldsymbol{\ell} - \boldsymbol{\ell})\right]^2 C^\psi_{|\boldsymbol{\ell}-\boldsymbol{\ell}'|} C^{\Theta E}_{\ell'} \cos^2 (\phi_{\ell'} - \phi_\ell), \tag{2.65}$$

where $\phi_{\ell'}$ and ϕ_ℓ are the angles between $\hat{\mathbf{n}}$ and $\boldsymbol{\ell}'$ and $\boldsymbol{\ell}$ respectively. The result in Eq. (2.63) neglects the contribution of the lensing of the primordial B-modes, which are expected to be small. In this case, the lensed B-modes power spectrum is generated from lensing of the unlensed E-mode field and on large scales it has an amplitude which is independent of ℓ (see Fig. 2.10). This can be easily derived from the previous Equation in the limit $|\boldsymbol{\ell}| \ll |\boldsymbol{\ell}'|$. Since the lensed B modes is a convolution of primordial E-modes in the harmonic domain the contributions to the lensing B-modes power come from all multipoles where there is non-zero E and lensing potential power. It is important to note that the B-modes generated from the lensing of E modes can potentially be a contaminant for the detection of the primordial B-modes signal generated by the gravitational waves coming from inflation [110, 111]. The effect of lensing on the E-modes is similar to the effect on the temperature and the convolution with the lensing potential smooths out the acoustic peaks and troughs of the power spectrum. Since polarization peaks are sharper than in the temperature case, this means that the effect of lensing is quantitatively more important on the E-polarization spectrum. On very small scales the unlensed polarization is damped, as in the temperature case, and lensing transfer power from large to small scales, therefore on this area of the spectrum we expect to observe the same power in both B and E polarization (cf. Fig. 2.10). The more general and accurate results on the computation of polarized lensed spectra can be found in [105, 108].

2.2.3. Constraining physics with CMB lensing

Although the lensing effect on the CMB power spectrum is significant, the overall effect on recovered constraints on parameters for flat models is not so important [112]. The CMB lensing data allow to break the so called geometrical degeneracy between DE and spatial curvature [113]. ΛCDM

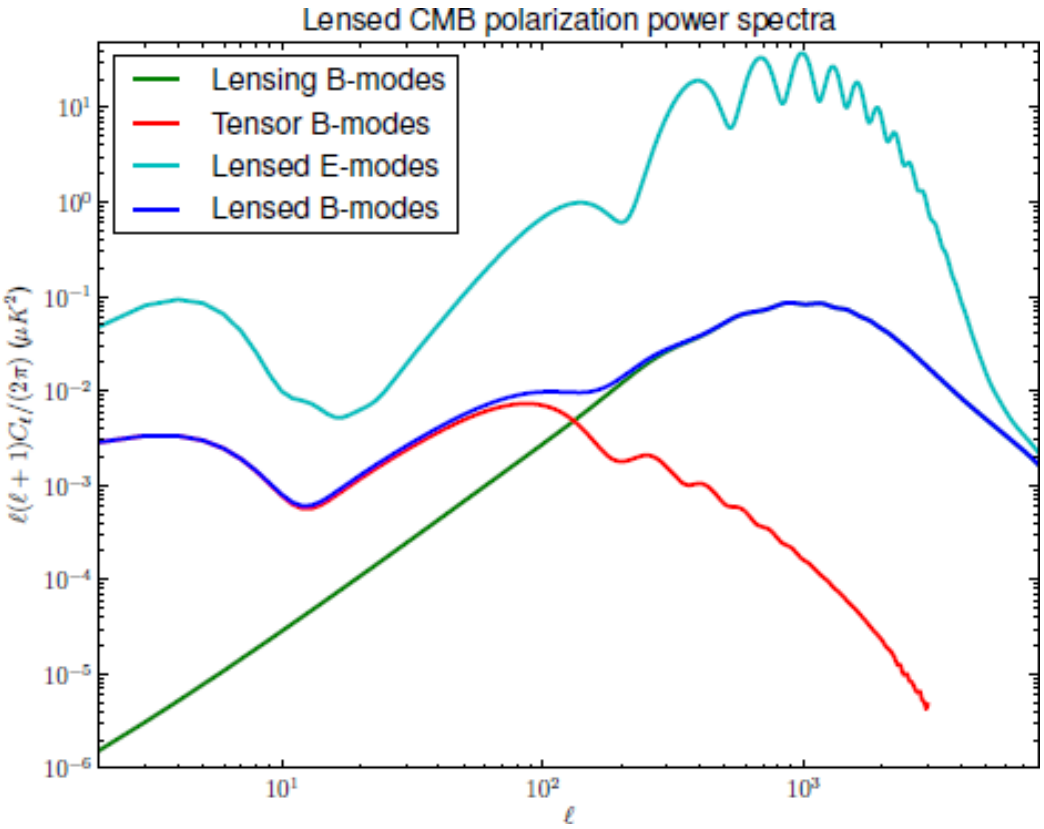

Figure 2.10 Lensed CMB E and B-modes polarization power spectra. The tensor and lensing contribution to the observed B-modes signal are plotted separately. At very small scale we expect E and B-modes to display the same power.

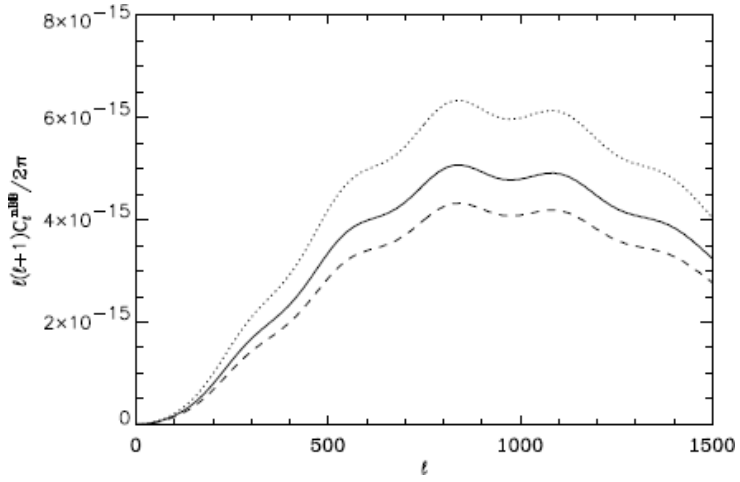

Figure 2.11 From [117]: Lensed BB power spectra for DE models with a time-varying equation of state parametrised as $w(a) = w_1 + (w_0 - w_1)a$. The curves represent models with $(w_0, w_1) = (-0.9, -0.4)$ (solid line), $(w_0, w_1) = (-0.8, -0.56)$ (dotted line) and $(w_0, w_1) = (-0.965, 0.3)$ (dashed line).

model can, in fact, be mimic by a closed Universe with low density of dark energy, producing an identical unlensed power spectrum. This degeneracy can be broken by lensing because the closed models predict too much power in the lensing potential. This allowed to constrain simultaneously the curvature and the DE density, as done recently by [28] where $\Omega_K = 0.0096 \pm 0.01$ and $\Omega_\Lambda = 0.67 \pm 0.027$.

However, there are few parameters to which the CMB alone is not very sensitive but that can be studied in detail analysing simultaneously the CMB with the lensing potential. The latter is in fact sensitive to parameters which affect primarily the structure formation but not necessarily the CMB; like the masses of neutrino, the dark energy and the dark radiation. If the power spectra can be reconstructed precisely the extra information imprinted in the lensing potential can be exploited to improve our knowledge of cosmology [114, 115, 116].

The cross correlation of the lensing potential with the lensed CMB can help constraining the curvature and the DE model though the ISW effect. These probes are however not very precise as they are plagued by the cosmic variance uncertainties. A more direct imprint of DE can be inferred from the lensing potential itself because DE affects the growth function of the large-scale structure [117], as seen in Fig. 2.11. The effects on massive neutrinos however can be separated by the differences in the scale-

dependence of their effect on the lensing potential power spectrum [115]. Nevertheless a complete separation of the two effect from CMB alone is complicated because they influence effectively all the scales in a nearly degenerate way especially on the lensed B-modes level [118], which is the signal more sensitive the LSS evolution. Using CMB and lensing potential can help constraining also time dependent DE equation of state and/or the presence early dark energy [119]. These early DE models follow from physics where DE traces the energy density of the dominant component of the Universe, as in high energy physics and string theory models (see e.g. [120, 121]). The presence of a non negligible component of DE at early times has important impacts on the sound horizon scale, structure formation, and secondary anisotropies and a joint CMB plus lensing analysis can become a good probe for this kind of model as this combination is sensitive to all the effects. The constraints can also be improved using additional external data from weak lensing and dark energy optical surveys (see [122] and references therein) or, in the future, from 21cm observations [123, 124]. An accurate account of the possible improvement expected on DE and neutrino physics constraints from cross correlation between different data sets can be found in [125].

2.3. Measuring the CMB angular power spectra

After the first detection of CMB anisotropies by the COBE satellite many experiments have managed to observe successfully the CMB. The first acoustic peaks where observed by MAXIMA [126] and Boomerang [127] balloons with high precision and resolution. Satellite missions than strike back with WMAP which was able not only to analyse the CMB temperature field in all its glory, but also shading a first light on polarization together with the ground base experiment DASI, who first detected E-modes of polarization [128]. The latest measurements of the CMB spectrum to date are provided by the ACT, SPT [129, 130]. Atacama Cosmology Telescope (ACT) and South Pole Telescope (SPT) are small-scales, ground experiments that observed the sky from the Atacama desert (Chile) and South Pole respectively and were capable to measure the CMB anisotropies power spectrum up to the arc-minute scale. The ultimate and most accurate measurements of CMB temperature was made available in the spring 2013 and later in 2015 with the latest generation of satellite mission: Planck. Its wide frequency coverage and low instrumental noise allow to produce high fidelity maps of the microwave sky to study in details galactic and extra-galactic emissions in our Universe together with CMB characterisation, limited by the cosmic-variance only [1]. Figure 2.12 shows the an-

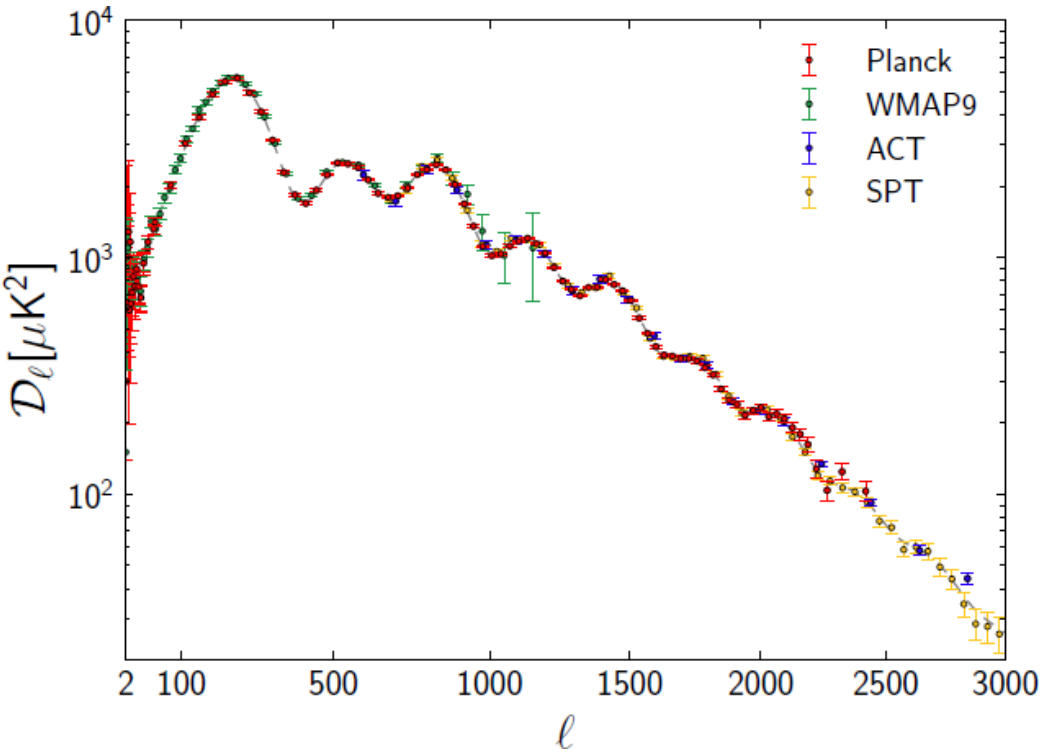

Figure 2.12 From [1] Measured angular power spectra of Planck, WMAP9, ACT, and SPT with the best fit model curve (dashed) obtained from a joint analysis of Planck temperature, WMAP polarization, ACT, and SPT data.

gular power spectra of temperature fluctuations, as measured by different probes quoted above. These data support, to extreme accuracy the ΛCDM concordance model for cosmology.

Alongside with observations of pure intensity, the era of CMB polarization has begun with the first detection of the E-modes by [131, 128]. The ACTPol collaboration has recently provided an accurate reconstruction of the temperature, E-modes and their correlations at small scales ($\ell \in [200, 9000]$, [132]). The WMAP satellite had access to the largest scales reconstructing the E-modes power spectrum for $\ell \in [26, 500]$ [133]. The final realise of Planck in 2015 reaches the peaks in terms of reconstructing the angular power spectrum basically at all scales of interest, cf. Fig. 2.13. The Figure shows the temperature fluctuations (TT) as well as E-modes and TE correlation angular power spectrum; these plots represent simply the best cosmology and CMB physics can reach nowadays, in terms of accuracy, controlling systematics and constraining power. The most striking result of this mission is the impressive consistency of the

different cosmological parameter extracted from those spectra: cosmological parameters returned by the TT, TE or EE likelihoods are consistent with each other, and the residuals of the (frequency combined) TE and EE spectra after subtracting the temperature ΛCDM best-fit are consistent with zero. This is the best illustration up to date of the predictive power of the minimal 6-parameters cosmological model, and, at the same time, the best tool for constraining interesting, physically-motivated deviations from that model.

The B-modes power spectrum is a key issue for fully understanding the standard model of cosmology. The motivation for its detection therefore leads the way to designing a large set of ground based spatial or balloon experiments. B-modes were still imperceptible to our instruments up to the beginning of 2014. Indeed, the POLARBEAR experiment has directly detected the lensed B-modes at small angular scales ($\ell \in [500, 2100]$) for the first time in [84]. The reconstructed lensed B-modes power spectrum is displayed on Figure 2.14 as blue points. In March 2014, the BICEP2 team claimed the very first detection of the primordial B-modes in the multipole range of $\ell \in [30, 150]$ in [134]. The corresponding data points are displayed in black in the same Figure. The data should suggest a value of the tensor-to-scalar ratio r to $r = 0.2^{+0.07}_{-0.05}$. However, their results are controversial mainly due to the way they remove the foregrounds, that are thought to be underestimated (see Mortonson and Seljak (2014) or Flauger et al. (2014) for instance). In February 2015, a joint analysis of data from BICEP2/Keck Array and Planck has provided a definitive answer to this matter [135], finding a strong evidence for dust contamination in the signal and no statistically significant evidence for tensor modes. The final result was translated as a likelihood curve for r, which yields an upper limit $r_{0.05} < 0.12$ at 95% confidence level. This results has been obtained primarily by exploiting the polarization sensitive 353 GHz channel of the High Frequency Instrument on-board Planck, the only good observation of dust polarization we have to date. On the other hand, the Planck sensitivity is not suitable for a dust monitoring to required accuracy for B-modes experiments, and that is the reason of the not stringent limit obtained by combining Planck, BICEP2 and Keck array data. In the same paper, the two teams report an amplitude of lensing effect in the B-modes of $A_L = 1.13 \pm 0.18$, with a significance of detection of 7σ. At this moment, sub-orbital experiments are sustaining the effort of equipping themselves with multi-frequency set-ups, in order to observe, and subtract, the Galactic diffuse emission with required sensitivity and angular resolution. Combining Planck data on large angular scales (which are inaccessible for ground based experiments) with ACT and SPT data on small scales up to

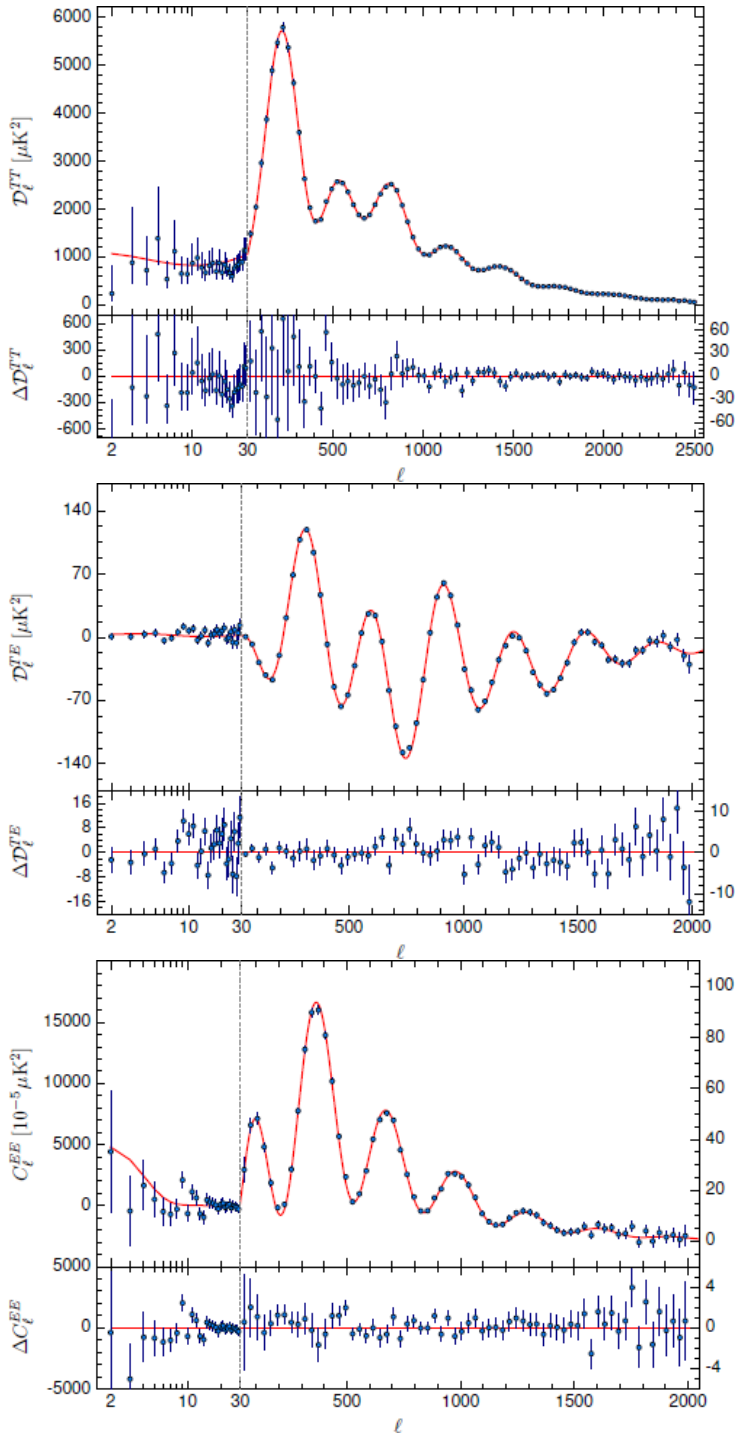

Figure 2.13 From [28]: Planck 2015 [28] temperature power spectrum (Top) and frequency-averaged TE (Middle) and EE (Bottom) spectra. The best-fit base ΛCDM theoretical spectrum fitted to the Planck TT+lowP likelihood is plotted in the upper panels (red line) comparing with the data spectra. Residuals with respect to this model are shown in the lower panels. The error bars show $\pm 1\sigma$ uncertainties. In all the panels, the horizontal scale changes from logarithmic to linear at the "hybridisation" scale, $\ell = 29$ (representing the division between the low-ℓ and high-ℓ likelihoods). Note that angular power spectra are shown as $\mathcal{D}_\ell = \ell(\ell+1)\, C_\ell/(2\pi)$ for TT and TE, but not for EE, where simply C_ℓ^{EE} are plotted.

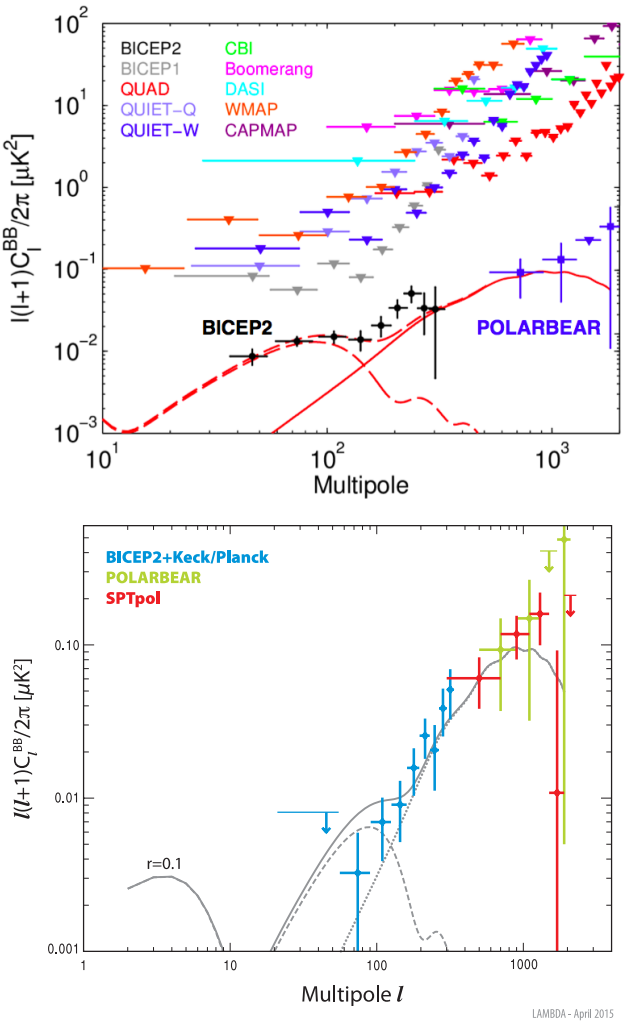

Figure 2.14 **Top panel**: Observed B-mode power from CMB experiments, earlier constraints and current measurements. The BICEP2 [134] data should suggest a value of the tensor-to-scalar ratio r to $r = 0.2^{+0.07}_{-0.05}$. **Bottom panel**: update plot using BICEP2+Keck/Planck join analysis [135]; POLARBEAR [3], and SPTpol [4] are included. The BICEP2+Keck/Planck data points show results with dust foreground subtraction based on measured cross-power between Planck and BICEP2+Keck. For comparison, a theoretical curve is shown for a fiducial ΛCDM model with tensor-to-scalar ratio reduced to $r = 0.1$, signalling the importance of dust contamination (and thus subtraction) in the observed B-modes of CMB polarization. The gravitational lensing component is shown as a dotted curve.

$\ell = 3000$ - where the contribution of extra-galactic secondary anisotropies (thermal SZ effect, dusty galaxies, extra-galactic point sources etc.) starts being significant - confirm with excellent agreement the prediction of a standard flat ΛCDM 6-parameters model. Besides, best-fit ΛCDM model can provide strong predictions for the distance scale. This prediction can be compared to the measurements provided by other measurements, such as studies of Type Ia SNe and baryon acoustic oscillations (BAO). A mild tension can be found between CMB data and the (relative) distance scale inferred from compilations of SNe [31]. In contrast, results are in excellent agreement with the BAO distance scale compiled in [136]. No strong evidence can be found to favour any extension to the base ΛCDM cosmology, either from the CMB temperature power spectrum alone or combination with Planck lensing power spectrum and other astrophysical datasets. The measured values of the ΛCDM parameters are relatively robust to the inclusion of different parameters, though a few do broaden significantly if additional degeneracies are introduced. Despite the remarkable success of the 6-parameters standard ΛCDM model in explaining CMB data, the agreement is not perfect. A weak evidence for discrepancies can be seen in the Planck data on large scales: at $\ell \lesssim 30$ the spectrum seems to manifest a deficit of power. Interpretation of such anomalies is difficult, they do leave an open window for new physics on large scales. In addition, cosmology derived from CMB is in tension with the results derived from surveys of galaxy cluster counts selected through thermal SZ effect in Planck data. This catalogue tends to prefer a Universe with lower matter density with respect to the one derived from CMB only for reasons which are still unclear and maybe connected to the lack of knowledge of cluster physics or their mass bias.

Future experiments

Furthermore, the current experiments dedicated to the B modes detection among which POLARBEAR 2 [137] or the Keck array [138] will be upgraded in the coming years. Also the QUBIC experiment [139] based on bolometric interferometry is one of the promising forthcoming B modes experiments to be built. The upgraded versions of ACT and SPT, ACTpol and SPTpol [5, 4], are currently taking data to measure temperature and polarization anisotropies at high-multipoles at the level of POLARBEAR and BICEP, to probe the spectral index of inflation, the primordial helium abundance, and neutrino properties. Moreover, B modes observation over the full celestial sphere would give access to the crucial low multipoles, including the reionisation bump, of the B modes power spectrum. Several spatial experiments such as LiteBIRD (which design is described in [140])

or a Core-like satellite [141] are under studies to be proposed in the coming years to the spatial agencies.

2.3.1. CMB lensing measurements and cosmological applications

Lensing effects on CMB were first discovered by [142] and [143] correlating CMB with large scale structure tracers. ACBAR data [144] found direct evidence of lensing looking at 2-points statistics: their measurements preferred a lensed CMB angular power spectrum. However, only recently we were able to reach high sensitivity at small scale in CMB temperature; experiment like ACT and SPT reconstructed CMB lensing potential for the first time. [145, 146] detected a signal with a significance of 4 and 6 σ respectively for the reconstructed lensing potential power spectrum. [9] showed how detection of CMB lensing potential at high significance has important constraining power on DE using CMB data alone. The latest Planck 2015 full-mission release presented the most significant measurement of CMB lensing potential to date, at a stunning 40σ significance level, using temperature and polarization data. CMB lensing potential obtained from the reconstruction was found to be in agreement with the prediction of the ΛCDM model; in Fig. 2.15 the lensing potential angular power spectrum is shown, compared with the previous 2013 Planck release, together with ACT and SPT data points.

In a broader context, CMB lensing helps breaking the degeneracy between several cosmological parameter; e.g. Planck 2013 [1] constrained the amplitude of the primordial of the CMB power spectrum A_S and optical depth to reionisation τ, taking advantage of the fact that lensing power spectrum does not depend on the optical depth. The value of optical depth reported by Planck-2013 discards the value which can be obtained assuming the recombination instantaneous at $z_{re} \approx 6$ at 95%, and supports the idea of reionisation as extended and continuous process. Lensing-only results can constrain the sub-space of Ω_m, H_0, and σ_8. Figure 2.16 shows those corresponding constraints from CMB lensing, along with tighter constraints from combining with additional external BAO data, compared to the constraints from the Planck CMB power spectra. The contours overlap in a region of acceptable Hubble constant values, and hence are compatible. A band in the $\Omega_m - \sigma_8$ plane can be defined, thus constrain a preferred direction corresponding approximately to $\sigma_8\Omega_m^{0.25} = 0.591 \pm 0.021$ at 68% CL. Finally, Planck 2015 [147] combines the determination of the lensing potential with the E-mode polarization also measured by the satellite to generate an estimate of the lensing B-mode. The mission found evidence of a correlation between this lensing B-mode estimate and

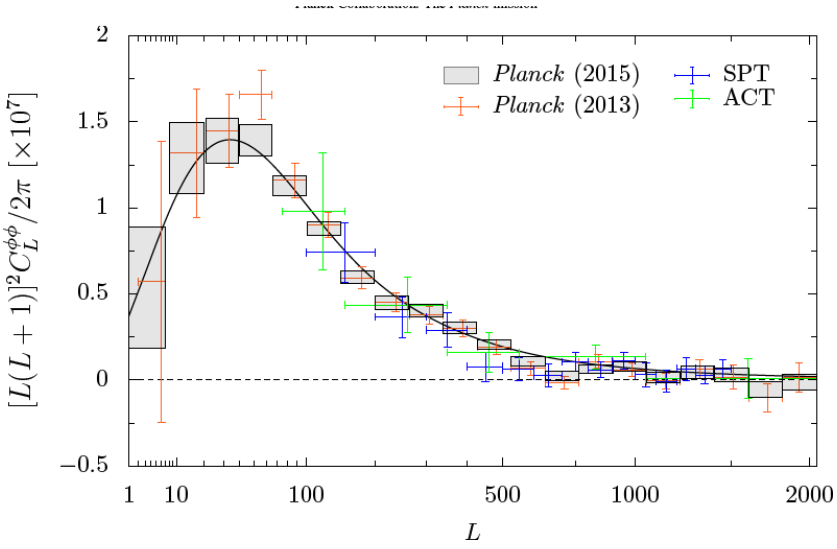

Figure 2.15 Lensing potential power spectrum estimate from the 2015 data release [147], based on the CMB reconstructed map where the diffuse foregrounds were subtracted using a procedure parametrizing the Galactic emission in the harmonic domain (SMICA, see [148]), as well as previous reconstructions from Planck and other experiments for comparison.

the B-modes observed directly by Planck, with a statistical significance of 10σ. This can be translated into an overall amplitude of the lensing B-mode power spectrum $\hat{A}^B$ relative to the predicted spectrum in the fiducial model; for a large bin $8 \leq \ell_B \leq 2048$ Planck measured an amplitude of $\hat{A}^B_{8\to 2048} = 0.93 \pm 0.08$ for the standard, minimum variance lensing potential estimation inferred using both temperature and polarization data.

2.3.2. Cross-correlation between CMB and LSS surveys

Cross-correlation of CMB with LSS tracers has become one of the most lively and important research areas in the CMB field, thanks to the sensitive lensing potential reconstruction. The CMB lensing potential is an integrated measure of the matter in the Universe back to the last scattering surface which receives the bulk of the contribution from a broad window in redshift space around $z \sim 2$. For this reason it is possible to correlate it with a wide range of optical and infrared catalogue of LSS, to constraint parameters like the bias of the population of this sources. This was done for ACT, SPT and Planck data [9, 8, 149] and the correlation was detected with a significance up to 10σ. The Planck collaboration, for instance, has

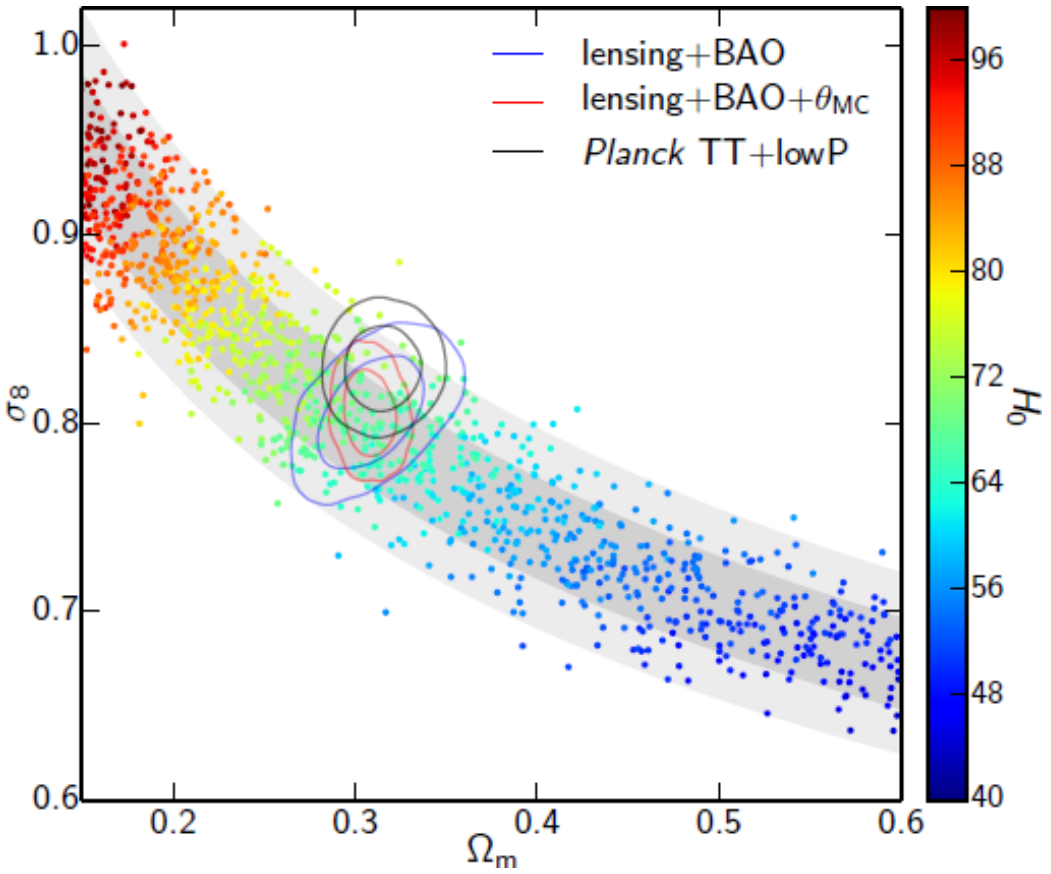

Figure 2.16 From [147]: Parameter constraints from CMB lensing alone in the ΛCDM model; grey bands give the corresponding 1σ and 2σ constraints using the approximate fit $\sigma_8\Omega_m^{0.25} \approx \text{const.}$. Solid coloured contours constraints when additional datasets is included: BAO data from SDSS and 6DF, in blue; same but fixing the CMB acoustic-scale parameter $\theta_{\rm MC}$ to a CMB power spectrum fit, red; solid black contours show the constraint from the Planck CMB power spectra (Planck temperature+low-ℓ polarization). See [147] for all references.

exploited its wide frequency coverage to correlate the CMB lensing potential with the Cosmic Infrared Background (CIB) anisotropies, which are generated by thermal emission of intergalactic dust reheated by UV radiation from young stars. The correlation of the two observables was found to be on the level of 80% with a detection significance of 42σ for the 545 GHz channel of Planck.

More recently, [150] has cross-correlated data from the *Herschel*-ATLAS (H-ATLAS) survey covering about 600 deg^2 with the lensing potential derived from Planck. This galaxy catalogue covers sub-millimeter sources in redshift range $1 \lesssim z \lesssim 5$, where the CMB lensing is mostly sensitive to matter fluctuations. Hence they represent perfect candidates for cross-correlation studies, as they are high star-forming galaxies (few hundred $M_\odot$ yr^{-1}) and strongly clustered [151, 152], implying that they are tracers of large-scale overdensities. Their properties are consistent with them being the progenitors of local massive elliptical galaxies [153]. A 25σ significance detection confirm the validity of this technique, a results which is even more astonishing since the galaxy catalogue used covers only 1.4% of the sky, demonstrates the potential of CMB lensing correlations with sub-millimeter surveys (cf. Fig. 2.17). The scientific goal of this work was to evaluate the galaxy (linear) bias parameter, b, using a joint analysis of the cross-power spectrum and of the auto-power spectrum of the galaxy density contrast. The bias is found to be consistent with earlier estimates for H-ATLAS galaxies at similar redshifts, $b = 2.80^{+0.12}_{-0.11}$, even if data suggest a higher value of the amplitude of the cross-correlation $A_{\kappa g} = 1.62 \pm 0.16 > 1$ higher than expected from the standard model. A possible explanation can be related to the difficult treatment of the redshift estimation for a single object in the Herschel field. The catalogues are in fact constructed using photometric redshifts, which have a intrinsically high uncertainty - especially for low-z - due to the template fitting to the spectral energy distribution of the galaxy [153, 154, 155].

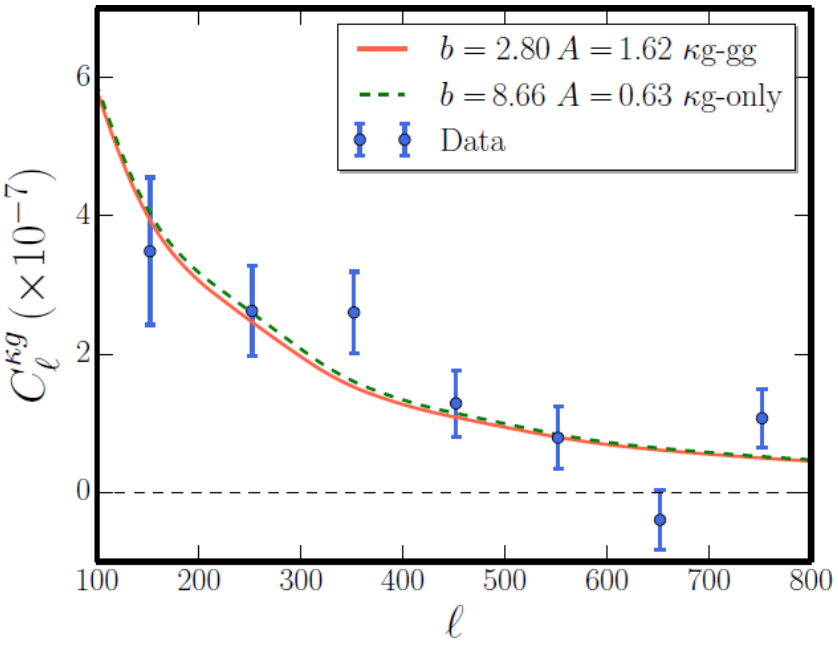

Figure 2.17 From [150]: The CMB convergence-galaxy density cross-spectrum as measured from Planck and Herschel data. The data points are shown in blue, with error bars computed using the full covariance matrix obtained from Monte Carlo realisations of convergence maps. Theoretical spectra calculated with the bias values inferred from the likelihood analysis using the cross-correlation data only (solid red line) and the cross-correlation together with the galaxy auto-correlation data (dot-dashed green line) are also shown. The null (no correlation) hypothesis is rejected at the 20σ level.

CHAPTER 3

CMB N-Body lensing

> Numerical simulations are believed by no one except those who conducted them.
> Experimental results are believed by everyone except those who performed them.
>
> *Anonymous researcher*

The most accurate way to obtain predictions for observables of weak-lensing surveys is to perform ray-tracing through large, high resolution N-Body numerical simulations to study the full non-linear and hierarchical growth of cosmic structures. Although these approaches are computationally very demanding, they allow to check and balance the approximations and assumptions made in widely-used semi-analytic models, adjusting and extending these models if necessary.

Numerous ray-tracing methods have been developed so far in the context of both strong and weak gravitational lensing. Though exact algorithm are available [156], they are not suitable for application targeting observations of large fraction of the sky for computational reasons. A simpler and popular approach consists in using the matter distribution in the N-Body simulations to calculate lensing observables by ray-tracing along "unperturbed", i.e. undeflected light paths in the so-called Born approximation (e.g. [157, 158, 99]). In particular, [100] applied this technique to study a set of N-Body simulation with different cosmologies and DE dynamics, to investigate the variation of the lensing pattern with respect to the standard ΛCDM model. [159], conversely, showed that the integrated matter distribution used to lens incoming CMB photons in the Born approximation can be properly reconstructed using standard lensing reconstruction techniques and quadratic estimator [160].

However, when facing a complex cosmological structure, we must take into account that each light ray undergoes several distortions due to matter inhomogeneities, i.e. approximating the actual path of a photon instead of adopting a single effective deviation from the unperturbed, line-of-sight integral assumed in Born approximation. The single effective lens must therefore be replaced by a multiple-lens (ML) approach, where large volumes of matter are projected onto a series of lens planes [161, 63, 162, 65, 163] so that the continuous deflection experienced by a light ray is approximated by finite deflections at each of the planes. A ML full-sky CMB lens-

ing application was sketched in [164] who simulated lensed CMB maps in temperature only with an angular resolution of $0.9'$. However, detailed comparison of the effective Born approximation method and the ML approach was not discussed and only the results derived in the Born approximation scenario were presented.

In this Thesis, we implemented a multiple plane ray-tracing algorithm to lens CMB temperature and polarization fields combining the aforementioned work by [164] and using the light cone reconstruction from a single N-Body simulation as [165]. The final rationale will be to investigate DE effects in different cosmologies at arc-minutes scales, where are expected to be most noticeable. At these scales, the Born approximation is expected not to trace with high accuracy local deviations due to small-scales inhomogeneities, and thus a more precise and realistic method is needed. Moreover, in order to be successful, we need to be able to control and discriminate between physical non-linearities of the N-Body simulations from numerical issues connected to the various approximations in both the lensing algorithm and the simulation itself. A detailed analysis of these issues together with their impact on the lensed CMB observables will thus be presented.

This Chapter is organised as follows: in the Section 3.1, we briefly recall some of the theoretical background and notation used for our lensing algorithm. In Section 3.2 we discuss our ray-tracing technique, throughout its various steps, starting from a N-Body box (Sec. 3.2.1) which is converted into a series of 2D spherical maps (Sec. 3.2.2) that act as lens planes for the CMB photons (Sec. 3.2.3). Section 3.3 is dedicated to test and evaluate this procedure, both on the map-level and using 2-points statistics (Sec. 3.3.1) of the angular power spectrum. Section 3.4 shows the final results for the lensed temperature and polarization fields of the CMB Sec.3.4.2, but first it focuses on the numerical issues affecting lensing itself and the N-Body simulation (Sec. 3.4.1). All the Figures reported in the following have been shown first in [15], as this Chapter is directly based on the aforementioned paper.

3.1. THEORETICAL TOOLBOX

The theoretical framework of this Chapter has already been extensively described in the previous pages; repetition, in this case, is not helpful for the reader. However, we will describe in details the various steps of our algorithm, recalling some previous definitions and Equations.

The main idea is to apply a ML formalism to the lensing of CMB, as

described for the standard weak lensing scenario in Sec. 1.2.2. We apply the discretised Eq. (1.76), thus considering N concentric shells, each of comoving thickness $\Delta\chi$. The matter in the k-th shell is projected onto a spherical, two-dimensional sheet which is positioned in the middle of the two edges of the matter shell[1], at comoving distance $\chi_k \equiv \chi^{(k)}$. We remind the reader that we will use angular differential operators defined on the sphere instead of spatial ones, since we will be working with 2D spherical projections of the matter distribution.

A photon in the k-th shell at χ_k is deflected by an angle $\boldsymbol{\alpha}^{(k)}$, Eq. (1.77), due to the presence of matter represented as a 2D lensing potential on the sphere $\psi^{(k)}$, Eq. (1.78). N-Body simulations can provide a possible representation of the matter structures as they evolve in time. Poisson equation can relate the mass distribution, in particular the mass overdensity, with the gravitational potential in the shell, as

$$\nabla^2\Psi = \frac{4\pi G}{c^2}\frac{\rho-\bar{\rho}}{(1+z)^2}, \tag{3.1}$$

where $\bar{\rho}$ is the mean matter density of the Universe at redshift z. As in [166], we can integrate the above equation along the line of sight to obtain the two dimensional version of the Poisson equation for the k-th mass shell:

$$\nabla^2_{\hat{\mathbf{n}}}\Phi^{(k)}(\hat{\mathbf{n}}) = \frac{8\pi G}{c^2}\frac{f_K(\chi_k)}{(1+z_k)^2}\Delta^{(k)}_{\Sigma}(\hat{\mathbf{n}}), \tag{3.2}$$

where the surface mass density is defined as

$$\Delta^{(k)}_{\Sigma}(\hat{\mathbf{n}}) = \int_{\chi_k-\Delta\chi/2}^{\chi_k+\Delta\chi/2}(\rho-\bar{\rho})\mathrm{d}\tilde{\chi}. \tag{3.3}$$

In Eq (3.2) we have dropped the term containing the derivatives in the radial direction, ignoring thus long wavelength fluctuations along the line-of-sight via the Limber approximation [63]. However, as argued by [164, 163], this is, at best, an approximation. In particular [167] showed that this assumption neglects extra terms that become non-zero in presence of realistic finite width lens plane. The problem arises because the matter distribution and, thus, the potential itself may become discontinuous at the boundaries if periodic conditions are not enforced. Nevertheless, these corrections to the lens-plane approach adopting the Born approximation which has been used for this work (see Sect. 3.2) confine this problem to the single shells. In fact, partial derivatives in the transverse plane commute with the integral evaluated along the whole line of sight, resulting in

[1]The shell index k increases as moving away from the source plane.

the cancellation of line-of-sight modes as required in the Limber approximation[2].
We use the following definition for the convergence field $K^{(k)}$ at the k-th shell,

$$K^{(k)}(\hat{\mathbf{n}}) = \frac{4\pi G}{c^2}\frac{f_K(\chi_k)}{(1+z_k)^2}\Delta_\Sigma^{(k)}(\hat{\mathbf{n}}), \tag{3.4}$$

to rewrite Eq. (3.2) as

$$\nabla^2_{\hat{\mathbf{n}}}\Phi^{(k)}(\hat{\mathbf{n}}) = 2K^{(k)}(\hat{\mathbf{n}}). \tag{3.5}$$

The lensing potential on the sphere is related to K via Eq. (3.5), and it can be easily computed by expanding both sides of the Poisson equation in spherical harmonics, obtaining the following algebraic relation between the harmonic coefficients of the two fields:

$$\Phi_{\ell m} = \frac{2}{\ell(\ell+1)}K_{\ell m}. \tag{3.6}$$

The monopole term in the lensing potential does not contribute to the deflection field: therefore in order to avoid any divergence in the above equation we can safely set to zero $\Phi_{\ell m}$ for $\ell = 0$ in all calculations. The quantity K is directly computed when the matter distribution in the shell is radially projected onto the spherical map; as discussed in Sect. 3.2.2, it is useful to define an angular surface mass density $\Delta^\theta_\Sigma(\hat{\mathbf{n}})$ as the mass per steradians,

$$\Delta_\Sigma^{\theta(k)}(\hat{\mathbf{n}}) = \int_{\chi_k-\Delta\chi/2}^{\chi_k+\Delta\chi/2}(\rho-\bar{\rho})\frac{f_K(\tilde{\chi})^2}{(1+\tilde{z})^3}\mathrm{d}\tilde{\chi}. \tag{3.7}$$

such that Eq. (3.4) can be rewritten as:

$$K^{(k)}(\hat{\mathbf{n}}) = \frac{4\pi G}{c^2}\frac{(1+z_k)}{f_K(\chi_k)}\Delta_\Sigma^{\theta(k)}(\hat{\mathbf{n}}). \tag{3.8}$$

Finally, the vector field $\boldsymbol{\alpha}(\hat{\mathbf{n}})$ will be synthesised, as described in [168, 169], from the spherical harmonic components of the potential in terms of spin-1 spherical harmonics. The multiple-plane lens formalism can be also applied to exploit the effective or single-plane approximation to lens the CMB. Eqs. (1.69) and (1.75) can be discretised into the following sums,

$$\psi^{\mathrm{1st}}(\hat{\mathbf{n}}) = \sum_j \frac{f_K(\chi_* - \chi_j)}{f_K(\chi_*)}\Phi^{(j)}, \tag{3.9}$$

[2]Note for example that assuming a flat-sky approximation, unlike what has been done in this work, is a stronger assumption with respect to the Limber approximation and results in a well-known excess of power on large scales as seen, e.g., by [103].

$$\kappa^{\rm 1st}(\hat{\mathbf{n}}) = \sum_j \frac{f_K(\chi_* - \chi_j)}{f_K(\chi_*)} K^{(j)}, \tag{3.10}$$

where we used the previous definitions of quantities on the j-th lens. Based on the definition in Eq. (1.75), the angular power spectrum of the convergence becomes

$$C_\ell^{\kappa\kappa} = \frac{9H_0^4\Omega_{m,0}^2}{4c^4} \int_0^{\chi_*} {\rm d}\chi P(k,z) \left(\frac{f_K(\chi_* - \chi)}{f_K(\chi_*)a} \right)^2, \tag{3.11}$$

where $P(k,z)$ is 3D matter power spectrum, computed via the Limber approximation at $k = \ell/f_K(\chi(z))$, valid for $\ell > 10$ within a few percent accuracy [166]. The discretised equation reads:

$$C_\ell^{\kappa\kappa} = \frac{9H_0^4\Omega_{m,0}^2}{4c^4} \sum_k \Delta\chi \; P(\ell/f_K(\chi_k), z_k) \left(\frac{f_K(\chi_* - \chi_k)}{f_K(\chi_*)a_k} \right)^2, \tag{3.12}$$

summing all over the k lens plane. Note that the convergence field can be converted into lensing potential using the Poisson equation, or in terms of the angular power spectrum:

$$C_\ell^{\psi\psi} = \frac{4}{\ell^2(\ell+1)^2} C_\ell^{\kappa\kappa}. \tag{3.13}$$

3.2. The Algorithm

In the previous Section we have described the basic formalism and equations to evaluate the weak lensing effects on the full sky. In this Section we proceed outlining the basic steps of the algorithm used to lens the CMB photons throughout:

(i) starting from an N-Body simulation, we create 3D simulated matter distribution around a chosen observer;

(ii) taking advantage of the proper sampling in redshift of the simulation, we select different shells of matter at different times to reconstruct our past light-cone and mimic cosmological evolution;

(iii) we project all the matter in a given shell over a single 2D spherical map which acts as lensing plane;

(iv) we solve the full-sky Poisson equation in the harmonic domain and compute the lensing potential map for the single lens plane and for the integrated potential of Eq. (3.9);

(v) we use this lensing potential map to lens the CMB source plane;

(vi) we repeat step (iii)-(v) for all the selected shells, thus following the evolution of the source plane.

In our analysis we have used a N-Body simulation of cosmic structure formation in a flat ΛCDM universe with an underlying cosmology described by the following set of cosmological parameters:

$$\{\Omega_{dm}, \Omega_b, \Omega_\Lambda, n_s, \sigma_8, H_0\} = \{0.226, 0.0451, 0.729, 0.966, 0.809, 70.3\,\mathrm{Km/s/Mpc}\}.$$

The simulation follows the evolution of the matter distribution in a cubic (comoving) volume $(1000\ h^{-1}\mathrm{Mpc})^3$ from redshift $z = 10$ to present time using a modified TreePM version of GADGET[3], specifically developed to include all the additional physical effects that characterize different dark energy models (see [170] for a detailed description of the code). The whole numerical project goes under the name of COupled Dark Energy Cosmological Simulation, or CoDECS[4]. At present, they include two distinct set of publicly available runs, the L-CoDECS and the H-CoDECS. The L-CoDECS simulations consist in 1024^3 CDM and 1024^3 baryon particles, both treated with collisionless dynamics only, which means that baryonic particles are not considered as gas particles but just as a different family of collisionless particles distinguished from CDM. This is done in order to account for the effect of the uncoupled baryon fraction in DE models which would not be correctly represented by CDM-only simulations. The mass resolution at $z = 0$ for this set of simulations is $M_{CDM} = 5.84 \times 10^{10} M_\odot/h$ for CDM and $M_b = 1.17 \times 10^{10} M_\odot/h$ for baryons, while the gravitational softening is set to $\epsilon_s = 20$ comoving kpc/h, corresponding to 0.04 times the mean linear inter-particle separation. The H-CoDECS simulations are instead adiabatic hydrodynamical simulations on much smaller scales, which we do not consider in the present work.

3.2.1. Constructing mass shells

N-Body simulations are usually stored as a series of snapshots, each representing the simulation box at a certain stage of its evolution. As a first step, we fix the observer. We consider the last snapshot, at redshift $z = 0$, and compute the centre of mass of the whole simulation. This centre represents the origin of our new system of reference, which sees all the CMB

[3] www.mpa-garching.mpg.de/gadget

[4] www.marcobaldi.it/CoDECS

radiation around it. As we explore the universe around the new origin, the further we move in space, the more we look back in time and see how structures develop and grow, until we reach a volume large enough to carry out the integration for CMB lensing. One of the difficulties in this approach is that, even though the size of the simulation box is limited, we need to use the box to reconstruct the full backwards lightcone. Therefore, we need to replicate the box volume several times in space, so that the entire observable volume is covered. In particular, as described in [171], the simulation volume needs to be repeated along both the positive and negative directions of the three principal Cartesian axes x, y, and z, keeping the origin centred on the observer.

To construct the all-sky past light cone we exploit the simulation outputs at different times which are equally spaced in the logarithm of the scale factor, $log_{10}(a)$, corresponding to an average spacing of 150 h^{-1}Mpc comoving. The need to repeat the simulation volume due to its finite size immediately means that, without augmenting large-scale structures, the maps will suffer from a deficit of lensing power on large angular scales, due to the finite box size. More importantly, a scheme is required to avoid the repetition of the same structures along the line of sight. Previous studies that constructed simulated lightcone maps for small patches of the sky typically simply randomised each of the repeated boxes along the past lightcone by applying independent random translations and reflections (e.g. [172]). However, in the present application this procedure would produce artefacts like ripples in the simulated deflection-angle field, because the gravitational field would become discontinuous at box boundaries, leading to jumps in the deflection angle. It is therefore mandatory that the simulated lensing potential of our all sky maps is everywhere continuous on the sky, which requires that the 3D tessellation of the peculiar gravitational potential is continuous transverse to every line of sight.

Following [171, 99], our solution is to divide up the volume out to the redshift covered by the simulation z_{max} into larger spherical shells, each of thickness 1 h^{-1}Gpc comoving (as the box size). All the simulation boxes falling into the same larger shell are made to undergo the same, coherent randomisation process, i.e. they are all translated and rotated with the same random vectors generating a homogeneous coordinate transformation throughout the shell. But this randomisation changes from shell to shell. Figure 3.1 shows a schematic sketch of this process, which was also exploited in earlier works [171, 99]. As already mentioned, the need to repeat the simulation volume due to its finite size implies that the maps will suffer from a non proper description of the large angular scales. We note however that if the box size is sufficiently big like in e.g. [173] this

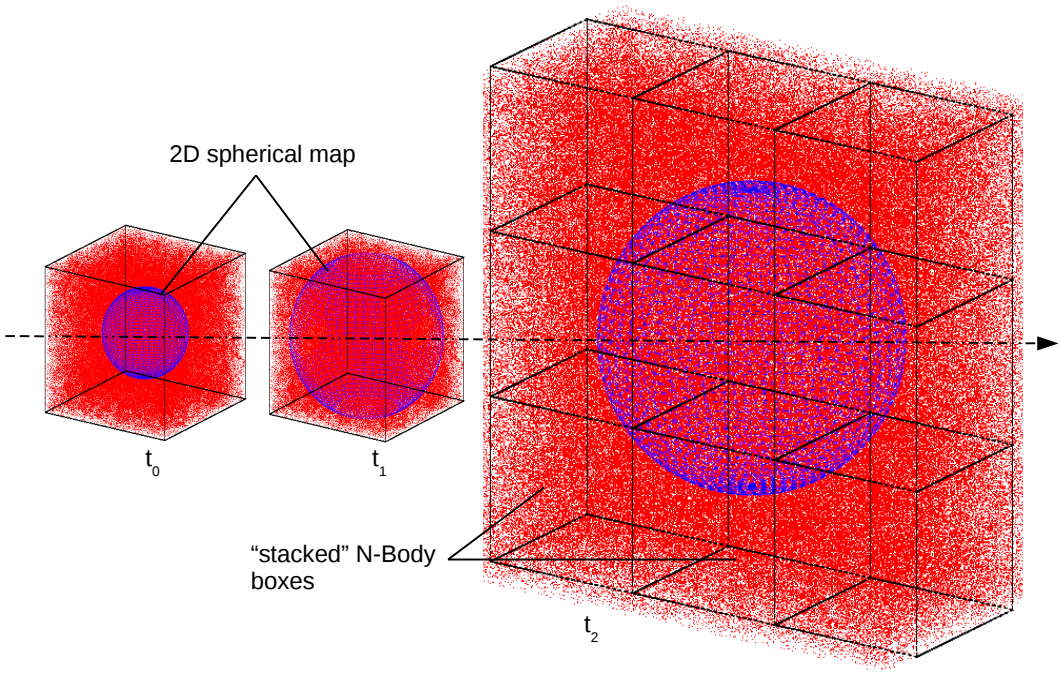

Figure 3.1 Sketch of the adopted stacking process. We use several outputs of the N-Body, each box at a different time (t_0, t_1, ...) as the simulation evolves with time. The simulation is used to trace the dark matter distribution of the Universe (red dots, representing a DM particle). A lensing plane for each output is then constructed by projecting the matter onto a 2D spherical map (blue surface), as explained in the text. In order to fill the entire matter shell, we need to stack and replicate the boxes of the N-Body simulation as we move further away from the observer and we need to consider even bigger volumes (third picture from the left).

procedure is no longer necessary, at least up to the redshift covered by the simulation size. The final results of the whole process is a series of concentric shells that substitutes our snapshots. For our specific input N-body simulation, we get 25 matter shells, building a lightcone spanning from $z = 0$ to $z_{max} = 10$.

3.2.2. From shells to maps

Following the scheme proposed in [164], we convert the position of a particle distributed within a 3D matter shell into its angular position on the 2D spherical map of the (projected) surface matter density. Note that among all the particles in the simulation, only the ones falling within the radii of

the spherical shell of width 150 h^{-1}Mpc are projected onto the 2D spherical map. We then assign each particle to a specific sky pixel in the HEALPix[5] pixelisation scheme starting from its spherical coordinates (θ,ϕ) and using the ang2pix routine of the HEALPix suite. We place the particle mass into the pixel so that each sky pixel reads $\Sigma_p^\theta = m_p/\Omega_{pix}$, where Ω_{pix} is the area of a pixel in steradians. If n particles fall inside the beam defined by a pixel, the pixel will have a surface mass density of $n\Sigma_p^\theta$. In HEALPix, the resolution is controlled by the parameter NSIDE which determines the number N_{pix} of pixels of equal area into which the entire sphere is divided through the relation $N_{pix} = 12\times\texttt{NSIDE}^2$, so that each pixel has an area of $\Omega_{pix} = 4\pi/N_{pix}$ sterad. The angular resolution is often expressed through the number $\theta_{res} = \sqrt{\Omega_{pix}}$. For a value of NSIDE set to 2048 (4096), the corresponding an angular resolution is $1'.717$ ($0'.858$).
The real interesting quantity in our lensing calculation, in addition to the surface mass density, is the convergence map $K^{(k)}(\hat{\mathbf{n}})$ on the lens-plane k. In order to get this quantity we first compute the overdensity maps ($\Delta\Sigma^\theta$) using the average surface mass density of the 2D map. Then we multiply by this map by its geometrical weight $(1 + z_k)/f_K(\chi_k)$, depending on the lens plane distance from the observer and its redshift, assumed to be an average between the time at the beginning and the end of the shell (see Eq. 3.8). As a final step, we produce a convergence map from each shell of the lightcone which will become our lensing planes to lens the CMB signal.
From the convergence map $K^{(k)}(\hat{\mathbf{n}})$ we then extract the gravitational potential $\psi^{(k)}$ following Eq. (3.6), using the HEALPix Spherical Harmonics Transform (SHT) routines to decompose $K^{(k)}(\hat{\mathbf{n}})$ into its harmonic coefficients $K_{\ell m}$. Note that we correct the smoothing of the true underlying continuous field on the pixel scale directly in the harmonic domain when we solve for the Poisson equation.

3.2.3. Lensing the CMB

In order to propagate the CMB photons through the different shells we adopt a pixel-based approach first presented in [112]. Starting from the $\psi_{\ell m}$ coefficients, we compute the deflection field for each shell $\boldsymbol{\alpha}^{(k)}$ evaluating Eq. (1.77) in the harmonic domain. Being the deflection field purely a gradient field (i.e. a spin-1 curl-free vector field), it can can be easily evaluated with a spin-1 SHT. The E and B decomposition of the field reads:

$$ {}_1\alpha^{E\ (k)}_{\ell m} = \sqrt{\ell(\ell+1)}\psi^{(k)}_{\ell m}, \qquad {}_1\alpha^{B\ (k)}_{\ell m} = 0. \tag{3.14}$$

[5] http://healpix.sourceforge.net

Once the deflection field is given, each pixel-based method remaps the CMB field as a function of the position on the sky assuming the lensed signal observed along a direction $\hat{\mathbf{n}}$ equal to the signal coming from another direction $\hat{\mathbf{n}}'$,

$$\hat{\mathbf{n}}'^{(k)} = \hat{\mathbf{n}}^{(k-1)} + \boldsymbol{\alpha}^{(k)}, \tag{3.15}$$

where $\hat{\mathbf{n}}^{(k-1)}$ represents the unlensed position of the CMB photons at the previous step. To our level of approximation $\|\nabla\Phi\|$ is assumed to be constant between $\hat{\mathbf{n}}^{(k-1)}$ and $\hat{\mathbf{n}}'^{(k)}$, consistent with working out the lensing potential in the Born approximation between two consecutive shells. In this work we adopted the publicly available code `LensPix`[6] [112] to propagate the CMB signal through all the lensing shells. `LensPix` implements a pixel-based lensing method using a bi-cubic polynomial interpolation scheme to evaluate the source plane along the displaced direction. This method has been shown to be accurate at the sub-percent level to produce temperature and E-modes signal. However, the recovery of the B-modes of the CMB polarization is more difficult because B-modes are more sensitive to numerical effects like the involved resolution and the choice of the band-limit (i.e. the power cut-off ℓ_{max}) in the calculation. We will discuss the impact on the relevant numerical effects in Section 3.4 and we refer the reader to [174] for a complete discussion of the numerical problems and accuracy of pixel based methods.
Finally, note that the simulated lightcone recovers the distribution of matter in the Universe up to $z_{max} = 10$, and therefore the primordial CMB fields are lensed by LSS only in this specific redshift interval. In other words, photons are ray-traced in a Universe evolving from z_{max} to $z = 0$. The impact of high-redshifts contributions is besides the goal of this algorithm, which will be tested against analytical and semi-analytical computations which we have modified accordingly to perform CMB lensing only in this redshift range.

3.3. Test and Convergence

In this section we assess the reliability of our code by performing sanity checks similarly to [164] to ensure that all the steps of the algorithm give stable and robust results. For the first test, we show that the total mass selected in each 3D matter slice is equal to the theoretical mass expected from the assumed cosmological model in the simulation, given by

$$M_{slice}^{theory} = 4\pi\Omega_{m,0}\rho_c\bar{\chi}^2\Delta\chi, \tag{3.16}$$

[6] `http://cosmologist.info/lenspix/`

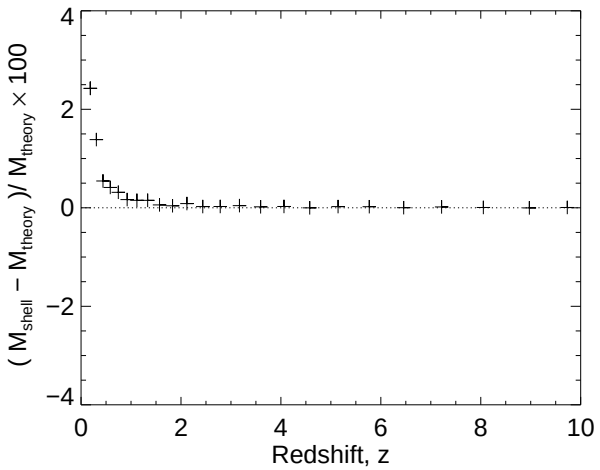

Figure 3.2 The total mass for each shell compared with the one expected from theory (fractional difference) as function of redshift.

where $\Delta\chi$ is the comoving thickness of the slice at a comoving (average) distance χ, ρ_c is the critical density and $\Omega_{m,0}$ corresponds to the present value of the matter density parameter. We compare this quantity with the total mass obtained from the surface density maps (Σ^θ) drawn with our procedure,

$$M_{slice} = \sum_{p=1}^{N_{pix}} \Sigma_p^\theta \, \Omega_{pix}, \tag{3.17}$$

by summing on all pixels of the spherical map. Figure 3.2 shows the fractional difference between the two masses for the different redshifts at which each spherical map is located. The agreement is very good within a few percent. As similarly found by [164], fluctuations respect to the theory appear at low z, due to the tension between the small comoving volume as seen by the observer, and a highly-clustered matter distribution at late times. Including or excluding large dark matter halos in the selection process therefore leads to differences between the mass extracted from the maps and the theoretical one.

As a second test, we make sure that the projection from the simulation box onto the map has been properly performed. Figure 3.3 displays the Probability Density Function (PDF) as recovered from the surface mass density maps, compared with analytic PDFs, drawn from the data, such as the Gaussian and log-normal ones (as in [175, 176]). The extracted PDFs are quite similar to the ones found by [164], even if - as already observed by the same authors - the analytical PDFs could not fit well the data especially at high surface mass density where the non-linearities becomes important

and where accurate models are yet unknown.

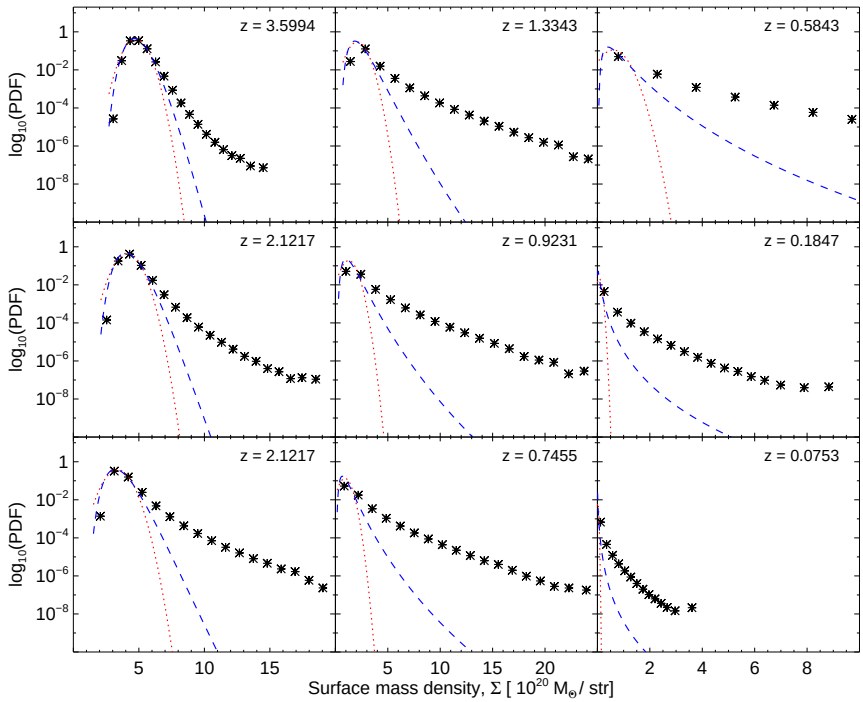

Figure 3.3 PDF of the surface mass density in the lensing-planes (crosses) compared with the Gaussian (red, dotted line) and the log-normal (blue, dashed line).

3.3.1. Lensing potential maps

Once surface density maps have been validated, we can move one step forward and verify lensing quantities. As described in Section 3.1, the effective convergence plane is computed by weighting the surface mass density planes with appropriate geometrical factors. We validated such convergence maps by comparing the extracted power spectra to the theoretical expectations based on semi-analytical computations of the matter perturbation evolution as implemented in the publicly available Boltzmann code CAMB[7]. Adopting the Born approximation, we drew an "effective" convergence map, as described in Eq. (3.10), using the matter shells at different redshifts. We then compute, in Limber approximation of Eq. (3.11), the theoretical convergence angular power spectrum, exploiting directly

[7] http://camb.info

the 3D matter power spectrum computed with CAMB. The comparison between the simulated and the analytical power spectra are shown in Figure 3.4. In both cases we perform the integration up to a specific redshift z^* to assess the validity of the maps at different times. We observe that the measured spectra agree at high accuracy with the theoretical predictions on a large interval of angular scales, indicating the validity of our map-making procedure. As expected, the lack of power at small multipoles $\ell \lesssim 50$ is due to the finite box size of the N-Body simulation. A source of possible contamination of the signal is the so-called *shot-noise*, due to the finite particle density in the N-Body simulation. The shot-noise power spectrum can be computed analytically substituting the shot noise power spectrum $P^{Shot}(k,z) = 1/\bar{n}_k$ in Eq. (3.12), where $\bar{n}_k = N_k/\left(4\pi\chi_k^2\Delta\chi\right)$ and N_k is the total number of particles in the k-th shell, we obtain the shot-noise contribution to the convergence:

$$C_\ell^{\kappa\kappa,\mathrm{Shot}} = \frac{9H_0^4\Omega_{m,0}^2}{4c^4}\sum_k \Delta\chi\,\frac{1}{\bar{n}_k}\left(\frac{f_K(\chi_* - \chi_k)}{f_K(\chi_*)a_k}\right)^2. \tag{3.18}$$

For the N-body simulation used in this code the shot-noise is small at all redshifts given the high spatial resolution and high number of particles employed (see Figure 3.4). Figure 3.5 shows a comparison of the partial contributions to lensing potential angular power spectrum computed at different redshifts with the corresponding analytical signal given by Eqs. (3.12) and (3.13) in which we insert the 3D matter power spectrum extracted from CAMB. In this case, the label z refers to the redshift of the matter spherical map which contributes to the lensing potential at that time. Each power spectrum represents the "real" map given as input to LensPix in order to obtain the final CMB lensed maps in the multiple plane approach. Here the Limber approximation is necessary to solve the Poisson equation using the transverse part of the Laplacian only, thus neglecting line-of-sight contributions as previously discussed in Sec. 3.1. The agreement between simulated and analytical $C_\ell^{\psi\psi}$ as a function of the redshift is clearly observable from Figure 3.5. The recovered signal is stable and coherent on a whole range of multipoles. As discussed in the following, we assume a very conservative choice for the map resolution and power cutoff ℓ_{max} (NSIDE $= \ell_{max} = 4096$). Therefore, we do not expect this result to be affected by power aliasing given that an HEALPix grid with resolution set by NSIDE parameter should be able to properly sample modes up to $\ell \approx 2\times$ NSIDE. An interesting and comprehensive way to see how the lensing process behaves at different scales is to look at the integrated potential, as computed in Born approximation using Eq. (3.9). In Figure 3.6 we show

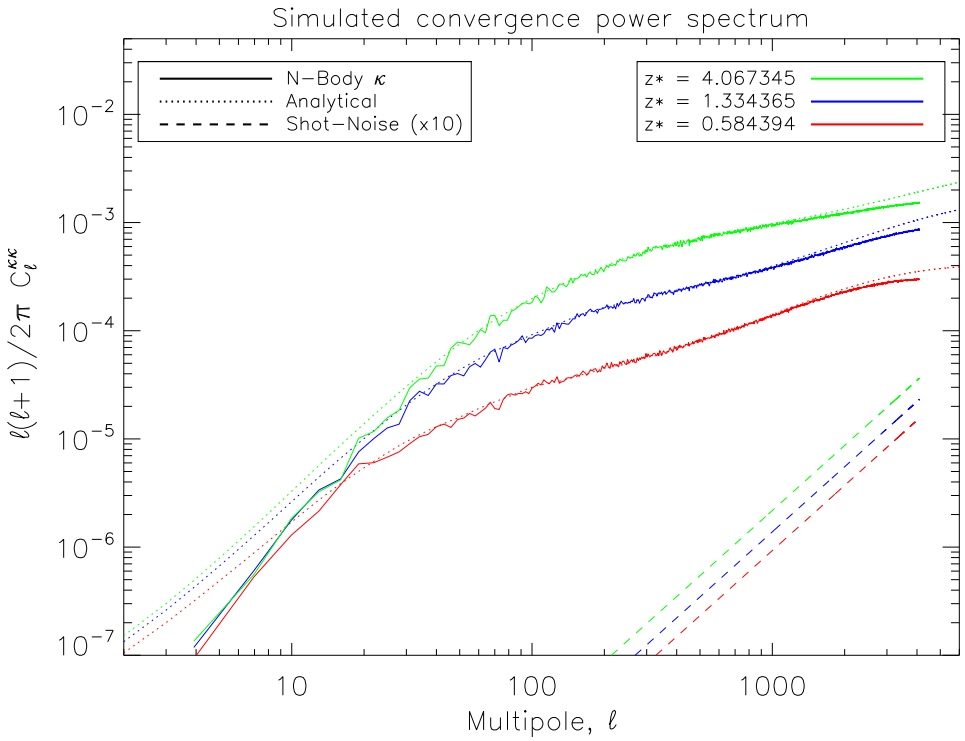

Figure 3.4 Angular power spectrum from the "effective" convergence map (solid lines) compared with theory predictions (dotted line) at three different redshifts, $z^* \simeq 0.6$, 1.3, 4. Dashed lines quantify the shot-noise contribution for each maps. Note that the shot-noise power spectra are multiplied by a factor of 10 for visualisation purposes.

the angular power spectrum for the effective lensing potential and its shot-noise contribution, compared to the semi-analytical realisations by `CAMB`, where we fix the maximum redshift of the integration, z_{max}, to be the same as the maximum redshift used in our map-making procedure. Also in this case, we find a very good agreement between the two methods, within the 1σ uncertainty for the semi-analytical spectrum. As in Figures 3.4 and 3.5 the spectrum shows a lack of power due to the finite size of the simulation box for $\ell < 50$. Note that the shot-noise contribution is negligible, as we have multiplied it by a factor of 10 such that it could be compared with the lensing potential signal. In general, at intermediate scales our spectra show a small deficit of power, within 3% with respect to the `Halofit` prescription [102], while at small scales, even after the shot-noise subtraction (blue lines), the signal seems to increase towards $\ell \approx 3500$, likely due to the underlying non-linear clustering underestimated by the analytical models. Since the simulated spectra agree within percent level with the

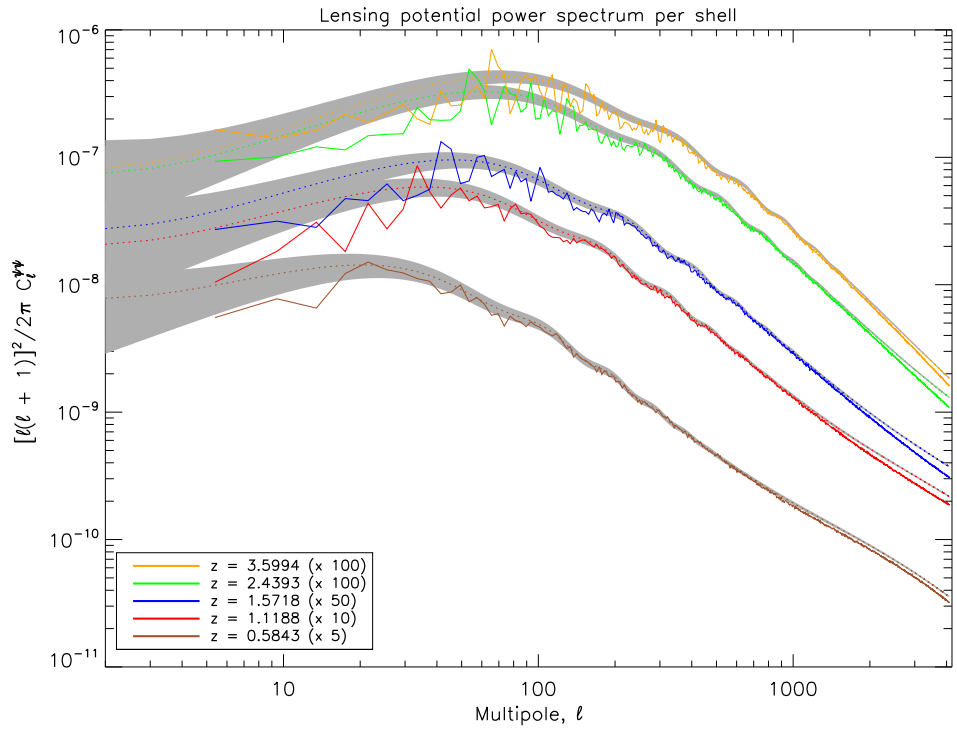

Figure 3.5 Comparison between the angular power spectrum of the lensing potential computed with our algorithm (solid lines) and the analytical results obtained using the Limber equation (dotted lines) at different redshift. The spectra have been multiplied by a constant factor for displaying purposes. The grey area displays the cosmic variance 1σ uncertainty for the theoretical spectra.

semi-analytical realisation of CAMB, this means that our map-making procedure traces with good accuracy the evolving matter distribution.

3.4. Results

Pixel-based methods for CMB lensing, though in general very efficient, are subjected to several numerical problems. The first one is related to the bandwidths of the lensed CMB fields generated as a result of the calculation. Because the lensing effect happens before the intervention of any instrumental response, the synthesis and analysis of relevant sky signals in the pixel-based lensing methods (CMB source plane and lensing potential map) require using a resolution sufficient to support the signal up to the intrinsic bandwidth ℓ_{max} set by the user specific application and its required accuracy. However, since mathematically the lensing effects act

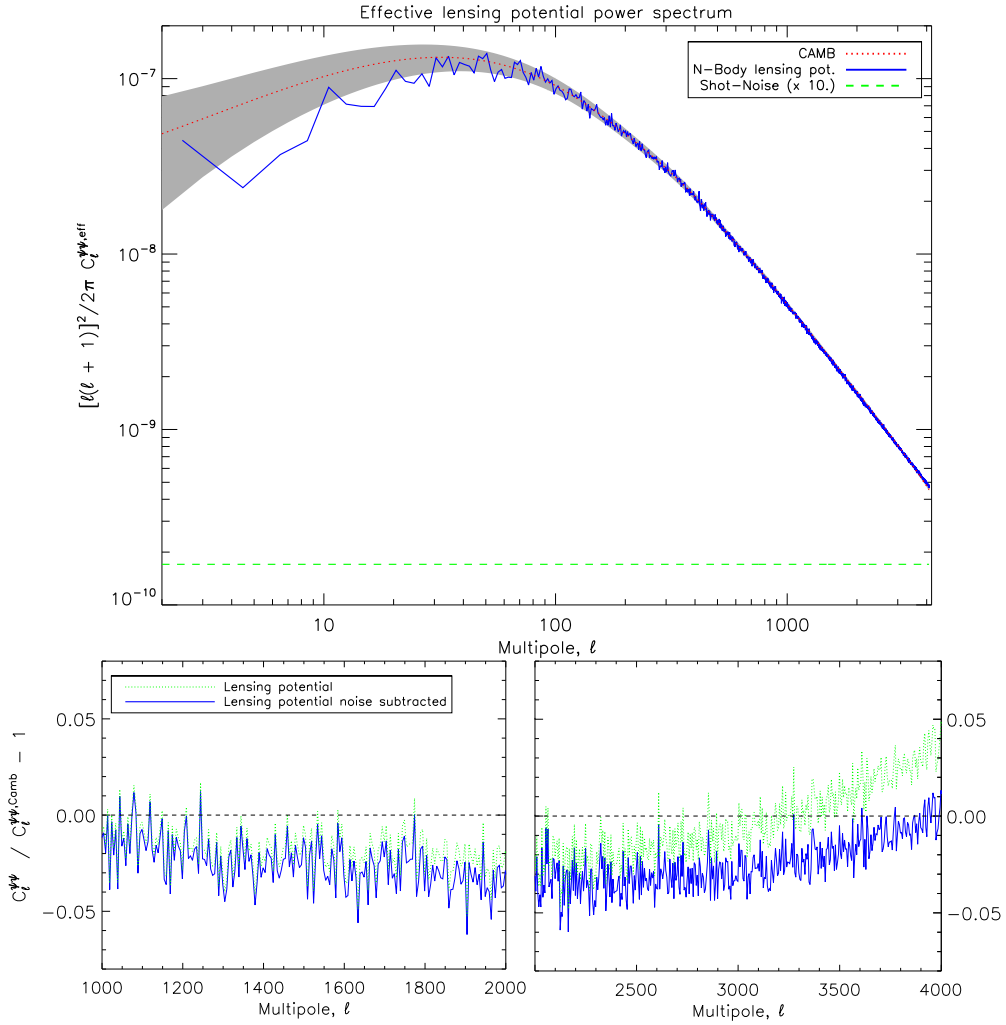

Figure 3.6 **Top panel**: Integrated lensing potential ψ^{eff} obtained in the Born approximation from the simulation (green) and the CAMB result based on semi-analytical approximation of the non-linear evolution (red). **Bottom panels**: fractional difference between the two for some intermediate and high multipoles scales. The results obtained after the shot-noise subtraction are displayed in blue solid lines. Note that the shot-noise spectrum in the top panel is multiplied by an arbitrary factor of 10 to be seen clearly in the Figure.

as a convolution in the harmonic domain, the bandwidth of the resulting lensed field is broader than the one of the unlensed CMB and of the lensing potential. Therefore, given the bandwidth used to synthesise the CMB source plane (ℓ_{max}^{CMB}), i.e before undergoing any deflection, and the one used to solve the Poisson equation and to create the deflection field for a given shell (ℓ_{max}^{ψ}), the resulting lensed CMB will have an approximate band-limit of $\ell_{max}^{CMB} + \ell_{max}^{\psi}$[8]. Consequently, the lensed map should have its resolution appropriately chosen to eliminate potential power aliasing effects on these angular scales [174]. We note moreover that these aliasing effects are even more important in the case of the ML approach because the bandwidth extension induced by lensing happens each time the lensed CMB is propagated through a single shell.
The second challenge arises from the fact that the displaced direction at each iteration $\hat{\mathbf{n}}'^{(k)}$ does not correspond in general to the pixel centres of any iso-latitudinal grid on the sphere. The values of the CMB signal at those locations thus cannot be computed with the aid of fast SHT algorithm and a more elaborated approach is needed. In the context of pixel-based simulation methods, interpolation is the most popular workaround of the need to directly calculate values of the unlensed fields for every displaced directions. The exact solution, which consist in a direct re-summation of the spherical harmonics at the displaced position, is in fact infeasible even for moderate resolutions [112, 174]. Any interpolation in this context, however, is not without its dangers because interpolations tend to smooth the underlying signals and - as a consequence - to hide aliasing effects in the lensed maps. For this reason we chose the bandwidth of our signal ($\ell_{max}^{CMB} = \ell_{max}^{\psi} = 4096$) and the resolution of our grid (`NSIDE`=4096) following the recipe provided in [174] to minimise all of these effects simultaneously. This choice however limits the multipole range where the lensing signal can be reproduced with high reliability especially in the case of B-modes of polarization to $\ell \lesssim 2500$ (see Sec 3.4.2).

3.4.1. Shot-noise contribution

In this section we estimate the impact of the intrinsic discretisation of the N-Body simulation on the final lensed CMB power spectra. Since we expect changes in the power spectrum on the order of few percent, it is mandatory to be able to control numerical artefacts with the same level of precision. For this study we use the analytical modelling of weak lensing

[8] We note that in general this band-limit is only approximate and the resulting function is strictly not band-limited unlike the input source plane.

in the harmonic domain discussed in [103]. This treats lensing as an effective convolution in Fourier space between the unlensed CMB and the lensing potential and it is based on a second order Taylor expansion around the unperturbed photons direction. The formulae are accurate to better than the percent level on the angular scales considered in this work, especially in the case of B-modes, and allow to quantify more easily the impact of the choice of the band-limit on the recovered result. In the specific case of B-modes, the convolution reads:

$$\tilde{C}^{BB}_{\tilde{\ell}_B} = O(\tilde{\ell}_B, C^{\psi\psi}_{\ell}) \cdot C^{BB}_{\tilde{\ell}_B} + \frac{1}{2} \sum_{\ell_E, \ell_\psi} \frac{|{}_2F_{\tilde{\ell}_B \ell_E \ell_\psi}|^2}{(2\tilde{\ell}_B + 1)} C^{\psi\psi}_{\ell_\psi} \left[C^{EE}_{\ell_E}(1 - (-1)^L) + C^{BB}_{\ell_E}(1 + (-1)^L) \right], \tag{3.19}$$

where we denote with tilde a lensed quantity and $L = \tilde{\ell}_B + \ell_E + \ell_\psi$. We refer the reader to [174] for a detailed discussion of the properties of the convolution kernels $F_{\tilde{\ell}_B \ell_E \ell_\psi}$ and to the $O(\tilde{\ell}_B, C^{\psi\psi}_{\ell})$ factor. Similar expression can also be derived for the TT, TE and EE power spectra [103]. Since this formalism does not make any assumption on the explicit form nor the origin of $C^{\psi\psi}_{\ell}$, we can plug in Eq. (3.19) the shot-noise power spectrum instead of the lensing potential extracted from the N-body simulation, to estimate the fraction of the recovered signal generated by the limited resolution of our simulated data. For this purpose we truncated the sum of Eq. (3.19) to the same band-limit value used in the lensing simulation, i.e. $\ell^E_{max} = \ell^{\psi}_{max} = 4096$.

We first evaluate the shot-noise contribution to the ψ^{eff} lensing potential starting from Eq. (3.18) and assuming the average number density to be the one of the ψ^{eff} field, $\bar{n}^{eff}_k$. This is then used as an input for the analytical formulae of Eq. (3.19), assuming the primordial B-modes C^{BB}_{ℓ} to be zero as it is the case for the unlensed CMB realisations used in the following. To validate the analytical shot-noise predictions we also produce 100 Monte Carlo realisations of shot-noise for the effective lensing potential. We use those maps to extract a deflection field which is then given as input to `LensPix` to lens a random realisation of the CMB signal. The final average of all the power spectra of these set of lensed CMB maps contains thus only the lensing effect due to the shot-noise acting on primordial anisotropies.

To evaluate the shot-noise contribution to the ML method we compute Eq. (3.18) for each k-shell and then apply the analytical convolution iteratively assuming as input CMB spectrum for the k-th shell the lensed one emerging from lensing of the previous $(k-1)$-th iteration.

As discussed in the following Section, if we assume a power cut-off for

the incoming CMB and the lensing potential to be ℓ_{max}^{CMB} and ℓ_{max}^{ψ} respectively, the lensed CMB after each deflection shows power up to a multipole $\tilde{\ell} \approx \ell_{max}^{CMB} + \ell_{max}^{\psi}$, due to the properties of the lensing convolution kernels in the harmonic domain [174]. The evaluation of the lensing kernels requires in fact a computationally-heavy summation of Wigner-$3j$ symbols up to high multipoles. We therefore have assumed that for the iteration $k > 0$ the incoming CMB has power at most up to $\ell = 8192$. This additional cut-off is high enough not to affect significantly the results on the scale considered in this work. The analytical formulae were validated also in this case with Monte Carlo simulation where for each shell the noise realisations were generated starting from the shot-noise power spectrum of the single shell.
In Figure 3.7 we show the results obtained from both these methods, for the B-mode power spectrum, which is the most sensitive to the details of the lensing potential being entirely lens-induced in our case (no primordial tensor modes). The TT and EE spectra are conversely quite insensitive to the the shot-noise which impacts the results at the sub 0.1% level (see Figure 3.8). Both the analytical and Monte Carlo estimates of the shot-noise contribution in the Born approximation agree extremely well at all angular scales. The shot-noise contribution in the ML approach is comparable to the effective case at $\ell \lesssim 2000$ though the difference is less than 0.5%.

3.4.2. Angular power spectrum

Similarly to the case of the lensing potential extraction, we now take into consideration two different approaches also for the evaluation of the angular power spectrum of the lensed CMB. The first set of primary CMB maps are lensed in the Born approximation, while the second set by mean of the ML approach. In Figure 3.8 we show the comparison between the expected CMB lensed temperature and the E-modes of polarization power spectra, (C_ℓ^{TT} and C_ℓ^{EE}), estimated using semi-analytical halo mass function implemented in `CAMB` [101, 102], and the spectra extracted from our lensed CMB maps. For both these cases the simulated power spectra follow precisely the `CAMB` signal. In particular, the shot-noise-induced contribution (evaluated following the recipe of the Section 3.4.1) for these two observables is negligible given that the effect of lensing per-se is already minor. Thus, changes introduced at percent variation in the lensing potential are further mitigated and hidden in the numerical noise. After having subtracted the shot-noise induced lensing contribution, the fractional difference between `CAMB` and the N-Body lensed spectra shows no significant

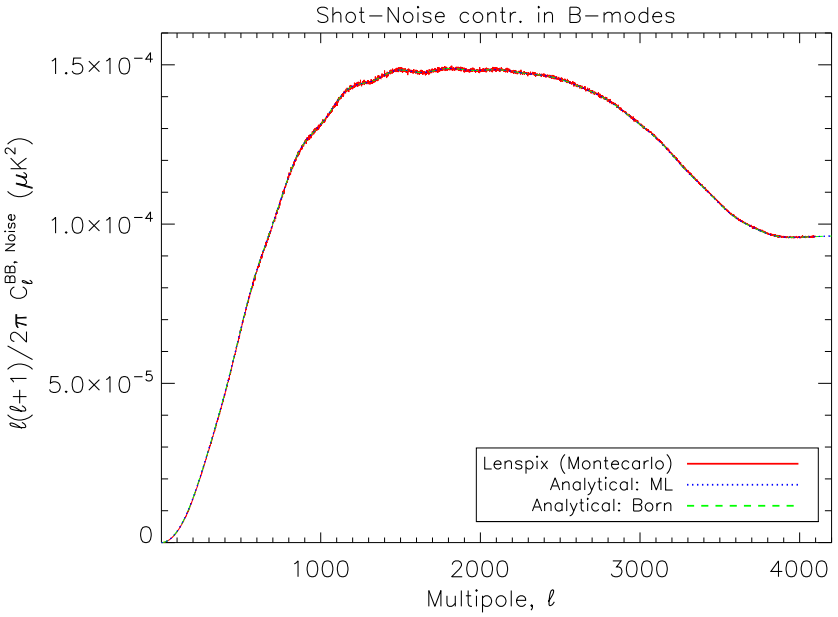

Figure 3.7 Angular power spectrum for the lensed B-modes induced by the simulation shot-noise. The red, solid line is computed using 100 realisations of the algorithm in the Born approximation scenario. The green-dotted and the blue-dashed lines are evaluated with the analytical formula for - respectively - the Born and the multiple plane scenario.

bias up to $\ell \approx 3000$ where we start seeing effects due to the choice of ℓ_{max}^{CMB}. The latter is not high enough to properly resolve power on those scales with high-accuracy. The difference between the results obtained with the Born and ML method is negligible and important only towards scales $\ell \approx \ell_{max}$ (see Figure 3.9). The abrupt decrease in power observed on those scales for the ML approach with respect to the Born approximation is due to the effect of polynomial interpolation. As the latter tends to smooth the underlying signal, the consecutive application effectively removes more power on small angular scale with respect to the Born approach, for which the interpolation is performed only once.

The situation however is different for the B-modes of polarization, as shown in Figure 3.10. This signal is entirely caused by lensing as we have set the primordial tensor modes to zero. Its behaviour is therefore a clear imprint of how the LSS process the primary CMB field and thus we expect this observable to reflect more directly the features observed in the lensing potential. As expected from the analysis of the lensing potential in Section 3.3.1, the BB spectrum shows a lack of of power at percent level with respect to `CAMB` spectra, in agreement with the matter power spectrum of the N-Body simulation, though this effect is partially compensated by the increase in power at small scales in the lensing potential. This feature is not observable in the lensed T or E field, where power coming from primordial anisotropies is dominant over the lensing-induced one. Moreover, while negligible in the TT and EE cases, we found the shot-noise contribution to be important at the percent level for the BB power spectrum at small scales. This is expected given that B-modes are very sensitive to non-linear power, which is affected by shot-noise for $\ell \gg 2000$ (see bottom panel of Figure 3.6). The lack of power due to the choice of ℓ_{max}^{CMB} starts to be important on angular scales larger than the ones affected in T and E-modes power spectra. This can be explained considering that at those scales a non-negligible fraction of the contribution to the BB power spectrum starts to come from progressively higher multipoles of both E and ψ. At $\ell_B \sim 4000$, for instance, a 25% contribution to the power in the B-modes comes from scales in the E and ψ fields at $\ell > \ell_{max} = 4096$ [174]. Since our algorithm is band-limited to this ℓ_{max}, cutting power for those high ℓ, produce a loss of about 25% in the BB power spectrum at that particular multipole (as shown in Figure 3.10).

As argued in Section 3.4, one of the major numerical problem affecting the simulation of CMB B-modes is the power aliasing due to bandwidth extension induced by lensing. In Figure 3.11 we show the impact of this effect as a function of the map resolution on the B-modes power spectrum recovery. For this tests we extracted the lensing potential maps

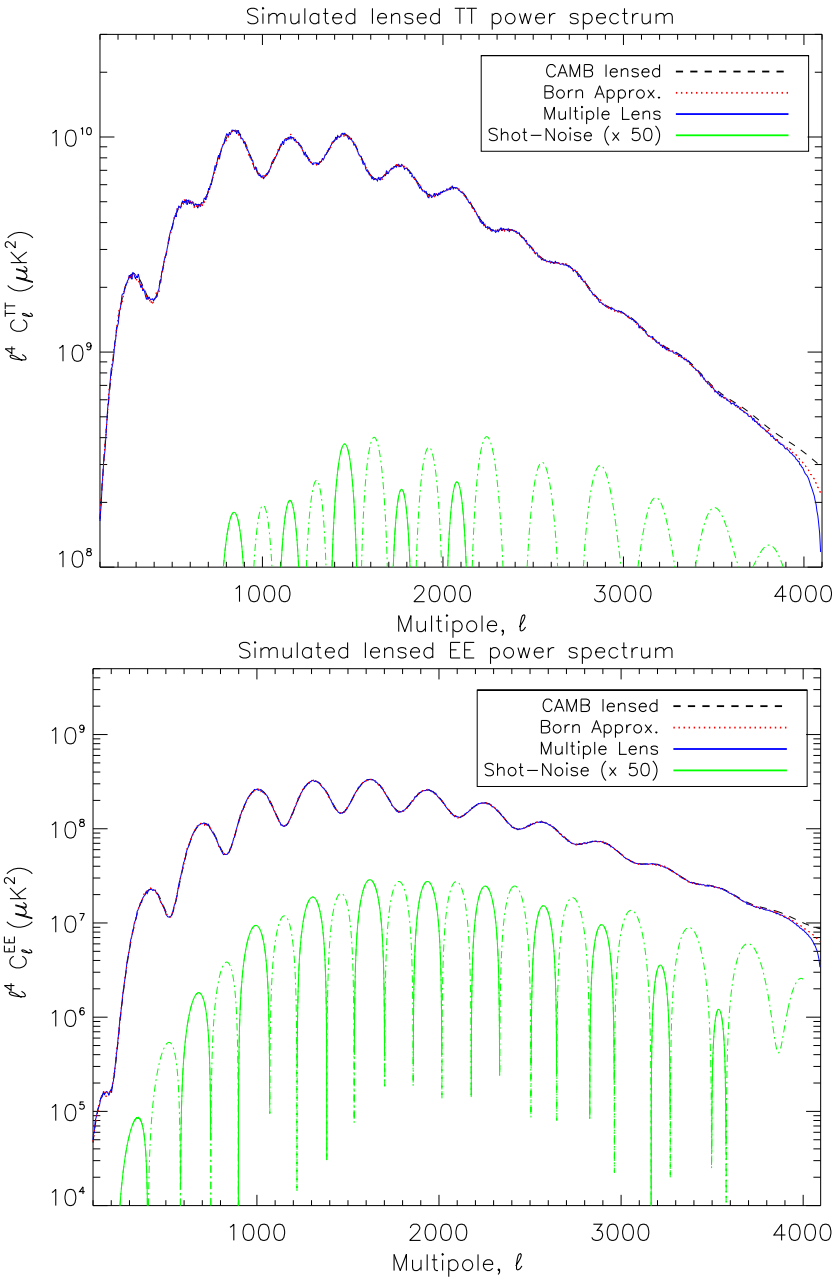

Figure 3.8 Angular power spectrum of the (lensed) total intensity T (top panel) and the E-mode polarization of the CMB (bottom panel). Black dashed lines are CAMB realisation of a lensed spectra. Red dotted line uses the lensing field as in the Born approximation, while for the blue solid line the CMB is lensed through multiple planes. Green lines in both panels show the shot-noise contribution to the lensed TT and EE spectra; green, dot-dashed lines represent the absolute value of this contribution. Note that the shot-noise power spectra are multiplied by a factor of 50 for visualisation purposes.

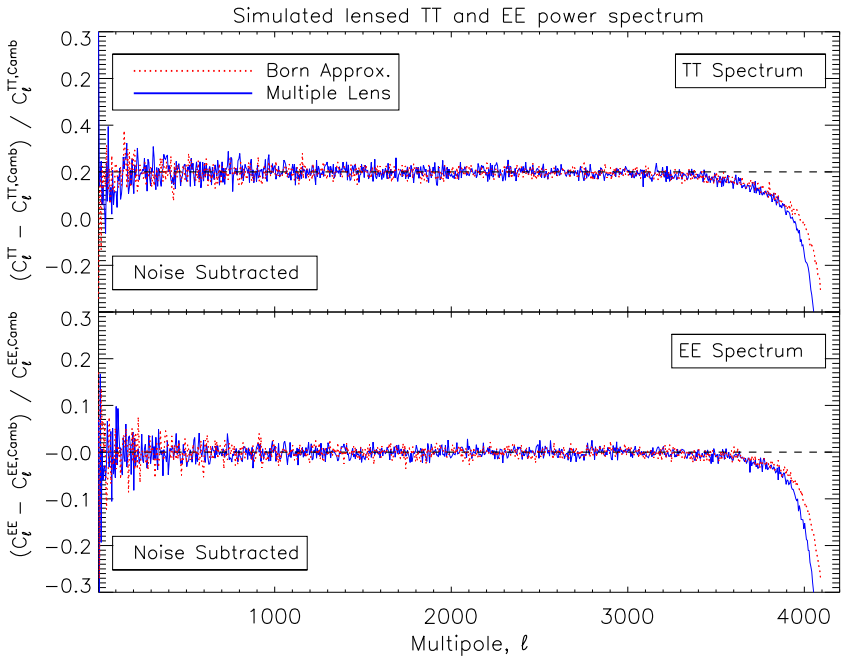

Figure 3.9 Fractional difference for the angular power spectrum of the temperature (top panel) and E-mode polarization (bottom panel) with respect to CAMB. Red dotted lines are obtained in the Born approximation, while blue solid in the multiple lens plane approach. The shot-noise has been subtracted in both cases.

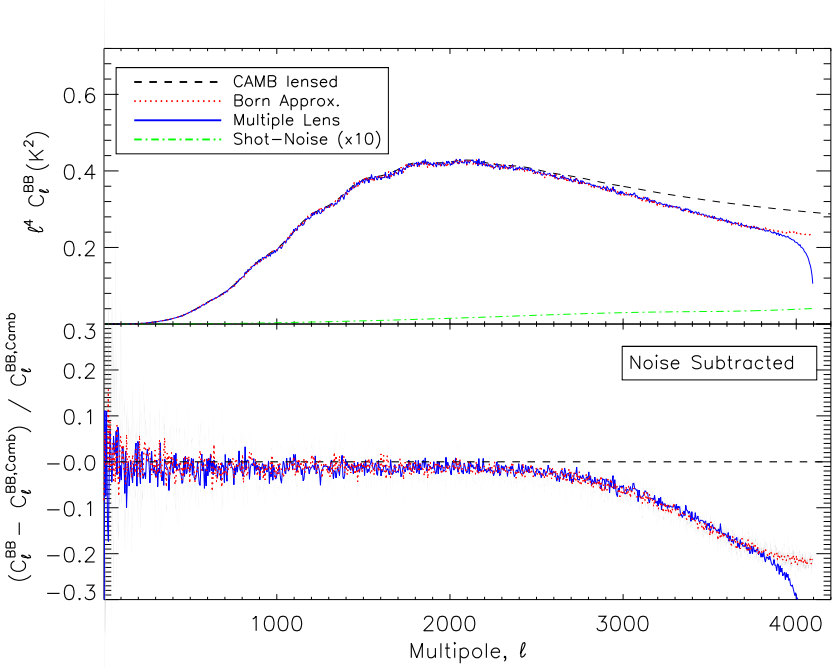

Figure 3.10 Angular power spectrum for the B-mode polarization of CMB. Black dashed lines are CAMB realisation of a lensed spectra. Red dotted lines are obtained in the Born approximation, while blue solid lines in the multiple lens planes approach. The green dot-dashed line is a lensed spectrum produced from a shot-noise-only lensing map. Note that the shot-noise power spectra are multiplied by a factor of 10 for visualisation purposes. In the bottom panel, it is shown the fractional difference with the reference CAMB spectrum. In this panel, the noise power spectrum has been subtracted from the original signal.

for both Born and ML approach using two different HEALPix grid at $\texttt{NSIDE} = 2048, 4096$ and refer to these two set-up as the low and high resolution case respectively. We then synthesised on the same grid the CMB source plane assuming the same band-limit $\ell_{max}^{CMB} = 4096$, as done for the results discussed above, and propagate it through the lensing plane(s). As shown in Figure 3.11, the Born approximation method is quite insensitive to the choice of NSIDE because the polynomial interpolation is effective in removing most of the aliasing. However, for the ML scenario the situation is worse as the aliasing generated by multiple deflection can add up, becoming progressively more important. This can then lead to a misinterpretation of the result obtained using the ML, which seems to be significantly different from the once obtained in the Born approximation. The fact that this difference vanishes in the high-resolution case is a demonstration of the high level of control of numerical effects which needs to be achieved for this kind of algorithms. Even though these effects were limited in the set-up considered here, we expect those to become more important when targeting accurate lensing simulations on scales $\ell \gg 2000$.

Finally, we compare the differences in the angular power spectra between the Born approximation and the multiple planes approach. First we define the quantity O_ℓ^X as the difference between the angular power spectra extracted with the multiple lens approach and the one computed in the Born approximation,

$$O_\ell^X = C_\ell^{X,\mathrm{ML}} - C_\ell^{X,\mathrm{Born}}, \tag{3.20}$$

where X = TT, EE, BB. Its uncertainty is given by the cosmic variance affecting both spectra, or

$$\sigma_{O_\ell^X} = \sqrt{\frac{2}{2\ell+1}\left(|C_\ell^{X,\mathrm{ML}}|^2 + |C_\ell^{X,\mathrm{Born}}|^2\right)}. \tag{3.21}$$

Starting from these quantities we can define a reduced chi-square $\tilde{\chi}^2$ statistics

$$\tilde{\chi}^2 = \frac{1}{\ell_{max}-1}\sum_{\ell=2}^{\ell_{max}} \frac{O_\ell^2}{\sigma_{O_\ell}^2}, \tag{3.22}$$

to assess whether the two methods are inconsistent. Since we expect $O_\ell^X/\sigma_{O_\ell}^2$ to be a Gaussian random variable, we can we also perform a Kolmogorov-Smirnov (KS) to test whether this hypothesis is verified or systematic differences exists between the two methods. In defining both theses tests and the sample variance of Eq. (3.22), we assumed that the covariance of the lensed power spectra is Gaussian. This assumption neglects the

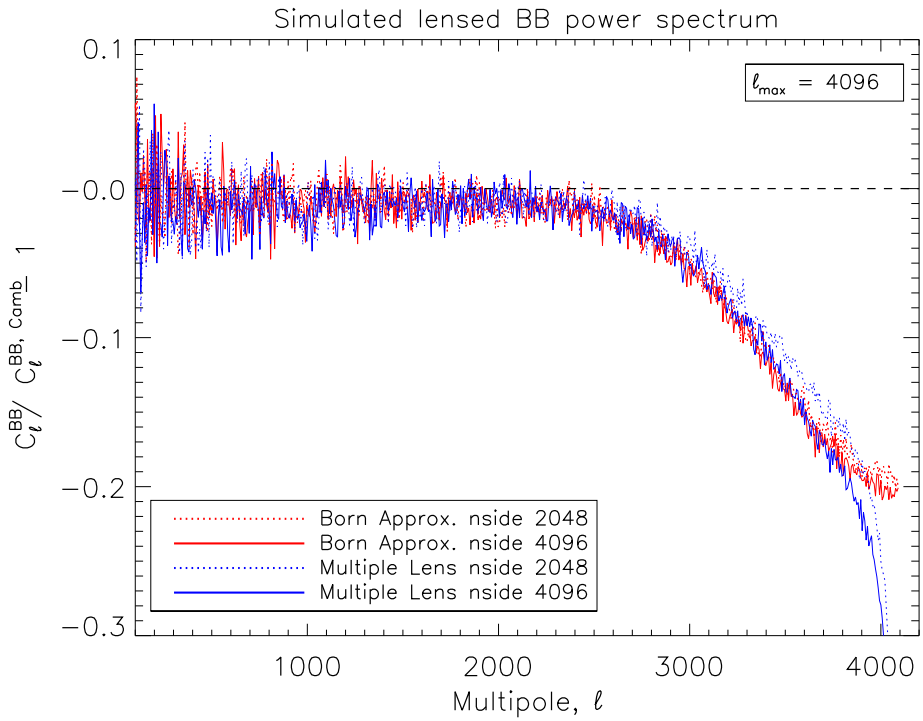

Figure 3.11 Fractional difference of angular power spectrum of the BB power spectrum with respect to the reference CAMB spectrum. Dotted lines refers to the map at low resolution (NSIDE=2048), while solid lines to the map with NSIDE=4096. Red lines plot the effective, Born approximation case, blue lines are connected to the multiple plane approach. Note that for this comparison, the noise power spectrum has not been subtracted from the original signal.

C_ℓ^X	Significance P_{KS}	Significance $P_{\tilde{\chi}^2}$
TT	0.47	0.70
EE	0.19	0.51
BB	0.21	0.19

Table 3.1 Results of statistical tests on difference between lensed CMB angular power spectra in the Born approximation and multiple lens planes approach. The significance level probability for the null hypothesis using a Kolmogorov-Smirnov test (P_{KS}) and a reduced chi-square $\tilde{\chi}^2$ statistics ($P_{\tilde{\chi}^2}$) show no difference between the power spectra computed with the two methods on a statistical level.

fact that lensing introduces non-Gaussian correlations between different modes [177, 178], but this effect is mainly important for B-modes, for which the Gaussianity assumption underestimates the sample variance.

In Table 3.1 we report the results of both those tests expressed as the significance level probability. In both cases we find that the power spectra obtained in the Born approximation and with the ML method are statistically consistent. A further possible test to compare the two methods would be to reconstruct the effective integrated matter density from the simulated lensed CMB maps as done in [159], but we leave this option to future work.

CHAPTER 4

High resolution CMB lensing simulations

> Men who wish to know about the world must learn about it in its particular details.
>
> *Heraclitus*

> Most people don't have time to master the very mathematical details of theoretical physics.
>
> *Stephen Hawking*

The idea of this Chapter originates immediately after the last lines written in the previous pages, as our simulations show no appreciable statistical difference between the standard, Born approximation, first-order result and the multiple lens-planes implementation of our algorithm. This outcome is on one side reassuring, it means that approximations used so far by the community have been proven right, but on the other side, it opens other new questions: in the end, is our approach correct, or we are ignoring some important and crucial facts? Are we modelling accurately the travel of a photon though the matter distribution in the Universe? How can we improve our analysis to fully unleash the power of the multiple lens approximation?

This Chapter attempts to address this issues following two different but connected paths: first, we decide to push the limits of our algorithm by reaching higher resolutions and by exploring all the lensing information we can extract from our maps, i.e. we study the full magnification matrix as described in a previous Section, Sec. 1.2.3. Secondly, we move towards a theoretical and analytical description of the multiple deflections of a CMB photons, as we look at high-order corrections in the power spectrum prescribed by perturbation theory. The broader scientific goal, though, will especially target the lensing-generated B-modes, both for their sensitivity to the LSS distribution and as the main contaminant of any primordial B-modes signal, holy grail of current and future CMB observations. Since sensitivities of the CMB polarization arrays are rapidly improving, the experiments aiming at setting constraints on values of the tensor-to-scalar

ratio parameter $r \lesssim 10^{-2}$ are expected to be ultimately limited by the lensing signal [179]. As already stated previously in the Thesis, the scientific community needs new simulations of very accurate, high-resolution maps of the CMB total intensity and polarization, covering a large fraction of the sky and with lensing effects included.

This Chapter reflects our double approach: in the first Section, we expand the theoretical and analytical background of our algorithm by detailing high-order effects on the angular power spectrum, and their consequences on the simulated lensing fields. Sec. 4.2 characterises the full magnification matrix, as we improve our algorithm by using new remapping technique by means of the `lenS`^{2}`HAT` routines [174]. As done in the previous Chapter, we focus our attention on the 2-points statistic of the angular power spectrum (Sec 4.2.1) for different lensing observables. The final Section, Sec. 4.3, is dedicated to study those secondary effects on the CMB fields from a theoretical point of view, especially regarding B-modes of CMB polarization induced by gravitational lensing.

4.1. HIGH ORDER EFFECTS ON THE FULL MAGNIFICATION MATRIX

In this Section we briefly recall some formulae to describe the behaviour of a light-ray when deflected by the presence of matter. The description of such formalism has already been developed in details in Sec. (1.2), however to facilitate the reader I reproduce here only the results relevant to this work.

In weak lensing calculations, the effect of deflectors along the entire line is governed by the lens equation, which maps the final position $(t, \boldsymbol{\beta}, \chi)$ of the photon to the position of its source, i.e.

$$\beta_i(\boldsymbol{\theta}, \chi) = \theta_i - \frac{2}{c^2} \int_0^\chi \frac{f_K(\chi - \chi')}{f_K(\chi) f_K(\chi')} \Phi_{,\beta_i} \left(t(\chi'), \boldsymbol{\beta}(\boldsymbol{\theta}, \chi'), \chi'\right) \mathrm{d}\chi', \tag{4.1}$$

given a gravitational potential $\Phi(t, \boldsymbol{\beta}, \chi)$ acting on the photon during its travel. The relative position of nearby light rays is quantified by:

$$\begin{aligned} A_{ij}(\boldsymbol{\theta}, \chi) &= \frac{\partial \beta_i(\boldsymbol{\theta}, \chi)}{\partial \theta_j} = \\ &= \delta^K_{ij} - \frac{2}{c^2} \int_0^\chi \frac{f_K(\chi - \chi')}{f_K(\chi) f_K(\chi')} \Phi_{,\beta_i \beta_k} \left(t(\chi'), \boldsymbol{\beta}(\boldsymbol{\theta}, \chi'), \chi'\right) A_{kj}(\boldsymbol{\theta}, \chi') \mathrm{d}\chi', \end{aligned} \tag{4.2}$$

where δ^K_{ij} is the Kronecker delta. The image distortions of small light sources can be described by the distortion matrix $\mathbf{A}(\boldsymbol{\theta}, \chi) \equiv \{A_{ij}(\boldsymbol{\theta}, \chi)\}$,

which holds the information of the mapping induced by lensing between the original and the current position (i.e. Jacobian $\boldsymbol{\theta} \rightarrow \boldsymbol{\beta}$). Note that the potential Φ is evaluated at the ray angular position $\boldsymbol{\beta}(\boldsymbol{\theta}, \chi)$, while the distortion itself - which is present at the r.h.s of Eq (4.2), *lens-lens coupling* - is computed at the "background" position $\boldsymbol{\theta}$. The magnification matrix $\mathbf{A}$ is typically decomposed into four fields describing how the light rays coming from a source at $\chi \equiv \chi_s$ are transformed by the passage through the matter distribution,

$$A_{ij} = \begin{pmatrix} 1-\kappa-\gamma_1 & -\gamma_2+\omega \\ -\gamma_2-\omega & 1-\kappa+\gamma_1 \end{pmatrix}, \tag{4.3}$$

where we assumed that the rotation angle $\omega(\boldsymbol{\theta}, \chi_s)$ which defines a rotation of the lensed image, is small. The field $\kappa(\boldsymbol{\theta}, \chi_s)$ is the convergence while $\gamma(\boldsymbol{\theta}, \chi_s) = \gamma_1(\boldsymbol{\theta}, \chi_s) + i\gamma_2(\boldsymbol{\theta}, \chi_s)$ defines the complex shear, describing the shearing of the image, and can be decomposed in to a rotation-free part, $\gamma_E(\boldsymbol{\theta}, \chi_s)$ and a divergence-free one, $\gamma_B(\boldsymbol{\theta}, \chi_s)$.

The presence of a rotation ω authorize the introduction of an auxiliary curl potential Ω with a slightly abuse of notation, such that the deflection angle may be expressed as a combination of the standard gradient contribution from a scalar field ψ, and a curl contribution [67]:

$$\boldsymbol{\beta} = \boldsymbol{\theta} - \nabla\psi - \nabla \times \Omega, \tag{4.4}$$

where we defined the two-dimensional curl $(\nabla \times \Omega)_i = \epsilon_{ij}\partial\Omega$. This potential Ω has to be intended as an "effective", Born-like potential, integrated along the line of sight, that encodes all the information about the rotation of the image as curl-like patterns are originated in the signal through multiple deflections. All of the above quantities can be treated on the sphere using the spin-s spherical harmonic decomposition of the full-sky [103, 163]. In particular, this section combines results from [103] and [180] to derive the relationships between the rotation, convergence, E- and B-mode shear power spectra. See [67] for the equivalent flat-sky formalism. The full-sky magnification matrix can be written as

$$\begin{aligned} A_{ij} &= (1-\kappa)\delta^K_{ij} - \gamma_{ij} + \omega\epsilon_{ij} \\ &= \delta^K_{ij} - \sum_{\ell m} \left(\psi_{\ell m}\nabla_i\nabla_j Y_{\ell m} + \Omega_{\ell m}\epsilon^k_j\nabla_i\nabla_k Y_{\ell m}\right), \end{aligned} \tag{4.5}$$

where γ_{ij} is a symmetric, traceless tensor, where we recall that

$$\gamma_{ij} = \begin{pmatrix} -\gamma_1 & -\gamma_2 \\ -\gamma_2 & \gamma_1 \end{pmatrix}, \tag{4.6}$$

$\omega\epsilon_{ij}$ is the antisymmetric part and $(1-\kappa)\delta^K_{ij}$ is the non-zero trace part, following previous Eq. (4.4). [103, 163] shows that by comparing the two previous Eqs (4.5) and applying the relations between derivatives of scalar and spin-s spherical harmonics by [103], we get the classic result

$$\kappa = -\frac{1}{2}\sum_{\ell m}\ell(\ell+1)\psi_{\ell m}Y_{\ell m} \tag{4.7}$$

$$\omega = -\frac{1}{2}\sum_{\ell m}\ell(\ell+1)\psi_{\ell m}Y_{\ell m} \tag{4.8}$$

$$\gamma_1 \pm i\gamma_2 = \frac{1}{2}\sum_{\ell m}\sqrt{\frac{(\ell+2)!}{(\ell-2)!}}\left(\psi_{\ell m} \pm i\Omega_{\ell m}\right)_{\pm 2}Y_{\ell m}. \tag{4.9}$$

These equations with $\Omega_{\ell m} \equiv 0$ where presented in [103]. Using naturally the standard E and B modes decomposition for the spin-2 $\boldsymbol{\gamma}$ shear field, these relations between the harmonic coefficients hold:

$$E^{\gamma}_{\ell m} \equiv \frac{1}{2}\sqrt{\frac{(\ell+2)!}{(\ell-2)!}}\psi_{\ell m}, \tag{4.10}$$

$$B^{\gamma}_{\ell m} \equiv \frac{1}{2}\sqrt{\frac{(\ell+2)!}{(\ell-2)!}}\Omega_{\ell m}. \tag{4.11}$$

We can then obtain the following relations between convergence, rotation, shear E- and B-mode angular power spectra:

$$C^{\kappa\kappa}_{\ell} = \frac{1}{4}\ell^2(\ell+1)^2 C^{\psi\psi}_{\ell}, \tag{4.12}$$

$$C^{\omega\omega}_{\ell} = \frac{1}{4}\ell^2(\ell+1)^2 C^{\Omega\Omega}_{\ell}, \tag{4.13}$$

$$C^{\epsilon\epsilon}_{\ell} = \frac{1}{\ell^2(\ell+1)^2}\frac{(\ell+2)!}{(\ell-2)!}C^{\kappa\kappa}_{\ell}, \tag{4.14}$$

$$C^{\beta\beta}_{\ell} = \frac{1}{\ell^2(\ell+1)^2}\frac{(\ell+2)!}{(\ell-2)!}C^{\omega\omega}_{\ell}, \tag{4.15}$$

where ϵ and β refers to the E-mode and B-mode components of the γ field, respectively. The relations between $C^{\psi\psi}_{\ell}$, $C^{\epsilon\epsilon}_{\ell}$ and $C^{\kappa\kappa}_{\ell}$ where presented in [103]. The cross-spectra $C^{\epsilon\beta}_{\ell}$, $C^{\omega\kappa}_{\ell}$, $C^{\kappa\beta}_{\ell}$, and $C^{\omega\epsilon}_{\ell}$ are all zero assuming that the Universe is statistically parity invariant (i.e. $\langle\psi\Omega^*\rangle = 0$, see [67]). The rest of the cross-spectra can be computed from the relations above as well. Finally, note that at small scales or high-ℓ, the factor

$$\lim_{\ell\to\infty}\frac{1}{\ell^2(\ell+1)^2}\frac{(\ell+2)!}{(\ell-2)!} \approx 1, \tag{4.16}$$

thus reproducing the results of several previous authors [180, 67, 181].

The magnification tensor for sources at a single redshift can be rewritten implicitly as (see e.g. [182])

$$\Psi_{ij}(\boldsymbol{\theta}) = A_{ij}(\boldsymbol{\theta}) - \delta^K_{ij}, \tag{4.17}$$

highlighting the deformation component of the tensor. Within this definition, Eq (4.2) becomes:

$$\Psi_{ij}(\boldsymbol{\theta}, \chi_s) = 2\int \mathrm{d}\chi g(\chi, \chi_s)\Phi_{,ik}\left(\boldsymbol{\beta}, \chi\right)\left[\delta^K_{kj} + \Psi_{kj}(\boldsymbol{\theta}, \chi)\right], \tag{4.18}$$

where commas represents spatial derivatives. Repeated indices are summed over the 2 transverse directions. The presence of Ψ in the integral reflects a foreground lens affecting the deformation from a more distant lens - or "lens-lens coupling". The lensing efficiency $g(\chi, \chi')$ is the standard geometrical factor,

$$g(\chi, \chi') = \begin{cases} \frac{f_K(\chi')f_K(\chi-\chi')}{f_K(\chi)}, & \chi' < \chi \\ 0, & \chi' \geq \chi. \end{cases} \tag{4.19}$$

Here the gravitational potential Φ is evaluated at a deflected position[1]

$$\boldsymbol{\beta}(\boldsymbol{\theta}, \chi) = \boldsymbol{\theta} f_K(\chi) + \delta\boldsymbol{\beta}(\boldsymbol{\theta}, \chi), \tag{4.20}$$

$$\delta\boldsymbol{\beta}_i(\boldsymbol{\theta}, \chi) = -2\int \mathrm{d}\chi' g(\chi', \chi)\frac{f_K(\chi)}{f_K(\chi')}\Phi_{,i}\left(\boldsymbol{\beta}, \chi'\right), \tag{4.21}$$

where the deflections are confined to the transverse plane. Note that Eq. (4.18) is implicit in both the deformation tensor and the potential along the full geodesic $\Phi(\boldsymbol{\beta}, \chi)$, where $\boldsymbol{\beta}(\boldsymbol{\theta}, \chi)$ again depends on the potential via the lens equations, Eq (4.1). By assuming small initial deformations $\Psi^{(0)} \approx 0$ (neglecting of lens-lens coupling) and evaluating the potential along the unperturbed geodesic $\boldsymbol{\beta}^{(0)} \approx \boldsymbol{\theta}$, i.e. the Born approximation, the well-known first-order result holds:

$$\Psi^{(1)}_{ij}(\boldsymbol{\theta}, \chi) = 2\int_0^{\chi} \mathrm{d}\chi' g(\chi', \chi)\Phi_{,ij}\left(\boldsymbol{\theta}, \chi\right). \tag{4.22}$$

In the literature the use of the Born approximation generally implies neglecting lens-lens coupling as well, since they appear at the same order in perturbation theory. In terms of angular power spectrum, we can write in Limber approximation as done in previous pages,

$$C_\ell^{\kappa\kappa,\mathrm{1st}} = \ell^4 \int_0^{\chi_s} \mathrm{d}\chi \frac{g^2(\chi, \chi_s)}{f_K^6(\chi)} P_{\Phi\Phi}\left(\frac{\ell}{f_K(\chi)}, \chi\right), \tag{4.23}$$

[1]Formally $f_K(\chi)\boldsymbol{\theta} \to f_K(\chi)\boldsymbol{\theta}_\perp + \chi\boldsymbol{\theta}_\parallel$ in an open universe but components parallel to the fiducial line of sight drop out in the Limber approximation.

and $C_\ell^{\epsilon\epsilon,1\mathrm{st}} = C_\ell^{\kappa\kappa,1\mathrm{st}}$ while $C_\ell^{\beta\beta,1\mathrm{st}} = C_\ell^{\omega\omega,1\mathrm{st}} = 0$. The lack of B-modes in the signal to first order in the perturbations has been considered as a possible test of instrumental and astrophysical systematic effects. At first order, weak lensing by matter only generate E-modes. However, as studied in previous works [183, 67, 181], deviations from the Born approximation can generate B-modes in the shear field.

Corrections to the Born approximation can be calculated by Taylor expanding the potential in Eq. (4.18) to second order in the deflection of Eq. (4.20),

$$\Phi(\boldsymbol{\theta} + \delta\boldsymbol{\beta}) \approx \Phi(\boldsymbol{\theta}) + \Phi_{,i}\,(\boldsymbol{\theta})\delta\boldsymbol{\beta}_i + \frac{1}{2}\Phi_{,ij}\,(\boldsymbol{\theta})\delta\boldsymbol{\beta}_i\delta\boldsymbol{\beta}_j + ... \tag{4.24}$$

Since we are considering perturbative corrections to the power spectrum $\propto \Phi^4$, all terms up to third order in the potential must be kept here because they can couple to first order contribution. Several authors [183, 184, 67, 181, 185] have computed high order corrections to the angular power spectrum by iteratively inserting the result for the deformation tensor into the full expression of Eq. (4.18); the generic second-order correction for the 2-points statistics takes the form of

$$C_\ell^{XX,\mathrm{type}} = F^{XX,\mathrm{type}} \int \mathrm{d}\chi \frac{g^2(\chi,\chi_s)}{f_K^6(\chi)} \int \frac{\mathrm{d}^2\ell'}{(2\pi)^2} G^{XX,\mathrm{type}}(\boldsymbol{\ell},\boldsymbol{\ell}') M(\ell',\ell''), \tag{4.25}$$

where $F^{XX,\mathrm{type}}$ is a constant factor, different for the different type of second-order correction or the lensing field considered - $X = \kappa, \omega$, shear E-modes ϵ or shear B-modes β; $G^{XX,\mathrm{type}}(\boldsymbol{\ell},\boldsymbol{\ell}')$ is a generic geometrical factor depending the different modes $\boldsymbol{\ell}$ and their geometrical orientation; $M(\ell,\ell';\chi)$ is the mode coupling integrand or

$$M(\ell,\ell';\chi) = \int \mathrm{d}\chi' \frac{g^2(\chi',\chi)}{f_K^6(\chi')} P_{\Phi\Phi}(\frac{\ell'}{f_K(\chi')};\chi') P_{\Phi\Phi}(\frac{\ell}{f_K(\chi)};\chi), \tag{4.26}$$

and $\boldsymbol{\ell}'' = \boldsymbol{\ell} - \boldsymbol{\ell}'$. These expressions are analogous to the Born series in quantum scattering theory and similar diagrammatic representations of the arising terms exist. The various contributions can all physically be attributed to the coupling of lenses at different redshifts of the form $\Phi_{,im}\,\Psi_{mj}$, non-local Born-corrections of the form $\Phi_{,ijk}\,\delta\boldsymbol{\beta}_k$ or a combination of both effects at third order.

4.2. HIGH RESOLUTION LENSING SIMULATIONS

A detailed outline of the algorithm, concerning the construction of the past light-cone and the map-making procedure, has been given in a earlier

Chapter 3 and [15]. In the following, we explain some improvements and changes to the last steps of such algorithm, as we trace the light travelling throughout the N-Body simulation.

In order to propagate the CMB photons through the different shells we have adopted a pixel-based approach [112, 186, 174], exploiting the publicly available code `LensPix` [112]. For this work, however, we change this part of the algorithm by using the code `lenS`^{2}`HAT` to re-map the CMB signal through all the lensing shells. The list of operations on our light-cone maps is still the same as in the previous implementation: starting from the $\psi_{\ell m}$ coefficients, we compute the deflection field for each shell $\boldsymbol{\alpha}^{(k)}$. We then take advantage of the deflection field as purely a gradient field (i.e. a spin-1 curl-free vector field), to be synthesised with a spin-1 SHT. Once the deflection field is obtained, each pixel-based method remaps the CMB field as a function of the position on the sky assuming the lensed signal observed along a direction $\hat{\mathbf{n}}$ equal to the signal coming from another direction $\hat{\mathbf{n}}'$,

$$\hat{\mathbf{n}}'^{(k)} = \hat{\mathbf{n}}^{(k-1)} + \boldsymbol{\alpha}^{(k)}, \tag{4.27}$$

where $\hat{\mathbf{n}}^{(k-1)}$ represents the un-lensed position of the CMB photons at the previous step. Although algorithmically similar, `lenS`^{2}`HAT` is definitely more suitable for our studies of high-resolution lensing maps, as the code itself presents a series of improvements with respect to the benchmark `LensPix`.

The first advantage of this code comes from its flexibility as we can produce lensed maps in a number of different pixelization schemes used in cosmological applications. Internally, it uses grids based on the Equidistant Cylindrical Projection (ECP) pixelization where grid points, or pixel centres, are arranged in a number of equidistant iso-latitudinal rings, with points along each ring assumed to be equidistant. This pixelization supports a perfect quadrature for band-limited functions, which in the context of this work permits minimizing undesirable leakages that typically plague codes of this type.

`lenS`^{2}`HAT` implements a pixel-based lensing method using a Nearest Grid Points (NGP) assignment scheme to evaluate the source plane along the displaced direction, i.e. we assign to every deflected direction a value of the sky signal computed at the nearest grid points defined by the centres of a pixel of the assumed pixelization scheme. NGP assignment is quick and simple, in particular the precision of the method is driven by the single parameter defining the grid resolution. Remarkably, no smoothing is needed in the signal beyond the scale of the pixel, as done, for instance, in `LensPix`. To reach a resolution high enough for our study, we simply need to increase the number of points sampled by the grid. A suffi-

cient resolution required will in general depend on the intrinsic sky signal prior to the lensing procedure, as well as the resolution of the final maps to be produced; in a typical case these are expected to be very high and the computations involved in the problem may quickly become very expensive. Nevertheless, the overall computational time in this case is only somewhat longer than that involved in some other interpolation schemes, while the memory requirement can be significantly lower.

To sidestep the problem of computing spherical harmonic transforms with a huge number of grid points and a very high band limit, `lenS`^{2}`HAT` resorts to parallel computers and massively parallel numerical applications. In our implementation, we used the publicly available spherical harmonic transform `S`^{2}`HAT` library[2]. This library provides a set of routines designed to perform harmonic analysis of arbitrary spin fields on the sphere on distributed memory architectures. It has a nearly perfect memory scalability obtained via a memory distribution of all main pixel and harmonic domain objects (i.e., maps and harmonic coefficients), and ensures very good load balance from the memory and calculation points of view. It is a very flexible tool that allows a simultaneous, multi-map analysis of any iso-latitude pixelization, symmetric with respect to the equator, with pixels equally distributed in the azimuthal angle, and provides support for a number of pixelization schemes, including the above mentioned ECP. This library has been shown to be accurate at the sub-percent level to produce temperature and E-modes signal.

Finally, another important aspect is the possibility within `S`^{2}`HAT` library to compute the first derivative of an arbitrary spin-s field with respect to coordinates on a sphere (θ, ϕ). The code implements recurrence relations based on the Wigner D-matrices derivatives [187], as done in `HEALPix` but only for the spin-2 case. Numerical tests conducts so far have shown that derivatives of the same field on a sphere, computed with `S`^{2}`HAT` or `HEALPix`, are equal within the numerical error. We refer the reader to [174] for a further discussion of the numerical issues, accuracy and performance of `lenS`^{2}`HAT` code.

4.2.1. Angular power spectra

In the following, we exploit this algorithm to propagate the full magnification matrix throughout the N-Body box; to be more specific, we apply the discretised Equations described in Sec. 1.2.2, as we apply the multiple

[2] `http://www.apc.univ-paris7.fr/APC_CS/Recherche/Adamis/MIDAS09/software/s2hat/s2hat.htm`

lens scenario to our bundle of CMB photons, i.e. the source plane is at $z \approx 1100$, see Eqs (1.76-1.79) of Sect. 1.2.2.

In Figure 4.1 we show the angular power spectrum for different lensing observables: convergence, $C_\ell^{\kappa\kappa}$, rotation $C_\ell^{\omega\omega}$ and E- and B-mode of shear, $C_\ell^{\epsilon\epsilon}$, $C_\ell^{\beta\beta}$. As done in the previous Chapter, we plot the semi-analytical prediction of `CAMB` as benchmark and reference. The spectra have been synthesised using a fixed $\ell_{max} = 1024$, while the resolutions of the input (`HEALPix`-like map) has a `NSIDE`$= 4096$. As stated above, `lenS`^{2}`HAT` works with an internal ECP pixelization scheme, whose resolution can be expressed in terms of `NSIDE`≈ 10000. Simulated spectra are in a good agreement with the semi-analytical result; besides, we can finally see the imprints of the multiple deflections of photons: $C_\ell^{\omega\omega}$ and $C_\ell^{\beta\beta}$ are not zero as expected from the first order approximation. In this case, the study of the full magnification tensor has allowed us to unveil this effect which is however several orders of magnitude lower than the scalar signal of convergence and shear E-modes: an effect in fact hidden when we look at the resulting CMB lensed fields as done in the previous Chapter. Note that such signal arising from second order effects of weak lensing is highly relevant from a physical point of view. In a recent paper [70], updating and correcting a previous estimate of [68], showed that an eventual curl mode in the displacement field is much more efficient in converting primordial E- into B-modes though lensing. Therefore, even if the amount of this signal is small, it can leave a detectable imprint on top of the standard signal generated by the gradient mode. Besides, it has various implications on how the standard estimator for lensing are constructed. In fact, lensing potential can be reconstructed statistically using the 4-point function of the lensed CMB as the popular un-biased, quadratic estimator on the observed CMB field proposed in [160] which exploits the off-diagonal correlation between distinct modes. This estimator, however, becomes biased by the terms higher than the first order which are, in fact, neglected in the standard derivation. In addition, [69] have shown how it is possible to construct an analogous quadratic estimator of the curl mode of the displacement field which can be estimated simultaneously to the standard gradient-like one, although the potential higher order bias effects have not been estimated yet. The ultimate goal for this study would be to assess and quantify the relevance of a curl mode arising from second order effects of weak lensing on current estimators of lensing potential.

The presence of a non-zero rotation allows us to test previous analytical relations derived in the previous Section. In particular, we would like to test the consistency relations that links convergence $C_\ell^{\kappa\kappa}$ and shear E-modes $C_\ell^{\epsilon\epsilon}$, rotation $C_\ell^{\omega\omega}$ and shear B-modes $C_\ell^{\beta\beta}$, as deflections origi-

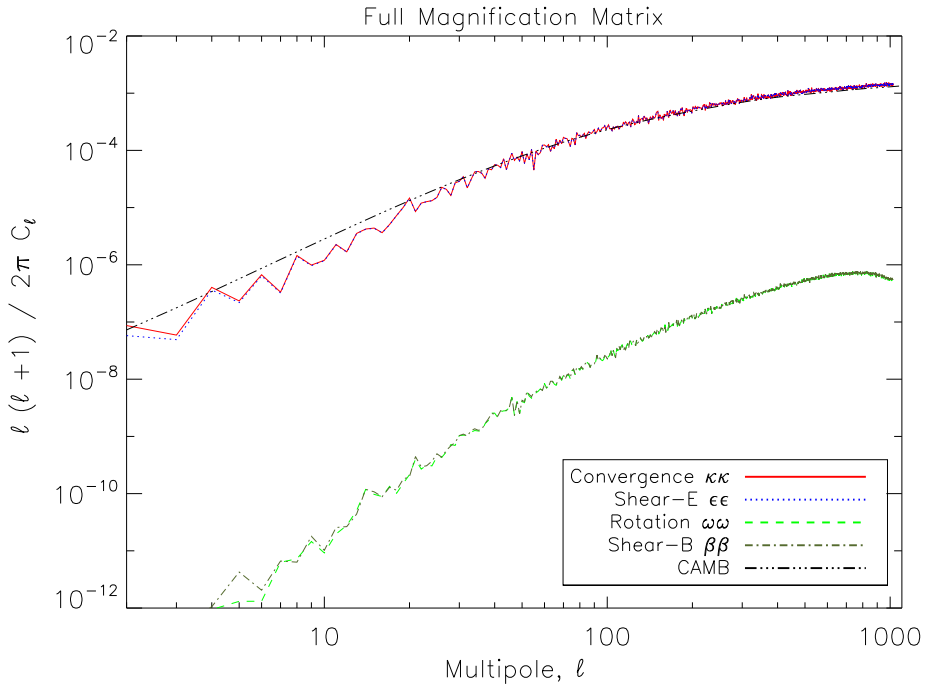

Figure 4.1 The convergence, shear and rotation angular power spectra for CMB lensing, as red continuous line ($\kappa\kappa$), blue dotted line ($\epsilon\epsilon$), green dashed ($\omega\omega$) and dark green, dot-dashed line ($\beta\beta$). The black line dot-dot-dashed line is the reference convergence angular power spectrum as computed by CAMB.

nate from the influence of two different physical phenomena, the standard scalar (lensing) potential ψ and the auxiliary (lensing) curl potential Ω. As shown in Figure 4.2, we compare the ratio of such angular power spectra with theoretical expectations of Eqs (4.12): a spectacular agreement can be found for "scalar-originated" fields, where the spectra duly follow the analytical predictions. A higher scatter in the signal can be observed for "rotation-induced" fields, even if for the ℓ range of our interest the ratio is very close to 1, and it is far better than a similar numerical test performed by other authors (see e.g. [163]). In the same Figure, the bottom panels show the ratio between the fields belonging to the propagated magnification matrix and the ones computed using the deflection angle itself, therefore extracting from our lensing maps the information of the angular power spectra of the two acting potentials, i.e. $C_\ell^{\psi\psi}$ and $C_\ell^{\Omega\Omega}$ of aforementioned Eqs. (4.5, 4.12). This is a good consistency test to see if our numerical implementation of the multiple lens approach is indeed correct when propagating the full magnification matrix throughout the simulation. Again, there is a nice agreement for all observables, with the exception of the rotation induced ω and shear B-modes β at large angular scales, at low multipoles.

In the Figures above we have shown how our algorithm is now able - thanks to its new improvements - to fully study and characterise the magnification matrix. This is not only a nice numerical test, but it carries as well some important physical implications: we recover a non-null signal induced by the multiple deflections of CMB photons, which is internally consistent with analytical expectation if we assume the rotation of the image to play its part though the potential Ω. The signal disappears if we use a first order approach by the means of the Born approximation, thus signalling that the implementation of multiple lens algorithm can be useful to fully explore the physics of CMB lensing. This result is indeed robust against changes in resolution of our simulated maps, which in any case have been synthesised to a very high precision and accuracy. In Figure 4.3 we show how the signal is stable even when reaching high resolution and looking at small scales, as we synthesise our maps using different band-limit $\ell_{max} = \{1024, 2048, 4096\}$. The expected cut-off in power nearby ℓ_{max} is in fact very visible in the Figure, as for each deflection plane we have a fixed band-limit in the reconstruction. As the reader could imagine, B-modes are more sensitive to this numerical effects, and this Figure is a further proof of that. This is still a ongoing project; the main expectations from this work involve excluding any possible contamination of numerical artefacts in the computation, as we intend to model and characterise the effect of the intrinsic resolution of the N-Body, for instance to set some

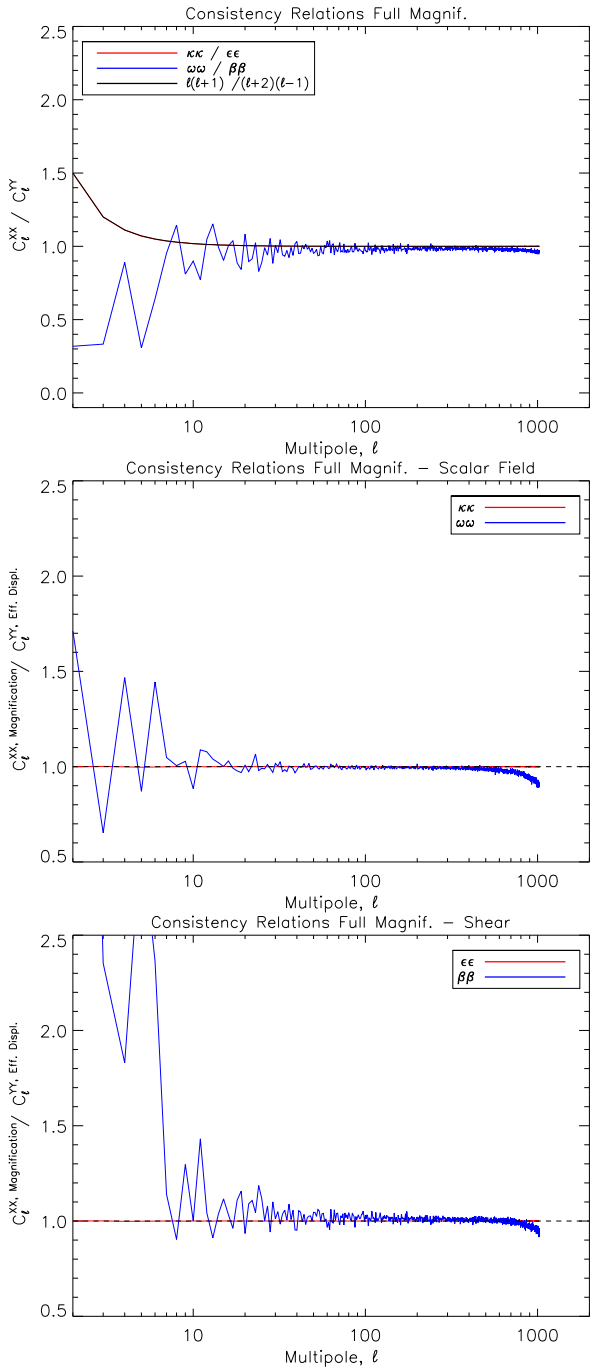

Figure 4.2 **Top panel**: Ratio of angular power spectra of different lensing observables as extracted from the full magnification matrix. Red line refers to "scalar field" induced by the lensing potential ψ, $C_\ell^{\kappa\kappa}/C_\ell^{\epsilon\epsilon}$. On the contrary, blue line is the ratio between $C_\ell^{\omega\omega}/C_\ell^{\beta\beta}$, induced by a rotation, "curl-like" auxiliary potential Ω, both expected to be zero at first order. Black line is the analytical prediction Eq. (4.16). **Middle and Bottom panels** show consistency relations for the scalar and vector fields extracted from the propagated magnification matrix and compared with the prediction using directly the potentials ψ and Ω of Eqs (4.12). Middle panel treats scalar field κ, ω while bottom panel shows results for the shear γ fields.

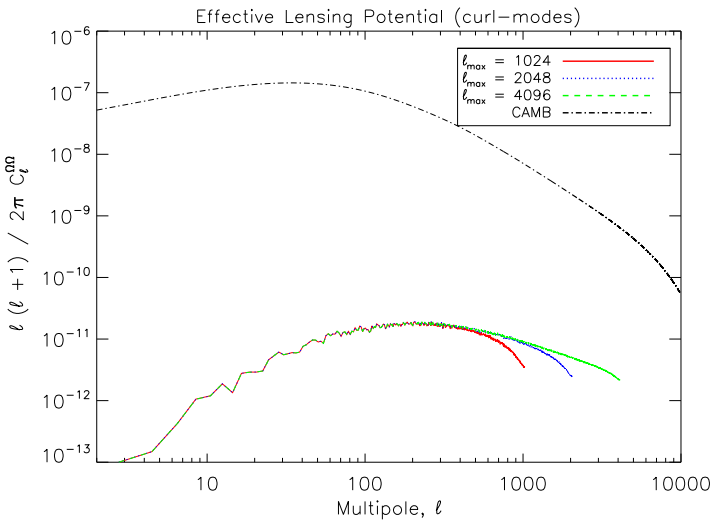

Figure 4.3 Angular power spectrum for the effective curl - lensing potential Ω, $C_\ell^{\Omega\Omega}$ for different ℓ_{max}. Black line is the reference CAMB line, which shows signal for the (standard) lensing potential ψ.

limits on the reconstruction of some lensing observables given a certain N-Body numerical simulation, and vice-versa. Finally, the broader goal is to quantify the impact of such non-zero signal due to the photons' rotation on current and future CMB surveys, and its relevance for B-modes of CMB polarization.

4.3. Second order corrections to CMB lensing

In the previous Section we have shown some preliminary results on the full magnification matrix, as we discover a non-zero signal which is due to the multiple deflections a photon experiences while travelling though the matter distribution of the N-Body simulations. Apart from numerical studies regarding the overall algorithm and its accuracy limits, we would like to characterise such signal using a more theoretical approach, applying high-order corrections to the power spectrum.

Several authors have adopted this formalism. [183], for instance, have considered a standard weak lensing scenario, with a source emitting at redshift $z_s = 1$, computing several high-order corrections (at 4th order in the gravitational potential Φ) to the angular power spectrum of the standard lensing observables: convergence, shear and rotation. They found these corrections to be at least two orders of magnitude below the power in the convergence, or E-mode shear, at the first order level as predicted

by the Born approximation. While these corrections are larger than cosmic variance at $\ell \gtrsim 100$, they are unlikely to affect the interpretation of the next generation of surveys. Their analytical calculations are consistent with previous numerical estimates: the rotational power spectrum generated by the coupling between two lenses agree with numerical measurements by [63]. Relatively small contribution to the lensing observables suggest that higher order corrections related to the Born approximation and coupling between two lenses are unlikely to affect the current estimates of weak lensing statistics.

However, a recent paper [185] computed those corrections in our case of interest of CMB lensing ($z_s = 1100$), and they found important deviations at the power spectrum level from the first-order analytical result. They quantified these effects to be important even for B-modes of CMB polarization, with a $\sim 10\%$ variation of the signal on the B-modes lensing peak $\ell \sim 1000$. We have exploited as well these formulae to the CMB-lensing scenario, using a `CAMB`-generated $P(k)$ for our analytical computations. Figure 4.4 shows the total second-order correction to the convergence ($\kappa\kappa^2$). Our calculations reach the same conclusion as [185]: second-order contributions to the convergence angular power spectrum seem to be quite important for CMB-lensing. There are important deviations at the power spectrum level from the first-order analytical result, although those same deviations are not seen in our ray-tracing simulations which assess the validity of the Born approximation even at reasonably high-ℓ.

To investigate the nature of this discrepancy, we can test these formulae against what already has been analysed in the literature. In particular, we refer to a ML method developed by [65] to ray-trace (weak) lensing of luminous sources throughout the Millennium Simulation. [65] found that the power spectra from the ray-tracing are in very good agreement with the 1^{st}-order prediction, the difference is $\lesssim 2$ % for $\ell < 10^4$. However, the same analytical calculations of [184] show a significant departure - especially for sources at redshift $z_{source} = 2$ - from the standard first-order spectrum, definitely more evident than the limits inferred from simulations, for small scales ($\ell > 1000$), see Figure 4.5 for a ratio of the analytical spectra in the two cases. Note that for this comparison, to be consistent with the different numerical set-up, we have used the matter power spectrum directly extracted from the Millennium Simulation. A tension seems to exist between numerical and analytical results, because important second-order corrections to the convergence do not arise either using our procedure for a CMB lensing scenario or referring to [65] accurate algorithm for weak-lensing.

In Figure 4.6 we show the effect of these corrections on a lensed CMB

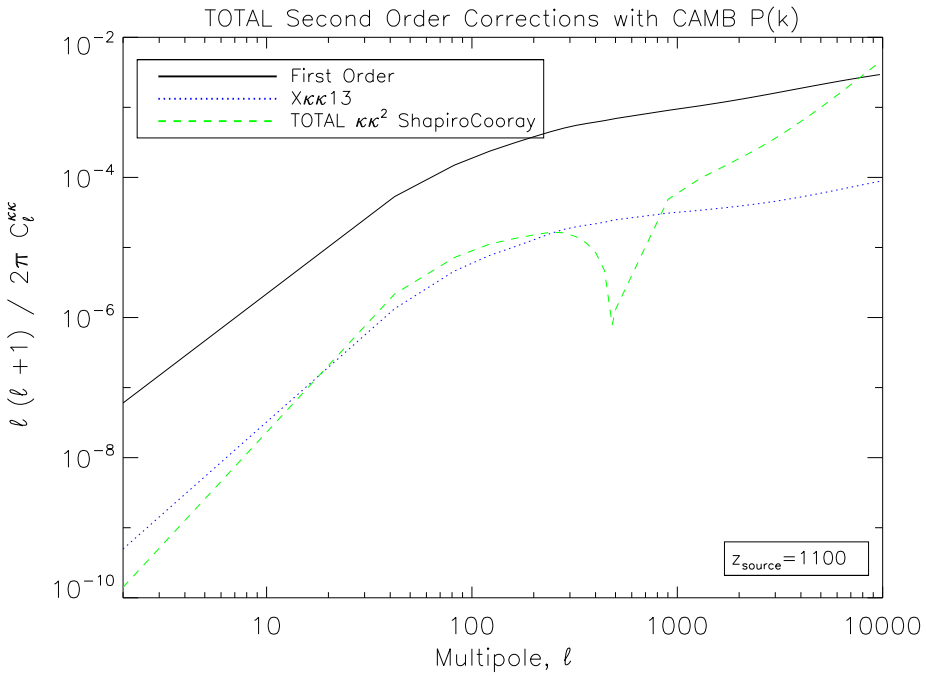

Figure 4.4 Total second-order contribution to the convergence angular power spectrum $\kappa\kappa^2$ in dot-dashed green line, while the dotted-blue one is just the $X\kappa\kappa$ correction computed by [184]. The black line is the well-known first-order result. The matter power spectrum used in this computation is the CAMB realization given the background cosmology of our N-Body simulations. The source-plane is considered at redshift 1100.

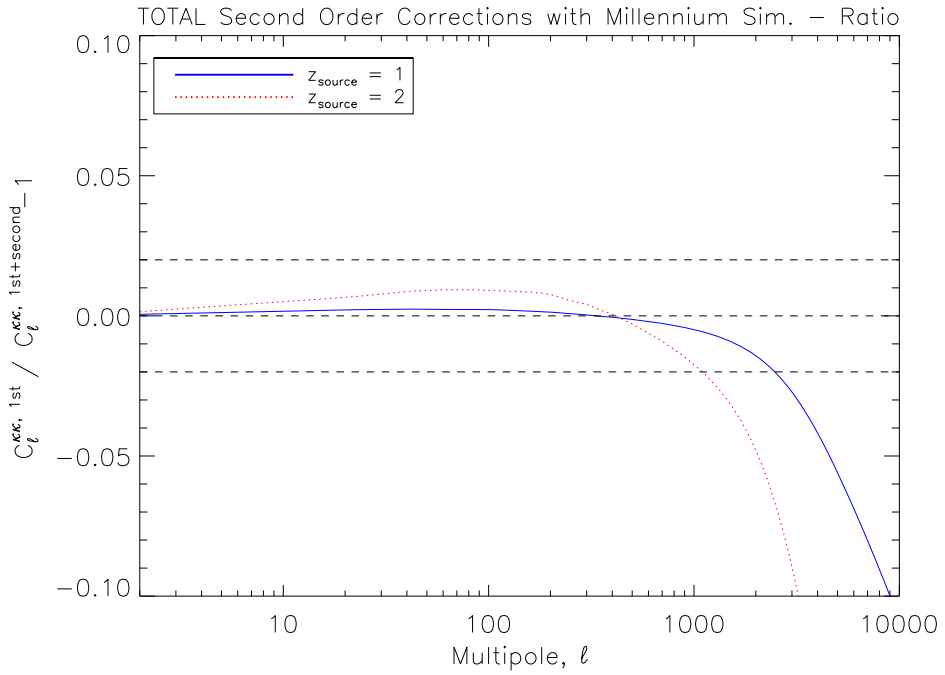

Figure 4.5 Ratio between first-order $\kappa\kappa^{(1)}$ and (first+second)-order, $\kappa\kappa^{(1)} + \kappa\kappa^{(2)}$, corrections of the convergence power spectrum. Dashed-horizontal lines refers to the limits found by [65].

field, in particular on the B-modes of polarization which are very sensitive to gravitational lensing. The primordial CMB field has been lensed using `LensPix`, which creates a Gaussian realization of the gravitational potential from the given convergence power spectrum. Two cases are shown here: the first-order-only result, where we considered only the standard first-order analytical power spectrum, and the (first+second)-order corrections one, exploiting previous formulae. We have produced several Monte-Carlo realizations given the same power spectrum as input - using a similar technique explained previously in the Thesis to estimate the contribution to the lensed CMB field of the shot-noise present in the N-Body simulation; lines plotted here are averaged over the whole ensemble. Figure 4.7 shows the difference power spectrum - between the standard analytical result and the second-order corrected one - for the lensed B-modes of CMB polarization with respect to the shot-noise-induced one, which accounts for the numerical noise present in our N-Body simulation due to its intrinsic discretization. It is very difficult to distinguish between the two for $\ell < 1200$; Figure 4.8 shows the same plot as the previous Figure but for the total intensity (TT) and E-mode of CMB polarization. In this case the effect of second-order corrections cannot be distinguish from the shot-noise coming from the N-Body simulations. Reaching the accuracy required to test these corrections is still a work in progress, thanks to the algorithm improvements of our code adopting `lenS`^{2}`HAT` routines. The next steps would include analysing the effects on other lensing observables encoded in the magnification matrix, as we compare them with our numerical results discussed in the previous Section. Finally, we stress that such analytical calculations may require a further expansion of the series to higher perturbative orders, to check whenever higher terms may cancel out the second-order contributions computed by [183, 184].

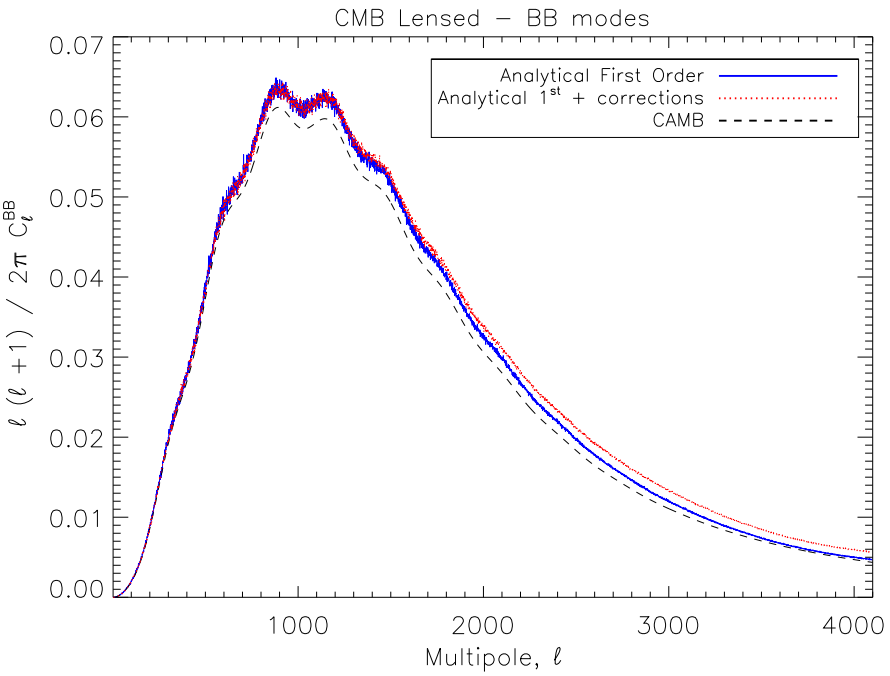

Figure 4.6 Angular power spectrum for the lensed B-modes of CMB polarization. The black line is the CAMB semi-analytical result, while the blue-continuous line is obtained from the the first-order-only spectrum of the convergence and the red-dotted line is obtained by including also second-order corrections.

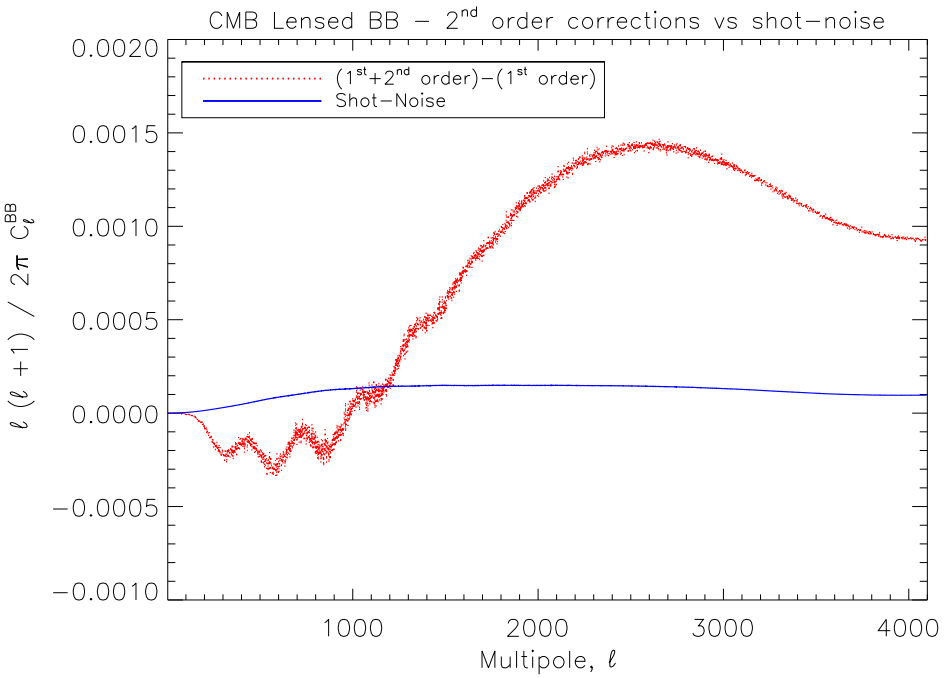

Figure 4.7 Angular power spectrum for the B-modes of CMB polarization as induced by the shot-noise present in our N-Body simulation (blue, continuous line). The red-dotted one is the difference between a lensed BB power spectrum extracted from a first-order-only lensing potential and a full one corrected with second-order terms.

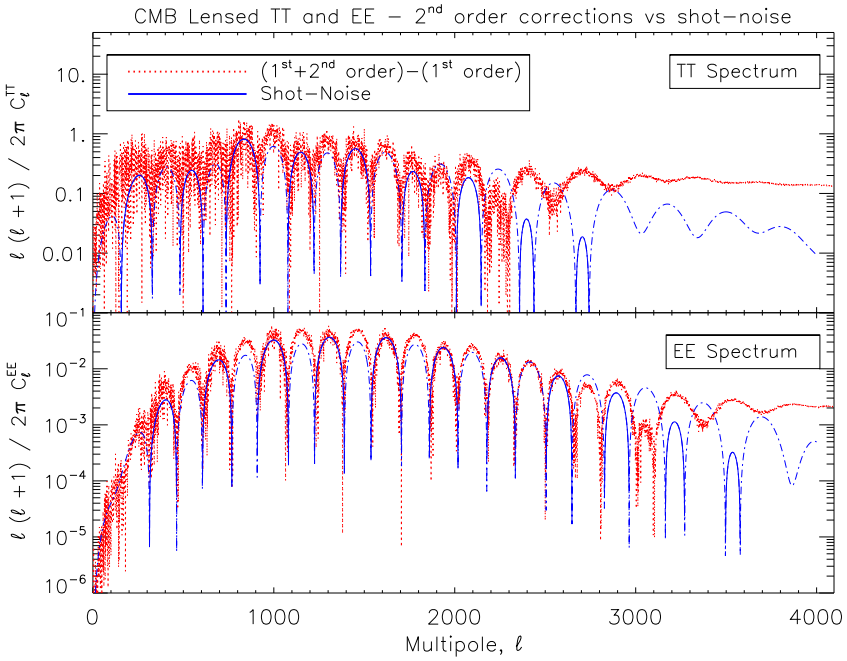

Figure 4.8 Angular power spectrum for the total intensity (TT - top panel) and E-mode of CMB polarization (EE - bottom panel) as induced by the shot-noise present in our N-Body simulation (blue, continuous line). The red-dotted one is the difference between a lensed power spectrum extracted from a first-order-only lensing potential and a full one corrected with second-order terms.

CHAPTER 5

Cross-Correlation simulations

> Imitation is not just the sincerest form of flattery - it's the sincerest form of learning.
>
> George Bernard Shaw

The final Chapter of this Thesis starts to address the final piece to the puzzle of modern cosmology, as we exploit the full potential of gravitational lensing of CMB by cross correlating it with LSS tracers. Although N-Body simulations can give a detailed picture of the abundance and clustering of dark-matter haloes, and how matter evolves as the Universe expands, they still do not represent what we really observe when we look up to the sky, and we see little sparkling points we call stars and galaxies. To be less prosaic, galaxy surveys constitute today the backbone of any astrophysical as well as cosmological study. However, in order to fully exploit and interpret the observed data it is essential to produce a link between the properties of the halo we model and simulate and galaxy populations we observe and measure. This "link" can be achieved producing the so-called *(galaxy) mock catalogues* [188, 189, 190, 191, 192, 193, 194, 195, 196].

The standard paradigm assumes that galaxies form by the cooling and condensation of gas inside these dark matter haloes. Besides cooling, however, other much more complicate phenomena such as star formation, merging, tidal interactions and several feedback processes determine galaxy formation and its evolution. In recent years a big effort has been devoted to generate mock galaxy catalogues that reproduce the observed Universe, as we can finally investigate different galaxy formation scenarios, test various statistical approaches and apply several computational technologies. Moreover, mock catalogues can help to design and calibrate "real" galaxy surveys, to study their selection effects and systematic errors, to test new techniques to measure cosmological parameters, or to calibrate other astrophysical estimators.

The basic approach is to start from the correct spatial clustering properties of the Universe, which is given by an N-Body (dark matter only, usually) simulation. Dark matter haloes found in the simulations serve as the seed points to place galaxies. Conversely, different recipes exist to populate the dark matter haloes with galaxies. We can distinguish three different approaches to link galaxy and dark matter halo.

To start, we can include hydro-dynamics in the N-Body simulation itself (e.g., [197, 198, 199, 200] and for a review [201]), usually dealing with physics on scales much smaller than those relevant for cosmological applications. However, this type of simulations are computationally very expensive, and there is always a tension between the high resolution required for the small-scale physics and the huge volumes needed for cosmological exploitations. A tension which cannot be easily solved.

A second approach is to use Semi-Analytic Models (SAMs) (e.g., [202, 203, 204, 205, 206, 207, 208]), which attempt to simulate galaxy formation and evolution using simple analytic and phenomenological prescriptions to approximate star formation and feedback processes. The downside is the huge number of free parameters that need to be included to model the small-scale physics, whose value is fixed "ad hoc" to match real observations.

The third and final approach require extensions of the halo model formalism [209] to describe the non-linear gravitational clustering. Again, within this formalism we can relate dark-matter haloes with galaxies in three ways: (i) using the Halo/Sub-Halo Abundance Matching (HAM/SHAM) technique (e.g. [210, 211, 212, 213, 214]), which assumes a monotonic relation between some determined galaxy property and the mass (or the dynamics) of the halo; (ii) adopting the Halo Occupation Distribution (HOD) (e.g. [215, 216, 217, 218, 219, 220, 221]) to describe the galaxy bias in terms of a probability distribution that a dark-matter halo of mass M_h contains N_g galaxies of a given type; finally (iii) with the Conditional Luminosity Function (CLF) (e.g. [222, 223, 224, 225]), which extends the HOD approach and gives the number of galaxies that resides in a halo of mass M_h as a function of luminosity.

In this final Chapter we introduce and develop our own method to populate dark matter halos. In Sec. 5.1 we describe the main steps of the algorithm, from the N-Body simulation (Sec. 5.1.1) to the mock galaxies (Sec. 5.1.2) built within the abundance matching formalism to link dark halos and observed quantities such as fluxes and luminosities. In Section 5.2 we show an example of the potentialities of our pipeline, as we cross-correlate those LSS tracers with the lensing of CMB, both extracted - as described in the previous pages - from the same N-Body simulation.

5.1. METHOD

In the following analysis we have used a set of different N-Body simulations of cosmic structure formation in a flat ΛCDM Universe. The sim-

ulations adopt a similar background cosmology, but they differ in mass resolution and size of the simulated box, which give us the opportunity to study and model mock catalogues at different scales, using different configurations. In this Chapter we will analyse and investigate ΛCDM simulations produced within two different projects: the Dark Energy Universe Simulations (DEUS) consortium[1] [226] and the aforementioned CoDECs database of N-Body simulations. As said in Chapter 3, the latter is made of a series of snapshots following the evolution of the matter distribution in a cubic (co-moving) volume $(1000\ h^{-1}\text{Mpc})^3$ from redshift $z = 10$ to present time using a modified TreePM version of GADGET [170]. Previously, we have described the L-CoDECs suite of simulations, as we recall their mass resolution at $z = 0$, $m_{dm} = 5.84 \times 10^{10} M_\odot/h$ for CDM and $m_b = 1.17 \times 10^{10} M_\odot/h$ for baryons, while the gravitational softening is set to $\epsilon_s = 20$ co-moving kpc/h, corresponding to 0.04 times the mean linear inter-particle separation. Mock catalogue capture physical phenomena at the galaxies scale, and this is the reason we ought to use the H-CoDECs suite of simulations as well. H-CoDECs simulations are adiabatic hydrodynamical simulations on much smaller scales, with a cosmological box of 80 co-moving Mpc/h filled with 512^3 CDM and 512^3 gas particles. The mass resolution at $z = 0$ for this set of simulations is $m_{dm} = 2.39 \times 10^8 M_\odot/h$ for CDM and $m_b = 4.78 \times 10^7 M_\odot/h$ for baryons, while the gravitational softening is set to $\epsilon_s = 3.5$ co-moving kpc/h, also corresponding to 0.04 times the mean linear inter-particle separation. For these simulations hydrodynamical forces are included in the dynamical evolution of the baryonic particles. These are computed by means of the entropy-conserving formulation of Smoothed Particle Hydrodynamics (SPH, [198]) implemented in GADGET. No other non-adiabatic processes such as gas cooling, start formation, and feedback mechanisms from supernovae or Active Galactic Nuclei are included in any of the H-CoDECs runs.

The Dark Energy Universe Simulation Series (DEUSS) [227, 228, 229] aim at investigating the imprints of realistic dark energy models on cosmic structure formation. They are publicly available to the community through the "Dark Energy Universe Virtual Observatory" (DEUVO), and the DEUS consortium. The ΛCDM run consist of 10 snapshots at different redshift, covering a volume of 162 comoving Mpc/h with 1024^3 DM particles only. Particles evolution is computed with the Adaptive Mesh Refinement (AMR) code RAMSES[2] [230, 231], therefore implementing a different numerical method with respect to the previous set of simulations. Table 5.1 summarizes the main features of the different simulations, as

[1] www.deus-consortium.org/

[2] www.ics.uzh.ch/~teyssier/ramses/RAMSES.html

Simulation	$m_{dm}[M_\odot/h]$	$m_b[M_\odot/h]$	N_p	Box Size [Mpc/h]	ϵ_s [kpc/h]
L-CoDECs	5.84×10^{10}	1.17×10^{10}	2×1024^3	1000	20
H-CoDECs	2.39×10^8	4.78×10^7	2×512^3	80	3.5
DEUS-ΛCDM	2.86×10^8	-	1024^3	162	2.47

Table 5.1 Simulations resolution, expressed as dark matter or baryon particle mass (m_{dm} or m_b), number of particles N_p, size of the simulated box and gravitational softening length, ϵ_s.

well as the slightly different background cosmology used for the different set-ups, Eqs (5.1). Note how - for computational reasons mainly - low resolutions correspond to big box sizes; besides, the DEUS-ΛCDM and H-CoDECs simulations are directly comparable, as their particle mass (which sets the minimum mass scale reproducible by the N-Body) or gravitational softening length (ϵ_s, the corresponding length scale accessible) are indeed very similar.

$$\begin{aligned}\{\Omega_{dm}, \Omega_b, \Omega_\Lambda, n_s, \sigma_8, H_0\}_{\rm CoDECs} = \\ \{0.226, 0.0451, 0.729, 0.966, 0.809, 70.3\,{\rm Km/s/Mpc}\}; \\ \{\Omega_{dm}, \Omega_b, \Omega_\Lambda, n_s, \sigma_8, H_0\}_{\rm DEUS} = \\ \{0.22, 0.04, 0.74, 0.96, 0.79, 72\,{\rm Km/s/Mpc}\}.\end{aligned} \tag{5.1}$$

In the following pages we will describe in details the various parts of our mock catalogue algorithm; here we outline the basic steps to populate our simulations with galaxies:

(i) starting from an N-Body simulation, we find dark matter halos using an halo-finder algorithm: they represent the host site for our galaxies;

(ii) each halos can be identified by its mass, M_h and by its redshift z_h given the simulation output we are investigating;

(iii) we then associate to each halo, using some analytical fitting functions, several astrophysical quantities like luminosity or Star Formation Rate (SFR), i.e. $L \equiv L(M_h, z_h)$ or SFR≡SFR(M_h, z_h), functions of only the redshift and the mass of each halos;

(iv) for each halo we can then contruct a PDF of the wanted astrophysical quantity, usually adoping a Gaussian or a log-Normal shape (depending on the quantity we are looking at), where the mean value

is computed at point (iii) and the width of the distribution, σ is obtained from real data; we can randomly sample from those PDFs the final astrophysical observable to associate to those DM halos, thus accounting for statistical dispertion in the mock data;

(v) we correct our galaxy sample by ignore too massive DM groups, and by considering only active galaxy, by means of their bursting time $t_{\rm burst}$;

(vi) using the algorithm developed in Sec. 3.2, we can create spherical maps of those mock galaxy; realistic observation can be simulated as well as we introduce some survey requirements and specifications, namely we consider cuts in the catalogue given the emitted flux (in a specific bands) of our galaxies;

(vii) we repeat step (i)-(vi) for all the simulated snapshots of our simulation, thus following the evolution of our galaxy sample in time.

The final result is a series of 2D spherical maps - recalling the 2D CMB convergence maps we obtain using our multiple-lens code - which simulate a real survey observation of galaxies emitting at different redshifts.

5.1.1. Finding Halos in N-Body

The first step towards finding gravitationally bound structure is to identify dark matter halos. These can be easily done using a Friend-of-Friend (FoF) algorithm, a powerful tool to look for assembled structures [232, 233, 234, 200]. FoF selects groups of particles in which every object has at least one neighbour within a specified linking length b_l. If the separation between two dark matter particles is e.g. 20% of the average separation between particles (thus linking length $b_l = 0.20$), then they are placed in the same group. At this point, if a particle is at the same distance b_l from these linked particles (friend of friends, precisely), it is also gathered in the same group, and the process is thus iterated. In this way, particle groups are formed that correspond to regions approximately enclosed by isodensitiy contours with threshold value $\rho \propto 1/b_l^3$. The length b_l is set to have such a group with an average overdensity of $\frac{\langle \rho_{halo} \rangle}{\langle \rho \rangle} \approx 200$, close to the predicted value for a top-hat spherical collapse [235] in the Einstein-De Sitter cosmology, and is usually regarded as a justification for using $b \sim 0.2$ in analysis of simulations. The code sets also a minimum number of dark matter particles to be part in a FoF group, such that spurious

structures, due to numerical effects in the simulation, are discarded. Baryonic particles are placed in a particular group if the nearest dark matter neighbour is a part of that group. FoF is both simple and efficient, and its group catalogues agree quite well with predictions of Press-Schechter theory [236]. An attractive feature of the FoF algorithm is its relatively simplicity: the result depends solely on the linking length in units of the mean inter-particle separation, b_l. FoF algorithm does not assume any particular halo shape, therefore it can better match the generally triaxial mass distribution in halos forming in hierarchical structure formation models. In addition, studies over the last decade [237, 238, 234, 239, 240, 241] indicate that mass function of FoF halos is universal for different redshifts and cosmologies at least to $\sim 10\%$, although real systematic variations can exist.

In Figure 5.1 we show the halo mass distribution obtain from our simulations, in particular from the L-CoDECs and H-CoDECs suites. Note that we sample the dark matter halos not from the FoF catalogue itself, but directly from the halos *in the light-cone*, as we are able - thanks to the algorithm detailed in Sec. 3.2 - to construct and simulated a whole, full-sky Universe around a chosen observer. Data points are compared with analytical expectations by [239], for five different redshift outputs. The agreements is very good at all times, and we can observe how points reflect the different mass resolutions of the two simulations: the high-resolution one (H-CoDECs) has access to the low-mass part of the halo mass function, sampling objects up to a minimum mass of $\sim 10^{10} M_{\odot}/h$. Low resolutions and higher box sizes (e.g. L-CoDECs simulation), on the contrary, cover the high-mass part of the plot, as we reach at $z = 0$ massive DM halos of about $10^{15} M_{\odot}/h$. Similar result can be found using the DEUS-ΛCDM simulation.

5.1.2. From Halos to Galaxies

Once we have identified single halos within our simulation, we can populate them using different recipes. We adopt a one-to-one correspondence (one halo, one galaxy) based on the abundance matching formalism [214]. In this part we will describe the main step of the algorithm, as we refer the reader to the quoted paper for an extended and complete discussion on this technique.

Populating halos with galaxies

[214] has used abundance matching technique to link the stellar and black hole content of galaxies to the gravitationally dominant dark matter com-

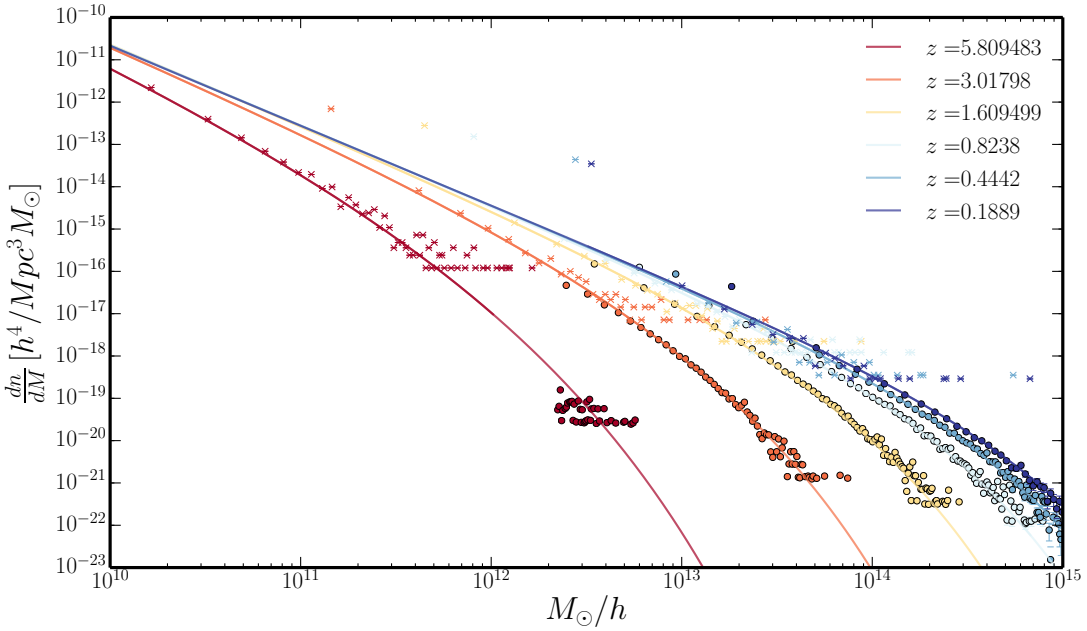

Figure 5.1 Halo mass distribution, for five different redshift sample. Points are extracted directly from the simulations, circle from the L-CoDECs, which has a big box size (1 h^{-1}Gpc) but a small resolution in mass ($m_{dm} \simeq 10^{10} M_\odot/h$); crosses, instead, belong to the H-CoDECs suite of numerical simulations: with their high mass resolution ($m_{dm} \simeq 10^{8} M_\odot/h$) snapshots are able to cover the low-mass part of the halo mass distribution, reaching bound objects of minimum mass of $\sim 10^{10} M_\odot/h$. The continuous lines are analytically computed using a Tinker halo mass function [239]. DEUS-ΛCDM shows similar results, and it covers a mass range similar to H-CoDECs.

ponent. The basic hypothesis is to consider one galaxy hosted in one halo with a black hole in its centre, with the assumption that all the relations between the different masses are monotonic. From observations it is possible to construct number density of object given a certain halo mass $\mathrm{d}N/\mathrm{d}M_h$, or a certain galaxy mass $\mathrm{d}N/\mathrm{d}M_{gal}$, or a certain black hole mass $\mathrm{d}N/\mathrm{d}M_{BH}$; the main idea is to match these number densities to construct some 1-to-1 relations for each different mass considered. This matching can be done at different redshifts using several observations; an intrinsic statistical scatter is thus present and will be taken into account by working with probability distribution, i.e. PDF. The next step would be to link masses and luminosity: [214] shows how it can be simply done as above by matching different number density, with the addition of considering the effect of the duty cycle. The luminosity number density $\mathrm{d}N/\mathrm{d}L$, in fact, can be measured only if a galaxy is active, and this is controlled and modelled by the parameter t_{burst}, duration of the galaxy burst in activity. The resulting relationships constitute a benchmark for galaxy formation and evolution model, and provide analytic fits to the relationships derived from the abundance matching technique. From the algorithm's point of view, we would compute from the halo mass - found by `FoF` algorithm - a simulated, observable quantity, like the luminosity in a certain band or the SFR. [214] fit observed data points using a functional form for different observables Y, $Y \equiv Y(M)$ by adopting a double power-law shape:

$$Y(M_h, z) = N(z) \times \left[\left(\frac{M_h}{M_b(z)} \right)^{\alpha(z)} + \left(\frac{M_h}{M_b(z)} \right)^{\beta(z)} \right]^{-1}, \tag{5.2}$$

where the normalization $\log N(z)$, the mass parameter of the break $\log M_b(z)$, and the characteristic slopes $\alpha(z)$ and $\beta(z)$ evolve with the redshift according to the same parametrization, i.e.

$$p(z) = p_0 + k_{p_1}\eta + k_{p_2}\eta^2 + k_{p_3}\eta^3, \tag{5.3}$$

with

$$\eta = \log \frac{1+z}{1+z_0} \tag{5.4}$$

and $z_0 = 0.1$. Basically, high luminosities correspond to massive halos. We refer to Table 2 of [214] for the correct values of parameters used in our mock catalogue algorithm. These relations are to be intended in a statistical sense: they represent the mean value of a probability function (a Gaussian or a log-Normal distribution) with a certain dispersion σ, given the statistical uncertainties in the observed data points. For a chosen halo of mass M_h, the final value of a particular astrophysical quantity, say e.g.

its luminosity in the infrared band, will be randomly sampled from the probability distribution made of a mean value - computed with Eq (5.2) - and dispersion σ reported in the aforementioned Table. The final result will be a list of FoF objects characterized by several astrophysical quantities, a mock catalogue.

Mass cut for higher-mass halos
A one-to-one correspondence between galaxy and halo could be a problem in case of very massive DM group, since they more likely will represent cluster or groups of galaxies instead of a single, huge central galaxies. Therefore, we need to cut our galaxy sample, factoring out objects too big to host only one galaxy. To do so, we need to compute the analytic galactic halo mass function, i.e., the mass function associated to halos hosting *one* individual galaxy. The computation actually includes two steps: (i) to account for the possibility that a halo contains various sub-halos each hosting a galaxy; (ii) to probabilistically *exclude* halos corresponding to galaxy systems rather than to individual galaxies.

Our starting point is the sub-halo mass function, as recently determined by [242]. The distribution of sub-halos with mass between m and $m+\mathrm{d}m$ in a halo of mass M_h at redshift z_h can be well fitted by the function

$$N_{\mathrm{sub}}(\log\psi) = \gamma\psi_\alpha e^{-\beta\psi^\omega}\ln 10 \tag{5.5}$$

where $\psi = m/M_h$. Actually if m is taken as the sub-halo mass at accretion, the resulting un-evolved sub-halo mass function is universal for any mass M_h; however, we are more interested in taking m as the mass of the surviving, self-bound entity at redshift z, which is reduced with respect to that at accretion due to mass stripping and dynamical friction. The resulting evolved sub-halo mass function is then described by the parameter set $[\gamma,\alpha,\beta,\omega] = [0.31f_s, 0.82, 50.00, 4.00]$ and depends on the host halo mass and redshift through the quantity f_s. The latter may be determined through the computation of the halo dynamical time within the spherical collapse framework [242, 214]. Now we turn to compute the probability distribution for a given halo to contain one individual galaxy. The first step is to obtain the Halo Occupation Number (HON), i.e., the average number of sub-halos inside a host halo of mass M_h:

$$\langle N\rangle(M_h,z) = \int_{\log m_{min}/M_h}^{0} \mathrm{d}\log\psi N(\log\psi); \tag{5.6}$$

here m_{min} represents a minimum mass for sub-halos, required to avoid the divergence in the above integral; this will be set by comparison with

numerical simulations and observational datasets ($m_{min} = 10^{11.1} M_{\odot}$). The HON represents the average number of sub-halos inside a host halo, but we need instead the probability distribution $P(N|\langle N\rangle)$ of having N sub-halos given the average number $\langle N\rangle(M_h, z)$. Numerical simulations and HOD models aimed at reproducing various galaxy observables (see Zehavi et al. 2005, 2011; Zheng et al. 2007, 2009; Tinker et al. 2013) indicate that such a distribution is well approximated by a Poissonian. Then one can easily compute the cumulative probability $P(< N|\langle N\rangle)$ of having less than N sub-halos; this reads

$$P(< N|\langle N\rangle) = \frac{\Gamma(\underline{N+1}, \langle N\rangle)}{\underline{N}!}, \tag{5.7}$$

where $\Gamma(a, z) = \int_z \mathrm{d}t\, t^{a-1} e^{-t}$ is the incomplete complementary Γ-function, $\underline{x}$ is the floor function (the closest integer lower than x), and $n! = 1 \times 2 \times ... \times n$ the factorial function. We stress that in such a probability the dependence on host halo mass and redshift are encased into the HON $\langle N\rangle(M_h, z)$. In our case, we impose the host halo to have only one central galaxy, therefore $N = 1$, while HON $\langle N\rangle$ is the "free" variable in our computation. At the algorithm level, we simply toss a coin, if the resulting random number is less than the computed cumulative probability, then the halos of mass M_h is a possible candidate to host an active galaxy; otherwise, it is too massive to be associated with a single galaxy, and it will be discarded.

Is a galaxy active?
For reasons that will be explained later, we are interested in studying a high-redshift sample of galaxies, which obviously have passed through several different stages in their evolution. The observations have undoubtedly confirmed that the SFR in high-redshift galaxies must have proceeded at very high rates ($\sim 3 \times 10^2 M_{\odot} yr^{-1}$) under heavily dust-enshrouded conditions over a time-scale around 0.5 - 1 Gyr (see [243]). In addition, the observed fraction of far-IR detected host galaxies in X-ray and optically selected AGNs points toward a SFR abruptly shutting off after this period of time. In the analysis by [243] this rapid quenching is interpreted as due to the energy feedback from the super-massive BH growing at the centre of the star-bursting galaxy. In the first stages of galaxy evolution, the BH is still rather small and the nuclear luminosity is much less than that associated to the star formation in the host; the SFR stays roughly constant with time being regulated by feedback from SN explosions is then regulated by feedback from SN explosions, while the AGN luminosity increases exponentially. After a period 1 Gyr in massive galaxies the nuclear luminosity

becomes dominant, blowing away most of the gas and dust from the ambient medium and hence quenching abruptly the star formation in the host. Actually the data concur to indicate that such phenomenon does not occur in less luminous galaxies, since in these objects the BH cannot grow to large masses, and the nuclear luminosity remains always smaller than that associated to the star formation; as a consequence, the latter may proceed for times up to a factor of 10 longer. On this basis, [243] prescribe that the time-scale for the duration of the starburst is given by

$$t_{\rm burst} = 7 \times 10^8 \ {\rm yr} \ \left(\frac{1+z}{3.5}\right)^{-1.5} \ 1 + \frac{9}{2}\left[{\rm erfc}\left(\log \frac{L_h}{10^{11} L_\odot}\right)\right], \qquad (5.8)$$

where erfc is the (complementary) error function, and L_{SFR} depend by the halo mass using previous relations. The dependence on cosmic times mirrors that of the dynamical/condensation time, in turn reflecting the increase of the average density in the ambient medium. We then can confront this burst-time with the Hubble time,

$$t_H(z) = \int_0^{\frac{1}{1+z}} \frac{{\rm d}a}{aH(a)}, \qquad (5.9)$$

giving a ratio $\delta_r = t_{\rm burst}(M_h, z)/t_H(z)$ for each halo of mass M_h. Again in the algorithm, we toss another coin: if the random number is less than the ratio δ_r (or $\delta_r > 1$, thus $t_{\rm burst} > t_H$), then the galaxy is active and accepted in our catalogue. In Figure 5.2 we recap all the previous steps, as we show the luminosity function (number density) as extracted from our simulations of the galaxy sample so far selected. We can confront our mock galaxies with real observations by [153]. The agreement is satisfactory for most of the luminosity range, and for different redshift ranges. The high-redshift sample is the most problematic, but it is probably due to a mismatch between the redshift of the single outputs of the N-Body (e.g. all selected galaxies at $z = 3.01$), and the broad redshift range of the data, which covers objects emitting radiation between $z = 2.4$ and $z = 4$. Again, we can find very similar results using the DEUS-ΛCDM simulation.

5.2. Simulation of CMB-LSS XC

As already explained in previous pages, LSS leaves an imprint in CMB anisotropies by gravitationally deflecting CMB photons during their path from the last-scattering surface to us. On the other hand, in the standard structure formation scenario galaxies reside in DM halos, as signpost of

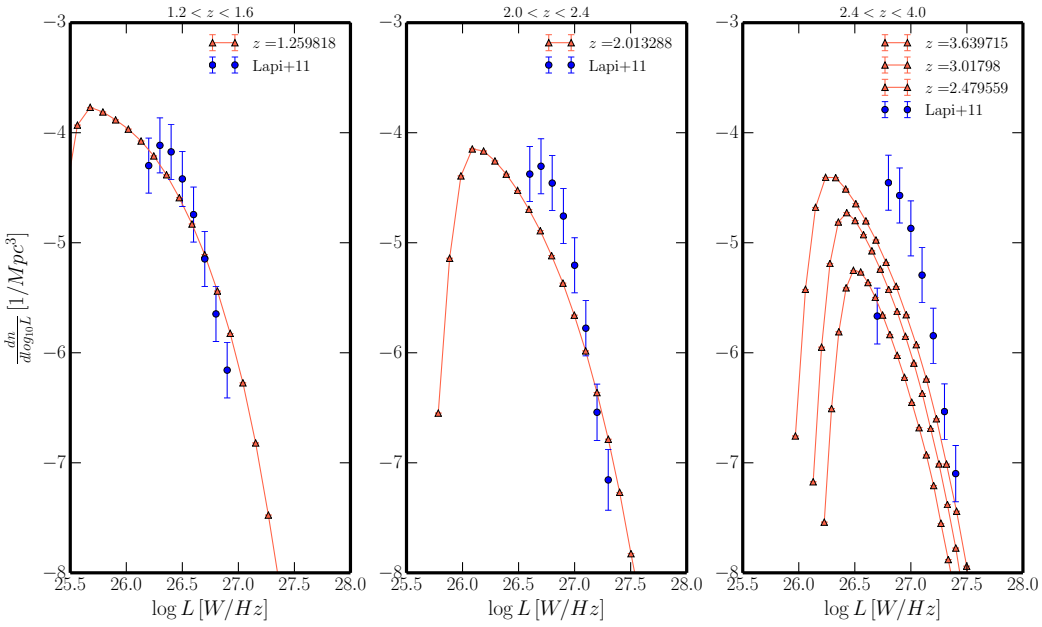

Figure 5.2 Luminosity function distribution, for three different redshift samples for the H-CoDECs ΛCDM simulation, from left to right, from low to high redshift. Blue points are extracted directly from the simulations, for three redshift sample. Red continuous lines represent observed data by [153]. Note how in the right panels the mismatch between data points and the curves extracted from N-Body simulations is mainly due to the difference between the redshift of the simulation outputs and the redshift sample of the dataset (which covers a high range from $z = 2.4$ to $z = 4$).

structures that act as lenses for CMB photons. The cross-correlation between CMB lensing maps with tracers of large-scale structure can thus improve simultaneous constraints of cosmological and astrophysical parameters, such as the structure growth rate and bias b relating fluctuations in luminous and dark matter, allowing existing degeneracies to be broken [244]. Sub-millimeter (sub-mm) surveys have the power of unveil the distant Universe in the redshift range $1 \lesssim z \lesssim 5$, where the CMB lensing is mostly sensitive to matter fluctuations, and hence represent perfect candidates for cross-correlation studies. Moreover, bright sub-mm galaxies constitutes the progenitors of massive spheroids, and as such represent a population of objects strongly biased relative to the background matter distribution. Previous cross-correlation studies involving CMB lensing and galaxy or quasar density maps have been reported by [245, 143, 8, 149, 246, 150, 247, 248].

Is a galaxy observable in a survey?
The *Herschel* Space observatory [249] has carried out observation of the sky in five wavebands between 100 to 500 μm, enabling an exquisite mapping of the sub-mm galaxies. The full H-ATLAS data field [250] has surveyed about 600 deg^2 with the survey area divided into five fields: the north galactic pole (NGP), the south galactic pole (SGP) and the three GAMA fields (G09, G12, G15). We are interested in replicating those observations as mock catalogues for our XC studies, therefore the algorithm we have so far presented intend to exploit and select this peculiar sample of galaxies: high-z, high-star-forming, strongly clustered massive galaxies, tracers of large-scale overdensities. Previous studies [154, 153, 150] have shown how particular criteria on the galaxy emission can shrink the Herschel sample to that specific group of objects we are interested in. The idea is to apply these survey cuts to our simulated galaxies, to precisely mimic an *Herschel*-like observation. Sub-mm sources are selected and considered inside our mock catalogue if they obey to the following criteria: (i) the flux at 250μm to be $S_{250} > 35$ mJy; (ii) the ratio between the flux at 350μm and the flux at 250 μm to be greater than 0.6; (iii) the ratio between the flux at 500μm and the flux at 350 μm to be greater than 0.4. These final two criteria, so called "colour criteria" are intended to select only high-redshift objects as observed by [154]. Obviously, we can compute the fluxes from our simulated galaxy luminosity:

$$S_{\lambda_{obs}} = \frac{L_{\lambda_{obs}}}{4\pi d_L^2(z)} \frac{\mathrm{SED}\left(\lambda_{obs}/(1+z)\right)}{\mathrm{SED}(\lambda_{obs})}(1+z) \tag{5.10}$$

at three different bands: $\lambda_{obs} = 250\ \mu m$, 350 μm and 500 μm. So far we have

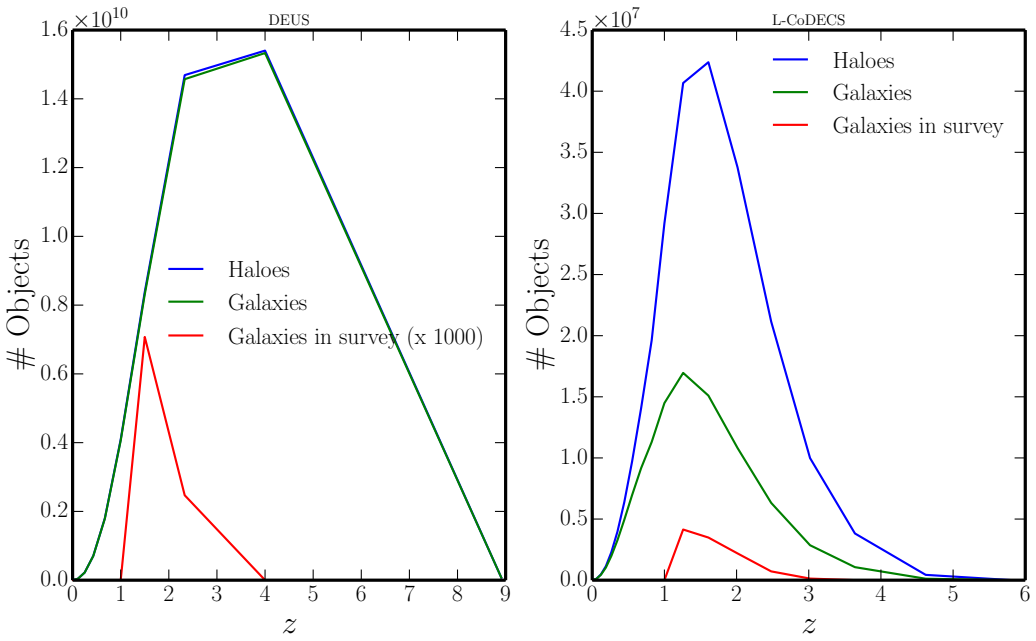

Figure 5.3 Number of objects per redshift bin, dN/dz. **Left panel**, computed for the DEUS simulation; **right panel** for the L-CoDECs one. In both panels blue line is the number of halos, green represent all galaxy while red refers to "galaxy in survey", therefore galaxies selected throughtout the above flux criteria. Note how in the left panel, the number of objects per redshift has been multiplied by a factor of 1000 for viewing purpose.

in fact considered bolometric luminosity $L(M_h)$, while for this set of objects we are interested in the emission at a particular electromagnetic band (L_λ). This can be easily computed using the Spectral Energy Distribution (SED) of said galaxies, as in [152]. In Figure 5.3 we can see the distribution of objects selected using the above criteria as a function of redshift, i.e. dN/dz, for two sets of simulation, L-CoDECs and DEUS. Note that, despite being quite different, in terms of resolutions, box sizes, background cosmology and simulation code, their dN/dz has roughly the same shape and amplitude, with the peak of objects (about $\sim 5\ 10^6$) for both found at the same redshift, $z \sim 1.5$.

Finally, Figure 5.4 show the XC angular power spectrum $C_\ell^{\kappa g}$ computed cross-correlating galaxies and CMB lensing maps. Blue points in the Figure are real observations from [150], obtained using Planck-2013 lensing map and Herschel data, while green line is the theoretical angular power spectrum. The orange points are the quantity of interest here, as they originates from mock catalogues and CMB lensing maps both extracted from

the same N-Body simulations, computed using the algorithm described in the previous Sections as well as in Chapter 3. Comparison between the different curves suggest that our mock catalogue recipes is on a good track, since is able to fairly reproduce the expected theoretical signal and the observed one[3]. Note that a detail astrophysical modelling of the signal is still under investigation, as we plan to investigate the impact and relative importance of different phenomena on the recovered and simulated XC signal. The Figure shown here is obtained using the L-CoDECs N-Body boxes; we expect similar results for the H-CoDECs and DEUS case, even perhaps a better signal as they simulate smaller objects at higher resolutions. A full comparison among the different simulation suites is still in progress as we plan to address it in a future paper. In this sense, the overall algorithm is a staring point, not a final destination *per sè*, as we intend to upgrade and improve it; for instance, we would like to drop the working assumption that one halo can host only one galaxy, by modelling the halo (and sub-halo) physics through a HOD formalism.

The exploitation of this simulation setup has been use so far in support to the simulation of the signal in the context of cross-correlating CMB lensing data with infrared observations for Herschel. We plan to study in details the evolution of the XC signal in time, aiming at the CMB lensing tomography which is still at an early stage of development but it will improve enormously in the upcoming years. High signal-to-noise ratios will be reached due to the augmented sensitivity of both galaxies surveys, like DES, Euclid, LSST, DESI, and CMB lensing experiments, such as the new phase of the POLARBEAR experiment. In the near future, the LSS will be mapped at different wavelengths out to high redshifts, enabling a thorough investigation of structure formation over cosmic time and allowing for a better understanding of cosmology and astrophysics. Mock catalogues will become therefore necessary to be able to control all possible systematic or contamination in the observed signal, as well as to predict the impact of different cosmological models or astrophysical scenarios. Mock catalogues are indeed very flexible: different surveys' requirements and specifications can be easly coded in the algorithm, for instance, by changing the selection criteria of our objects; we plan to adjust our pipeline to reproduce Euclid-like galaxy catalogues in order to explore the many scientific possibilities allowed by this forthcoming spacecraft. Mock catalogues represent up to date the best way to study the interactions between this two branches of physics, as by playing with the several recipes,

[3]Note that observed data seem to indicate a higher amplitude than expected; this particular aspect is still not well understood, and it may be due to astrophysical contamination and systematics, see discussion in [150].

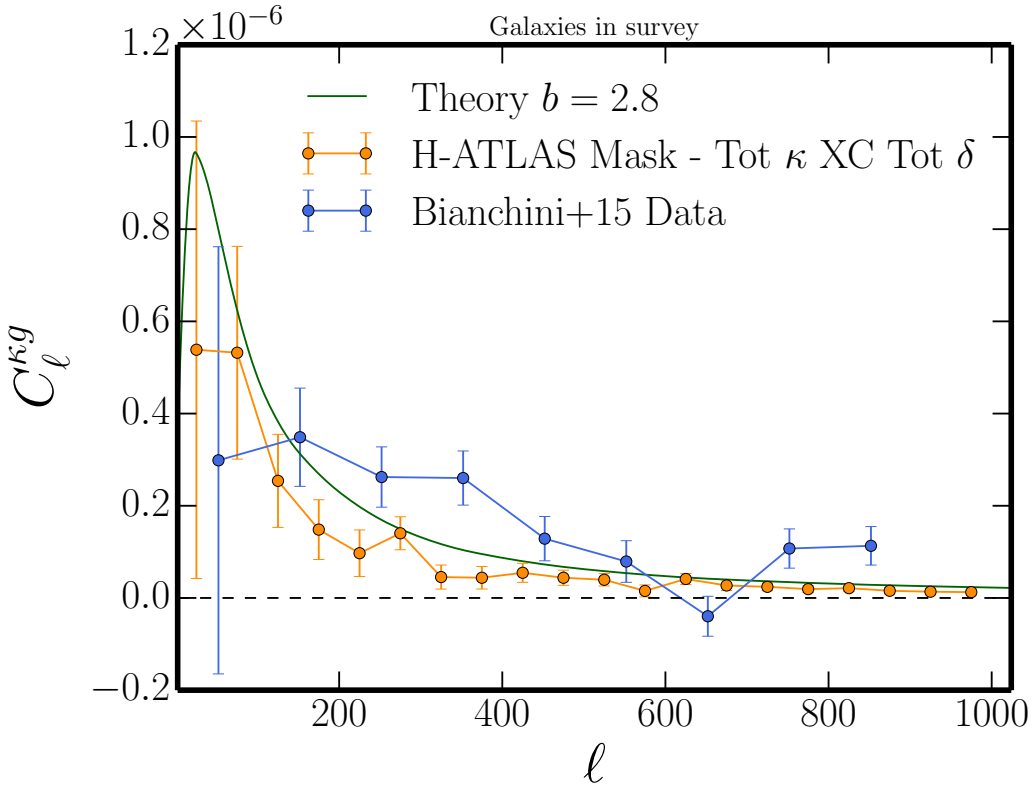

Figure 5.4 Angular power spectrum of the cross-correlation between CMB-convergence and galaxies map. The blue point are from [150], obtained using Planck-2013 lensing map and Herschel data; orange points are computed using the algorithm described in the previous pages, as both CMB convergence and mock galaxy catalogues are extracted from the same N-Body simulation (L-CoDECs). The green line is the theoretical angular power spectrum for a bias parameter of $b = 2.8$, which is an average value for this type of galaxy. Dashed horizontal lines refers to null XC case. Error bars are computed directly from the maps as in [150].

parameters and models we can forecast the best observational set-up able to push the ΛCDM model to its limits.

CHAPTER 6

Conclusions

The physics of the evolving and expanding Universe is at present well described by the ΛCDM model. Several challenges to this model have been proposed in recent years; and even if the standard paradigm is rock-solid, robust against the many cosmological and astrophysical measurements, numerous experiments are increasingly trying to improve sensitivity and accuracy to put always finer and tighter constraints on the whole set of parameters describing our Universe.

The Mother of all cosmological observations is, obviously, the light coming from the recombination era, as photons decouple from matter carrying precious information of the initial perturbations present in the Universe. This light is of course known as Cosmic Microwave Background, CMB, and its discovery and analysis represent the peak of the scientific knowledge of the Universe. However, the main topic of this Thesis deals with the life and times of CMB photons *after* decoupling, as they travel through an expanding and evolving Universe towards us, the observers. Secondary anisotropies are as rich of cosmological information as primary CMB: among the former, a prominent role is played by the deflections due to the interaction of photons with the gravitational potential arising from LSS, or CMB lensing. In the upcoming years, a continuous flow of data is going to foster a growing attention of the community on the potential of this observable and the implications that a precise measurement of the lensing power spectrum from CMB can reflect on our knowledge about cosmology and astrophysics.

The goal of this Thesis has been a full characterization and modelling of the CMB lensing signal, including also second-order and non-linear effects which become more important as the experimental sensitivity improves. To this aim, we have developed and tested a new algorithm to study the gravitational lensing of the CMB on the full sky. As we summarize here, so far, we have used it to study the lensing statistics, probing the validity of existing approximations, calculating the full distortion tensor, creating a simulation pipeline for CMB lensing - LSS cross-correlation for current and forthcoming datasets.

The starting point are the snapshots of a full N-Body numerical simulation, from which we can reconstruct a whole light-cone around the observer, mocking a real observation from the Earth. A light-cone is made of a series of different spherical maps onto which the matter distribution of the LSS is projected. The spherical shells are then used as lensing planes

to deflect the primordial CMB photons as they travel throughout the Universe. In such approach, the continuous deflections of photons is approximated by a series of multiple lens-planes (ML) that bend the light rays.

In order to fully characterize the signal, we need first to test all the possible approximations used so far in the literature. The Born approximation, where the deflection is considered as an integrated effect along the line-of-sight, has been widely tested by several authors, and was chosen as benchmark to highlight the range of validity and applicability of our algorithm, in particular in reproducing non-linearities from the N-Body simulation at small scales. The projection of the N-Body matter distribution onto concentric spherical maps allows to compress all the interesting information from the N-Body simulation into a more manageable light-cone, mimicking a realistic distribution of large scale structure as observed by present and future large galaxy surveys. The pipeline has been tested on several HPC clusters, and for a medium-size simulation (of about some billion particles), we can reconstruct the whole evolution of the light-cone using few thousands CPU-hours, managing few Gigabytes of high-resolution 2D spherical maps instead of a whole, heavy numerical simulation.

We validated the lensing planes reconstruction both at the map and statistical level using the 2-point correlation function in the spherical harmonics domain evaluated for all the spherical maps constructed across the past light-cone. We found the latter to be reproduced fairly well by semi-analytical approximations to the non-linear evolution implemented in widely used Boltzmann codes, though deviations at the percent level were clearly observed, mainly due to the intrinsic mass resolution of our N-Body simulations. We also analysed the final, lensed CMB anisotropies in both temperature and polarization for the effective as well as the multiple plane approach, paying a particular attention to the B-modes of polarization. These are in fact the most sensitive quantities both to the overall lensing process and to numerical effects. In the latter case, we have discussed in detail how to minimize their impact. We found however that these numerical effects are usually negligible for the temperature and E-modes polarization field and important only for B-modes. Our pipeline has managed to recover the expected signal at the percent level up to $\ell \approx 4000$ for the intensity (T) and E-modes of CMB polarization. The B-modes signal was found to be lower than the one computed using the semi-analytical result, following the general trend measured in the extracted lensing potential power spectrum. However, we have reconstructed the B-modes induced by lensing with the same precision of the other CMB fields to $\ell \approx 2000$, where the observed lack of power at higher multipoles

is only due to the chosen resolution of the lensing maps, as we have discussed its impact on the overall lensing kernels. Finally, we have extended the control of the validity of the Born approximation to the limiting resolution of the present set-up of our simulations. Our results indicate that, when checking the angular power spectra of lensing observables, including CMB lensed fields, the latter approximation describes well the ray-tracing performed by the ML approach. However we expect the latter to perform better for studies aiming at investigating the statistics of the signal at smaller angular scales, or in presence of distortion from isolated, sharp structures.

Science usually unveils more questions than it answers, and that happened also in this case: motivated by the lack of statistical differences between multiple lens approach and the Born approximation, we decided to push the limits of our algorithm by, on one side, reaching higher resolutions in the numerical simulations and by looking at other lensing observables, while on the other side by describing the signal via a theoretical and analytical framework thanks to a perturbative expansion of the angular power spectra. We have been able to reproduce the full magnification matrix which encodes all the information about the image of a bundle of light-rays coming from the last scattering surface. This result has been achieved by improving our pipeline by linking new routines to deal with high-resolution maps required for this study. Our analysis on the 2-points statistics shows the arising of a second-order signal in terms of rotation (or B-modes of the lensing shear) of the image, which is only present if we take into accounts the several deflections a photon experiences, i.e. this is the first effect of high-order corrections to the Born approximation. The signal is present at all scales of interest, up to $\ell \approx 2000$, and it is almost two order of magnitudes weaker than the first order signal. It has been proven robust against different numerical tests: an ongoing work is related to quantify this impact on current and future surveys for B-modes of CMB polarization, since - as repeatedly said during this Thesis - they are the most sensitive probe to any changes or effects in the lensing potential induced by LSS. The presence of a curl mode in the potential, arising from second order effects of weak lensing, has a direct impact on the current statistical estimators of the lensing potential through the lensed CMB fields. We plan in the next future to assess and quantify its relevance, both as a contaminant of present algorithms and as a tool to explore new methods and physics.

We have also computed the second-order corrections to the angular power spectra of the lensing observables (convergence, shear and rotation) predicted by perturbation theory up to the fourth order in the gravi-

tational potential. The various contributions can be attributed to the coupling between lenses at different redshifts, or non-local Born-corrections or a combination of both effects at the third order. They have been tested both numerically and observationally in the weak lensing scenarios, where the source plane is reasonably near the observer, at $z_s \approx 1$, 2; several authors have concluded that these corrections are not relevant for the galaxy weak-lensing case being orders of magnitude lower than the first-order contribution. On the contrary, if we apply the same recipes to the CMB-lensing case, we recover a large excess in the B-modes power spectrum with respect to the first-order one: these corrections seem to affect the CMB lensing potential at very small scales and, consequently, the B-mode power spectrum at all the multipoles. A tension seems to exist between our numerical results, where only a small second-order effect on the rotation power spectrum is recovered, and the analytical calculation which prescribes a 10 % variation of the lensing peak of the B-modes ($\ell \approx 1000$). Again, this is under investigation as we struggle to improve the numerical set-up to properly simulate both the CMB lensing per sé and the LSS evolution below the smallest angular scales considered in this Thesis; the main goal is to test the validity of this perturbative approach to high-ℓ for a source plane and lens planes at very high redshift.

Finally, constraints on the cosmological parameters can be improved not only by considering CMB lensing as a separate observable, but also by taking into account the cross-correlation between CMB lensing and galaxy angular distributions. This process enhances the contribution to the unperturbed CMB by the gravitational potential as we are able to relate it to the structures producing the deflections themselves. Furthermore, the cross-correlation of different data sets allows us to identify and gain control on the different systematics, peculiar to each experiment, and lower their bias on the final results. This aspect becomes even more important when considering the fact that nowadays cosmological and astrophysical surveys are now increasingly dominated by systematic, rather than statistical uncertainties.

To this end, we have developed a simulation pipeline to construct mock galaxy catalogues. The main idea is to start from the same N-Body simulation and extract, on one hand, a series of lensing potential maps to build up our light-cone, as described above. On the other hand, using the appropriate halo-finder, we can produce mock halo catalogues from the simulation. One-to-one relations between the halo mass and galaxy observables quantities (luminosity, SFR, stellar mass, ...) can be analytically computed within the abundance matching formalism, and they have been verified using real observed galaxy datasets. We then populate our

catalogue of simulated halos with galaxies, creating a series of spherical 2D maps, mimicking a real measurements of galaxy emissions from an observer on Earth, i.e. *a mock catalogue*. We have applied this technique to study the cross-correlation between Planck and Herschel data, recovering a nice agreement with the expected theory and the measured data. This pipeline, however, can be particularly useful in different cross-correlation studies between the CMB with other tracers of mass and foreground sources. The tomography of LSS, which is an intrinsic feature of the two lensing approaches analysed in this work, can be exploited to investigate different cosmological scenarios, looking at the effects of different dark energy models on small scales as well on the whole evolution of structures in the Universe. These feature will be of great importance for upcoming projects such as the Euclid satellite that can fully exploit the capabilities of cross-correlation as cosmological probe. The Euclid case is particularly relevant, as the collaboration needs mock catalogues and simulations of XC to be able to tightly focus its scientific objectives, to prioritise its observations and to study possible systematics, numerical as well as physical contaminations in measured the signal.

As we stated in the first line of this Thesis, we are heading towards a new era for cosmology, *precision cosmology* era where we should be able to measure, model and predict cosmological observables with absolute high accuracy and resolution. This Thesis walks into this direction, as it tries to simulate and understand the effect of gravitational lensing on CMB photons in its profound details. It will be a long haul, as we plan for the near future to exploit our pipeline using new numerical simulations which will reach even higher resolutions, thus allowing us to study the signal to smaller scales. This is mandatory since sub-orbitals and satellite experiments aim to full characterise lensing effects to always higher multipoles, and the community hungers for accurate and precise reconstruction of such effects. Another area of research will involve adopting different cosmologies and dark energy scenarios with respect to the standard ΛCDM so far analysed, as our algorithm can post-process any type of numerical simulations. The ultimate goal would be to reach the limit of the constraining power of the CMB itself or the XC with other observables, to explore the unknown dark sector of the current cosmological model.

Bibliography

[1] Planck Collaboration, P. A. R. Ade, N. Aghanim, C. Armitage-Caplan, M. Arnaud, M. Ashdown, F. Atrio-Barandela, J. Aumont, C. Baccigalupi, A. J. Banday, and et al. Planck 2013 results. XVI. Cosmological parameters. A&A, 571:A16, November 2014.

[2] B. Reichborn-Kjennerud, A. M. Aboobaker, P. Ade, F. Aubin, C. Baccigalupi, C. Bao, J. Borrill, C. Cantalupo, D. Chapman, J. Didier, M. Dobbs, J. Grain, W. Grainger, S. Hanany, S. Hillbrand, J. Hubmayr, A. Jaffe, B. Johnson, T. Jones, T. Kisner, J. Klein, A. Korotkov, S. Leach, A. Lee, L. Levinson, M. Limon, K. MacDermid, T. Matsumura, X. Meng, A. Miller, M. Milligan, E. Pascale, D. Polsgrove, N. Ponthieu, K. Raach, I. Sagiv, G. Smecher, F. Stivoli, R. Stompor, H. Tran, M. Tristram, G. S. Tucker, Y. Vinokurov, A. Yadav, M. Zaldarriaga, and K. Zilic. EBEX: a balloon-borne CMB polarization experiment. In *Society of Photo-Optical Instrumentation Engineers (SPIE) Conference Series*, volume 7741 of *Society of Photo-Optical Instrumentation Engineers (SPIE) Conference Series*, July 2010.

[3] Z. D. Kermish, P. Ade, A. Anthony, K. Arnold, D. Barron, D. Boettger, J. Borrill, S. Chapman, Y. Chinone, M. A. Dobbs, J. Errard, G. Fabbian, D. Flanigan, G. Fuller, A. Ghribi, W. Grainger, N. Halverson, M. Hasegawa, K. Hattori, M. Hazumi, W. L. Holzapfel, J. Howard, P. Hyland, A. Jaffe, B. Keating, T. Kisner, A. T. Lee, M. Le Jeune, E. Linder, M. Lungu, F. Matsuda, T. Matsumura, X. Meng, N. J. Miller, H. Morii, S. Moyerman, M. J. Myers, H. Nishino, H. Paar, E. Quealy, C. L. Reichardt, P. L. Richards, C. Ross, A. Shimizu, M. Shimon, C. Shimmin, M. Sholl, P. Siritanasak, H. Spieler, N. Stebor, B. Steinbach, R. Stompor, A. Suzuki, T. Tomaru, C. Tucker, and O. Zahn. The POLARBEAR experiment. In *Society of Photo-Optical Instrumentation Engineers (SPIE) Conference Series*, volume 8452 of *Society of Photo-Optical Instrumentation Engineers (SPIE) Conference Series*, September 2012.

[4] J. E. Austermann, K. A. Aird, J. A. Beall, D. Becker, A. Bender, B. A. Benson, L. E. Bleem, J. Britton, J. E. Carlstrom, C. L. Chang, H. C. Chiang, H.-M. Cho, T. M. Crawford, A. T. Crites, A. Datesman, T. de Haan, M. A. Dobbs, E. M. George, N. W. Halverson, N. Harrington, J. W. Henning, G. C. Hilton, G. P. Holder, W. L. Holzapfel, S. Hoover,

N. Huang, J. Hubmayr, K. D. Irwin, R. Keisler, J. Kennedy, L. Knox, A. T. Lee, E. Leitch, D. Li, M. Lueker, D. P. Marrone, J. J. McMahon, J. Mehl, S. S. Meyer, T. E. Montroy, T. Natoli, J. P. Nibarger, M. D. Niemack, V. Novosad, S. Padin, C. Pryke, C. L. Reichardt, J. E. Ruhl, B. R. Saliwanchik, J. T. Sayre, K. K. Schaffer, E. Shirokoff, A. A. Stark, K. Story, K. Vanderlinde, J. D. Vieira, G. Wang, R. Williamson, V. Yefremenko, K. W. Yoon, and O. Zahn. SPTpol: an instrument for CMB polarization measurements with the South Pole Telescope. In *Society of Photo-Optical Instrumentation Engineers (SPIE) Conference Series*, volume 8452 of *Society of Photo-Optical Instrumentation Engineers (SPIE) Conference Series*, September 2012.

[5] M. D. Niemack, P. A. R. Ade, J. Aguirre, F. Barrientos, J. A. Beall, J. R. Bond, J. Britton, H. M. Cho, S. Das, M. J. Devlin, S. Dicker, J. Dunkley, R. Dünner, J. W. Fowler, A. Hajian, M. Halpern, M. Hasselfield, G. C. Hilton, M. Hilton, J. Hubmayr, J. P. Hughes, L. Infante, K. D. Irwin, N. Jarosik, J. Klein, A. Kosowsky, T. A. Marriage, J. McMahon, F. Menanteau, K. Moodley, J. P. Nibarger, M. R. Nolta, L. A. Page, B. Partridge, E. D. Reese, J. Sievers, D. N. Spergel, S. T. Staggs, R. Thornton, C. Tucker, E. Wollack, and K. W. Yoon. ACTPol: a polarization-sensitive receiver for the Atacama Cosmology Telescope. In *Society of Photo-Optical Instrumentation Engineers (SPIE) Conference Series*, volume 7741 of *Society of Photo-Optical Instrumentation Engineers (SPIE) Conference Series*, July 2010.

[6] A. A. Fraisse, P. A. R. Ade, M. Amiri, S. J. Benton, J. J. Bock, J. R. Bond, J. A. Bonetti, S. Bryan, B. Burger, H. C. Chiang, C. N. Clark, C. R. Contaldi, B. P. Crill, G. Davis, O. Doré, M. Farhang, J. P. Filippini, L. M. Fissel, N. N. Gandilo, S. Golwala, J. E. Gudmundsson, M. Hasselfield, G. Hilton, W. Holmes, V. V. Hristov, K. Irwin, W. C. Jones, C. L. Kuo, C. J. MacTavish, P. V. Mason, T. E. Montroy, T. A. Morford, C. B. Netterfield, D. T. O'Dea, A. S. Rahlin, C. Reintsema, J. E. Ruhl, M. C. Runyan, M. A. Schenker, J. A. Shariff, J. D. Soler, A. Trangsrud, C. Tucker, R. S. Tucker, A. D. Turner, and D. Wiebe. SPIDER: probing the early Universe with a suborbital polarimeter. J. Cosmology Astropart. Phys., 4:47, April 2013.

[7] C. D. Sheehy, P. A. R. Ade, R. W. Aikin, M. Amiri, S. Benton, C. Bischoff, J. J. Bock, J. A. Bonetti, J. A. Brevik, B. Burger, C. D. Dowell, L. Duband, J. P. Filippini, S. R. Golwala, M. Halpern, M. Hasselfield, G. Hilton, V. V. Hristov, K. Irwin, J. P. Kaufman, B. G. Keating, J. M. Kovac, C. L. Kuo, A. E. Lange, E. M. Leitch, M. Lueker, C. B.

Netterfield, H. T. Nguyen, R. W. Ogburn, IV, A. Orlando, C. L. Pryke, C. Reintsema, S. Richter, J. E. Ruhl, M. C. Runyan, Z. Staniszewski, S. Stokes, R. Sudiwala, G. Teply, K. L. Thompson, J. E. Tolan, A. D. Turner, P. Wilson, and C. L. Wong. The Keck Array: a pulse tube cooled CMB polarimeter. *ArXiv e-prints*, April 2011.

[8] L. E. Bleem, A. van Engelen, G. P. Holder, K. A. Aird, R. Armstrong, M. L. N. Ashby, M. R. Becker, B. A. Benson, T. Biesiadzinski, M. Brodwin, M. T. Busha, J. E. Carlstrom, C. L. Chang, H. M. Cho, T. M. Crawford, A. T. Crites, T. de Haan, S. Desai, M. A. Dobbs, O. Doré, J. Dudley, J. E. Geach, E. M. George, M. D. Gladders, A. H. Gonzalez, N. W. Halverson, N. Harrington, F. W. High, B. P. Holden, W. L. Holzapfel, S. Hoover, J. D. Hrubes, M. Joy, R. Keisler, L. Knox, A. T. Lee, E. M. Leitch, M. Lueker, D. Luong-Van, D. P. Marrone, J. Martinez-Manso, J. J. McMahon, J. Mehl, S. S. Meyer, J. J. Mohr, T. E. Montroy, T. Natoli, S. Padin, T. Plagge, C. Pryke, C. L. Reichardt, A. Rest, J. E. Ruhl, B. R. Saliwanchik, J. T. Sayre, K. K. Schaffer, L. Shaw, E. Shirokoff, H. G. Spieler, B. Stalder, S. A. Stanford, Z. Staniszewski, A. A. Stark, D. Stern, K. Story, A. Vallinotto, K. Vanderlinde, J. D. Vieira, R. H. Wechsler, R. Williamson, and O. Zahn. A Measurement of the Correlation of Galaxy Surveys with CMB Lensing Convergence Maps from the South Pole Telescope. ApJ, 753:L9, July 2012.

[9] B. D. Sherwin, S. Das, A. Hajian, G. Addison, J. R. Bond, D. Crichton, M. J. Devlin, J. Dunkley, M. B. Gralla, M. Halpern, J. C. Hill, A. D. Hincks, J. P. Hughes, K. Huffenberger, R. Hlozek, A. Kosowsky, T. Louis, T. A. Marriage, D. Marsden, F. Menanteau, K. Moodley, M. D. Niemack, L. A. Page, E. D. Reese, N. Sehgal, J. Sievers, C. Sifón, D. N. Spergel, S. T. Staggs, E. R. Switzer, and E. Wollack. The Atacama Cosmology Telescope: Cross-correlation of cosmic microwave background lensing and quasars. Phys. Rev. D, 86(8):083006, October 2012.

[10] N. Hand, A. Leauthaud, S. Das, B. D. Sherwin, G. E. Addison, J. R. Bond, E. Calabrese, A. Charbonnier, M. J. Devlin, J. Dunkley, T. Erben, A. Hajian, M. Halpern, J. Harnois-Déraps, C. Heymans, H. Hildebrandt, A. D. Hincks, J.-P. Kneib, A. Kosowsky, M. Makler, L. Miller, K. Moodley, B. Moraes, M. D. Niemack, L. A. Page, B. Partridge, N. Sehgal, H. Shan, J. L. Sievers, D. N. Spergel, S. T. Staggs, E. R. Switzer, J. E. Taylor, L. Van Waerbeke, and E. J. Wollack. First

Measurement of the Cross-Correlation of CMB Lensing and Galaxy Lensing. *ArXiv e-prints*, November 2013.

[11] P. A. R. Ade, Y. Akiba, A. E. Anthony, K. Arnold, M. Atlas, D. Barron, D. Boettger, J. Borrill, S. Chapman, Y. Chinone, M. Dobbs, T. Elleflot, J. Errard, G. Fabbian, C. Feng, D. Flanigan, A. Gilbert, W. Grainger, N. W. Halverson, M. Hasegawa, K. Hattori, M. Hazumi, W. L. Holzapfel, Y. Hori, J. Howard, P. Hyland, Y. Inoue, G. C. Jaehnig, A. Jaffe, B. Keating, Z. Kermish, R. Keskitalo, T. Kisner, M. Le Jeune, A. T. Lee, E. Linder, E. M. Leitch, M. Lungu, F. Matsuda, T. Matsumura, X. Meng, N. J. Miller, H. Morii, S. Moyerman, M. J. Myers, M. Navaroli, H. Nishino, H. Paar, J. Peloton, E. Quealy, G. Rebeiz, C. L. Reichardt, P. L. Richards, C. Ross, I. Schanning, D. E. Schenck, B. Sherwin, A. Shimizu, C. Shimmin, M. Shimon, P. Siritanasak, G. Smecher, H. Spieler, N. Stebor, B. Steinbach, R. Stompor, A. Suzuki, S. Takakura, T. Tomaru, B. Wilson, A. Yadav, O. Zahn, and Polarbear Collaboration. Measurement of the Cosmic Microwave Background Polarization Lensing Power Spectrum with the POLARBEAR Experiment. *Physical Review Letters*, 113(2):021301, July 2014.

[12] D. Hanson, S. Hoover, A. Crites, P. A. R. Ade, K. A. Aird, J. E. Austermann, J. A. Beall, A. N. Bender, B. A. Benson, L. E. Bleem, J. J. Bock, J. E. Carlstrom, C. L. Chang, H. C. Chiang, H.-M. Cho, A. Conley, T. M. Crawford, T. de Haan, M. A. Dobbs, W. Everett, J. Gallicchio, J. Gao, E. M. George, N. W. Halverson, N. Harrington, J. W. Henning, G. C. Hilton, G. P. Holder, W. L. Holzapfel, J. D. Hrubes, N. Huang, J. Hubmayr, K. D. Irwin, R. Keisler, L. Knox, A. T. Lee, E. Leitch, D. Li, C. Liang, D. Luong-Van, G. Marsden, J. J. McMahon, J. Mehl, S. S. Meyer, L. Mocanu, T. E. Montroy, T. Natoli, J. P. Nibarger, V. Novosad, S. Padin, C. Pryke, C. L. Reichardt, J. E. Ruhl, B. R. Saliwanchik, J. T. Sayre, K. K. Schaffer, B. Schulz, G. Smecher, A. A. Stark, K. T. Story, C. Tucker, K. Vanderlinde, J. D. Vieira, M. P. Viero, G. Wang, V. Yefremenko, O. Zahn, and M. Zemcov. Detection of B-Mode Polarization in the Cosmic Microwave Background with Data from the South Pole Telescope. *Physical Review Letters*, 111(14):141301, October 2013.

[13] R. Laureijs, J. Amiaux, S. Arduini, J. . Augueres, J. Brinchmann, R. Cole, M. Cropper, C. Dabin, L. Duvet, A. Ealet, and et al. Euclid Definition Study Report. *ArXiv e-prints*, October 2011.

[14] L. Amendola, S. Appleby, D. Bacon, T. Baker, M. Baldi, N. Bartolo, A. Blanchard, C. Bonvin, S. Borgani, E. Branchini, C. Burrage, S. Camera, C. Carbone, L. Casarini, M. Cropper, C. de Rham, C. Di Porto, A. Ealet, P. G. Ferreira, F. Finelli, J. García-Bellido, T. Giannantonio, L. Guzzo, A. Heavens, L. Heisenberg, C. Heymans, H. Hoekstra, L. Hollenstein, R. Holmes, O. Horst, K. Jahnke, T. D. Kitching, T. Koivisto, M. Kunz, G. La Vacca, M. March, E. Majerotto, K. Markovic, D. Marsh, F. Marulli, R. Massey, Y. Mellier, D. F. Mota, N. Nunes, W. Percival, V. Pettorino, C. Porciani, C. Quercellini, J. Read, M. Rinaldi, D. Sapone, R. Scaramella, C. Skordis, F. Simpson, A. Taylor, S. Thomas, R. Trotta, L. Verde, F. Vernizzi, A. Vollmer, Y. Wang, J. Weller, and T. Zlosnik. Cosmology and Fundamental Physics with the Euclid Satellite. *Living Reviews in Relativity*, 16:6, September 2013.

[15] M. Calabrese, C. Carbone, G. Fabbian, M. Baldi, and C. Baccigalupi. Multiple lensing of the cosmic microwave background anisotropies. J. Cosmology Astropart. Phys., 3:49, March 2015.

[16] M. Calabrese, G. Fabbian, C. Carbone, and S. Hilbert. High resolution simulations of CMB lensing. *In prep.*

[17] F. Bianchini, A. Lapi, M. Calabrese, P. Bielewicz, J. Gonzalez-Nuevo, C. Baccigalupi, and L. Danese. Toward a Tomographic analysis of the cross-correlation between Planck CMB lensing and H-ATLAS galaxies. *In prep.*

[18] M. Calabrese, F. Bianchini, A. Lapi, P. Bielewicz, and L. Danese. Cross-correlation between galaxy mock catalogue and simulated lensing potential maps. *In prep.*

[19] William C. Keel. *The Road to Galaxy Formation*. Springer-Praxis., 2007.

[20] J.A. Peacock, A.F. Heavens, and A.T. Davies. *Physics of the Early Universe: Proceedings of the Thirty Sixth Scottish Universities Summer School in Physics, Edinburgh, July 24 - August 11 1989*. Scottish Graduate Series. Taylor & Francis, 1990.

[21] T. Padmanabhan. *Structure Formation in the Universe*. Cambridge University Press, 1993.

[22] P. J. E. Peebles. Light Out of Darkness vs Order Out of Chaos. *Comments on Astrophysics and Space Physics*, 4:53, March 1972.

[23] H. P. Robertson. Relativistic cosmology. *Rev. Mod. Phys.*, 5:62–90, Jan 1933.

[24] H. P. Robertson. Kinematics and World-Structure II. ApJ, 83:187, April 1936.

[25] A. Friedmann. Über die Krümmung des Raumes. *Zeitschrift fur Physik*, 10:377–386, 1922.

[26] A. Friedmann. Über die Möglichkeit einer Welt mit konstanter negativer Krümmung des Raumes . *Zeitschrift fur Physik*, 21:326, 1924.

[27] G. Lemaître. Un Univers homogène de masse constante et de rayon croissant rendant compte de la vitesse radiale des nébuleuses extra-galactiques. *Annales de la Société Scientifique de Bruxelles*, 47:49–59, 1927.

[28] Planck Collaboration, P. A. R. Ade, N. Aghanim, M. Arnaud, M. Ashdown, J. Aumont, C. Baccigalupi, A. J. Banday, R. B. Barreiro, J. G. Bartlett, and et al. Planck 2015 results. XIII. Cosmological parameters. *ArXiv e-prints*, February 2015.

[29] B. E. J. Pagel. Beryllium and the Big Bang. Nature, 354:267–268, November 1991.

[30] S. Perlmutter, M. S. Turner, and M. White. Constraining Dark Energy with Type Ia Supernovae and Large-Scale Structure. *Physical Review Letters*, 83:670–673, July 1999.

[31] A. Conley, J. Guy, M. Sullivan, N. Regnault, P. Astier, C. Balland, S. Basa, R. G. Carlberg, D. Fouchez, D. Hardin, I. M. Hook, D. A. Howell, R. Pain, N. Palanque-Delabrouille, K. M. Perrett, C. J. Pritchet, J. Rich, V. Ruhlmann-Kleider, D. Balam, S. Baumont, R. S. Ellis, S. Fabbro, H. K. Fakhouri, N. Fourmanoit, S. González-Gaitán, M. L. Graham, M. J. Hudson, E. Hsiao, T. Kronborg, C. Lidman, A. M. Mourao, J. D. Neill, S. Perlmutter, P. Ripoche, N. Suzuki, and E. S. Walker. Supernova Constraints and Systematic Uncertainties from the First Three Years of the Supernova Legacy Survey. ApJS, 192:1, January 2011.

[32] L. Gao, N. Yoshida, T. Abel, C. S. Frenk, A. Jenkins, and V. Springel. The first generation of stars in the Λ cold dark matter cosmology. MNRAS, 378:449–468, June 2007.

[33] M. Tegmark, J. Silk, M. J. Rees, A. Blanchard, T. Abel, and F. Palla. How Small Were the First Cosmological Objects? ApJ, 474:1, January 1997.

[34] A. H. Guth. Inflationary universe: A possible solution to the horizon and flatness problems. Phys. Rev. D, 23:347–356, January 1981.

[35] S. W. Hawking. The development of irregularities in a single bubble inflationary universe. *Physics Letters B*, 115:295–297, September 1982.

[36] G. F. Smoot, C. L. Bennett, A. Kogut, E. L. Wright, J. Aymon, N. W. Boggess, E. S. Cheng, G. de Amici, S. Gulkis, M. G. Hauser, G. Hinshaw, P. D. Jackson, M. Janssen, E. Kaita, T. Kelsall, P. Keegstra, C. Lineweaver, K. Loewenstein, P. Lubin, J. Mather, S. S. Meyer, S. H. Moseley, T. Murdock, L. Rokke, R. F. Silverberg, L. Tenorio, R. Weiss, and D. T. Wilkinson. Structure in the COBE differential microwave radiometer first-year maps. ApJ, 396:L1–L5, September 1992.

[37] I. A. Strukov, A. A. Brukhanov, D. P. Skulachev, and M. V. Sazhin. Anisotropy of the microwave background radiation. *Soviet Astronomy Letters*, 18:153, May 1992.

[38] A. H. Guth and S.-Y. Pi. Fluctuations in the new inflationary universe. *Physical Review Letters*, 49:1110–1113, October 1982.

[39] A. D. Linde. Scalar field fluctuations in the expanding universe and the new inflationary universe scenario. *Physics Letters B*, 116:335–339, October 1982.

[40] V. F. Mukhanov and G. V. Chibisov. Quantum fluctuations and a nonsingular universe. *ZhETF Pisma Redaktsiiu*, 33:549–553, May 1981.

[41] A. A. Starobinsky. Dynamics of phase transition in the new inflationary universe scenario and generation of perturbations. *Physics Letters B*, 117:175–178, November 1982.

[42] P. Peter and J.P. Uzan. *Primordial Cosmology*. Oxford Graduate Texts. OUP Oxford, 2013.

[43] N. Bartolo, S. Matarrese, and A. Riotto. Enhancement of non-gaussianity after inflation. *Journal of High Energy Physics*, 4:6, April 2004.

[44] S. Renaux-Petel. Combined local and equilateral non-Gaussianities from multifield DBI inflation. J. Cosmology Astropart. Phys., 10:12, October 2009.

[45] A. Lewis. The real shape of non-Gaussianities. J. Cosmology Astropart. Phys., 10:26, October 2011.

[46] W. Dehnen and J. I. Read. N-body simulations of gravitational dynamics. *European Physical Journal Plus*, 126:55, May 2011.

[47] M. Trenti and P. Hut. Gravitational N-body Simulations. *ArXiv e-prints*, June 2008.

[48] J. S. Bagla and T. Padmanabhan. Cosmological N-body simulations. *Pramana*, 49:161, August 1997.

[49] M. Tegmark, M. A. Strauss, M. R. Blanton, K. Abazajian, S. Dodelson, H. Sandvik, X. Wang, D. H. Weinberg, I. Zehavi, N. A. Bahcall, F. Hoyle, D. Schlegel, R. Scoccimarro, M. S. Vogeley, A. Berlind, T. Budavari, A. Connolly, D. J. Eisenstein, D. Finkbeiner, J. A. Frieman, J. E. Gunn, L. Hui, B. Jain, D. Johnston, S. Kent, H. Lin, R. Nakajima, R. C. Nichol, J. P. Ostriker, A. Pope, R. Scranton, U. Seljak, R. K. Sheth, A. Stebbins, A. S. Szalay, I. Szapudi, Y. Xu, J. Annis, J. Brinkmann, S. Burles, F. J. Castander, I. Csabai, J. Loveday, M. Doi, M. Fukugita, B. Gillespie, G. Hennessy, D. W. Hogg, vZ. Ivezić, G. R. Knapp, D. Q. Lamb, B. C. Lee, R. H. Lupton, T. A. McKay, P. Kunszt, J. A. Munn, L. O'Connell, J. Peoples, J. R. Pier, M. Richmond, C. Rockosi, D. P. Schneider, C. Stoughton, D. L. Tucker, D. E. vanden Berk, B. Yanny, and D. G. York. Cosmological parameters from SDSS and WMAP. Phys. Rev. D, 69(10):103501, May 2004.

[50] C. S. Frenk. Simulating the formation of cosmic structure. *Royal Society of London Philosophical Transactions Series A*, 360:1277, June 2002.

[51] A. E. Evrard, T. J. MacFarland, H. M. P. Couchman, J. M. Colberg, N. Yoshida, S. D. M. White, A. Jenkins, C. S. Frenk, F. R. Pearce, J. A. Peacock, and P. A. Thomas. Galaxy Clusters in Hubble Volume Simulations: Cosmological Constraints from Sky Survey Populations. ApJ, 573:7–36, July 2002.

[52] A. Jenkins, C. S. Frenk, F. R. Pearce, P. A. Thomas, J. M. Colberg, S. D. M. White, H. M. P. Couchman, J. A. Peacock, G. Efstathiou, and A. H. Nelson. Evolution of Structure in Cold Dark Matter Universes. ApJ, 499:20–40, May 1998.

[53] C. Power, J. F. Navarro, A. Jenkins, C. S. Frenk, S. D. M. White, V. Springel, J. Stadel, and T. Quinn. The inner structure of ΛCDM haloes - I. A numerical convergence study. MNRAS, 338:14–34, January 2003.

[54] S. Weinberg. *Gravitation and Cosmology: Principles and Applications of the General Theory of Relativity*. July 1972.

[55] S. Dodelson. *Modern cosmology*. 2003.

[56] J.A. Peacock. *Cosmological Physics*. Cambridge Astrophysics. Cambridge University Press, 1999.

[57] F. Bernardeau, S. Colombi, E. Gaztañaga, and R. Scoccimarro. Large-scale structure of the Universe and cosmological perturbation theory. Phys. Rep., 367:1–248, September 2002.

[58] T. Buchert. Lagrangian perturbation theory - A key-model for large-scale structure. A&A, 267:L51–L54, January 1993.

[59] M. Bartelmann and P. Schneider. Weak gravitational lensing. Phys. Rep., 340:291–472, January 2001.

[60] M. Bartelmann. TOPICAL REVIEW Gravitational lensing. *Classical and Quantum Gravity*, 27(23):233001, December 2010.

[61] U. Seljak. Large-scale structure effects on the gravitational lens image positions and time delay. ApJ, 436:509–516, December 1994.

[62] S. Dodelson, E. W. Kolb, S. Matarrese, A. Riotto, and P. Zhang. Second order geodesic corrections to cosmic shear. Phys. Rev. D, 72(10):103004, November 2005.

[63] B. Jain, U. Seljak, and S. White. Ray-tracing Simulations of Weak Lensing by Large-Scale Structure. ApJ, 530:547–577, February 2000.

[64] S. Seitz and P. Schneider. Some remarks on multiple deflection gravitational lensing. A&A, 287:349–360, July 1994.

[65] S. Hilbert, J. Hartlap, S. D. M. White, and P. Schneider. Ray-tracing through the Millennium Simulation: Born corrections and lens-lens coupling in cosmic shear and galaxy-galaxy lensing. A&A, 499:31–43, May 2009.

[66] P. Schneider, J. Ehlers, and E. E. Falco. *Gravitational Lenses*. 1992.

[67] C. M. Hirata and U. Seljak. Reconstruction of lensing from the cosmic microwave background polarization. Phys. Rev. D, 68(8):083002, October 2003.

[68] Chao Li and Asantha Cooray. Weak lensing of the cosmic microwave background by foreground gravitational waves. *Phys. Rev. D*, 74:023521, Jul 2006.

[69] T. Namikawa, D. Yamauchi, and A. Taruya. Constraining cosmic string parameters with curl mode of CMB lensing. Phys. Rev. D, 88(8):083525, October 2013.

[70] H. Padmanabhan, A. Rotti, and T. Souradeep. Comparison of CMB lensing efficiency of gravitational waves and large scale structure. Phys. Rev. D, 88(6):063507, September 2013.

[71] D. J. Fixsen, E. S. Cheng, J. M. Gales, J. C. Mather, R. A. Shafer, and E. L. Wright. The Cosmic Microwave Background Spectrum from the Full COBE FIRAS Data Set. ApJ, 473:576, December 1996.

[72] J. C. Mather, E. S. Cheng, D. A. Cottingham, R. E. Eplee, Jr., D. J. Fixsen, T. Hewagama, R. B. Isaacman, K. A. Jensen, S. S. Meyer, P. D. Noerdlinger, S. M. Read, L. P. Rosen, R. A. Shafer, E. L. Wright, C. L. Bennett, N. W. Boggess, M. G. Hauser, T. Kelsall, S. H. Moseley, Jr., R. F. Silverberg, G. F. Smoot, R. Weiss, and D. T. Wilkinson. Measurement of the cosmic microwave background spectrum by the COBE FIRAS instrument. ApJ, 420:439–444, January 1994.

[73] Planck Collaboration, R. Adam, P. A. R. Ade, N. Aghanim, Y. Akrami, M. I. R. Alves, M. Arnaud, F. Arroja, J. Aumont, C. Baccigalupi, and et al. Planck 2015 results. I. Overview of products and scientific results. *ArXiv e-prints*, February 2015.

[74] A. Kosowsky. Cosmic microwave background polarization. *Annals of Physics*, 246:49–85, February 1996.

[75] W. Hu and N. Sugiyama. Anisotropies in the cosmic microwave background: an analytic approach. ApJ, 444:489–506, May 1995.

[76] W. Hu and N. Sugiyama. Toward understanding CMB anisotropies and their implications. Phys. Rev. D, 51:2599–2630, March 1995.

[77] W. Hu and N. Sugiyama. Small-Scale Cosmological Perturbations: an Analytic Approach. ApJ, 471:542, November 1996.

[78] U. Seljak and M. Zaldarriaga. A Line-of-Sight Integration Approach to Cosmic Microwave Background Anisotropies. ApJ, 469:437, October 1996.

[79] R. K. Sachs and A. M. Wolfe. Perturbations of a Cosmological Model and Angular Variations of the Microwave Background. ApJ, 147:73, January 1967.

[80] Nicolas Ponthieu. *Polarisation du fond diffus cosmologique et de l'émission des poussières galactiques*. Theses, Université Joseph-Fourier - Grenoble I, July 2003.

[81] A. G. Polnarev. Polarization and Anisotropy Induced in the Microwave Background by Cosmological Gravitational Waves. Soviet Ast., 29:607–613, December 1985.

[82] W. Hu and M. White. A CMB polarization primer. New A, 2:323–344, October 1997.

[83] J.J. D. *Classical Electrodynamics*. John Wiley, 1975.

[84] POLARBEAR Collaboration, P. A. R. Ade, Y. Akiba, A. E. Anthony, K. Arnold, M. Atlas, D. Barron, D. Boettger, J. Borrill, S. Chapman, Y. Chinone, M. Dobbs, T. Elleflot, J. Errard, G. Fabbian, C. Feng, D. Flanigan, A. Gilbert, W. Grainger, N. W. Halverson, M. Hasegawa, K. Hattori, M. Hazumi, W. L. Holzapfel, Y. Hori, J. Howard, P. Hyland, Y. Inoue, G. C. Jaehnig, A. Jaffe, B. Keating, Z. Kermish, R. Keskitalo, T. Kisner, M. Le Jeune, A. T. Lee, E. Linder, E. M. Leitch, M. Lungu, F. Matsuda, T. Matsumura, X. Meng, N. J. Miller, H. Morii, S. Moyerman, M. J. Myers, M. Navaroli, H. Nishino, H. Paar, J. Peloton, E. Quealy, G. Rebeiz, C. L. Reichardt, P. L. Richards, C. Ross, I. Schanning, D. E. Schenck, B. Sherwin, A. Shimizu, C. Shimmin, M. Shimon, P. Siritanasak, G. Smecher, H. Spieler, N. Stebor, B. Steinbach, R. Stompor, A. Suzuki, S. Takakura, T. Tomaru, B. Wilson, A. Yadav, and O. Zahn. Measurement of the Cosmic Microwave Background Polarization Lensing Power Spectrum with the POLARBEAR experiment. *ArXiv e-prints*, December 2013.

[85] A. Melchiorri and N. Vittorio. Polarization of the Microwave Background: Theoretical Framework. In C. H. Lineweaver, J. G. Bartlett, A. Blanchard, M. Signore, and J. Silk, editors, *NATO Advanced Science Institutes (ASI) Series C*, volume 502 of *NATO Advanced Science Institutes (ASI) Series C*, page 419, 1997.

[86] M. Zaldarriaga and U. Seljak. All-sky analysis of polarization in the microwave background. Phys. Rev. D, 55:1830–1840, February 1997.

[87] M. Kamionkowski, A. Kosowsky, and A. Stebbins. Statistics of cosmic microwave background polarization. Phys. Rev. D, 55:7368–7388, June 1997.

[88] A. Challinor and H. Peiris. Lecture notes on the physics of cosmic microwave background anisotropies. In M. Novello and S. Perez, editors, *American Institute of Physics Conference Series*, volume 1132 of *American Institute of Physics Conference Series*, pages 86–140, May 2009.

[89] N. Aghanim, S. Majumdar, and J. Silk. Secondary anisotropies of the CMB. *Reports on Progress in Physics*, 71(6):066902, June 2008.

[90] W. Hu and S. Dodelson. Cosmic Microwave Background Anisotropies. ARA&A, 40:171–216, 2002.

[91] W. Hu. CMB temperature and polarization anisotropy fundamentals. *Annals of Physics*, 303:203–225, January 2003.

[92] R. A. Sunyaev and I. B. Zeldovich. Microwave background radiation as a probe of the contemporary structure and history of the universe. ARA&A, 18:537–560, 1980.

[93] M. Birkinshaw. The Sunyaev-Zel'dovich effect. Phys. Rep., 310:97–195, March 1999.

[94] J. E. Carlstrom, G. P. Holder, and E. D. Reese. Cosmology with the Sunyaev-Zel'dovich Effect. ARA&A, 40:643–680, 2002.

[95] J. Weller, R. A. Battye, and R. Kneissl. Constraining Dark Energy with Sunyaev-Zel'dovich Cluster Surveys. *Physical Review Letters*, 88(23):231301, June 2002.

[96] R. A. Battye and J. Weller. Constraining cosmological parameters using Sunyaev-Zel'dovich cluster surveys. Phys. Rev. D, 68(8):083506, October 2003.

[97] V. Acquaviva, C. Baccigalupi, and F. Perrotta. Weak lensing in generalized gravity theories. Phys. Rev. D, 70(2):023515, July 2004.

[98] A. Lewis and A. Challinor. Weak gravitational lensing of the CMB. Phys. Rep., 429:1–65, June 2006.

[99] C. Carbone, C. Baccigalupi, M. Bartelmann, S. Matarrese, and V. Springel. Lensed CMB temperature and polarization maps from the Millennium Simulation. MNRAS, 396:668–679, June 2009.

[100] C. Carbone, M. Baldi, V. Pettorino, and C. Baccigalupi. Maps of CMB lensing deflection from N-body simulations in Coupled Dark Energy Cosmologies. J. Cosmology Astropart. Phys., 9:4, September 2013.

[101] R. E. Smith, J. A. Peacock, A. Jenkins, S. D. M. White, C. S. Frenk, F. R. Pearce, P. A. Thomas, G. Efstathiou, and H. M. P. Couchman. Stable clustering, the halo model and non-linear cosmological power spectra. MNRAS, 341:1311–1332, June 2003.

[102] R. Takahashi, M. Sato, T. Nishimichi, A. Taruya, and M. Oguri. Revising the Halofit Model for the Nonlinear Matter Power Spectrum. ApJ, 761:152, December 2012.

[103] W. Hu. Weak lensing of the CMB: A harmonic approach. Phys. Rev. D, 62(4):043007, August 2000.

[104] A. Challinor and G. Chon. Geometry of weak lensing of CMB polarization. Phys. Rev. D, 66(12):127301, December 2002.

[105] A. Challinor and A. Lewis. Lensed CMB power spectra from all-sky correlation functions. Phys. Rev. D, 71(10):103010, May 2005.

[106] D. Blas, J. Lesgourgues, and T. Tram. The Cosmic Linear Anisotropy Solving System (CLASS). Part II: Approximation schemes. J. Cosmology Astropart. Phys., 7:34, July 2011.

[107] B. Audren and J. Lesgourgues. Non-linear matter power spectrum from Time Renormalisation Group: efficient computation and comparison with one-loop. J. Cosmology Astropart. Phys., 10:37, October 2011.

[108] M. Zaldarriaga and U. Seljak. Gravitational lensing effect on cosmic microwave background polarization. Phys. Rev. D, 58(2):023003, July 1998.

[109] U. Seljak. Gravitational Lensing Effect on Cosmic Microwave Background Anisotropies: A Power Spectrum Approach. ApJ, 463:1, May 1996.

[110] U. Seljak and C. M. Hirata. Gravitational lensing as a contaminant of the gravity wave signal in the CMB. Phys. Rev. D, 69(4):043005, February 2004.

[111] W. Hu. Dark energy and matter evolution from lensing tomography. Phys. Rev. D, 66(8):083515, October 2002.

[112] A. Lewis. Lensed CMB simulation and parameter estimation. Phys. Rev. D, 71(8):083008, April 2005.

[113] R. Stompor and G. Efstathiou. Gravitational lensing of cosmic microwave background anisotropies and cosmological parameter estimation. MNRAS, 302:735–747, February 1999.

[114] L. Perotto, J. Lesgourgues, S. Hannestad, H. Tu, and Y. Y Y Wong. Probing cosmological parameters with the CMB: forecasts from Monte Carlo simulations. J. Cosmology Astropart. Phys., 10:13, October 2006.

[115] M. Kaplinghat, L. Knox, and Y.-S. Song. Determining Neutrino Mass from the Cosmic Microwave Background Alone. *Physical Review Letters*, 91(24):241301, December 2003.

[116] W. Hu. Dark synergy: Gravitational lensing and the CMB. Phys. Rev. D, 65(2):023003, January 2002.

[117] V. Acquaviva and C. Baccigalupi. Dark energy records in lensed cosmic microwave background. Phys. Rev. D, 74(10):103510, November 2006.

[118] S. Smith, A. Challinor, and G. Rocha. What can be learned from the lensed cosmic microwave background B-mode polarization power spectrum? Phys. Rev. D, 73(2):023517, January 2006.

[119] R. de Putter, O. Zahn, and E. V. Linder. CMB lensing constraints on neutrinos and dark energy. Phys. Rev. D, 79(6):065033, March 2009.

[120] C. Wetterich. Cosmology and the fate of dilatation symmetry. *Nuclear Physics B*, 302:668–696, June 1988.

[121] M. Doran, G. Robbers, and C. Wetterich. Impact of three years of data from the Wilkinson Microwave Anisotropy Probe on cosmological models with dynamical dark energy. Phys. Rev. D, 75(2):023003, January 2007.

[122] S. Das and E. V. Linder. CMB polarization impact on cosmological constraints. Phys. Rev. D, 86(6):063520, September 2012.

[123] O. Zahn and M. Zaldarriaga. Lensing Reconstruction Using Redshifted 21 Centimeter Fluctuations. ApJ, 653:922–935, December 2006.

[124] J. R. Pritchard and E. Pierpaoli. Constraining massive neutrinos using cosmological 21cm observations. Phys. Rev. D, 78(6):065009, September 2008.

[125] S. Joudaki and M. Kaplinghat. Dark energy and neutrino masses from future measurements of the expansion history and growth of structure. Phys. Rev. D, 86(2):023526, July 2012.

[126] S. Hanany, P. Ade, A. Balbi, J. Bock, J. Borrill, A. Boscaleri, P. de Bernardis, P. G. Ferreira, V. V. Hristov, A. H. Jaffe, A. E. Lange, A. T. Lee, P. D. Mauskopf, C. B. Netterfield, S. Oh, E. Pascale, B. Rabii, P. L. Richards, G. F. Smoot, R. Stompor, C. D. Winant, and J. H. P. Wu. MAXIMA-1: A Measurement of the Cosmic Microwave Background Anisotropy on Angular Scales of 10'-5$\deg$. $\mathrm{ApJ}, 545 : L5 - -L9, December 2000.$

[127] P. de Bernardis, P. A. R. Ade, J. J. Bock, J. R. Bond, J. Borrill, A. Boscaleri, K. Coble, B. P. Crill, G. De Gasperis, G. De Troia, P. C. Farese, P. G. Ferreira, K. Ganga, M. Giacometti, E. Hivon, V. V. Hristov, A. Iacoangeli, A. H. Jaffe, A. E. Lange, L. Martinis, S. Masi, P. Mason, P. D. Mauskopf, A. Melchiorri, L. Miglio, T. Montroy, C. B. Netterfield, E. Pascale, F. Piacentini, D. Pogosyan, F. Pongetti, S. Prunet, S. Rao, G. Romeo, J. E. Ruhl, F. Scaramuzzi, D. Sforna, and N. Vittorio. Detection of anisotropy in the Cosmic Microwave Background at horizon and sub-horizon scales with the BOOMERanG experiment. *ArXiv Astrophysics e-prints*, November 2000.

[128] J. M. Kovac, E. M. Leitch, C. Pryke, J. E. Carlstrom, N. W. Halverson, and W. L. Holzapfel. Detection of polarization in the cosmic microwave background using DASI. Nature, 420:772–787, December 2002.

[129] S. Das, T. A. Marriage, P. A. R. Ade, P. Aguirre, M. Amiri, J. W. Appel, L. F. Barrientos, E. S. Battistelli, J. R. Bond, B. Brown, B. Burger, J. Chervenak, M. J. Devlin, S. R. Dicker, W. Bertrand Doriese, J. Dunkley, R. Dünner, T. Essinger-Hileman, R. P. Fisher,

J. W. Fowler, A. Hajian, M. Halpern, M. Hasselfield, C. Hernández-Monteagudo, G. C. Hilton, M. Hilton, A. D. Hincks, R. Hlozek, K. M. Huffenberger, D. H. Hughes, J. P. Hughes, L. Infante, K. D. Irwin, J. Baptiste Juin, M. Kaul, J. Klein, A. Kosowsky, J. M. Lau, M. Limon, Y.-T. Lin, R. H. Lupton, D. Marsden, K. Martocci, P. Mauskopf, F. Menanteau, K. Moodley, H. Moseley, C. B. Netterfield, M. D. Niemack, M. R. Nolta, L. A. Page, L. Parker, B. Partridge, B. Reid, N. Sehgal, B. D. Sherwin, J. Sievers, D. N. Spergel, S. T. Staggs, D. S. Swetz, E. R. Switzer, R. Thornton, H. Trac, C. Tucker, R. Warne, E. Wollack, and Y. Zhao. The Atacama Cosmology Telescope: A Measurement of the Cosmic Microwave Background Power Spectrum at 148 and 218 GHz from the 2008 Southern Survey. ApJ, 729:62, March 2011.

[130] K. T. Story, C. L. Reichardt, Z. Hou, R. Keisler, K. A. Aird, B. A. Benson, L. E. Bleem, J. E. Carlstrom, C. L. Chang, H.-M. Cho, T. M. Crawford, A. T. Crites, T. de Haan, M. A. Dobbs, J. Dudley, B. Follin, E. M. George, N. W. Halverson, G. P. Holder, W. L. Holzapfel, S. Hoover, J. D. Hrubes, M. Joy, L. Knox, A. T. Lee, E. M. Leitch, M. Lueker, D. Luong-Van, J. J. McMahon, J. Mehl, S. S. Meyer, M. Millea, J. J. Mohr, T. E. Montroy, S. Padin, T. Plagge, C. Pryke, J. E. Ruhl, J. T. Sayre, K. K. Schaffer, L. Shaw, E. Shirokoff, H. G. Spieler, Z. Staniszewski, A. A. Stark, A. van Engelen, K. Vanderlinde, J. D. Vieira, R. Williamson, and O. Zahn. A Measurement of the Cosmic Microwave Background Damping Tail from the 2500-Square-Degree SPT-SZ Survey. ApJ, 779:86, December 2013.

[131] E. M. Leitch, J. M. Kovac, C. Pryke, J. E. Carlstrom, N. W. Halverson, W. L. Holzapfel, M. Dragovan, B. Reddall, and E. S. Sandberg. Measurement of polarization with the Degree Angular Scale Interferometer. Nature, 420:763–771, December 2002.

[132] S. Naess, M. Hasselfield, J. McMahon, M. D. Niemack, G. E. Addison, P. A. R. Ade, R. Allison, M. Amiri, N. Battaglia, J. A. Beall, F. de Bernardis, J. R. Bond, J. Britton, E. Calabrese, H.-m. Cho, K. Coughlin, D. Crichton, S. Das, R. Datta, M. J. Devlin, S. R. Dicker, J. Dunkley, R. Dünner, J. W. Fowler, A. E. Fox, P. Gallardo, E. Grace, M. Gralla, A. Hajian, M. Halpern, S. Henderson, J. C. Hill, G. C. Hilton, M. Hilton, A. D. Hincks, R. Hlozek, P. Ho, J. Hubmayr, K. M. Huffenberger, J. P. Hughes, L. Infante, K. Irwin, R. Jackson, S. Muya Kasanda, J. Klein, B. Koopman, A. Kosowsky, D. Li, T. Louis, M. Lungu, M. Madhavacheril, T. A. Marriage, L. Maurin,

F. Menanteau, K. Moodley, C. Munson, L. Newburgh, J. Nibarger, M. R. Nolta, L. A. Page, C. Pappas, B. Partridge, F. Rojas, B. L. Schmitt, N. Sehgal, B. D. Sherwin, J. Sievers, S. Simon, D. N. Spergel, S. T. Staggs, E. R. Switzer, R. Thornton, H. Trac, C. Tucker, M. Uehara, A. Van Engelen, J. T. Ward, and E. J. Wollack. The Atacama Cosmology Telescope: CMB polarization at 200 l 9000. J. Cosmology Astropart. Phys., 10:7, October 2014.

[133] D. Larson, J. Dunkley, G. Hinshaw, E. Komatsu, M. R. Nolta, C. L. Bennett, B. Gold, M. Halpern, R. S. Hill, N. Jarosik, A. Kogut, M. Limon, S. S. Meyer, N. Odegard, L. Page, K. M. Smith, D. N. Spergel, G. S. Tucker, J. L. Weiland, E. Wollack, and E. L. Wright. Seven-year Wilkinson Microwave Anisotropy Probe (WMAP) Observations: Power Spectra and WMAP-derived Parameters. ApJS, 192:16, February 2011.

[134] BICEP2 Collaboration, P. A. R Ade, R. W. Aikin, M. Amiri, D. Barkats, S. J. Benton, C. A. Bischoff, J. J. Bock, J. A. Brevik, I. Buder, E. Bullock, G. Davis, C. D. Dowell, L. Duband, J. P. Filippini, S. Fliescher, S. R. Golwala, M. Halpern, M. Hasselfield, S. R. Hildebrandt, G. C. Hilton, V. V. Hristov, K. D. Irwin, K. S. Karkare, J. P. Kaufman, B. G. Keating, S. A. Kernasovskiy, J. M. Kovac, C. L. Kuo, E. M. Leitch, N. Llombart, M. Lueker, C. B. Netterfield, H. T. Nguyen, R. O'Brient, R. W. Ogburn, IV, A. Orlando, C. Pryke, C. D. Reintsema, S. Richter, R. Schwarz, C. D. Sheehy, Z. K. Staniszewski, K. T. Story, R. V. Sudiwala, G. P. Teply, J. E. Tolan, A. D. Turner, A. G. Vieregg, P. Wilson, C. L. Wong, and K. W. Yoon. BICEP2 II: Experiment and Three-Year Data Set. *ArXiv e-prints*, March 2014.

[135] BICEP2/Keck and Planck Collaborations, P. A. R. Ade, N. Aghanim, Z. Ahmed, R. W. Aikin, K. D. Alexander, M. Arnaud, J. Aumont, C. Baccigalupi, A. J. Banday, and et al. Joint Analysis of BICEP2/Keck Array and Planck Data. *Physical Review Letters*, 114(10):101301, March 2015.

[136] L. Anderson, E. Aubourg, S. Bailey, D. Bizyaev, M. Blanton, A. S. Bolton, J. Brinkmann, J. R. Brownstein, A. Burden, A. J. Cuesta, L. A. N. da Costa, K. S. Dawson, R. de Putter, D. J. Eisenstein, J. E. Gunn, H. Guo, J.-C. Hamilton, P. Harding, S. Ho, K. Honscheid, E. Kazin, D. Kirkby, J.-P. Kneib, A. Labatie, C. Loomis, R. H. Lupton, E. Malanushenko, V. Malanushenko, R. Mandelbaum, M. Manera, C. Maraston, C. K. McBride, K. T. Mehta, O. Mena,

F. Montesano, D. Muna, R. C. Nichol, S. E. Nuza, M. D. Olmstead, D. Oravetz, N. Padmanabhan, N. Palanque-Delabrouille, K. Pan, J. Parejko, I. Pâris, W. J. Percival, P. Petitjean, F. Prada, B. Reid, N. A. Roe, A. J. Ross, N. P. Ross, L. Samushia, A. G. Sánchez, D. J. Schlegel, D. P. Schneider, C. G. Scóccola, H.-J. Seo, E. S. Sheldon, A. Simmons, R. A. Skibba, M. A. Strauss, M. E. C. Swanson, D. Thomas, J. L. Tinker, R. Tojeiro, M. V. Magaña, L. Verde, C. Wagner, D. A. Wake, B. A. Weaver, D. H. Weinberg, M. White, X. Xu, C. Yèche, I. Zehavi, and G.-B. Zhao. The clustering of galaxies in the SDSS-III Baryon Oscillation Spectroscopic Survey: baryon acoustic oscillations in the Data Release 9 spectroscopic galaxy sample. MNRAS, 427:3435–3467, December 2012.

[137] T. Tomaru, M. Hazumi, A. T. Lee, P. Ade, K. Arnold, D. Barron, J. Borrill, S. Chapman, Y. Chinone, M. Dobbs, J. Errard, G. Fabbian, A. Ghribi, W. Grainger, N. Halverson, M. Hasegawa, K. Hattori, W. L. Holzapfel, Y. Inoue, S. Ishii, Y. Kaneko, B. Keating, Z. Kermish, N. Kimura, T. Kisner, W. Kranz, F. Matsuda, T. Matsumura, H. Morii, M. J. Myers, H. Nishino, T. Okamura, E. Quealy, C. L. Reichardt, P. L. Richards, D. Rosen, C. Ross, A. Shimizu, M. Sholl, P. Siritanasak, P. Smith, N. Stebor, R. Stompor, A. Suzuki, J.-i. Suzuki, S. Takada, K.-i. Tanaka, and O. Zahn. The POLARBEAR-2 experiment. In *Society of Photo-Optical Instrumentation Engineers (SPIE) Conference Series*, volume 8452 of *Society of Photo-Optical Instrumentation Engineers (SPIE) Conference Series*, page 1, September 2012.

[138] Z. Staniszewski, R. W. Aikin, M. Amiri, S. J. Benton, C. Bischoff, J. J. Bock, J. A. Bonetti, J. A. Brevik, B. Burger, C. D. Dowell, L. Duband, J. P. Filippini, S. R. Golwala, M. Halpern, M. Hasselfield, G. Hilton, V. V. Hristov, K. Irwin, J. M. Kovac, C. L. Kuo, M. Lueker, T. Montroy, H. T. Nguyen, R. W. Ogburn, R. O'Brient, A. Orlando, C. Pryke, C. Reintsema, J. E. Ruhl, R. Schwarz, C. Sheehy, S. Stokes, K. L. Thompson, G. Teply, J. E. Tolan, A. D. Turner, A. G. Vieregg, P. Wilson, D. Wiebe, and C. L. Wong. The Keck Array: A Multi Camera CMB Polarimeter at the South Pole. *Journal of Low Temperature Physics*, 167:827–833, June 2012.

[139] M. Piat, E. Battistelli, A. Baù, D. Bennett, L. Bergé, J.-P. Bernard, P. de Bernardis, M.-A. Bigot-Sazy, G. Bordier, A. Bounab, E. Bréelle, E. F. Bunn, M. Calvo, R. Charlassier, S. Collin, A. Cruciani, G. Curran, L. Dumoulin, A. Gault, M. Gervasi, A. Ghribi, M. Giard, C. Giordano, Y. Giraud-Héraud, M. Gradziel, L. Guglielmi, J.-C. Hamilton,

V. Haynes, J. Kaplan, A. Korotkov, J. Landé, B. Maffei, M. Maiello, S. Malu, S. Marnieros, J. Martino, S. Masi, L. Montier, A. Murphy, F. Nati, C. O'Sullivan, F. Pajot, C. Parisel, A. Passerini, S. Peterzen, F. Piacentini, L. Piccirillo, G. Pisano, G. Polenta, D. Prêle, D. Romano, C. Rosset, M. Salatino, A. Schillaci, G. Sironi, R. Sordini, S. Spinelli, A. Tartari, P. Timbie, G. Tucker, L. Vibert, F. Voisin, R. A. Watson, and M. Zannoni. QUBIC: the QU Bolometric Interferometer for Cosmology. *Journal of Low Temperature Physics*, 167:872–878, June 2012.

[140] T. Matsumura, Y. Akiba, J. Borrill, Y. Chinone, M. Dobbs, H. Fuke, A. Ghribi, M. Hasegawa, K. Hattori, M. Hattori, M. Hazumi, W. Holzapfel, Y. Inoue, K. Ishidoshiro, H. Ishino, H. Ishitsuka, K. Karatsu, N. Katayama, I. Kawano, A. Kibayashi, Y. Kibe, K. Kimura, N. Kimura, K. Koga, M. Kozu, E. Komatsu, A. Lee, H. Matsuhara, S. Mima, K. Mitsuda, K. Mizukami, H. Morii, T. Morishima, S. Murayama, M. Nagai, R. Nagata, S. Nakamura, M. Naruse, K. Natsume, T. Nishibori, H. Nishino, A. Noda, T. Noguchi, H. Ogawa, S. Oguri, I. Ohta, C. Otani, P. Richards, S. Sakai, N. Sato, Y. Sato, Y. Sekimoto, A. Shimizu, K. Shinozaki, H. Sugita, T. Suzuki, A. Suzuki, O. Tajima, S. Takada, S. Takakura, Y. Takei, T. Tomaru, Y. Uzawa, T. Wada, H. Watanabe, M. Yoshida, N. Yamasaki, T. Yoshida, and K. Yotsumoto. Mission Design of LiteBIRD. *Journal of Low Temperature Physics*, 176:733–740, September 2014.

[141] The COrE Collaboration, C. Armitage-Caplan, M. Avillez, D. Barbosa, A. Banday, N. Bartolo, R. Battye, J. Bernard, P. de Bernardis, S. Basak, M. Bersanelli, P. Bielewicz, A. Bonaldi, M. Bucher, F. Bouchet, F. Boulanger, C. Burigana, P. Camus, A. Challinor, S. Chongchitnan, D. Clements, S. Colafrancesco, J. Delabrouille, M. De Petris, G. De Zotti, C. Dickinson, J. Dunkley, T. Ensslin, J. Fergusson, P. Ferreira, K. Ferriere, F. Finelli, S. Galli, J. Garcia-Bellido, C. Gauthier, M. Haverkorn, M. Hindmarsh, A. Jaffe, M. Kunz, J. Lesgourgues, A. Liddle, M. Liguori, M. Lopez-Caniego, B. Maffei, P. Marchegiani, E. Martinez-Gonzalez, S. Masi, P. Mauskopf, S. Matarrese, A. Melchiorri, P. Mukherjee, F. Nati, P. Natoli, M. Negrello, L. Pagano, D. Paoletti, T. Peacocke, H. Peiris, L. Perroto, F. Piacentini, M. Piat, L. Piccirillo, G. Pisano, N. Ponthieu, C. Rath, S. Ricciardi, J. Rubino Martin, M. Salatino, P. Shellard, R. Stompor, L. T. J. Urrestilla, B. Van Tent, L. Verde, B. Wandelt, and S. Withington. COrE (Cosmic Origins Explorer) A White Paper. *ArXiv e-prints*, February 2011.

[142] K. M. Smith, W. Hu, and M. Kaplinghat. Cosmological information from lensed CMB power spectra. Phys. Rev. D, 74(12):123002, December 2006.

[143] C. M. Hirata, S. Ho, N. Padmanabhan, U. Seljak, and N. A. Bahcall. Correlation of CMB with large-scale structure. II. Weak lensing. Phys. Rev. D, 78(4):043520, August 2008.

[144] C. L. Reichardt, P. A. R. Ade, J. J. Bock, J. R. Bond, J. A. Brevik, C. R. Contaldi, M. D. Daub, J. T. Dempsey, J. H. Goldstein, W. L. Holzapfel, C. L. Kuo, A. E. Lange, M. Lueker, M. Newcomb, J. B. Peterson, J. Ruhl, M. C. Runyan, and Z. Staniszewski. High-Resolution CMB Power Spectrum from the Complete ACBAR Data Set. ApJ, 694:1200–1219, April 2009.

[145] S. Das, B. D. Sherwin, P. Aguirre, J. W. Appel, J. R. Bond, C. S. Carvalho, M. J. Devlin, J. Dunkley, R. Dünner, T. Essinger-Hileman, J. W. Fowler, A. Hajian, M. Halpern, M. Hasselfield, A. D. Hincks, R. Hlozek, K. M. Huffenberger, J. P. Hughes, K. D. Irwin, J. Klein, A. Kosowsky, R. H. Lupton, T. A. Marriage, D. Marsden, F. Menanteau, K. Moodley, M. D. Niemack, M. R. Nolta, L. A. Page, L. Parker, E. D. Reese, B. L. Schmitt, N. Sehgal, J. Sievers, D. N. Spergel, S. T. Staggs, D. S. Swetz, E. R. Switzer, R. Thornton, K. Visnjic, and E. Wollack. Detection of the Power Spectrum of Cosmic Microwave Background Lensing by the Atacama Cosmology Telescope. *Physical Review Letters*, 107(2):021301, July 2011.

[146] A. van Engelen, R. Keisler, O. Zahn, K. A. Aird, B. A. Benson, L. E. Bleem, J. E. Carlstrom, C. L. Chang, H. M. Cho, T. M. Crawford, A. T. Crites, T. de Haan, M. A. Dobbs, J. Dudley, E. M. George, N. W. Halverson, G. P. Holder, W. L. Holzapfel, S. Hoover, Z. Hou, J. D. Hrubes, M. Joy, L. Knox, A. T. Lee, E. M. Leitch, M. Lueker, D. Luong-Van, J. J. McMahon, J. Mehl, S. S. Meyer, M. Millea, J. J. Mohr, T. E. Montroy, T. Natoli, S. Padin, T. Plagge, C. Pryke, C. L. Reichardt, J. E. Ruhl, J. T. Sayre, K. K. Schaffer, L. Shaw, E. Shirokoff, H. G. Spieler, Z. Staniszewski, A. A. Stark, K. Story, K. Vanderlinde, J. D. Vieira, and R. Williamson. A Measurement of Gravitational Lensing of the Microwave Background Using South Pole Telescope Data. ApJ, 756:142, September 2012.

[147] Planck Collaboration, P. A. R. Ade, N. Aghanim, M. Arnaud, M. Ashdown, J. Aumont, C. Baccigalupi, A. J. Banday, R. B. Bar-

reiro, J. G. Bartlett, and et al. Planck 2015 results. XV. Gravitational lensing. *ArXiv e-prints*, February 2015.

[148] Planck Collaboration, R. Adam, P. A. R. Ade, N. Aghanim, M. Arnaud, M. Ashdown, J. Aumont, C. Baccigalupi, A. J. Banday, R. B. Barreiro, and et al. Planck 2015 results. IX. Diffuse component separation: CMB maps. *ArXiv e-prints*, February 2015.

[149] Planck Collaboration, P. A. R. Ade, N. Aghanim, C. Armitage-Caplan, M. Arnaud, M. Ashdown, F. Atrio-Barandela, J. Aumont, C. Baccigalupi, A. J. Banday, and et al. Planck 2013 results. XVII. Gravitational lensing by large-scale structure. A&A, 571:A17, November 2014.

[150] F. Bianchini, P. Bielewicz, A. Lapi, J. Gonzalez-Nuevo, C. Baccigalupi, G. de Zotti, L. Danese, N. Bourne, A. Cooray, L. Dunne, S. Dye, S. Eales, R. Ivison, S. Maddox, M. Negrello, D. Scott, M. W. L. Smith, and E. Valiante. Cross-correlation between the CMB Lensing Potential Measured by Planck and High-z Submillimeter Galaxies Detected by the Herschel-Atlas Survey. ApJ, 802:64, March 2015.

[151] S. J. Maddox, L. Dunne, E. Rigby, S. Eales, A. Cooray, D. Scott, J. A. Peacock, M. Negrello, D. J. B. Smith, D. Benford, A. Amblard, R. Auld, M. Baes, D. Bonfield, D. Burgarella, S. Buttiglione, A. Cava, D. Clements, A. Dariush, G. de Zotti, S. Dye, D. Frayer, J. Fritz, J. Gonzalez-Nuevo, D. Herranz, E. Ibar, R. Ivison, M. J. Jarvis, G. Lagache, L. Leeuw, M. Lopez-Caniego, E. Pascale, M. Pohlen, G. Rodighiero, S. Samui, S. Serjeant, P. Temi, M. Thompson, and A. Verma. Herschel-ATLAS: The angular correlation function of submillimetre galaxies at high and low redshift. A&A, 518:L11, July 2010.

[152] J.-Q. Xia, M. Negrello, A. Lapi, G. De Zotti, L. Danese, and M. Viel. Clustering of submillimetre galaxies in a self-regulated baryon collapse model. MNRAS, 422:1324–1331, May 2012.

[153] A. Lapi, J. González-Nuevo, L. Fan, A. Bressan, G. De Zotti, L. Danese, M. Negrello, L. Dunne, S. Eales, S. Maddox, R. Auld, M. Baes, D. G. Bonfield, S. Buttiglione, A. Cava, D. L. Clements, A. Cooray, A. Dariush, S. Dye, J. Fritz, D. Herranz, R. Hopwood, E. Ibar, R. Ivison, M. J. Jarvis, S. Kaviraj, M. López-Caniego, M. Massardi, M. J. Michałowski, E. Pascale, M. Pohlen, E. Rigby, G. Rodighiero, S. Serjeant, D. J. B. Smith, P. Temi, J. Wardlow, and

P. van der Werf. Herschel-ATLAS Galaxy Counts and High-redshift Luminosity Functions: The Formation of Massive Early-type Galaxies. ApJ, 742:24, November 2011.

[154] J. González-Nuevo, A. Lapi, S. Fleuren, S. Bressan, L. Danese, G. De Zotti, M. Negrello, Z.-Y. Cai, L. Fan, W. Sutherland, M. Baes, A. J. Baker, D. L. Clements, A. Cooray, H. Dannerbauer, L. Dunne, S. Dye, S. Eales, D. T. Frayer, A. I. Harris, R. Ivison, M. J. Jarvis, M. J. Michałowski, M. López-Caniego, G. Rodighiero, K. Rowlands, S. Serjeant, D. Scott, P. van der Werf, R. Auld, S. Buttiglione, A. Cava, A. Dariush, J. Fritz, R. Hopwood, E. Ibar, S. Maddox, E. Pascale, M. Pohlen, E. Rigby, D. Smith, and P. Temi. Herschel-ATLAS: Toward a Sample of ˜1000 Strongly Lensed Galaxies. ApJ, 749:65, April 2012.

[155] E. A. Pearson, S. Eales, L. Dunne, J. Gonzalez-Nuevo, S. Maddox, J. E. Aguirre, M. Baes, A. J. Baker, N. Bourne, C. M. Bradford, C. J. R. Clark, A. Cooray, A. Dariush, G. De Zotti, S. Dye, D. Frayer, H. L. Gomez, A. I. Harris, R. Hopwood, E. Ibar, R. J. Ivison, M. Jarvis, M. Krips, A. Lapi, R. E. Lupu, M. J. Michałowski, M. Rosenman, D. Scott, E. Valiante, I. Valtchanov, P. van der Werf, and J. D. Vieira. H-ATLAS: estimating redshifts of Herschel sources from sub-mm fluxes. MNRAS, 435:2753–2763, November 2013.

[156] M. Killedar, P. D. Lasky, G. F. Lewis, and C. J. Fluke. Gravitational lensing with three-dimensional ray tracing. MNRAS, 420:155–169, February 2012.

[157] S. Hilbert, R. B. Metcalf, and S. D. M. White. Imaging the cosmic matter distribution using gravitational lensing of pre-galactic HI. MNRAS, 382:1494–1502, December 2007.

[158] H. M. P. Couchman, A. J. Barber, and P. A. Thomas. Measuring the three-dimensional shear from simulation data, with applications to weak gravitational lensing. MNRAS, 308:180–200, September 1999.

[159] C. Antolini, Y. Fantaye, M. Martinelli, C. Carbone, and C. Baccigalupi. N-body lensed CMB maps: lensing extraction and characterization. J. Cosmology Astropart. Phys., 2:39, February 2014.

[160] W. Hu and T. Okamoto. Mass Reconstruction with Cosmic Microwave Background Polarization. ApJ, 574:566–574, August 2002.

[161] R. Blandford and R. Narayan. Fermat's principle, caustics, and the classification of gravitational lens images. ApJ, 310:568–582, November 1986.

[162] F. Pace, M. Maturi, M. Meneghetti, M. Bartelmann, L. Moscardini, and K. Dolag. Testing the reliability of weak lensing cluster detections. A&A, 471:731–742, September 2007.

[163] M. R. Becker. CALCLENS: weak lensing simulations for large-area sky surveys and second-order effects in cosmic shear power spectra. MNRAS, 435:115–132, October 2013.

[164] S. Das and P. Bode. A Large Sky Simulation of the Gravitational Lensing of the Cosmic Microwave Background. ApJ, 682:1–13, July 2008.

[165] P. Fosalba, E. Gaztañaga, F. J. Castander, and M. Manera. The onion universe: all sky lightcone simulations in spherical shells. MNRAS, 391:435–446, November 2008.

[166] C. Vale and M. White. Simulating Weak Lensing by Large-Scale Structure. ApJ, 592:699–709, August 2003.

[167] B. Li, L. J. King, G.-B. Zhao, and H. Zhao. An analytic ray-tracing algorithm for weak lensing. MNRAS, 415:881–892, July 2011.

[168] M. Zaldarriaga and U. Seljak. All-sky analysis of polarization in the microwave background. Phys. Rev. D, 55:1830–1840, February 1997.

[169] M. Kamionkowski, A. Kosowsky, and A. Stebbins. Statistics of cosmic microwave background polarization. Phys. Rev. D, 55:7368–7388, June 1997.

[170] M. Baldi. The CoDECS project: a publicly available suite of cosmological N-body simulations for interacting dark energy models. MNRAS, 422:1028–1044, May 2012.

[171] C. Carbone, V. Springel, C. Baccigalupi, M. Bartelmann, and S. Matarrese. Full-sky maps for gravitational lensing of the cosmic microwave background. MNRAS, 388:1618–1626, August 2008.

[172] V. Springel, M. White, and L. Hernquist. Hydrodynamic Simulations of the Sunyaev-Zeldovich Effect(s). ApJ, 549:681–687, March 2001.

[173] W. A. Watson, J. M. Diego, S. Gottlöber, I. T. Iliev, A. Knebe, E. Martínez-González, G. Yepes, R. B. Barreiro, J. González-Nuevo, S. Hotchkiss, A. Marcos-Caballero, S. Nadathur, and P. Vielva. The Jubilee ISW project - I. Simulated ISW and weak lensing maps and initial power spectra results. MNRAS, 438:412–425, February 2014.

[174] G. Fabbian and R. Stompor. High-precision simulations of the weak lensing effect on cosmic microwave background polarization. A&A, 556:A109, August 2013.

[175] I. Kayo, A. Taruya, and Y. Suto. Probability Distribution Function of Cosmological Density Fluctuations from a Gaussian Initial Condition: Comparison of One-Point and Two-Point Lognormal Model Predictions with N-Body Simulations. ApJ, 561:22–34, November 2001.

[176] A. Taruya, M. Takada, T. Hamana, I. Kayo, and T. Futamase. Lognormal Property of Weak-Lensing Fields. ApJ, 571:638–653, June 2002.

[177] A. Benoit-Lévy, K. M. Smith, and W. Hu. Non-Gaussian structure of the lensed CMB power spectra covariance matrix. Phys. Rev. D, 86(12):123008, December 2012.

[178] K. M. Smith, W. Hu, and M. Kaplinghat. Weak lensing of the CMB: Sampling errors on B modes. Phys. Rev. D, 70(4):043002, August 2004.

[179] J. Errard and R. Stompor. Astrophysical foregrounds and primordial tensor-to-scalar ratio constraints from cosmic microwave background B-mode polarization observations. Phys. Rev. D, 85(8):083006, April 2012.

[180] A. Stebbins. Weak Lensing On the Celestial Sphere. *ArXiv Astrophysics e-prints*, September 1996.

[181] E. Krause and C. M. Hirata. Weak lensing power spectra for precision cosmology. Multiple-deflection, reduced shear, and lensing bias corrections. A&A, 523:A28, November 2010.

[182] P. Schneider, L. van Waerbeke, B. Jain, and G. Kruse. A new measure for cosmic shear. MNRAS, 296:873–892, June 1998.

[183] A. Cooray and W. Hu. Second-Order Corrections to Weak Lensing by Large-Scale Structure. ApJ, 574:19–23, July 2002.

[184] C. Shapiro and A. Cooray. The Born and lens lens corrections to weak gravitational lensing angular power spectra. J. Cosmology Astropart. Phys., 3:7, March 2006.

[185] S. Hagstotz, B. M. Schäfer, and P. M. Merkel. Born-corrections to weak lensing of the cosmic microwave background temperature and polarisation anisotropies. *ArXiv e-prints*, October 2014.

[186] S. Basak, S. Prunet, and K. Benabed. Simulating weak lensing of CMB maps. A&A, 508:53–62, December 2009.

[187] D.A. Varshalovich, A.N. Moskalev, and V.K. Khersonskiĭ. *Quantum Theory of Angular Momentum: Irreducible Tensors, Spherical Harmonics, Vector Coupling Coefficients, 3nj Symbols*. World Scientific Pub., 1988.

[188] S. Cole, S. Hatton, D. H. Weinberg, and C. S. Frenk. Mock 2dF and SDSS galaxy redshift surveys. MNRAS, 300:945–966, November 1998.

[189] R. G. Bower, A. J. Benson, R. Malbon, J. C. Helly, C. S. Frenk, C. M. Baugh, S. Cole, and C. G. Lacey. Breaking the hierarchy of galaxy formation. MNRAS, 370:645–655, August 2006.

[190] G. De Lucia and J. Blaizot. The hierarchical formation of the brightest cluster galaxies. MNRAS, 375:2–14, February 2007.

[191] S. Jouvel, J.-P. Kneib, O. Ilbert, G. Bernstein, S. Arnouts, T. Dahlen, A. Ealet, B. Milliard, H. Aussel, P. Capak, A. Koekemoer, V. Le Brun, H. McCracken, M. Salvato, and N. Scoville. Designing future dark energy space missions. I. Building realistic galaxy spectrophotometric catalogs and their first applications. A&A, 504:359–371, September 2009.

[192] A. Cabré and E. Gaztañaga. Have baryonic acoustic oscillations in the galaxy distribution really been measured? MNRAS, 412:L98–L102, March 2011.

[193] A. Font-Ribera, P. McDonald, and J. Miralda-Escudé. Generating mock data sets for large-scale Lyman-α forest correlation measurements. J. Cosmology Astropart. Phys., 1:1, January 2012.

[194] M. Manera, R. Scoccimarro, W. J. Percival, L. Samushia, C. K. McBride, A. J. Ross, R. K. Sheth, M. White, B. A. Reid, A. G. Sánchez, R. de Putter, X. Xu, A. A. Berlind, J. Brinkmann, C. Maraston,

B. Nichol, F. Montesano, N. Padmanabhan, R. A. Skibba, R. Tojeiro, and B. A. Weaver. The clustering of galaxies in the SDSS-III Baryon Oscillation Spectroscopic Survey: a large sample of mock galaxy catalogues. MNRAS, 428:1036–1054, January 2013.

[195] A. I. Merson, C. M. Baugh, J. C. Helly, V. Gonzalez-Perez, S. Cole, R. Bielby, P. Norberg, C. S. Frenk, A. J. Benson, R. G. Bower, C. G. Lacey, and C. d. P. Lagos. Lightcone mock catalogues from semi-analytic models of galaxy formation - I. Construction and application to the BzK colour selection. MNRAS, 429:556–578, February 2013.

[196] J. Carretero, F. J. Castander, E. Gaztañaga, M. Crocce, and P. Fosalba. An algorithm to build mock galaxy catalogues using MICE simulations. MNRAS, 447:646–670, February 2015.

[197] N. Katz, L. Hernquist, and D. H. Weinberg. Galaxies and gas in a cold dark matter universe. ApJ, 399:L109–L112, November 1992.

[198] V. Springel and L. Hernquist. Cosmological smoothed particle hydrodynamics simulations: a hybrid multiphase model for star formation. MNRAS, 339:289–311, February 2003.

[199] V. Springel. The cosmological simulation code GADGET-2. MNRAS, 364:1105–1134, December 2005.

[200] S. Gottlöber and G. Yepes. Shape, Spin, and Baryon Fraction of Clusters in the MareNostrum Universe. ApJ, 664:117–122, July 2007.

[201] V. Springel. Smoothed Particle Hydrodynamics in Astrophysics. ARA&A, 48:391–430, September 2010.

[202] S. D. M. White and M. J. Rees. Core condensation in heavy halos - A two-stage theory for galaxy formation and clustering. MNRAS, 183:341–358, May 1978.

[203] S. D. M. White and C. S. Frenk. Galaxy formation through hierarchical clustering. ApJ, 379:52–79, September 1991.

[204] G. Kauffmann, J. M. Colberg, A. Diaferio, and S. D. M. White. Clustering of galaxies in a hierarchical universe - I. Methods and results at z=0. MNRAS, 303:188–206, February 1999.

[205] S. Cole, C. G. Lacey, C. M. Baugh, and C. S. Frenk. Hierarchical galaxy formation. MNRAS, 319:168–204, November 2000.

[206] S. Hatton, J. E. G. Devriendt, S. Ninin, F. R. Bouchet, B. Guiderdoni, and D. Vibert. GALICS- I. A hybrid N-body/semi-analytic model of hierarchical galaxy formation. MNRAS, 343:75–106, July 2003.

[207] R. S. Somerville, P. F. Hopkins, T. J. Cox, B. E. Robertson, and L. Hernquist. A semi-analytic model for the co-evolution of galaxies, black holes and active galactic nuclei. MNRAS, 391:481–506, December 2008.

[208] A. J. Benson. G ALACTICUS: A semi-analytic model of galaxy formation. New A, 17:175–197, February 2012.

[209] A. Cooray and R. Sheth. Halo models of large scale structure. Phys. Rep., 372:1–129, December 2002.

[210] A. Klypin, S. Gottlöber, A. V. Kravtsov, and A. M. Khokhlov. Galaxies in N-Body Simulations: Overcoming the Overmerging Problem. ApJ, 516:530–551, May 1999.

[211] Q. Guo, S. White, C. Li, and M. Boylan-Kolchin. How do galaxies populate dark matter haloes? MNRAS, 404:1111–1120, May 2010.

[212] S. Trujillo-Gomez, A. Klypin, J. Primack, and A. J. Romanowsky. Galaxies in ΛCDM with Halo Abundance Matching: Luminosity-Velocity Relation, Baryonic Mass-Velocity Relation, Velocity Function, and Clustering. ApJ, 742:16, November 2011.

[213] A. P. Hearin, A. R. Zentner, A. A. Berlind, and J. A. Newman. SHAM beyond clustering: new tests of galaxy-halo abundance matching with galaxy groups. MNRAS, 433:659–680, July 2013.

[214] R. Aversa, A. Lapi, G. de Zotti, F. Shankar, and L. Danese. Black Hole and Galaxy Coevolution from Continuity Equation and Abundance Matching. *ArXiv e-prints*, July 2015.

[215] Y. P. Jing, H. J. Mo, and G. Börner. Spatial Correlation Function and Pairwise Velocity Dispersion of Galaxies: Cold Dark Matter Models versus the Las Campanas Survey. ApJ, 494:1–12, February 1998.

[216] E. Krause, C. M. Hirata, C. Martin, J. D. Neill, and T. K. Wyder. Halo occupation distribution modelling of green valley galaxies. MNRAS, 428:2548–2564, January 2013.

[217] J. L. Tinker. Redshift-space distortions with the halo occupation distribution - II. Analytic model. MNRAS, 374:477–492, January 2007.

[218] M. Magliocchetti and C. Porciani. The halo distribution of 2dF galaxies. MNRAS, 346:186–198, November 2003.

[219] Z. Zheng, I. Zehavi, D. J. Eisenstein, D. H. Weinberg, and Y. P. Jing. Halo Occupation Distribution Modeling of Clustering of Luminous Red Galaxies. ApJ, 707:554–572, December 2009.

[220] I. Zehavi, Z. Zheng, D. H. Weinberg, M. R. Blanton, N. A. Bahcall, A. A. Berlind, J. Brinkmann, J. A. Frieman, J. E. Gunn, R. H. Lupton, R. C. Nichol, W. J. Percival, D. P. Schneider, R. A. Skibba, M. A. Strauss, M. Tegmark, and D. G. York. Galaxy Clustering in the Completed SDSS Redshift Survey: The Dependence on Color and Luminosity. ApJ, 736:59, July 2011.

[221] A. Pujol and E. Gaztañaga. Are the halo occupation predictions consistent with large-scale galaxy clustering? MNRAS, 442:1930–1941, August 2014.

[222] J. A. Peacock and R. E. Smith. Halo occupation numbers and galaxy bias. MNRAS, 318:1144–1156, November 2000.

[223] L. Wang, A. Cooray, and S. Oliver. A Halo Model of Local IRAS Galaxies Selected at 60 Micron Using Conditional Luminosity Functions. *ArXiv e-prints*, October 2010.

[224] A. Cooray. Halo model at its best: constraints on conditional luminosity functions from measured galaxy statistics. MNRAS, 365:842–866, January 2006.

[225] F. C. van den Bosch, X. Yang, H. J. Mo, S. M. Weinmann, A. V. Macciò, S. More, M. Cacciato, R. Skibba, and X. Kang. Towards a concordant model of halo occupation statistics. MNRAS, 376:841–860, April 2007.

[226] J.-M. Alimi, V. Bouillot, Y. Rasera, V. Reverdy, P.-S. Corasaniti, I. Balmes, S. Requena, X. Delaruelle, and J.-N. Richet. DEUS Full Observable {\Lambda}CDM Universe Simulation: the numerical challenge. *ArXiv e-prints*, June 2012.

[227] Y. Rasera, J.-M. Alimi, J. Courtin, F. Roy, P.-S. Corasaniti, A. Füzfa, and V. Boucher. Introducing the Dark Energy Universe Simulation Series (DEUSS). In J.-M. Alimi and A. Fuözfa, editors, *American Institute of Physics Conference Series*, volume 1241 of *American Institute of Physics Conference Series*, pages 1134–1139, June 2010.

[228] I. Balmès, Y. Rasera, P.-S. Corasaniti, and J.-M. Alimi. Imprints of dark energy on cosmic structure formation - III. Sparsity of dark matter halo profiles. MNRAS, 437:2328–2339, January 2014.

[229] L. Blot, P. S. Corasaniti, J.-M. Alimi, V. Reverdy, and Y. Rasera. Matter power spectrum covariance matrix from the DEUS-PUR ΛCDM simulations: mass resolution and non-Gaussian errors. MNRAS, 446:1756–1764, January 2015.

[230] R. Teyssier. Cosmological hydrodynamics with adaptive mesh refinement. A new high resolution code called RAMSES. A&A, 385:337–364, April 2002.

[231] Y. Rasera and R. Teyssier. The history of the baryon budget. Cosmic logistics in a hierarchical universe. A&A, 445:1–27, January 2006.

[232] J. P. Huchra and M. J. Geller. Groups of galaxies. I - Nearby groups. ApJ, 257:423–437, June 1982.

[233] J. Einasto, A. A. Klypin, E. Saar, and S. F. Shandarin. Structure of superclusters and supercluster formation. III Quantitative study of the local supercluster. MNRAS, 206:529–558, February 1984.

[234] M. S. Warren, K. Abazajian, D. E. Holz, and L. Teodoro. Precision Determination of the Mass Function of Dark Matter Halos. ApJ, 646:881–885, August 2006.

[235] C. Lacey and S. Cole. Merger Rates in Hierarchical Models of Galaxy Formation - Part Two - Comparison with N-Body Simulations. MNRAS, 271:676, December 1994.

[236] W. H. Press and P. Schechter. Formation of Galaxies and Clusters of Galaxies by Self-Similar Gravitational Condensation. ApJ, 187:425–438, February 1974.

[237] A. Jenkins, C. S. Frenk, S. D. M. White, J. M. Colberg, S. Cole, A. E. Evrard, H. M. P. Couchman, and N. Yoshida. The mass function of dark matter haloes. MNRAS, 321:372–384, February 2001.

[238] M. White. The Mass Function. ApJS, 143:241–255, December 2002.

[239] J. Tinker, A. V. Kravtsov, A. Klypin, K. Abazajian, M. Warren, G. Yepes, S. Gottlöber, and D. E. Holz. Toward a Halo Mass Function for Precision Cosmology: The Limits of Universality. ApJ, 688:709–728, December 2008.

[240] M. Crocce, P. Fosalba, F. J. Castander, and E. Gaztañaga. Simulating the Universe with MICE: the abundance of massive clusters. MNRAS, 403:1353–1367, April 2010.

[241] J. Courtin, Y. Rasera, J.-M. Alimi, P.-S. Corasaniti, V. Boucher, and A. Füzfa. Imprints of dark energy on cosmic structure formation - II. Non-universality of the halo mass function. MNRAS, 410:1911–1931, January 2011.

[242] F. C. van den Bosch and F. Jiang. Statistics of Dark Matter Substructure: II. Comparison of Model with Simulation Results. *ArXiv e-prints*, March 2014.

[243] A. Lapi, S. Raimundo, R. Aversa, Z.-Y. Cai, M. Negrello, A. Celotti, G. De Zotti, and L. Danese. The Coevolution of Supermassive Black Holes and Massive Galaxies at High Redshift. ApJ, 782:69, February 2014.

[244] R. Pearson and O. Zahn. Cosmology from cross correlation of CMB lensing and galaxy surveys. Phys. Rev. D, 89(4):043516, February 2014.

[245] K. M. Smith, O. Zahn, and O. Doré. Detection of gravitational lensing in the cosmic microwave background. Phys. Rev. D, 76(4):043510, August 2007.

[246] T. Giannantonio and W. J. Percival. Using correlations between cosmic microwave background lensing and large-scale structure to measure primordial non-Gaussianity. MNRAS, 441:L16–L20, June 2014.

[247] Y. Omori and G. Holder. Cross-Correlation of CFHTLenS Galaxy Number Density and Planck CMB Lensing. *ArXiv e-prints*, February 2015.

[248] T. Giannantonio, P. Fosalba, R. Cawthon, Y. Omori, M. Crocce, F. Elsner, B. Leistedt, S. Dodelson, A. Benoit-Levy, D. Kirk, A. H. Bauer, B. A. Benson, G. M. Bernstein, J. Carretero, T. M. Crawford, R. Crittenden, E. Gaztanaga, G. Holder, D. Huterer, B. Jain, E. Krause, H. V. Peiris, W. J. Percival, C. L. Reichardt, A. J. Ross, B. Soergel, A. Stark, K. T. Story, J. D. Vieira, J. Weller, T. Abbott, F. B. Abdalla, S. Allam, R. Armstrong, M. Banerji, R. A. Bernstein, E. Bertin, D. Brooks, E. Buckley-Geer, D. L. Burke, D. Capozzi, J. E. Carlstrom, A. Carnero Rosell, M. Carrasco Kind, F. J. Castander, C. L. Chang,

C. E. Cunha, L. N. da Costa, C. B. D'Andrea, D. L. DePoy, S. Desai, H. T. Diehl, J. P. Dietrich, P. Doel, T. F. Eifler, A. E. Evrard, A. Fausti Neto, E. Fernandez, D. A. Finley, B. Flaugher, J. Frieman, D. Gerdes, D. Gruen, R. A. Gruendl, G. Gutierrez, W. L. Holzapfel, K. Honscheid, D. J. James, K. Kuehn, N. Kuropatkin, O. Lahav, T. S. Li, M. Lima, M. March, J. L. Marshall, P. Martini, P. Melchior, R. Miquel, J. J. Mohr, R. C. Nichol, B. Nord, R. Ogando, A. A. Plazas, A. K. Romer, A. Roodman, E. S. Rykoff, M. Sako, B. R. Saliwanchik, E. Sanchez, M. Schubnell, I. Sevilla-Noarbe, R. C. Smith, M. Soares-Santos, F. Sobreira, E. Suchyta, M. E. C. Swanson, G. Tarle, J. Thaler, D. Thomas, V. Vikram, A. R. Walker, R. H. Wechsler, and J. Zuntz. CMB lensing tomography with the DES Science Verification galaxies. *ArXiv e-prints*, July 2015.

[249] G. L. Pilbratt, J. R. Riedinger, T. Passvogel, G. Crone, D. Doyle, U. Gageur, A. M. Heras, C. Jewell, L. Metcalfe, S. Ott, and M. Schmidt. Herschel Space Observatory. An ESA facility for far-infrared and submillimetre astronomy. A&A, 518:L1, July 2010.

[250] S. Eales, L. Dunne, D. Clements, A. Cooray, G. de Zotti, S. Dye, R. Ivison, M. Jarvis, G. Lagache, S. Maddox, M. Negrello, S. Serjeant, M. A. Thompson, E. van Kampen, A. Amblard, P. Andreani, M. Baes, A. Beelen, G. J. Bendo, D. Benford, F. Bertoldi, J. Bock, D. Bonfield, A. Boselli, C. Bridge, V. Buat, D. Burgarella, R. Carlberg, A. Cava, P. Chanial, S. Charlot, N. Christopher, P. Coles, L. Cortese, A. Dariush, E. da Cunha, G. Dalton, L. Danese, H. Dannerbauer, S. Driver, J. Dunlop, L. Fan, D. Farrah, D. Frayer, C. Frenk, J. Geach, J. Gardner, H. Gomez, J. González-Nuevo, E. González-Solares, M. Griffin, M. Hardcastle, E. Hatziminaoglou, D. Herranz, D. Hughes, E. Ibar, W.-S. Jeong, C. Lacey, A. Lapi, A. Lawrence, M. Lee, L. Leeuw, J. Liske, M. López-Caniego, T. Müller, K. Nandra, P. Panuzzo, A. Papageorgiou, G. Patanchon, J. Peacock, C. Pearson, S. Phillipps, M. Pohlen, C. Popescu, S. Rawlings, E. Rigby, M. Rigopoulou, A. Robotham, G. Rodighiero, A. Sansom, B. Schulz, D. Scott, D. J. B. Smith, B. Sibthorpe, I. Smail, J. Stevens, W. Sutherland, T. Takeuchi, J. Tedds, P. Temi, R. Tuffs, M. Trichas, M. Vaccari, I. Valtchanov, P. van der Werf, A. Verma, J. Vieria, C. Vlahakis, and G. J. White. The Herschel ATLAS. PASP, 122:499–515, May 2010.